Hybrid photonic assemblies based on 3D-printed coupling structures

Zur Erlangung des akademischen Grades eines

DOKTORS DER INGENIEURWISSENSCHAFTEN
(Dr.-Ing.)

von der KIT-Fakultät für
Elektrotechnik und Informationstechnik
des Karlsruher Instituts für Technologie (KIT)

genehmigte

DISSERTATION

von

Yilin Xu, M.Sc.

geb. in Guangzhou, Guangdong, China

Tag der mündlichen Prüfung: 21.06.2022
Hauptreferent: Prof. Dr.-Ing. Christian Koos
Korreferent: Prof. Peter O'Brien, PhD
Korreferent: Prof. Dr.-Ing. Dr. h. c. Wolfgang Freude

Table of contents

Kurzfassung

Fortschritte in der Halbleitertechnologie und der lithografischen Herstellung integrierter elektronischer Schaltungen haben seit den 1960er Jahren die digitale Revolution vorangetrieben. Eine zunehmende Zahl von miteinander verbundenen Geräten, begleitet von zahlreichen neuen Diensten und Anwendungen, führt heute zu einem exponentiellen Wachstum des weltweiten Datenverkehrs. Optische Kommunikation wird aufgrund der hohen Bandbreite eingesetzt, um gewaltige Datenmengen sowohl über große Entfernungen als auch innerhalb von Datenzentren zu übertragen. Dies erfordert kostengünstige und energieeffiziente photonische Bauteile mit geringem Platzbedarf. Photonische integrierte Schaltkreise (engl. photonic integrated circuits, PIC) sollen diese Anforderungen erfüllen.

Ähnlich wie integrierte elektronische Schaltungen können PIC mit einer hohen Anzahl und Dichte photonischer Bauelemente in großem Maßstab auf Wafern hergestellt werden. Allerdings zeichnet sich die integrierte Photonik im Vergleich zur Mikroelektronik durch eine viel größere Diversität im Hinblick auf die verwendeten Materialsysteme aus, da viele unterschiedliche Bauelemente benötigt werden, die nicht auf jeder Plattform gleichermaßen realisierbar sind. Die Silizium-Photonik (SiP) profitiert beispielsweise von der ausgereiften CMOS-Fertigungstechnologie (engl. complementary metal-oxide-semiconductor). Der hohe Indexkontrast zwischen der dünnen Siliziumschicht und dem umgebenden Siliziumoxidmantel ermöglicht dabei stark führende optische Wellenleiter mit engen Biegeradien. Dadurch kann eine hohe Integrationsdichte erzielt werden. Andererseits verhindert der indirekte Bandübergang von Silizium aber auch eine effiziente Lichtemission. Zur Realisierung von Lasern und optischen Verstärkern werden stattdessen III-V-Verbindungshalbleiter wie Indiumgalliumarsenidphosphid (InGaAsP) verwendet, die eine direkte Bandlücke aufweisen. Die Notwendigkeit,

verschiedene Materialsysteme, z. B. innerhalb sogenannter Multi-Chip-Module zu kombinieren, erhöht die Gesamtkomplexität erheblich.

Die photonische Integration muss darüber hinaus das Problem lösen, optische Chips mit der Außenwelt zu verbinden. Um geringe Verluste zu erzielen, erfordern einmodige Verbindungen einen perfekten Modenfeldüberlapp zwischen den zu verbindenden Wellenleitern. Sie sind daher empfindlich gegenüber Fehlanpassung der Modenfeldgrößen, sowie gegenüber translatorischer und rotatorischer Fehlausrichtung. Gleichzeitig sind die Modenfelddurchmesser (MFD) sehr klein. Eine verlustarme Kopplung wird daher in der Regel nur mit aufwendigen und kostspieligen aktiven Ausrichtungsverfahren erreicht, bei denen die Platzierung der Komponenten auf Basis einer kontinuierlichen Messung der Kopplungseffizienz optimiert wird. Die optische Aufbau- und Verbindungstechnik ist daher ein erheblicher Kostentreiber für integriert-optische Systeme und ein begrenzender Faktor für die Massenfertigung ensprechender Produkte, obgleich auf Waferebene die Massenproduktion der Chips an sich ausgereift ist.

Die additive Mikrofertigung von dreidimensionalen (3D) optischen Freiform-Kopplungsstrukturen ist ein vielversprechendes Konzept zur Überwindung dieser Technologielücke. Die vorliegende Dissertation baut auf früheren Arbeiten [1, 2] auf und nutzt das Verfahren der Multiphotonenlithographie (MPL) zur Herstellung optischer Kopplungsstrukturen. Diese umfassen dielektrische Wellenleiter, sogenannte photonische Wirebonds (PWB), sowie Mikrolinsen an Bauteilfacetten (engl. facet-attached microlenses, FaML). Ausgehend von Prinzipstudien wurde die auf Mikrolinsen basierende Montagetechnologie wesentlich weiterentwickelt und in fortgeschrittenen, zuverlässigen Systemaufbauten demonstriert. Lösungen für die Laserintegration, die speziell auf das Problem der Empfindlichkeit gegenüber Rückreflexionen abzielen, werden sowohl für den auf PWB als auch für den auf Mikrolinsen basierenden Ansatz vorgestellt. Die einzelnen Kapitel dieser Arbeit behandeln folgende Themen:

Kapitel 1 erörtert die Bedeutung von photonischen integrierten Schaltkreisen und gibt eine kurze Einführung in das Themenfeld der photonischen Integration. Weiterhin werden Strategien vorgestellt, wie die Multiphotonenlithographie dabei

helfen kann, die Schwierigkeiten der optischen Aufbau- und Verbindungstechnik zu überwinden.

Kapitel 2 beschreibt die theoretischen und technologischen Grundlagen für die folgenden Kapitel. Die Grundlagen der Multiphotonenlithographie werden zusammengefasst, und es werden spezifische Methoden diskutiert, die für das Design und die Herstellung von 3D-gedruckten mikrooptischen Kopplungsstrukturen nützlich sind.

Kapitel 3 stellt einen schmalbandigen und weit abstimmbaren integrierten Diodenlaser mit externem Resonator (engl. external-cavity laser, ECL) vor. Ein PWB wird verwendet, um einen InP-Halbleiterlaserverstärkerchip mit einer auf SiP aufgebauten externen Rückkopplungsstruktur zu verbinden. Dies ist die erste Demonstration eines Lasers in Chipgröße, der auf einem 3D-gedruckten Kopplungselement innerhalb des Laserresonators beruht.

Kapitel 4 demonstriert die Fortschritte der optischen Montagetechnik unter Verwendung von Mikrolinsen. Die erhöhte Ausrichttoleranz erleichtert die gleichzeitige Verbindung mehrerer Elemente, die in Form eines Feldes angeordnet sind. Es werden verlustarme Kopplungen zwischen Einmodenfasern und SiP-Wellenleitern demonstriert sowie steckbare Faser-Chip-Verbindungen. Speziell entwickelte Linsen können die Freiraum-Koppeldistanz bis in den Millimeterbereich erhöhen, sodass diskrete optische Komponenten eingefügt werden können. Auch ein passiver Montageprozess wird gezeigt. Um Linienverbreiterung und Instabilitäten eines Halbleiterlasers zu vermeiden, kann der Anteil der Rückreflexion durch eine Kombination von Freiformlinsen und Prismen reduziert werden.

Kapitel 5 erweitert das Konzept der 3D-gedruckten Kopplungsstrukturen auf Quantenbauteile bei tiefen Temperaturen. Erstmalig werden supraleitende Nanodraht-Einzelphotonendetektoren (engl. superconducting nanowire single-photon detectors, SNSPD) durch gedruckte Mikrolinsen ergänzt, wodurch eine signifikante Vergrößerung der effektiven Lichtempfangsfläche erzielt wird.

Kapitel 6 fasst die vorliegende Arbeit zusammen und skizziert Ideen für eine Weiterentwicklung der Technologie für den 3D-Druck von Kopplungsstrukturen.

Mögliche zukünftige Forschungsrichtungen auf der Grundlage der bestehenden Technologie werden kurz diskutiert.

Preface

Advances in semiconductor technology and lithographic fabrication of integrated electronic circuits have powered the information-technology revolution since the 1960s. Today, an increasing number of interconnected devices, accompanied by numerous new services and applications, leads to an exponential growth of worldwide data traffic. High-bandwidth optical communications is used to transmit giant amounts of data over large distances as well as within data centers. This demands low-cost and energy efficient photonic devices with small footprint. Photonic integrated circuits (PIC) are expected to meet these requirements.

Similar to electronic integrated circuits, PIC containing a large number of densely integrated devices can be mass-fabricated on wafers. Photonics is, however, much more diverse than microelectronics, requiring a vast number of different devices which rely on different material platforms. Silicon photonics (SiP), for example, leverages mature complementary metal-oxide semiconductor (CMOS) fabrication technology. The high index contrast between the thin silicon device layer and the surrounding silicon-oxide cladding allows waveguides with strong optical confinement and tight bend radii, thereby leading to high integration density. The indirect band structure of silicon, however, prevents an efficient generation of light. Hence, direct-bandgap III-V compound semiconductors such as indium gallium arsenide phosphide (InGaAsP) are used for light sources and optical amplifiers. The necessity to combine different materials, e.g., by an assembly of multi-chip modules, adds significantly to the overall complexity.

In addition, photonic integration needs to solve the problem of connecting optical chips to the outside world. Single-mode waveguide connections require a perfect modal overlap to achieve low loss and are therefore sensitive to both modal

mismatch as well as to spatial and angular misalignment. At the same time, the mode field diameters (MFD) are tiny. Low-loss coupling is hence only achieved with time-consuming expensive active alignment techniques, where the positions of the components are optimized based on a continuous measurement of the coupling efficiency during the alignment process. Optical packaging has therefore been a significant cost driver for integrated optical systems and a limiting factor for mass-fabrication of corresponding products, despite the mature wafer level production of the chips themselves.

Additive micro-fabrication of three-dimensional (3D) free-form optical coupling structures is a promising concept to overcome this technology gap. This thesis builds upon previous work [1, 2] and uses multi-photon lithography (MPL) to fabricate dielectric waveguides, so-called photonic wire bonds (PWB), as well as facet attached microlenses (FaML). Starting from proof-of-principle studies, the assembly technology using FaML is advanced significantly, leading to sophisticated and reliable system demonstrations. Solutions for laser integration that specifically target the problem of sensitivity with respect to backreflections are presented for both the PWB and the FaML-based approach. The individual chapters of this work cover the following subjects:

Chapter 1 discusses the relevance of PIC and gives a short introduction to the field of photonic integration. The strategies how multi-photon lithography can help to overcome the difficulties of multi-chip assembly and optical packaging are introduced.

Chapter 2 lays the theoretical and technological foundation for the following chapters by reviewing the principles of multi-photon lithography and by discussing specific methods useful for the design and fabrication of 3D-printed micro-optical coupling structures.

Chapter 3 presents a widely tunable narrow linewidth external-cavity laser (ECL) that uses a PWB to efficiently connect an InP gain chip to a SiP external feedback circuit. This represents the first demonstration of a chip-scale laser that relies on a 3D-printed coupling element within the cavity.

Chapter 4 demonstrates advances in connecting waveguide arrays using FaML. Low-loss coupling between SMF and SiP waveguides and (re-)pluggable fiber-chip connections are demonstrated. Specially designed lenses increase the free-space coupling distance to the millimeter range such that discrete optical components can be inserted. A passive assembly process is shown. For avoiding linewidth broadening and instabilities of a semiconductor laser, the backreflection factor can be reduced by a combination of free-form lenses and prisms which are attached to the laser endface.

Chapter 5 extends the concept of 3D-printed coupling structures to quantum devices that are operated under cryogenic conditions. For the first time, superconducting nanowire single-photon detectors (SNSPD) are supplemented by free-form microlenses, resulting in a significant increase of the effective light-receiving area.

Chapter 6 summarizes the work in this thesis and outlines ideas for further improvement of the technology for 3D-printing of coupling structures. Potential future research directions based on existing technology are briefly discussed.

Achievements of the present work

In this thesis, both photonic wire bonds (PWB) and facet-attached microlenses (FaML) are used to demonstrate techniques for hybrid multi-chip and fiber-to-chip assemblies. Existing tools and methods for the design and fabrication of 3D-printed coupling structures are refined, enabling various novel applications. In particular, an assembly using FaML is advanced from proof-of-principle studies [2] to the realization of sophisticated system demonstrations. Solutions for laser integration that specifically target the problem of backreflection sensitivity are presented for both the PWB and the FaML-based approach.

A concise overview of the major achievements is given in the following list:

First demonstration of hybrid external-cavity lasers (ECL) with PWB as intra-cavity coupling elements: A new class of hybrid ECL is demonstrated, that rely on PWB to connect InP gain elements to external feedback circuits on SiP chips. A proof-of-concept device offers a tuning range of more than $50\,\mathrm{nm}$, a side mode suppression ratio (SMSR) above $40\,\mathrm{dB}$, and an intrinsic linewidth of $105\,\mathrm{kHz}$, see Section 3.2.4 and journal publication [J1] for details.

Implementation of an advanced software environment for simulation of micro-optical lens systems: The design of microlenses and micro-optical lens systems require fast and reliable wave-optical simulation tools. The previously existing simulation capabilities based on the scalar wave propagation method were significantly expanded within the scope of this thesis, building upon preliminary work [1], see Section 2.2. Many features commonly known from commercial optic design software have been implemented. These include object-oriented implementation of individual surface shapes, lenses, prisms and other optical elements and their assembly into complex compound micro-optical systems including

necessary coordinate transformations. Furthermore, wave-optical tolerancing has been implemented. Finally, a zeroth-order correction of Fresnel reflection losses within the scalar method has been introduced, see Section 2.2.3 for details.

Proof-of-principle demonstration of a phase-resolved mode-field measurement method: An entirely reliable microlens design procedure would require the knowledge of the optical phase distribution of the mode field at the facet plane rather than simply assuming a plane phase front. A phase-resolved measurement method is proposed, based on a modified Gerchberg-Saxton algorithm. The algorithm considers observed intensities at multiple planes. In a proof-of-principle demonstration, phase masks are 3D-printed to the facets of single-mode fibers (SMF), and the resulting phase distributions are reconstructed.

Ultra-low loss and alignment-tolerant edge coupling between single-mode fibers (SMF) and silicon photonic (SiP) waveguides, and first demonstration of a pluggable edge-coupled SMF-to-SiP connection: Using FaML, an SMF array with eight fibers is connected to a SiP chip with an average loss of $1.44\,\mathrm{dB}$ per connection. A $1\,\mathrm{dB}$ tolerance of $6\,\mathrm{\mu m}$ and $1.1°$ is achieved for radial and angular misalignment, respectively. This allows for pluggable SMF-to-chip connections with losses of $(1.9 \pm 0.5)\,\mathrm{dB}$, see Section 4.3 and the envisaged journal publication [J2] for details.

First demonstration of a passively aligned SMF-to-chip connection using 3D-printed microlenses: Machine vision assisted passive alignment requires that FaML-equipped chips emit precisely and consistently into the direction as expected from the chip geometry and measurement of the chip orientation within an assembly machine. To this end, the underlying processes for printing of FaML are thoroughly optimized. Automated alignment procedures are developed on an assembly machine similar to ones used by industrial manufacturers. A passively aligned assembly shows that no excess losses occur compared to active alignment, within a measurement uncertainty of $\pm 3\%$, see Section 4.4 and the envisaged journal publication [J2] for details.

Extension of microlens-based free-space coupling distances to the millimeter range, and first demonstration of a microlens coupled SMF-to-chip connection

with the insertion of an additional discrete optical component: A FaML-assisted fiber-chip assembly with an optimum free-space coupling distance of 3.3 mm is realized. The special FaML with a compact Galilean telescope design transforms an input mode-field diameter of 10 µm to a free-space beam waist of 60 µm. As an exemplary discrete optical component, a polarization beam splitter prism is inserted within the collimated free-space beam path. Further details are found in Section 4.4 and the envisaged journal publication [J2].

Demonstration of a novel micro-optics design for alignment-tolerant coupling of arrays of backreflection-sensitive angled-facet semiconductor lasers: A fiber-coupled laser module using facet-attached 3D-printed coupling elements is built. Within the module, a bar of highly backreflection-sensitive angled-facet InP distributed-feedback (DFB) lasers is connected to an SMF array using a novel micro-optics design that consists of a special combination of microlenses and prisms, and that offers average coupling losses of 2 dB alongside return losses of 44 dB or better. The performance is comparable to advanced lensed fibers with anti-reflection (AR) coating, while offering much larger alignment tolerances. In a rigorous study, the printed structures are found to neither spoil the laser spectrum nor to modify the threshold pump current. Further details are found in Section 4.5 and the envisaged journal publication [J2].

First demonstration of 3D-printed microlenses that supplement superconducting nanowire single-photon detectors (SNSPD) under cryogenic conditions: Free-form microlenses are printed on top of the sensitive area of SNSPD to increase the effective light-receiving area. Operation is demonstrated at a temperature of 4 K. Using a detector with $4.5\,\mu m \times 4.5\,\mu m$ sensitive area and a lens of 60 µm diameter, a 100-fold increased effective collection area is achieved for a plane-wave-like free-space illumination. Further details are found in Section 5.4 and journal publication [J3].

1 Introduction

Advances in semiconductor technology and lithographic fabrication of integrated electronic circuits have powered the information-technology revolution [3, 4] since the 1960s. Digital photography, personal computers and smartphones have become integral parts of today's world, and new types of interconnected devices continue to appear on the market. The increasing number of devices connected to the internet is accompanied by numerous new services and applications, such as remote work, video streaming, augmented and virtual reality, autonomous driving, as well as smart industrial production using advanced robotics. Global internet traffic is therefore ever-increasing and is expected to reach 4.8 zettabytes per year by 2022 [5]. High-bandwidth optical communications is used to transmit these giant amounts of data over large distances and within data centers [6]. Typically, however, data originate and are processed in electronic form. Apart from laser sources, optical communication thus requires devices for electro-optic conversion, i.e., modulators and photodiodes. Using integrated devices allows for fast, efficient and scalable optical communication systems [7]. Optical communication has therefore been the most important driver for photonic integration and photonic integrated circuit (PIC) technology.

Similar to electronic integrated circuits, PIC containing a large number of densely integrated photonic devices can be mass-fabricated on a wafer. The application areas of PIC are not limited to optical communication only. Recently, there is an increasing interest to utilize PIC technology for metrology and life science applications as well. Prominent examples include optical coherence tomography (OCT, [8, 9]), light detection and ranging (solid state LiDAR, [10, J4]), and waveguide-based photonic sensors [11] for point-of-care diagnostics. Driven by these demands, photonic integration technology currently advances at a fast pace.

Many developments previously seen in electronic integration are currently repeated in a similar way. There are, however, two major differences.

The first difference concerns the integrated devices and material platforms. In microelectronics, there is one most important device, the transistor, dominantly realized on the complementary metal-oxide semiconductor (CMOS) technology platform. Photonics is, however, much more diverse. A vast number of different devices are required, such as light sources, low-loss or special-property wave-guides, phase shifters, modulators, splitters, (ring) resonators and photodiodes. Naturally, all these devices are not equally well realizable on different material platforms. Silicon photonics (SiP), for example, leverages mature CMOS fabrication technology and exploits the fact that the high index contrast between the silicon device layer and the surrounding silicon-oxide cladding allows waveguides with strong optical confinement and tight bend radii. A high integration density can therefore be achieved. Silicon has a bandgap corresponding to the photon energy of light with 1.1 µm wavelength, and is therefore transparent for typical optical communication wavelengths around 1.3 µm and 1.5 µm. Apart from passive components such as waveguides, splitters and grating couplers, it is furthermore possible to realize efficient waveguide-coupled germanium (Ge) photodiodes [12] as well as electro-optic modulators based on the plasma dispersion effect [13]. On the other hand, the indirect band structure of silicon prevents efficient light emission. Instead, diode lasers at communication wavelengths are realized on an indium phosphide (InP) material platform and employ the III-V compound semiconductor indium gallium arsenide phosphide (InGaAsP) as a gain medium. Wafers of InP can be structured into complex PIC as well, and monolithic integration of entire transceivers on InP is possible [14]. However, the InP platform suffers from drawbacks including expensive raw material, technologically complex fabrication steps with lower yield, and brittleness that limits the wafer size. In addition to SiP and InP, there exist many more material platforms with distinct features. Most notably, various flavors of the silicon nitride (SiN) platform [15–17] extend the transparency window into the visible range [18]. Ultra low-loss SiN waveguides are particularly useful for frequency-selective resonant filters. These can be utilized within frequency-selective feedback circuits for highly-performant

compact tunable external-cavity lasers [19]. Furthermore, and in contrast to SiP, the optical power handling capability of SiN is much larger, because two-photon absorption (TPA) and TPA-induced free carrier absorption (FCA) [20] do not play a role. Instead, SiN shows a Kerr-nonlinearity [17] as well as anomalous dispersion for an appropriate waveguide cross-section. These effects are used for the generation of soliton Kerr frequency combs within high-Q SiN ring resonators [17, 21, 22]. Based on the aforementioned examples, it becomes clear that photonic integration often requires the combination of different material platforms. Heterogeneous integration methods combine different materials on the same die using wafer bonding technology [23, 24]. Hybrid integration techniques on the other hand combine different dies by an assembly of multi-chip modules, where light needs to be coupled from one chip to another. Heterogeneous integration is more suited for mass production, but it is technologically more complex [25], and not readily applicable for all material combinations. In comparison, hybrid integration is much more versatile. To date, there is no clear "winner", and intensive research is being conducted in both methods.

The second difference concerns the details of the assembly and packaging processes. In electronics, the challenges of connecting a chip to the outside world are essentially solved. Metal connection pads on the chip surface have a typical dimension in the order of $100\,\mu m \times 100\,\mu m$. Connecting a gold bond wire to such a metal pad thus requires only moderate precision, albeit high-frequency signals may require special care. Alternatively, a larger number of connections can be simultaneously established in a flip-chip bonding process using reflow soldering techniques. The situation is far more complicated for optical interconnects. The PIC needs to be connected to a single-mode fiber (SMF), and in case of hybrid multi-chip modules, different PIC need to be connected to each other in addition. Single-mode connections require a perfect modal overlap to achieve low loss and are therefore sensitive to both modal mismatch as well as to spatial and angular misalignment. At the same time, the involved mode field diameters (MFD) are tiny and may differ vastly. The largest MFD belongs to the SMF, with a size of $10\,\mu m$ at a wavelength of $1550\,nm$, whereas the MFD of on-chip SiP waveguides has a dimension in the order of merely $500\,nm$. Most SiP chips and InP lasers

employ mode expanding edge couplers, but the expanded MFD is typically still below $3\,\mu$m. Lateral alignment tolerances are extremely tight with such small mode field diameters. As an example, we assume that source and sink both possess perfectly matched Gaussian mode fields with MFD of $10\,\mu$m, corresponding to the MFD of a SMF. Even in this case, the radial $1\,$dB tolerance amounts only to $0.24 \times \mathrm{MFD} = 2.4\,\mu$m. The accuracy of passive alignment procedures is usually insufficient in comparison. Low-loss coupling is therefore commonly only achieved with slow, expensive active alignment techniques [26, 27], where the placement of the component is optimized based on continuous monitoring of the coupling efficiency. Such a process is complex and time consuming, especially if electrical or optical probing is needed to derive the monitored test signals, or when multiple connections are to be established at the same time. In many cases, some method of mode field adaption is necessary. Direct butt-coupling of an InP laser with $3\,\mu$m MFD to an SMF, for example, leads to a coupling loss of approximately $5.5\,$dB. Classical approaches for mode field matching, such as lensed fibers or small discrete optical components, increase the count of parts which need to be actively aligned. Optical packaging is therefore a significant cost driver [28] for integrated optical systems and a limiting factor for mass-fabrication of corresponding products, despite the mature wafer level production of the chips themselves. Colloquially, this technological gap has been referred to as the "valley of death" [29] between innovation in the lab and a commercial production.

Additive micro-fabrication of three-dimensional (3D) free-form optical coupling structures is a promising concept to overcome this gap. Multi-photon lithography (MPL, [30]) allows to fabricate near-arbitrary 3D structures with exceptionally small feature sizes down to below $100\,$nm [31, 32]. A tightly focused femtosecond laser beam initiates a localized polymerization of a precursor material, forming a transparent polymer structure. MPL systems share many similarities with nonlinear microscopes. As a result, microscopic imaging techniques such as bright field imaging, scanning confocal laser imaging, or nonlinear florescence imaging can be directly transferred to lithography systems and are used to precisely align printed structures with respect to optical interfaces on a chip. Alignment accuracies within $100\,$nm have been demonstrated [33]. Previous work studied hybrid multi-chip and

fiber-chip assembly using 3D-printed dielectric waveguides, so-called photonic wire bonds (PWB, [33, 34]), as well as fiber-chip coupling using facet-attached microlenses (FaML, [2]). The first approach using PWB is in analogy to electrical wire bonding. In this approach, photonic chips and fibers are first fixed in their final position with moderate accuracy. The position and orientation of optical coupling interfaces are subsequently detected within the MPL system. The starting and ending position of each PWB is adjusted accordingly and a suitable 3D trajectory is found. Tapered sections at the coupling points on either end of the PWB match the MFD of the individual coupling interfaces. In the second approach using FaML, beam-expanding microlenses are printed to the facets of each individual chip or fiber component prior to final assembly. The lenses match the mode-field diameters and thus relax lateral alignment tolerances. In a subsequent step, the lensed components are aligned with respect to each other, and the assembly is finally fixed with a glue. Due to the expanded beams, the alignment of lensed components is much simpler than without printed lenses, and passive assembly based on machine vision or self-aligning techniques becomes possible. One major difference of the PWB and the FaML-approach is the assembly order. The MPL step happens after fixing of the individual chips and fibers to a common submount in case of PWB, and before the final assembly step for FaML.

A detailed comparison of advantages and disadvantages of PWB versus FaML needs to consider fabrication-specific limitations as well as assembly-specific details. Only a few basic differences are elaborated in the following. We note but disregard the fact that long and thin PWB waveguides are at the very limit of MPL fabrication capabilities [1]. Evidently, photonic wire bonding has two conceptual advantages over FaML-assisted assembly strategies. First, alignment of photonic chips and fibers can be done more coarsely when using PWB. This is at least true if parameters such as maximum write field of the MPL system, or maximum PWB curvature do not become limiting and assuming that the question of polarization maintenance through arbitrary 3D trajectories [1] is of no relevance. In a lab environment, manual placement suffices, and a dedicated assembly machine is not necessary. Second, the printed volume of a PWB is by far smaller than the one of a FaML, leading to much faster fabrication times. However, the method

is only suited for bridging comparatively short distances (typically $< 400\,\mu m$) between devices. Furthermore, complying with the assembly order for PWB is not always feasible. For example, it might not be possible to safely expose the assembly or parts thereof to photoresist or associated developers due to chemical incompatibilities. In some cases, part of the assembly protrudes from the surface, and the working distance of the MPL objective, which typically amounts to a few hundred µm, becomes a limiting issue.

Research along both paths is therefore further pursued, and the experimental demonstrations within this thesis comprise both PWB and FaML. In particular, starting from proof-of-principle studies, the assembly technology using FaML is advanced significantly, leading to sophisticated and reliable system demonstrations. Using FaML, alignment-tolerant coupling between SMF and SiP waveguides is shown, allowing for simultaneous coupling of multiple connections with losses consistently as low as $1.4\,dB$, as well as (re-)pluggable fiber-chip connections. Specially designed lenses can increase the free-space coupling distance to the millimeter range such that discrete optical components can be inserted. A passively aligned FaML-aided assembly process is demonstrated.

When it comes to integration of semiconductor lasers, avoiding backreflection-associated linewidth broadening and laser instabilities is of particular importance and yet difficult to achieve. One solution which sidesteps this problem is to define the laser cavity by a multi-chip module instead of using a stand-alone laser diode. A PWB can connect an InP semiconductor optical amplifier chip with a SiP or SiN external feedback circuit, forming a chip-scale external-cavity laser (ECL). The resilience of ECL against backrelections is inherently higher than, e.g., for distributed feedback (DFB) lasers [35]. Alternatively, angled-facet DFB lasers can be combined with free-form lenses and prisms which are directly printed to the laser endface. A corresponding arrayed laser-to-SMF assembly demonstrates coupling losses of $2\,dB$ along with a backflection factor below $-44\,dB$.

Finally, 3D-printed coupling structures can be employed for novel applications that require cryogenic temperature levels. One application example is the increase

of the effective light-receiving area of superconducting nanowire single-photon detectors (SNSPD) by free-form microlenses.

2 Theoretical and technological background

This chapter covers the theoretical and technological background associated with 3D-printing of coupling structures via multi-photon lithography (MPL). Section 2.1 describes the fabrication tools and methods and gives a general introduction to MPL, followed by a brief description of the MPL machine used within this work. Printing of microlenses to vertical chip facets leads to a few intricacies, and the associated solutions developed in this work are presented at the end of Section 2.1. Section 2.2 covers the simulation of microlenses using a reformulation of the the scalar wave-propagation method (WPM) for step-index structures [36]. A modification to the algorithm for an approximative treatment of Fresnel losses within the scalar method is proposed. Section 2.3 discusses techniques for an accurate mode-field measurement. A phase-resolved mode-field measurement method is demonstrated in a proof-of-principle experiment. Finally, the influence of the facet-embedding medium on mode fields and mode-field measurements is discussed.

2.1 Multi-photon three-dimensional lithography

2.1.1 Fundamentals of multi-photon lithography

Multi-photon lithography (MPL) is a laser-based additive micro- and nanofabrication technique, which allows for fabrication of complex three-dimensional

structures with highest resolution. The technology has found its way into a vast range of applications, such as microfluidics [37], biological cell templates [38, 39], microrobots [40, 41], photonic crystals [42], metamaterials [43, 44], microlenses [2, 45, 46], diffractive optical elements [47, 48], and dielectric optical waveguides [33, 34]. We base our following review of the fundamental principles of MPL mainly on Chapters 1.3, 3.1, 7, and 8 of [30]. Additional references are given where appropriate.

The process of two-photon absorption was first predicted in 1931 by Maria Göppert-Mayer[1] [49]. Experimental demonstration of two-photon polymerization, however, required a high-power pulsed laser focused to a tiny spot, and it was therefore not until 1997 that Maruo et al. [50] pioneered two-photon lithography. Today, low-cost and compact fiber-based femtosecond lasers have largely replaced the significantly more expensive mode-locked titanium-sapphire lasers as MPL light sources, and commercial lithography machines have become readily available.

Almost all MPL systems employ a negative-tone photoresist, where exposed parts are solidified and thereby rendered insoluble to a solvent in a subsequent development process. The photoresist consists of soluble organic monomers and a photoactive substance. In the most common case of radical photopolymerization, the photoactive substance is referred to as photoinitiator[2]. The photoinitiator generates free radicals upon exposure to light and initiates a radical-polymerization chain reaction[3], where the monomers[4] with one or multiple functional groups are cross-linked to form a polymer chain or network. For an unrestrained propagating chain growth, the exposure in one small region of the photoresist would cause the entire material to be cross-linked. In practice however, the chain reaction is terminated by either encountering other radicals or inhibitors such as dissolved

---

[1]   The two-photon absorption cross-section is hence typically given in the non-SI unit Göppert-Mayer (GM), $1\,\mathrm{GM} = 1 \times 10^{-50}\,\mathrm{cm}^4$ s per photon and molecule.

[2]   Alternatively, the polymerization can be initiated using photogenerated cations (cationic photopolymerization [51]). The photoactive substance is then referred to as photoacid generator (PAG).

[3]   The addition of a photogenerated radical to a monomer forms a new radical, which in turn reacts with another monomer to form a larger (macro-)radical.

[4]   The most common monomers used for radical polymerization are (meth)acrylates [52].

molecular oxygen [52] or deliberately added quenchers [31]. These termination effects are typically strong enough such that the size of the polymerized volume element (voxel) is primarily determined by the exposure to the lithography radiation [53].

The locally achieved degree of polymerization within a small volume element is mainly determined by the (total) amount of generated radicals within this volume element. We further consider an exposure time τ, a local photon flux ϕ proportional to the laser power P, and a multiphoton excitation with nonlinearity order N, where N simultaneously absorbed photons are required to generate one radical. A deposited lithography dose D is therefore typically expressed as $D \propto \tau \phi^N \propto \tau P^N$ [54]. The order of nonlinearity N depends on the photoresist and the wavelength of the lithography laser. Many photoinitiators known from traditional photolithography with ultraviolet (UV) light also exhibit two-photon absorption ($N = 2$) around $800\,\mathrm{nm}$, i.e., at half the UV-photon energy[5]. Using such photoinitiators, the mechanisms for the generation of radicals may however still involve more complex absorption processes, such as cascaded absorption via a triplet state [54], leading to nonlinearity orders[6] of $N > 2$ in many cases.

Despite the complex reaction kinetics, it is possible to largely describe MPL using two simple assumptions [56, 57], the so-called "(step-)threshold model" and the so-called "accumulation model". According to the threshold model, the solubility of the exposed material behaves highly nonlinear with respect to the deposited dose and can be approximated by a step-like behavior: The material is only suffiencently cross-linked above a threshold dose D_{th}, and all regions with $D < D_{\mathrm{th}}$ are washed away during development of the sample. According to the accumulation model, the photoresist "integrates" the doses from exposures at the

---

[5]   Coincidentally, this also matches the wavelength of the historically used mode-locked titanium sapphire lasers, and may be regarded as the reason, why the lithography wavelength around 800 nm is still widely used to date.

[6]   The nonlinearity order has been experimentally studied by varying the lithography laser repetition rate and the pulse energy when exposing lines with a constant velocity [54], or alternatively by a two-beam initiation threshold (2-BIT) technique [55].

same or nearby locations. Effects such as diffusion or decay of radicals are thus entirely neglected[7].

For a point exposure, we may simulate the deposited dose distributions for different nonlinearity orders N and different vacuum wavelengths λ of the lithography laser, see Fig. 2.1. To this end, we consider the optical point-spread function (PSF) of a high numerical aperture (NA) lithography objective. The underlying optical PSF in Fig. 2.1 are numerically calculated based on the vectorial Debye approximation[8], see [61, 62] and Appendix C, Eqs. (C.4)-(C.7). Comparing Fig. 2.1(a) and Fig. 2.1(b), we find that at the same lithography wavelength of, e.g., 780 nm, the dose distribution for two-photon absorption ($N = 2$) is clearly more confined than the dose distribution for single photon absorption ($N = 1$). In general, an N-photon absorption process enhances the optical resolution approximately by a factor of $\sqrt{N}$. A common misconception based on this observation is the idea that the advantage of two- or multi-photon lithography would be the ability to produce a smaller individual polymerized voxel. This idea is wrong because of two reasons. First and foremost, by adjusting the laser power, one can ensure that only an arbitrary small portion of the dose distribution lies just barely above the threshold dose D_{th}. In Figure 2.1, this portion could be for example given by any of the contour lines. By virtue of the threshold model, an "arbitrarily small"[9] polymerized voxel can theoretically be generated, independent of lithography

---

7   The accumulation model has its limits for long exposure times and low intensities. In the extreme case of very low intensities, the dose may fail to accumulate, even if the same location is illuminated indefinitely. This is known as Schwarzschild effect [58], in analogy to a similar effect in analog photography.

8   Calculations are shown for an input plane-wave illumination with circular polarization. We further consider the nowadays predominent case of dip-in lithography [59], where the objective is in direct contact with the photoresist, which serves as index-matched immersion fluid at the same time. The space between objective and sample is thus filled with a homogeneous medium. The calculation of the PSF is more difficult when a cover glass and immersion oil is used, and the corresponding vectorial Debye theory for focusing through such stratified media is treated in [60].

9   The obvious limit is certainly that the volume element must still contain at least a few monomers and a few photoinitiator molecules. In practice, the degree of conversion and thus the mechanical strength of the polymerized material will furthermore depend on how far above threshold the dose is. Therefore, a "minimum feature size" or "linewidth" of a particular lithography system is still typically specified.

wavelength or nonlinearity order [56]. The size of the polymerized voxels are in particular not limited to the optical resolution according to the Abbe diffraction limit [63]. Second, assuming the same photoresist, which could be used both in a single photon as well as in a two-photon process, we would be rather inclined to compare the dose distribution for a two-photon process at the wavelength $\lambda = 780$ nm with the dose distribution for a single photon process at half the wavelength, $\lambda = 390$ nm, Figs. 2.1(b) and (c). Here, we find in fact that the optical resolution is better for the single-photon process at $\lambda = 390$ nm.
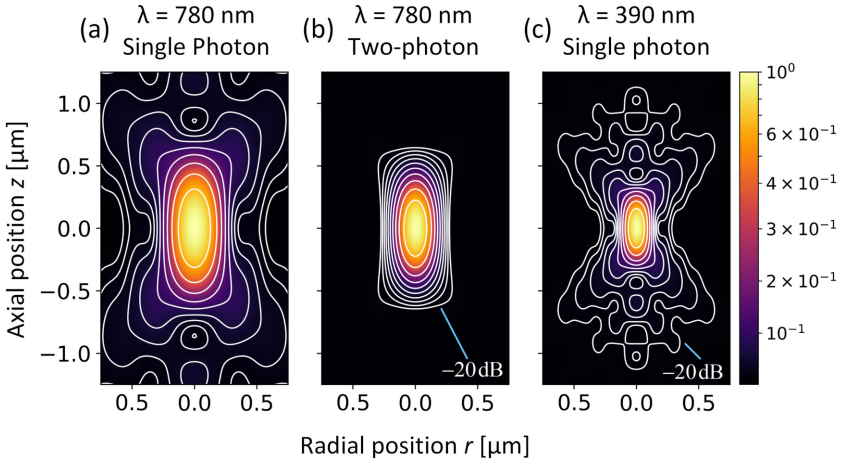
Fig. 2.1: Simulated normalized distributions of deposited lithography dose D for different lithography wavelengths λ and nonlinearity orders N, based on calculations of the optical point spread function (PSF). A microscope objective with numerical aperture of $\mathrm{NA} = 1.4$ is assumed, immersed in a photoresist with refractive index $n = 1.518$. The contour lines indicate 2 dB steps of deposited dose. **(a)** The dose distribution for single-photon absorption at $\lambda = 780$ nm shows a poor optical resolution and significant axial side lobes. Exposing adjacent positions hence leads to a strong dose accumulation in three dimensions. **(b)** For two-photon absorption at $\lambda = 780$ nm, the optical resolution is improved and the axial side lobes are significantly suppressed. **(c)** The optical resolution is even better for single-photon absorption at half the wavelength, $\lambda = 390$ nm. Axial side lobes are however still pronounced.

The true advantage of multi-photon lithography becomes only apparent for arbitrarily shaped three-dimensional bulk structures [56, 57]. The dose distributions

for a single photon process in Figs. 2.1(a) and (c) feature strong axial side lobes. When exposing multiple volumes close to each other, the deposited doses of each focus overlap in the entire volume according to the accumulation model. The threshold dose D_{th} is unintentionally exceeded in axial direction outside of the design geometry due to this proximity effect, thereby severely affecting the shape fidelity of the printed structure. This effect becomes particularly pronounced when structuring large thin sheets that are oriented perpendicular to the axial direction of the lithography beam and can be easily understood by the following strongly simplified argument, visualized in Fig. 2.2: For a point exposure within
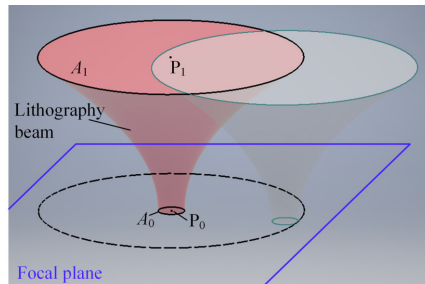
Fig. 2.2: Visualization of the proximity effect at an axially distant position, when structuring extended areas within the focal plane. In a simple model, we consider for each point exposure inside the focal plane a focal area A_0, with a uniform intensity I_0 and a uniform dose D_0 within. We pick a point P_0 in the focal plane, and consider the unintentionally accumulated dose D_1 at a point P_1, which is located at a certain axial distance from P_0. The lithography beam cross-section A_1 is m-fold larger in the plane of P_1, $A_1 = mA_0$, and the intensity I_1 at P_1 is hence m-fold smaller, $I_1 = I_0/m$. However, each exposed point on the focal plane within the projected area of A_1 (indicated by the dashed circle) leads to a dose accumulation at P_1. A nonlinearity order of at least $N > 2$ is required to significantly reduce the unintentionally accumulated dose at P_1.

the focal plane, we consider a focal area A_0, with a uniform intensity I_0 and a uniform dose D_0 within. The exposure of an extended area in the focal plane is thought of as being composed of individual non-overlapping point exposures. We pick one of these points P_0 in the focal plane, and consider the unintentionally accumulated dose D_1 at a point P_1, which is located at a certain axial distance from P_0. The lithography beam cross-section A_1 is m-fold larger in the plane of P_1, $A_1 = mA_0$, and the intensity I_1 at P_1 is hence m-fold smaller, $I_1 = I_0/m$.

However, each exposed point on the focal plane within the projected area of A_1 leads to a dose accumulation at P_1, and it takes m non-overlapping point exposures to fill this area. For a one-photon process, $D \propto I$, we hence find $D_1 \propto m \times I_0/m$. The unintentionally accumulated dose D_1 is hence independent of m and thus independent of the axial distance. In contrast, the axial side lobes are significantly suppressed for two-photon absorption, Fig. 2.1(b), leading to a much better shape fidelity. In this case, within our simple model, we find $D \propto I^2$, and hence $D_1 \propto m \times I_0/m^2 = I_0/m$. Obviously, a multi-photon process with $N > 2$ is even better in reducing the tails of the axial side lobes. Still, the dose distributions of very closely spaced voxels or lines will inevitably overlap, limiting the minimal achievable distance for which two adjacent features (lines) can still be distinguished. This minimum distance is given by the multi-photon Sparrow limit[10] [56] and referred to as "writing resolution of the lithography system".

Another key quality metric of an MPL system is the achievable polymerized voxel aspect ratio. A spherical voxel would obviously be ideal, but from Fig. 2.1(b), we find that the typical voxel shape is elongated (along the axial coordinate z), and that the exact shape of the voxel depends on how large the exposure dose is. We make the simplifying assumption that the most relevant center part of the dose distribution can be well approximated using an uncorrelated bivariate Gaussian distribution with standard deviations σ_z and σ_r in the axial direction z and in the radial direction r, respectively,

$$D(r, z) \propto e^{-\frac{r^2}{2\sigma_r^2}} e^{-\frac{z^2}{2\sigma_z^2}} . \tag{2.1}$$

An approximate aspect ratio is then given as σ_z/σ_r. To understand the influence of the objective on the aspect ratio, we first consider a low-NA objective. In this

---

[10] The Sparrow citerion for the resolution of conventional optical instruments corresponds to the limiting case where the joint intensity distribution from two neighboring spots produce a flat-top distribution. Similarly, the multi-photon Sparrow limit requires at least a barely existing minimum in the joint dose distribution between the two centers of exposure.

case, the lateral and axial optical resolution [64, 65] lead to $\sigma_r \propto (\lambda/n)/(NA/n)$ and $\sigma_z \propto (\lambda/n)/(NA/n)^2$, respectively. The aspect ratio hence scales as

$$\frac{\sigma_z}{\sigma_r} \propto \frac{\lambda/n}{(NA/n)^2} \bigg/ \frac{\lambda}{NA} = \frac{1}{NA/n} = \frac{1}{sin\theta_{max}} , \tag{2.2}$$

and is hence inversely proportional to the sine of the objective acceptance angle θ_{max}. Note that the exact numeric pre-factors for the best-fit Gaussian parameters σ_r and σ_z depend slightly on the nonlinearity order N. Values for $N = 1$ can, e.g., be found in [66]. For a high-NA objective, there is no closed form expression for the PSF. The exact values for σ_r, σ_z, and the exact scaling of the aspect ratio hence need to be extracted from numerical simulations such as the one shown in Fig. 2.1(b). Empirical approximation formulae based on numerical simulations are given for $N = 2$ and $NA > 0.7$ as[11] [67]

$$\sigma_r = \frac{0.230\,\lambda}{\sqrt{2}\,NA^{0.91}} , \tag{2.3}$$

$$\sigma_z = \frac{0.376\,\lambda}{\sqrt{2}} \left[\frac{1}{n - \sqrt{n^2 - NA^2}} \right] . \tag{2.4}$$

For the parameters used for the estimations in Fig. 2.1(b), where an objective with NA as high as 1.4 was assumed to be immersed in photoresist with index $n = 1.518$ at a lithography wavelength of $\lambda = 780\,nm$, we still find an approximate aspect ratio of $\sigma_z/\sigma_r = 2.4$ for a two-photon process ($N = 2$). Special techniques such as shaded ring filter [68] aperture stops have been utilized to further reduce the axial size σ_z and thereby the aspect ratio, at the expense of slightly increasing the radial size σ_r .

---

[11] To facilitate the comparison between different literature sources, note the conversions $w_{1/e} = \sqrt{2}\,\sigma$ and $w_{FWHM} = 2\sqrt{2\ln 2}\,\sigma$ between full width half maximum values w_{FWHM}, $1/e$ half widths $w_{1/e}$, and standard deviations σ of a Gaussian distribution.

2.1.2 Automated lithography machine

Fabrication of 3D-printed coupling structures for hybrid photonic assemblies requires not only high shape fidelity, but also extremely precise alignment of the printed structure with respect to, e.g., on-chip waveguides. A high level of automation is therefore required, including sophisticated hardware and software for detection of position and orientation of components within the lithography coordinate system. Within this dissertation, a lithography machine from preceding work [1] was used, see Fig. 2.3. Only minor modifications in processes, software and machine alignment were necessary to perform the experimental demonstrations in Chapter 3, 4 and 5.

The lithography system uses a femtosecond laser with an emission centered at 780 nm. A pulse compressor pre-compensates the group delay dispersion (GDD) of the remaining optical components. The optical power is modulated using an acousto-optic modulator (AOM). The beam is sent through an inverted microscope[12] and a high-NA microscope objective[13] focuses the beam into the liquid photoresist which serves as index-matched immersion fluid at the same time. The beam is scanned in the horizontal (x, y)-plane using fast galvanometric mirrors. In the vertical z direction, a piezo actuator controls the position of the objective. The highest possible NA and therefore the best possible voxel is only achieved if the rear aperture of the objective is fully illuminated[14]. This is ensured using a variable beam expander.

The lithography system crucially features, in addition to conventional bright-field imaging, both a confocal laser imaging path as well as a fluorescence imaging path. The confocal and fluorescence imaging systems complement each other and enable precise detection of on-chip features and aligned fabrication. Both imaging

---

[12] Contrary to a conventional microscope design, the objective points upwards and the sample is mounted upside-down.

[13] Different objectives can be used with this machine. All samples within this thesis have been fabricated with a $63\times / 1.4$ objective.

[14] A uniform illumination is ideal. For a Gaussian beam and disregarding the available laser power, overfilling the back aperture is therefore desirable.
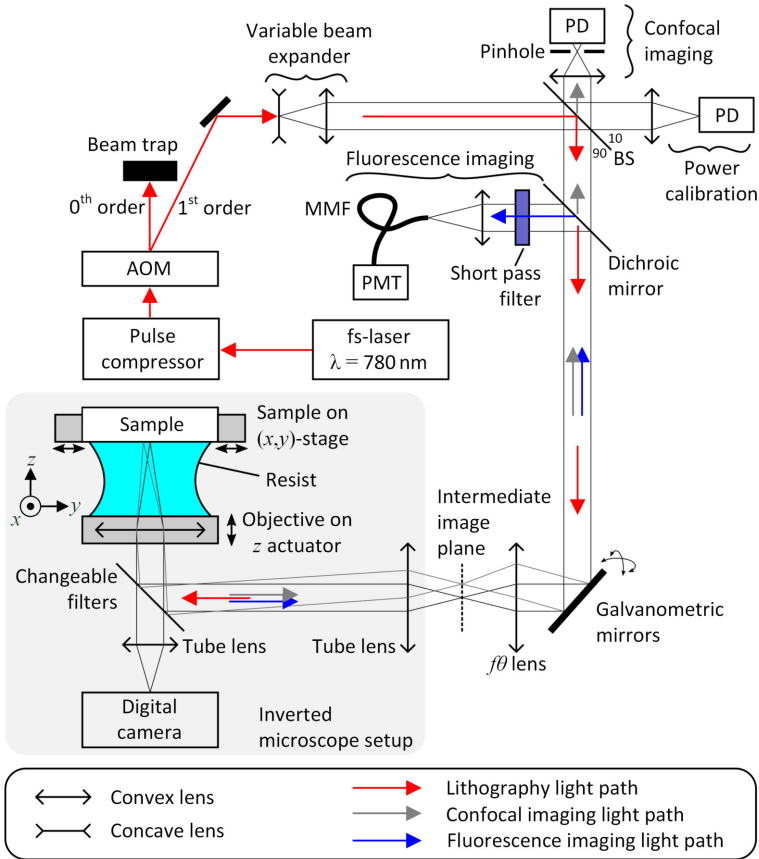
Fig. 2.3: Schematic optical setup of the MPL system [1] used for this work. Abbreviations: AOM – acousto-optic modulator; BS – beam splitter; PD – photodetector; MMF – multimode fiber; PMT – photo multiplier tube. The lithography system uses a femtosecond laser centered at 780 nm. The laser power is modulated using an acousto-optic modulator (AOM). A high-NA microscope objective focuses the beam into the liquid photoresist which serves as index-matched immersion fluid at the same time. The beam is scanned in the horizontal (x, y)-plane using fast galvanometric mirrors. In the vertical z direction, a piezo actuator controls the position of the objective. The lithography system features both a confocal laser imaging path as well as a fluorescence imaging path. The confocal and fluorescence imaging systems complement each other and enable precise part detection and aligned fabrication. The illumination for bright-field imaging has been omitted for brevity. Figure adapted with permission from [1].

modalities are operated at laser powers far below polymerization threshold. For the detection of strongly reflective surfaces, scanning confocal laser imaging allows to capture a large amount of the reflected light, leading to a high signal-to-noise ratio (SNR). In case of silicon photonic (SiP) chips, it is in particular possible to detect the location of the silicon device layer through the top oxide layer. However, finding the correct sample height based on a maximum of the confocal signal does depend on the axial alignment of the confocal pinhole. In contrast to this, fluorescence imaging relies on multi-photon excitation of the photoinitator and a "parasitic"[15] decay path [69], which leads to the emission of fluorescent light, whenever the focal spot is within the photoresist. The multi-photon fluorescence excitation is highly localized to the focal spot, see Fig. 2.1(b) in Section 2.1.1. Spatial filtering is therefore not required, and as much as possible avoided, by using a multimode fiber (MMF) with a large acceptance area[16]. Scanning perpendicularly through a weakly reflecting interface, e.g., a resist-glass interface, yields a sigmoid shape in the fluorescence intensity signal. This allows to accurately determine the interface height and monitor the optical resolution of the lithography system, see Appendix D of [1] for further details. Using a suitable test target[17] allows the calibration of the axial position of the confocal pinhole.

2.1.3 Printing of microlenses to vertical chip facets

Printing to vertical device facets leads to a situation where the lithography beam hits the device edge. If the device is opaque, part of the lithography beam is blocked, see Fig. 2.4(a), and a significant amount of power is lost. For a transparent device,

---

[15] The "parasitic" fluorescence decay path does not contribute to radical formation and thereby increases the polymerization threshold of the photoresist. Photoresists are therefore often optimized to exhibit low fluorescence. Sufficiently strong fluorescence is however of tremendous help in achieving reproducable machine alignment and sample-aligned fabrication.

[16] The MMF is in fact only used for convenience, the PMT could in principle be directly attached to the MPL setup.

[17] A resolution target with 120 nm-thin patterned chromium on glass (Thorlabs) is typically used. A confocal z-scan is performed on the chromium surface, and a fluorescence z-scan on a nearby location which is not covered with chromium. The difference in determined surface height is used to calibrate the axial position of the pinhole.

e.g., a single-mode fiber, part of the lithography beam passes through the device, is refracted, and experiences a different phase shift. In either case, diffraction effects lead to a voxel degradation. The strength of such effects depends on the position of the focal point with respect to the device edge, and a position-dependent adaption of the lithography laser power is therefore required in both cases. The topic has been extensively studied with simulations by M. Gödecke [70] in the context of photonic wire bonds (PWB). However, due to limited simulation resources, rigorous finite-difference time-domain (FDTD) studies have only be carried out for focal positions close to the device edge. Printing of larger structures, such as microlenses, hence still relied on heuristic power adaption functions, which in particular for opaque chips often provided unsatisfying lithography results at certain positions. In comparison, a simple analytically derived power adaption function, as described in the following Section 2.1.3.1, proved to be useful for a large position range.

When focusing through the edge of a transparent device, the combined effects of refraction, different phase shift within the material, as well as diffraction lead to a position-dependent focal shift [71]: The actual focus is found at a position which is predominantly vertically shifted with respect to the position without device. The task of aligning a PWB to a single-mode fiber (SMF) core with highest precision is therefore ideally done by connecting the remote end of the sample SMF to the photo multiplier tube (PMT) [72] in Fig. 2.3 through the connector that is otherwise used by the usual multimode fiber (MMF). The correct printing position is then found by scanning the focus of the lithography beam through the volume in front of the SMF facet and by measuring the position-dependent fluorescence power coupled into the SMF core. Slight deviations of the printed PWB trajectory from the design trajectory due to position-dependent focal shift do not contribute to the PWB loss significantly. In contrast, for facet-attached microlenses (FaML) it is important to ensure a high shape fidelity of the printed lens surface under any circumstances. In fact, within this thesis, shape deviation has also been observed for facet-attached microlenses (FaML) printed to opaque chip edges (where such effects are not to be expected). Upon further study, the origin of the deviations were confirmed to be of mechanical rather than optical nature, and can thus be

circumvented, e.g., by appropriate design of the printed structure. Section 2.1.3.2 raises the awareness concerning these issues and summarizes the current findings.

2.1.3.1 Position-dependent power adaption

A simple power adaption for printing to opaque vertical device facets is introduced in the following. We assume that the lithography beam is focused to a spot located at a vertical depth h below the surface of the chip, and at a horizontal distance d from the facet of the chip, see Fig. 2.4(a). The opening half-angle α of the light cone is dictated by the numerical aperture (NA) of the lithography objective and the refractive index of the photoresist. Part of the light is blocked by the chip edge. To find the power transmission $\eta(h, d)$, i.e., the fraction which is not blocked by the chip surface, we consider the intensity distribution $I(x, y, z = h)$ at the plane $z = h$ of the chip surface, see Fig. 2.4(b).
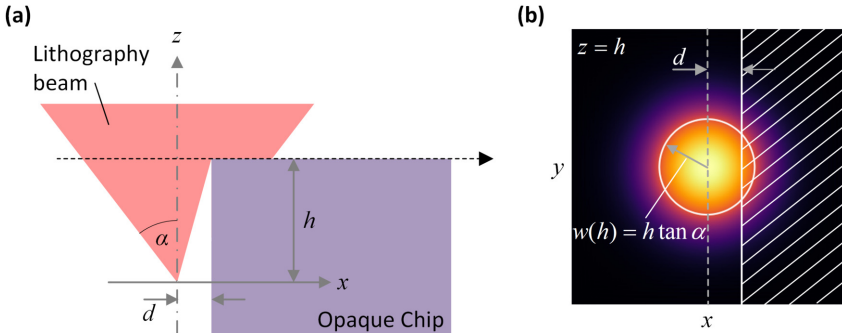
Fig. 2.4: Focusing over the edge of an opaque chip. **(a)** The lithography beam is focused to a spot located at a vertical depth h below the surface of the chip, and at a horizontal distance d from the facet of the chip. The opening half-angle α of the light cone is dictated by the numerical aperture of the lithography objective. Part of the light is blocked by the chip edge. **(b)** The intensity distribution $I(x, y, z = h)$ at the plane $z = h$ of the chip surface is considered using a Gaussian beam approximation. The dashed white circle indicates the lateral $1/e^2$ intensity with respect to the maximum. The hatched part is blocked by the chip edge. The amount of blocked (transmitted) light is found by integration over the hatched (non-hatched) area.

Using a Gaussian beam approximation, we describe the intensity distribution using the beam radius $w(h)$, or alternatively using the standard deviation $\sigma_{\mathrm{I}}(h)$ of the Gaussian intensity distribution at the plane $z = h$ of the chip surface,

$$
\begin{aligned}
I(x, y, z = h) &= I_0 \left(e^{-\frac{r^2}{w^2(h)}} \right)^2 \\
&= \widetilde{I}_0 \frac{1}{2\pi\sigma_{\mathrm{I}}^2(h)} e^{-\frac{r^2}{2\sigma_{\mathrm{I}}^2(h)}}
\end{aligned}
\tag{2.5}
$$

where

$$
\sigma_{\mathrm{I}}(h) = \frac{w(h)}{2} \approx \frac{h\tan\alpha}{2} .
\tag{2.6}
$$

In these relations, we assume that the depth h is much larger than the Rayleigh distance of the high NA lithography beam. The power transmission $\eta(h, d)$ is then found as

$$
\begin{aligned}
\eta(h, d) &= \frac{\displaystyle\int_{y=-\infty}^{\infty}\int_{x=-\infty}^{0} I(x, y, z = h)\,\mathrm{d}x\,\mathrm{d}y + \int_{y=-\infty}^{\infty}\int_{x=0}^{d} I(x, y, z = h)\,\mathrm{d}x\,\mathrm{d}y}{\displaystyle\int_{-\infty}^{\infty}\int_{-\infty}^{\infty} I(x, y, z = h)\,\mathrm{d}x\,\mathrm{d}y} \\[2mm]
&= \frac{\dfrac{1}{2}\widetilde{I}_0 + \widetilde{I}_0 \dfrac{1}{\sqrt{2\pi}\sigma_{\mathrm{I}}(h)} \displaystyle\int_0^d e^{-\frac{x^2}{2\sigma_{\mathrm{I}}^2(h)}}\,\mathrm{d}x}{\widetilde{I}_0} \\[2mm]
&= \frac{1}{2}\left(1 + \operatorname{erf}\left(\frac{d}{\sqrt{2}\sigma_{\mathrm{I}}(h)} \right) \right) = \frac{1}{2}\left(1 + \operatorname{erf}\left(\frac{\sqrt{2}d}{h\tan\alpha} \right) \right) .
\end{aligned}
\tag{2.7}
$$

Assuming a "regular" laser power P_0 for an optimum lithography result, the position-dependent corrected laser power P_{corr} when focusing over the opaque chip edge is hence found as

$$P_{\mathrm{corr}}(h, d) = \begin{cases} P_0 & \text{for } h \leq 0, \text{ above chip surface} \\ \frac{P_0}{\eta(h,d)} & \text{for } h > 0, \text{ below chip surface} \end{cases} . \qquad (2.8)$$

In addition to these power-transmission considerations, the voxel is in practice further deteriorated due to the missing part of the lithography beam. The corrected power below the chip surface should hence be chosen slightly larger, e.g., increased by a fixed percentage, than suggested according to Eq. (2.8) to reach a comparable two-photon dose as in the case of an unperturbed beam. In our derivation, we required that the depth h is much larger than the Rayleigh distance. Neglecting this limitation and applying Equations (2.7) and (2.8) up to the chip edge would lead to a discontinuity at the chip edge: $P_{\mathrm{corr}}(h < 0, 0) = P_0$ and $P_{\mathrm{corr}}(h > 0, 0) = 2P_0$. Within the lithography system, we hence apply a smooth transition instead. When transitioning from above to below the chip surface, the power is increased from the initial value P_0 to the increased value according to Eq. (2.8) over the depth-scale of approximately one voxel height.

This power correction scheme has been applied to the ultra-low-loss facet-attached microlenses (FaML) on silicon photonic (SiP) chips in [J2] and furthermore experimentally verified for a large range of depths $0 < h < 60$ µm and horizontal distances d over the entire write field. No signs of position-dependent underexposure nor position-dependent micro-explosions (due to a too high power) have been observed after correction.

2.1.3.2 Shape inaccuracies induced by mechanical deformation

Besides the optical effects at transparent device facets discussed in the beginning of Section 2.1.3, there are further aspects that may lead to shape inaccuracies. For example, the printed structure might still be subject to shape inaccuracies

induced by mechanical deformation. An exemplary case is depicted in Fig. 2.5. Figure 2.5(a) shows a CAD-model of a facet-attached microlens (FaML), printed to the vertical facet of a silicon photonic chip. The cross-section is overlayed with the optical field distribution obtained from a micro-optical simulation that relies on the scalar wave-propagation method, see Section 2.2. For better visibility, the color coding shows the radial intensity decay only, with the radial $1/e^2$ intensity drop marked by the white contour lines. The lens has been printed with the axis of the lithography beam oriented along the z-direction, and a layer build-up from bottom to top. A supposedly circular lens cross section is found to be deformed. In this case, the shape inaccuracy of the printed structure is clearly visible even in conventional bright-field microscopy images, when viewed perpendicular to the chip facet. A more detailed quantitative measurement can be obtained by volumetric scanning fluorescence imaging. To this end, the lithography machine is operated as a nonlinear fluorescence microscope at low laser power. The printed sample is re-mounted into the lithography machine and again immersed into photoresist. Compared to lithography, the sample mounting for measurement is rotated by 90°, such that the scanning laser beam is incident along the y-axis in Fig. 2.5(a). An exemplary slice cut at $y = 60\,\mu m$ through the scanned volume is shown in Fig. 2.5(b). The polymerized region appears dark due to depletion of the photoinitiator during the printing process. In comparison, the surrounding liquid unpolymerized photoresist appears bright. The cross-section of the printed shape is highlighted in red, while the correct shape is given by the blue circle.

In a series of experiments, mechanical deformation during the printing process was found to be the cause of the observed effects. An experimental evidence for this conclusion is shown in Fig. 2.6. Figure 2.6(a) depicts the CAD-model of a test structure (green). The test structure is printed to a gold coated glass block. The top surface of the chip is thus opaque, while the shadowed facet is transparent, effectively ruling out any optical influence in conjunction with highly reflecting vertical facets. The $40\,\mu m$ long trapezoidal test structure is angled on both the bottom and the top side, and therefore suited for printing both with layer build-up from bottom to top (↑) as well as from top to bottom (↓). The center of the test structure is located $30\,\mu m$ below the chip surface, and the angle of
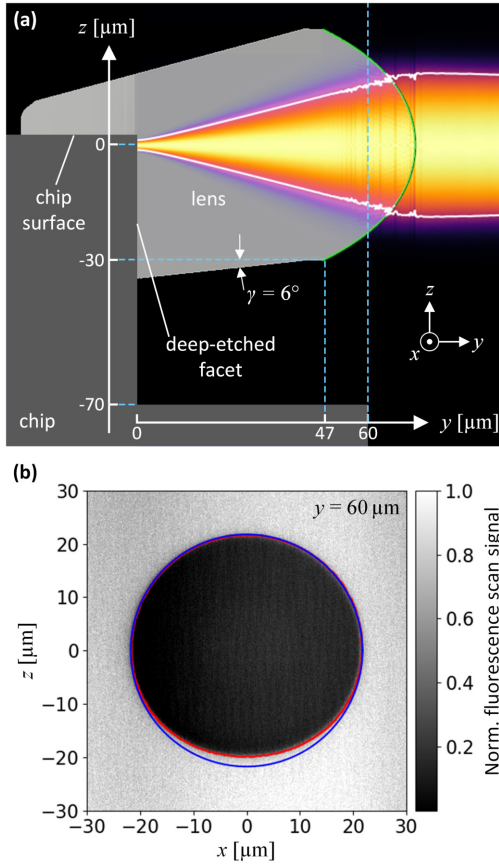
Fig. 2.5: Example of fabricated structure with shape inaccuracies. **(a)** Cross-section (CAD-model) of a microlens, printed to the vertical facet of a silicon photonic chip. The beam profile obtained from a micro-optical simulation using the scalar wave-propagation method described in Section 2.2 is overlayed. The lens has been printed with the lithography beam oriented along the z-axis and a print layer build-up from bottom to top. **(b)** Measurement of fabrication shape inaccuracies using volumetric scanning fluorescence imaging. A cut through the scanned volume is shown. The scanning laser beam is incident along the y-axis in Subfigure (a), and the data is visualized at the cut plane $y = 60\,\mu\text{m}$. The cross-section of the printed shape is highlighted in red, while the correct shape is given by the blue circle. The deviations are found to be caused by mechanical deformation during the printing process, and can thus be avoided by increasing the angle of the mechanical support structure in Subfigure (a) to $\gamma \gtrapprox 20°$.

25
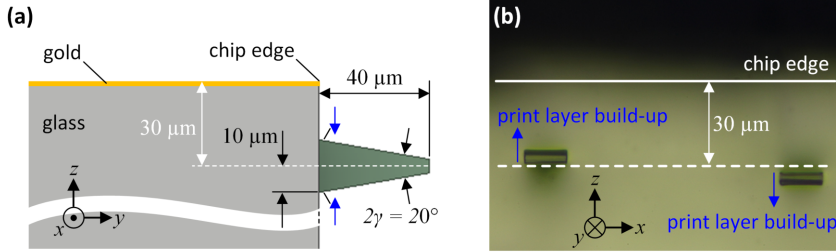
Fig. 2.6: Test structure for demonstrating mechanical deformation. **(a)** CAD-model of the test structure (green), printed to a glass block with a gold coating on the top surface. The $40\,\mu\text{m}$ long trapezoidal test structure is suited for printing both from bottom to top (↑) as well as from top to bottom (↓). The center of the test structure is located $30\,\mu\text{m}$ below the chip surface, and the angle of the trapezoidal shape is $\gamma = 10°$. **(b)** Microscope image of fabricated structures. The viewing direction is perpendicular to the facet, and the front surfaces of the test structures are in focus. The printed structures bend in the direction of the print layer build-up. The exact chip edge position has been determined by taking a separate image, where the facet is in focus.

the trapezoidal shape is $\gamma = 10°$. Figure 2.6(b) shows a microscope image of fabricated[18] structures. The viewing direction is perpendicular to the facet, i.e., along the y-direction in Fig. 2.6(a), and the front surfaces of the test structures are in focus. The printed structures bend in the direction of the print layer build-up. The exact chip edge position has been determined by taking a separate image, where the facet is in focus. The exact reason for the mechanical bending has yet to be clarified. Note in this context, however, that the bending in Figure 2.6(b) is slightly less severe when the structure is printed from bottom to top, compared to the case when it is printed from top to bottom.

To avoid shape inaccuracies for the lens in Fig. 2.5(a), it was found to be sufficient to increase the angle of the mechanical support structure to $\gamma \gtrsim 20°$. Alternatively, a segmented printing strategy, Fig. 2.7, helps as well. In this case, the lens is divided into multiple segments, which are printed one after another. Within each

---

[18]   The layer distance ("slicing distance") is $600\,\text{nm}$. The area within each layer is subdivided into straight lines with line distance ("hatching distance") of $100\,\text{nm}$. The lines are oriented along the x, respectively the y-direction, where the direction is alternated between layers, starting with the x-direction on the first layer.
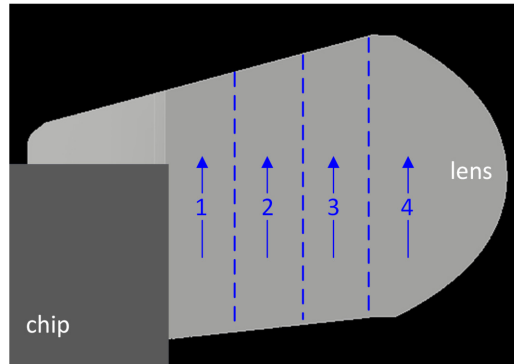
Fig. 2.7: Segmented printing strategy. The depicted lens is divided into four segments 1 . . . 4, which are printed one after another. Within each segment, the print layers are built up from bottom to top (blue arrows).

segment, the print layers are built up from bottom to top, indicated by the blue arrows.

2.2 Simulation of microlenses using the wave propagation method

A significant part of this work is related to 3D-printing of microlenses and compound micro-optical systems, which may consist of multiple lens surfaces, or combine lens surfaces with additional prism or mirror surfaces. Micro-optical elements are commonly used to collimate highly divergent beams or to focus beams to small spots for coupling into integrated devices. Ray optics is thus of limited use when it comes to design and simulation. Instead, wave-optical methods are required which go beyond the approximation of thin phase elements[19] and beyond the paraxial approximation. Fully vectorial rigorous methods such as the finite-difference time-domain (FDTD) method yield "exact" solutions, but the computation speed is typically by far too slow to address optimization problems which rely on a multitude of simulation runs[20]. The method of choice within this work is the formulation of the scalar wave propagation method (WPM) for step-index structures according to Schmidt *et al.* [36], which is detailed in Section 2.2.2. The WPM algorithm itself has been proposed earlier by Brenner [74] to overcome[21] the paraxial limitations of the standard beam propagation method (BPM). More recently, Schmidt et al. [36] found a computationally efficient implementation for step-index structures and demonstrated the advantages in computation time compared to newer wide-angle formulations of the BPM.

---

[19] Commonly also known as "thin element approximation" (TEA). The effect on the incoming wave (vacuum wavenumber k_0) of a micro-optical component with height profile $z(x, y)$ and index contrast Δn to the surrounding medium is approximated by a planar phase mask $\Delta\varphi(x, y) = k_0\Delta n z(x, y)$ [73].

[20] An FDTD reference simulation of a microlens in a computational cuboid of a few tens of µm side length took approximately 6 days on the IPQ institute's computation server with 16 CPU cores [1].

[21] Correctness of the refraction angle for incidence angles of up to at least $70°$ has been shown in [74]. Later publications [75, 76] claim a limit of up to $85°$, referring to the same results.

2.2.1 Validity of the scalar approximation

A brief summary regarding the validity of the scalar approximation shall be given, before the scalar WPM algorithm itself is introduced. We consider an isotropic, linear and non-magnetic medium. The time and position-dependent instantaneous electric field is denoted with $\mathbf{E}(t, \mathbf{r})$, and the corresponding magnetic field is denoted with $\mathbf{H}(t, \mathbf{r})$. The vacuum speed of light is c, and the position-dependent refractive index is $n(\mathbf{r})$, neglecting any frequency dependency of the refractive index within the frequency range of interest. Reshaping Maxwell's equations leads to the exact vector wave equations [77],

$$\nabla^2 \mathbf{E}(t, \mathbf{r}) + \mathrm{grad}\left((\mathrm{grad}\ln n^2) \cdot \mathbf{E}(t, \mathbf{r}) \right) = \frac{n^2}{c^2} \frac{\partial^2 \mathbf{E}(t, \mathbf{r})}{\partial t^2}, \tag{2.9}$$

$$\nabla^2 \mathbf{H}(t, \mathbf{r}) + (\mathrm{grad}\ln n^2) \times (\mathrm{curl}\,\mathbf{H}(t, \mathbf{r})) = \frac{n^2}{c^2} \frac{\partial^2 \mathbf{H}(t, \mathbf{r})}{\partial t^2}. \tag{2.10}$$

In each of these two equations, three of the six field components are coupled with each other. In order to solve a particular problem, it is only required to solve one of the equations, as the remaining field components directly follow from Maxwell's equations. The situation is further simplified, whenever the second term on the left hand side vanishes or can be neglected for one or both of the equations. Typical examples of such cases are homogeneous media ($\mathrm{grad}\ln n^2 = 0$) and weakly inhomogeneous media, where the refractive index does not change significantly over one optical wavelength. When expressing the vectorial fields using a Cartesian basis, the respective vector wave equation fully decomposes into three decoupled wave equations for three Cartesian components,

$$\nabla^2 \Psi(t, \mathbf{r}) = \frac{n^2}{c^2} \frac{\partial^2 \Psi(t, \mathbf{r})}{\partial t^2}, \tag{2.11}$$

where $\Psi(t, \mathbf{r})$ stands for the individual Cartesian field components $E_q(t, \mathbf{r})$ respectively $H_q(t, \mathbf{r})$ with $q \in \{x, y, z\}$. Equation (2.11), known as the scalar Helmholtz equation, can be solved with much reduced computational effort compared to its vectorial counterpart. Therefore, the scalar approximation is frequently employed

— even in cases such as microlenses with step-index profile and arbitrary geometry, where the simplification is not fully justified.

2.2.2 Scalar WPM algorithm

The previously existing simulation capabilities were significantly expanded within the scope of this thesis, building upon preliminary work by M. Blaicher [1]. Many features commonly known from commercial optic design software such as *OpticStudio (Zemax)* have been implemented. These include in particular a highly object-oriented implementation of individual surface shapes and of standard components such as lenses, prisms as well as their assembly into complex compound micro-optical systems including necessary coordinate transformations. Furthermore, wave-optical tolerancing has been implemented, to accurately assess the impact of tanslational and angular misalignment during fabrication of the microlenses as well as during assembly of multi-chip modules based on 3D-printed microlenses[22]. Finally, a zeroth-order correction of Fresnel reflection losses within the scalar method has been introduced, see Section 2.2.3. An introduction to the algorithm is given in the following.

We consider a monochromatic wave with angular frequency ω of the form $\underline{\mathcal{E}}(x, y, z, t) = \underline{E}(x, y, z)\mathrm{e}^{\mathrm{j}\omega t}$ which propagates through an inhomogeneous medium $n(x, y, z)$ along the principle propagation direction z. The vacuum wavenumber is $k_0 = \omega/c$ with c denoting the vacuum speed of light. The scalar WPM algorithm can be considered as a generalization of the angular spectrum method for a homogeneous medium. In both cases, the complex field $\underline{E}(x, y, z)$ is

---

[22] Optical assembly with 3D-printed microlenses is discussed both exprimentally and theoretically in detail in Chapter 4 and Appendix B.

first decomposed into plane-wave components with lateral propagation constants (k_x, k_y) by calculating its angular spectrum

$$
\begin{aligned}
\underline{\widetilde{E}}(k_x, k_y, z) &= \mathcal{F}_{xy}\{\underline{E}(x, y, z)\} \\
&= \frac{1}{2\pi} \int \underline{E}(x, y, z) \mathrm{e}^{\mathrm{j}(k_x x + k_y y)} \, \mathrm{d}x \, \mathrm{d}y \,,
\end{aligned}
\tag{2.12}
$$

where $\mathcal{F}_{xy}$ denotes a two-dimensional (spatial) Fourier transform with the inverse transformation consequentially given as

$$
\mathcal{F}_{xy}^{-1}\{\underline{\widetilde{E}}(k_x, k_y, z)\} = \frac{1}{2\pi} \int \underline{\widetilde{E}}(k_x, k_y, z) \mathrm{e}^{-\mathrm{j}(k_x x + k_y y)} \, \mathrm{d}k_x \, \mathrm{d}k_y \,.
\tag{2.13}
$$

Each plane wave component is then propagated independently along the z-direction by a slice distance of Δz and superimposed with all other waves to obtain the propagated field $\underline{E}(x, y, z + \Delta z)$ at the next z-slice. In case of the angular spectrum method for a homogeneous medium with $n(x, y, z) = n_0$, the propagated field is given by the well-known relation [73]

$$
\underline{E}(x, y, z + \Delta z) = \mathcal{F}_{xy}^{-1}\left\{ \mathrm{e}^{-\mathrm{j}\, k_z(k_x, k_y)\Delta z} \mathcal{F}_{xy}\{\underline{E}(x, y, z)\}\right\} \,,
\tag{2.14}
$$

with

$$
k_z(k_x, k_y) = \sqrt{n_0^2 k_0^2 - k_x^2 - k_y^2} \,.
\tag{2.15}
$$

Using the square root in Eq. (2.15) instead of any approximations thereof ensures the validity even for large divergence angles. The scalar WPM according to Brenner et al. [74] generalizes this computation scheme for an inhomogeneous medium. The propagated field $\underline{E}(x, y, z + \Delta z)$ is now given by

$$
\begin{aligned}
\underline{E}(x, y, z + \Delta z) &= \frac{1}{2\pi} \int \underline{\widetilde{E}}(k_x, k_y, z) \mathrm{e}^{-\mathrm{j}\, k_z(k_x, k_y, x, y)\Delta z} \\
&\quad \times \mathrm{e}^{-\mathrm{j}(k_x x + k_y y)} \, \mathrm{d}k_x \, \mathrm{d}k_y \\
&= \mathcal{F}_{xy}^{-1}\left\{ \mathrm{e}^{-\mathrm{j}\, k_z(k_x, k_y, x, y)\Delta z} \mathcal{F}_{xy}\{\underline{E}(x, y, z)\}\right\} \,,
\end{aligned}
\tag{2.16}
$$

$$k_z(k_x, k_y, x, y) = \sqrt{n^2(x, y, z + \Delta z/2)k_0^2 - k_x^2 - k_y^2}. \qquad (2.17)$$

Although this approach is intuitive, a systematic derivation starting from the Helmholtz-equation as given in Appendix A of [36] is non-trivial, due to the mixing of real and Fourier-space quantities in Eq. (2.17). The evaluation of Eq. (2.16) is computationally expensive for an arbitrary inhomogeneous refractive index distribution: The propagation factor $k_z(k_x, k_y, x, y)$ dependends on the position-dependent refractive index and thus on the spatial coordinates. As a result, the Fourier back-transform has to be computed separately for each lateral coordinate (x, y) on the computation grid without the possibility to exploit the scaling advantages of Fast-Fourier-Transforms (FFT).

However, this situation changes drastically when disregarding gradient-index media and only considering step-index structures with a limited set of refractive indices, where the structure can be decomposed into a finite number M of homogeneous pairwise disjoint subregions with corresponding refractive index n_m. In fact, most structures printed using multi-photon lithography (MPL) fall into this category. As an example, simulation of a typical 3D-printed microlens requires only a binary refractive index distribution, accounting for the refractive index of the lens material itself and for the surrounding, which might be vacuum, air or a dedicated optical cladding material. The stencil function $\Theta_{z,m}(x, y)$ describes whether or not subregion m is found at an axial position z and at a lateral position (x, y),

$$\Theta_{z,m}(x, y) = \begin{cases} 1 & \text{if } n(x, y, z) = n_m \\ 0 & \text{else} \end{cases}. \qquad (2.18)$$

In this case, Schmidt et al. [36] recently realized that Eq. (2.16) and (2.17) can be simplified to

$$\underline{E}(x, y, z + \Delta z) = \sum_{m=1}^{M} \Theta_{z,m}(x, y)$$
$$\times \mathcal{F}_{xy}^{-1} \left\{ e^{-j\,k_{z,m}(k_x, k_y)\Delta z} \mathcal{F}_{xy}\{\underline{E}(x, y, z)\} \right\}, \qquad (2.19)$$

with

$$k_{z,m}(k_x, k_y) = \sqrt{n_m^2 k_0^2 - k_x^2 - k_y^2}\,. \qquad (2.20)$$

This leads to a computationally efficient reformulation of the original WPM algorithm, which requires only one FFT-accelerated Fourier back-transform of a field matrix for each refractive index that occurs within the slice at the current axial position z. In practice, the Fourier transforms can be quickly calculated using the fast-Fourier-transform (FFT), in particular when carried out on a modern graphics processing unit (GPU). GPU acceleration allows in addition the massively parallel evaluation of the stencil function $\Theta_{z,m}(x, y)$. The current implementation of a GPU-accelerated WPM algorithm used in this work is based on the *arrayfire* software library [78].

The WPM algorithm has been compared to FDTD simulations and has been found to deliver exceptionally consistent results for typical microlenses [1, 36]. Experimental verification is found based on results of our research group, see Chapters 4 and 5, and journal publications [J2, J3, 79, J5, J6], as well as of other research groups using independent implementations of the same algorithm [48, 80–82].

However, there are still two drawbacks of the scalar WPM algorithm. The method is first of all unidirectional and thereby does not include counterpropagating reflections and standing wave phenomena. Furthermore, the amplitude change at interfaces according to Fresnel's formulas cannot be treated correctly, since reflection and transmission coefficients depend on the vectorial nature of light. A vectorial WPM algorithm does exist [75], but requires a significantly larger number of computational operations[23]. Note that total internal reflection (TIR) phenomena are covered by the WPM algorithm, but the unidirectional simulation

---

[23] We consider simulations in three dimensions with a total number of $N_{xy} = N_x N_y$ grid points on each transverse plane, N_z longitudinal slices, and a small number of discrete refractive index values. The scalar WPM requires $\mathcal{O}(N_z N_{xy} \log N_{xy})$ operations [36], while the vectorial WPM (VWPM) scales with $\mathcal{O}(N_z N_{xy}^2)$ [75, 76], in addition to a significantly larger memory requirement. In comparison to VWPM, the computational complexity of FDTD for typical free-space problems scales "only" with $\mathcal{O}((N_x N_y N_z)^{\frac{4}{3}})$ [83].

requires that the beam is redirected by less than $90°$. In practice, simulation of micro-optical elements which include TIR mirrors can be done by "unfolding" the corresponding optical paths, as long as it is certain that no TIR failure occurs.

2.2.3 Zeroth-order correction of Fresnel losses within the scalar method

The scalar WPM cannot treat amplitude changes at interfaces according to Fresnel's formulas correctly, and the error in terms of absolute power values can be enormous, in particular when modeling dielectric interfaces with large index differences. As an example, we may consider the simple case of a collimated beam impinging from vacuum into a material with refractive index $n > 1$. For perpendicular incidence, the magnitude of the electric field is found to be the same before and after the interface according to Eq. 2.19. The power within the material is hence found to be n-times higher than the incident power, grossly violating energy conservation. This observation leads to the idea of an intuitive zeroth-order correction of Fresnel losses within the scalar method, proposed in this work. The perpendicular amplitude Fresnel transmission coefficient from material m with refractive index n_m to material m' with refractive index $n_{m'}$ is

$$\tau_{m \to m'} = \frac{2n_m}{n_m + n_{m'}} \tag{2.21}$$

independent of polarization, and the propagation in Eq. (2.19) is then modified to

$$\underline{E}(x, y, z + \Delta z) = \sum_{m,m'=1}^{M} \tau_{m \to m'} \Theta_{z,m}(x, y)\Theta_{z+\Delta z,m'}(x, y)$$
$$\times \mathcal{F}_{xy}^{-1}\left\{ e^{-j\,k_{z,m}(k_x,k_y)\Delta z} \mathcal{F}_{xy}\{\underline{E}(x, y, z)\}\right\} . \tag{2.22}$$

For the propagation through a tilted surface, Eq. (2.22) treats the perpendicular transmission through the corresponding staircased surface instead. In this context, it should be noted that the scalar WPM algorithm itself is subject to intrinsic

amplitude errors [36], which become pronounced for steep refractive index changes in lateral direction, as well as for large propagation angles. A theoretical discussion for the leading error term in each propagation step is given in [36] for smoothly varying refractive index distributions and the analytical representation of the WPM algorithm according to Eqs. (2.16) and (2.17). However, a quantitative study of amplitude errors in conjunction with discrete refractive indices and discretized numerical implementation is missing.

To estimate the impact of these amplitude errors on the power transmission in WPM simulations, we perform a reference simulation with and without the zeroth-order correction of Fresnel reflection losses according to Eq. (2.22), see Fig. 2.8 and Fig. 2.9. We consider the simple case of a plane slab of uniform thickness, Fig. 2.8(a). A collimated Gaussian beam (wavelength $\lambda = 1.55\,\mu m$, beam diameter $30\,\mu m$) in vacuum ($n_0 = 1$) impinges on the slab (refractive index $n = 1.53$). We vary the incident angle $\vartheta = 0 \ldots 70°$ and and simulate the propagation both with and without correction. The transmitted beam after the slab propagates again parallel to the z-axis, and the power values before ($z = 0$) and after ($z = 200\,\mu m$) the slab are simply quantified by summing up the magnitude squared of the electric field over the respective lateral plane. For incident angles $\vartheta > 45°$, the reflected beam appears in the unidirectional WPM simulation as well, Fig. 2.8(b). The downwards propagating reflected beam hits an absorbing simulation boundary and thereby does not contribute to the simulated power transmission. The results are shown in Fig. 2.9. The black dots in Fig. 2.9(a) and (b) indicate the simulated power transmission T as a function of incidence angle ϑ without correction (black dots), i.e, according to Eq. (2.19). The correct values $T_p(\vartheta)$ (p-polarization, blue curve) and $T_s(\vartheta)$ (s-polarization, orange curve) according to Fresnel's formulae are shown for comparison. For the correct Fresnel solution, we neglect back-reflected beams and Fabry-Perot-like interference to mimic the forward-only propagation modeled by the WPM. Simulations are performed with a medium level of z-discretization, $\Delta z = \lambda/n/10$, Subfigure (b), and a very fine z-discretization, $\Delta z = \lambda/n/80$, Subfigure (c). Without correction, the simulated power transmission is $T = 1$ for perpendicular incidence ($\vartheta = 0$), ignoring the material interface. The simulated transmission then drops towards larger incidence angles, with the exact values
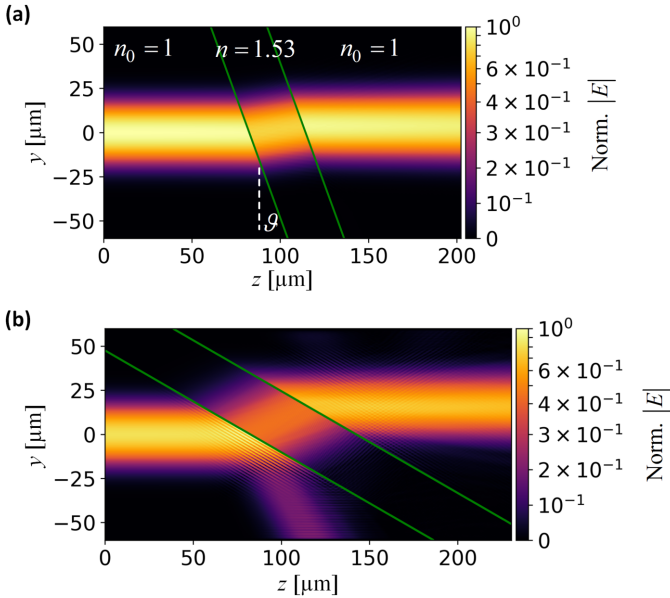
Fig. 2.8: Simulation setup quantifying power transmission errors in WPM simulations. The simulations have been performed with and without the zeroth-order correction of Fresnel reflection losses according to Eq. (2.22) — the field plots shown here were obtained from the simulations with correction. **(a)** A collimated Gaussian beam (wavelength $\lambda = 1.55\,\mu\text{m}$, beam diameter $30\,\mu\text{m}$) in vacuum ($n_0 = 1$) impinges on a tilted plane-parallel slab (refractive index $n = 1.53$, incident angle $\vartheta = 0\dots70°$). The depicted simulation utilizes the correction and the field magnitude within the slab and is therefore seen to be lower. **(b)** For incident angles $\vartheta > 45°$, the reflected beam appears in the unidirectional WPM simulation as well. The downwards propagating reflected beam hits an absorbing simulation boundary and thereby does not contribute to the simulated power transmission.

depending on the numerical z-discretization. Finally, Figs. 2.9(c) and (d) show the corresponding plots for the simulated power transmission with correction according to Eq. (2.22). The power transmission is accurate for perpendicular incidence ($\vartheta = 0$), and an angular dependency is again observed, with the exact shape and values depending on the z-discretization. Remarkably, a sufficiently fine z-discretization, $\Delta z = \lambda/n/80$, Subfigure (d), leads to a drop-off which approximates the theoretically correct curve $T_s(\vartheta)$ for s-polarization very well. However, at least on a quantitative level, this should be regarded as coincidence,
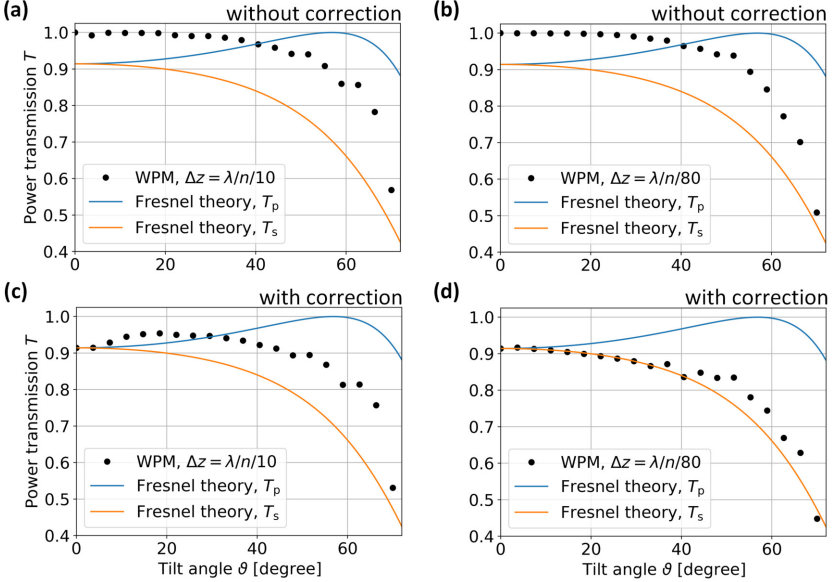
Fig. 2.9: Simulation results for the quantification of power transmission errors in WPM simulations with and without the zeroth-order correction of Fresnel reflection losses according to Eq. (2.22). **(a, b)** Angle-dependent simulated power transmission $T(\vartheta)$ without correction (black dots). The correct values $T_p(\vartheta)$ and $T_s(\vartheta)$ for p-and s-polarization according to Fresnel's formulae are shown for comparison. Simulations are performed with a medium level of z-discretization ($\Delta z = \lambda/n/10$, Subfigure a) and a very fine z-discretization ($\Delta z = \lambda/n/80$, Subfigure b). **(c, d)** Corresponding plots for the simulated power transmission with correction. We find that the correction helps in obtaining an accurate power transmission for perpendicular incidence ($\vartheta = 0$). The simulated power transmission drops towards larger incidence angle, with the exact values depending on the numerical z-discretization. Remarkably, a sufficiently fine z-discretization in Subfigure (d) leads to a drop-off which approximates the theoretically correct curve $T_s(\vartheta)$ for s-polarization very well.

considering the existence of intrinsic amplitude errors of the WPM algorithm. On the other hand, on a qualitative level, the s-polarization-like behavior found as opposed to a p-polarization-like behavior is not a coincidence. With the given geometry of the simulation, the scalar approximation is fully valid for s-polarization, because the s-polarized electric field consists of an x-component only, whereas $(\mathrm{grad}\ln n^2)$ in Eq. (2.9) has no x-component. As a consequence,

Eq. (2.9) can be written as a single scalar Helmholtz-type wave equation for the E_x-component. No such argument can be found for p-polarization.

The angle-dependent power transmission as seen in the simplistic reference simulation of Fig. 2.9 certainly has an influence on the exact shape of optimized high-NA lens surfaces. The drop-off towards larger incidence angles is, however, qualitatively similar in Figs. 2.9(a)-(d). Therefore, no significant shape difference has been found when optimizing actual microlenses with or without the correction. The correction is, however, useful, when absolute power values are of interest, e.g., for a more realistic prediction of achievable efficiencies in fiber-chip coupling using microlenses. No obvious disadvantage of the correction has been found, and it has therefore been employed in all microlens simulations of this work, see Chapters 4 and 5.

2.3   Measurement of mode fields

To reach the ultimate goal of providing a technologically mature toolset for hybrid photonic assemblies based on 3D-printed coupling structures, a complete process chain with predictable outcome must be established, starting at the level of individual integrated optical components and ending at the complete assembly. This obviously requires sophisticated lithography machines and techniques[24], as well as fast and reliable micro-optical simulation tools[25]. The first step in this chain, however, namely the precise knowledge of the mode field of each individual component, has surprisingly also proven to be troublesome. Specifications from component suppliers are often inaccurate and, in many cases, the problem cannot be tackled from the simulation side either, because the detailed layer stack of a particular photonic chip is either unprecisely known or belongs to the best-kept

---

[24]   Cf. Sections 2.1.2 and 2.1.3; a large amount of effort has also previously been invested in this context by M. Blaicher [1], M. R. Billah [34], P.-I. Dietrich [2] and T. Hoose [84].

[25]   See, e.g., Section 2.2.

secrets of manufacturers. A measurement of the mode-field prior to 3D-printing of coupling structures is therefore usually unavoidable.

2.3.1 Proof-of-principle demonstration of a phase-resolved mode-field measurement method

Apart from the mode-field size and location, an entirely predictable outcome would require the knowledge of the optical phase distribution of the mode field at the facet plane, rather than blindly assuming a plane phase front. A non-plane phase distribution can most prominently be found at the output of semiconductor lasers or amplifiers with strong gain guiding and insufficiently strong index guiding. A beam emitted from such a device suffers from astigmatism [85], usually with the beam waist in the vertical direction, i.e., perpendicular to the semiconductor substrate surface, located at the facet and a virtual beam waist in the horizontal direction, i.e., parallel to the semiconductor substrate, located behind the facet within the laser. In this case, the phase distribution at the facet plane is flat in the vertical direction and approximately parabolic in the horizontal direction. Note that assuming a correct mode-field diameter but erroneously assuming a flat phase may affect facet-attached microlens based assembly techniques [2, J2] in a much different way than photonic wire bond based assembly techniques [J1, 33, 34]. In the case of microlenses, the true phase distribution affects the divergence of a beam which emerges from a photonic chip, and may lead to a completely different illumination of the lens surface than designed. The beam shaped by the lens and any further component designed based on the assumed beam shape are therefore subject to a chain of "follow-up errors". Taking the correct phase distribution into account allows for aberration-correcting designs, using (multiple) non-rotationally symmetric lens surfaces, or a combination of lenses and prisms [85]. In the case of photonic wire bonds, coupling an incident field with a curved phase front to the eigenmode of a single-mode photonic wire bond waveguide simply leads to a certain deterministic excess loss at the coupling plane. Knowledge of the true phase distribution at best helps to explain excess losses *a posteriori*, but there is no full remedy.

Based on aforementioned arguments, we conclude that phase-resolved measurement of the aperture field of integrated optical components is a much desired characterization tool. The measurement should be based on observation through a microscope objective for practical reasons. In the following, we will describe approaches to mode-field characterization that exploit the idea of using an iterative Fourier transform algorithm (IFTA) to retrieve phase information from measured intensity distributions, which dates back to Gerchberg and Saxton [86]. Various minor modifications have been proposed, most prominently by Fienup [87]. The classical Gerchberg-Saxton (GS) algorithm, see Fig. 2.10, uses measured intensity distributions $I_0(x, y)$ and $I_1(x, y)$ at two Fourier-conjugated planes. The magnitudes of the complex electric fields at the respective planes are calculated from the square root of the intensities, $\left|E_0(x, y)\right| = \sqrt{I_0(x, y)}$ and $\left|E_1(x, y)\right| = \sqrt{I_1(x, y)}$. A retrieved approximation $\varphi_{0,\mathrm{ret}}(x, y)$ to the true phase distribution $\varphi_0(x, y)$ at the first plane is found based on an iterative method. The algorithm is divided into the following steps:

- An initially *guessed* phase distribution $\varphi_{0,\mathrm{g}}(x, y)$ and the measured magnitude $\left|E_0(x, y)\right| = \sqrt{I_0(x, y)}$ lead to an initial approximation of the complex field

$$\underline{E}_{0,\mathrm{g}}(x, y) = \left|E_0(x, y)\right| \mathrm{e}^{\mathrm{j}\, \varphi_{0,\mathrm{g}}(x,y)} \tag{2.23}$$

  at the first plane. A two-dimensional spatial Fourier transform

$$\underline{E}_{1,\mathrm{g}}(x, y) = \mathcal{F}_{xy}\{\underline{E}_{0,\mathrm{g}}(x, y)\} = \left|E_{1,\mathrm{g}}(x, y)\right| \mathrm{e}^{\mathrm{j}\, \varphi_{1,\mathrm{g}}(x,y)} \tag{2.24}$$

  is calculated, approximating the complex field at the second plane based on the initially guessed phase distribution at the first plane.

- A better approximation $\underline{E}_{1,\mathrm{r}}(x, y)$ for the complex field at the second plane is found by *replacing* the magnitude of the previously computed complex field $\underline{E}_{1,\mathrm{g}}(x, y)$ with the acutally measured magnitude $\left|E_1(x, y)\right| = \sqrt{I_1(x, y)}$ while keeping the computed phase,

$$\underline{E}_{1,\mathrm{r}}(x, y) = \left|E_1(x, y)\right| \mathrm{e}^{\mathrm{j}\, \varphi_{1,\mathrm{g}}(x,y)} . \tag{2.25}$$

- The Fourier back-transform

$$\underline{E}_{0,\mathrm{r}}(x,y) = \mathcal{F}_{xy}^{-1}\{\underline{E}_{1,\mathrm{r}}(x,y)\} = \left|E_{0,\mathrm{r}}(x,y)\right| \mathrm{e}^{\mathrm{j}\,\varphi_{0,\mathrm{r}}(x,y)} \qquad (2.26)$$

is computed to propagate the field back to the first plane.

- The magnitude of the back-transform $\left|E_{0,\mathrm{r}}(x,y)\right|$ is discarded and replaced by the actually measured magnitude $\left|E_0(x,y)\right| = \sqrt{I_0(x,y)}$ while keeping the computed phase. The algorithm enters the next iteration, using the phase distribution $\varphi_{0,\mathrm{r}}(x,y)$ as next guessed phase distribution $\varphi_{0,\mathrm{g}}(x,y)$.

- The algorithm is stopped after a sufficient round of iterations, and the last phase distribution $\varphi_{0,\mathrm{r}}(x,y)$ is considered as the retrieved phase $\varphi_{0,\mathrm{ret}}(x,y)$.
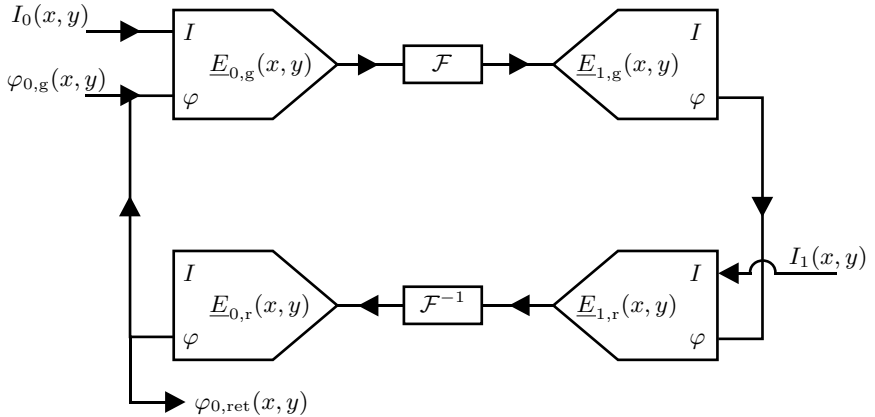
Fig. 2.10: Schematic of the classical Gerchberg-Saxton (GS) algorithm. Intensity distributions $I_0(x,y)$ and $I_1(x,y)$ are measured at two Fourier-conjugated planes. A retrieved approximation $\varphi_{0,\mathrm{ret}}(x,y)$ to the unknown phase distribution $\varphi_0(x,y)$ at the first plane is found based on an iterative method. Starting from an initially guessed phase distribution $\varphi_{0,\mathrm{g}}(x,y)$ and the known intensity distributions, the algorithm performs alternating Fourier transforms and back-transforms of the complex fields. Prior to each (back-)transform, the magnitude of the complex field is replaced by the square root of the actually measured intensity distribution of the respective plane, while the computed phase is kept.

The convergence is monitored by determining the "similarity" in each iteration between the computed (discarded) magnitude and the actually measured magnitude in one of the planes. A sum squared error (SSE) could be defined at either plane, e.g., in [88] for the second plane as

$$\text{SSE} = \frac{\iint \left(|E_1(x,y)| - |E_{1,\text{g}}(x,y)| \right)^2 \mathrm{d}x\,\mathrm{d}y}{\iint |E_1(x,y)|^2 \mathrm{d}x\,\mathrm{d}y} \, . \tag{2.27}$$

Typical shortcomings of the algorithm involve a slow convergence ("stagnation"), and a low tolerance towards noise in the measured intensity distributions. Furthermore, the solution is only unique under certain conditions [89] and may depend on the initially guessed phase distribution in the most general case. Various derivates of this algorithm exist, which promise improved performance for specific applications. Most of them differ from each other at the instances where the calculated magnitudes are replaced by the measured ones. This replacement may be done only in a spatially filtered region of interest [90], e.g., where significant amount of intensity is observed, and/or in a gradual fashion [87, 91, 92] by forming a linear superposition of the computed and measured magnitudes.

In this work, another modified variant of the algorithm is proposed, which is compatible with aforementioned improvements, and which is specifically tailored for the characterization of mode fields of integrated optical components, see Fig. 2.11. Instead of considering two Fourier-conjugated planes, we record multiple intensity distributions $I_0(x,y), I_1(x,y), I_2(x,y), \ldots, I_m(x,y)$ at corresponding planes $z = z_0, z_1, z_2, \ldots z_m$. For propagating light between these planes, the Fourier transform in the classical GS-algorithm is replaced by a scalar wide-angle free-space propagation, indicated by the propagator $\mathcal{P}$ in Fig. 2.11) according to Eqs. (2.12) and (2.15). The intensity distribution $I_0(x,y)$ is measured with the facet in focus at $z = z_0$, and the remaining z-slices cover an axial distance comparable to the typical size of a microlens. The redundant inclusion of data from multiple planes improves the robustness against measured noise. The choice of the axial position range of these planes ensures that any simulated beam
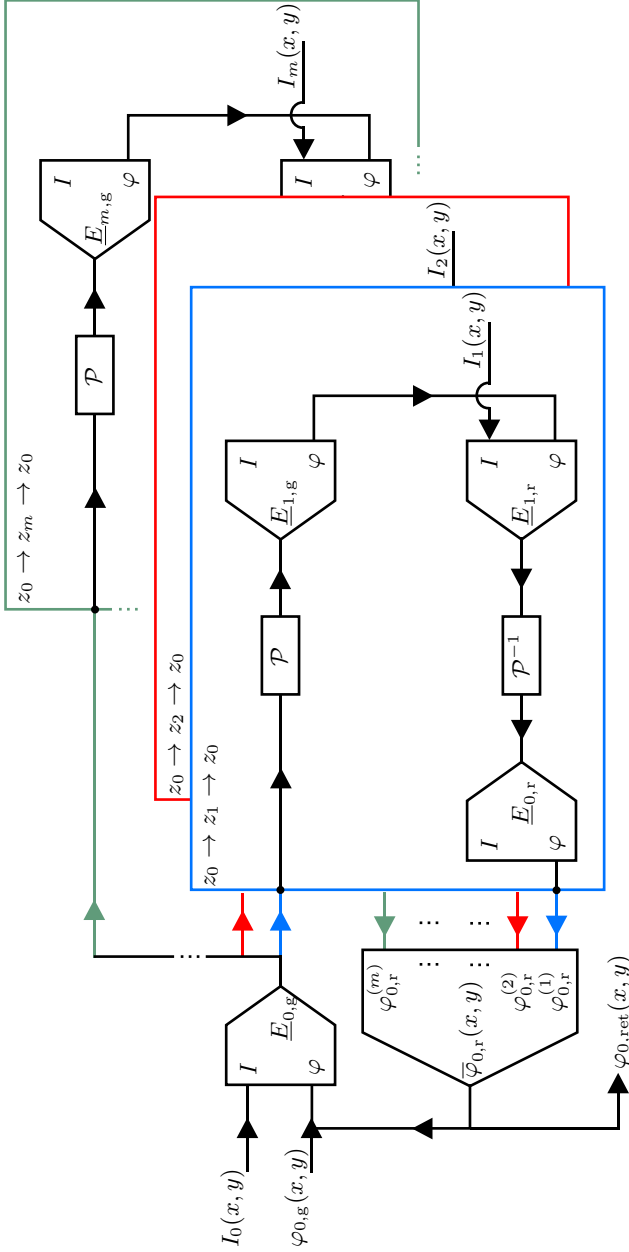
Fig. 2.11: Schematic of a modified phase retrieval algorithm for characterizing mode fields of integrated optical components. The algorithm uses multiple measured intensity distributions $I_0(x, y)$, $I_1(x, y)$, $I_2(x, y)$, . . . , $I_m(x, y)$ measured at multiple planes $z = z_0, z_1, z_2, . . . z_m$, where position z_0 is located at the device facet. A scalar wide-angle free-space propagation $\mathcal{P}$ according to Eqs. (2.12) and (2.15) is used to propagate the complex fields from one plane to another. Propagation of the initially assumed field from z_0 to z_1 and back (propagation scheme $z_0 \rightarrow z_1 \rightarrow z_0$, blue frame), alongside the magnitude replacement at the plane z_1, leads to a first candidate phase distribution $\varphi_{0,\mathrm{r}}^{(1)}(x, y)$. The analogous propagation schemes for the other planes are $z_0 \rightarrow z_2 \rightarrow z_0$, red frame, . . . , $z_0 \rightarrow z_m \rightarrow z_0$, green frame, leading to further candidate phase distributions $\varphi_{0,\mathrm{r}}^{(2)}(x, y), . . . , \varphi_{0,\mathrm{r}}^{(m)}(x, y)$. The algorithm enters the next iteration, using a suitable "average" $\overline{\varphi}_{0,\mathrm{r}}(x, y)$ according to Eq. (2.28).

evolution based on retrieved complex field data is sufficiently "correct" within the relevant distance range. An intuitive way of combining the data from multiple planes is proposed in Fig. 2.11: The initial approximation of the complex field is propagated from z_0 to z_1, where the magnitude is replaced by the measured magnitude $|E_1(x, y)| = \sqrt{I_1(x, y)}$. After back-propagation, a first candidate phase distribution $\varphi_{0,r}^{(1)}(x, y)$ is found (propagation scheme $z_0 \to z_1 \to z_0$, blue frame in Fig. 2.11). The analogous procedure is done for the other planes as well (propagation schemes $z_0 \to z_2 \to z_0$, red frame, ..., $z_0 \to z_m \to z_0$, green frame), leading to further candidate phase distributions $\varphi_{0,r}^{(2)}(x, y), \ldots, \varphi_{0,r}^{(m)}(x, y)$. The algorithm enters the next iteration, using a suitable "average" $\overline{\varphi}_{0,r}(x, y)$ as next guessed phase distribution $\varphi_{0,g}(x, y)$ at the facet plane. We perform the "averaging" using phasors instead of directly averaging the phases, to avoid issues related to 2π-periodic phase wrapping[26],

$$\overline{\varphi}_{0,r}(x, y) = \arg \left\{ \sum_{l=1}^{m} e^{j \, \varphi_{0,r}^{(l)}(x, y)} \right\}. \tag{2.28}$$

A measurement setup suitable to test the proposed algorithm is shown in Fig. 2.12. The setup is based on a horizontally mounted infrared (IR) microscope, using a $100\times / 0.8$ near infrared objective and an IR camera[27]. Horizontal mounting facilitates operation of the device under observation, which is usually mounted onto a horizontal fiber or chip holder. A semiconductor laser chip, for example, can be easily probed when mounted horizontally, or light can be coupled into a passive on-chip waveguide. The sample cannot be moved once contacted. Therefore, the entire microscope sits on a stage and is moved along the axial z-direction automatically. The infinity space, i.e., the collimated beam section between the objective and the tube lens, contains a set of exchangeable neutral density (ND) filters for observing the laser emission with pump currents far above threshold, without risk of damaging the IR-camera. A removable and adjustable polarizer

---

[26] Assuming phase angles in the interval $(-\pi, +\pi]$, i.e., a wrapping point at $\pm\pi$, and a small value $\delta > 0$, direct averaging of two phase angles $\pi - \delta$ and $-\pi + \delta$ would lead to the incorrect value of 0 instead of the correct value of $+\pi$.

[27] Allied Vision Goldeye G-032 TEC1, 25 µm per pixel

can be used for polarization-sensitive investigations. For a precise alignment of 3D-printed photonic wire bonds (PWB) or facet-attached microlenses (FaML) later on, the exact lateral position of the mode field with respect to the device facet needs to be characterized. Furthermore, in axial direction, an observation of the beam emitted from the device needs to clarify whether the observed beam waist corresponds to an aperture field at the device facet, or whether the beam waist is actually found within the chip. To these ends, the setup contains an additional illumination light path. The illumination uses two separate light sources, centered around the wavelengths of $1300\,\mathrm{nm}$ and $1550\,\mathrm{nm}$, respectively. Using a similar illumination wavelength as the emission wavelength of the device under observation minimizes errors related to the chromatic aberration of the objective lens.

The beam emitted by the integrated optical device diverges and leads to a strong dependency of the observed intensities on the axial position z. Therefore, an automatic exposure time adjustment is used to produce roughly the same maximum intensity on the recorded images. Background (dark) images are taken at each utilized exposure time and subtracted accordingly. Only a relevant subregion of the recorded image stack is taken into account for phase recovery. Data within this subregion are first interpolated on a grid of $2^M \times 2^N$ points ($M, N \in \mathbb{N}$), since the numerical implementation of the propagation according to Eqs. (2.12) and (2.15) relies on fast Fourier transforms.

For an experimental proof-of-principle demonstration, two types of thin phase-mask structures for light at a wavelength of $1550\,\mathrm{nm}$ are printed to the facets of single-mode fibers (SMF), see Fig. 2.13. The first type, Figure 2.13(a), is a thin step ("π-step") which covers half of the fiber core and which retards the phase by π compared to the uncovered part. The second type of structures are spiral phase plates[28] which generate orbital angular momentum (OAM) beams, and which can be designed for various OAM orders ν. The phase shift induced by such a spiral

---

[28]   Generation of OAM beams by spiral phase plates was first demonstrated in [93]. Multi-photon 3D-printed spiral phase plates have previously been published in [82].
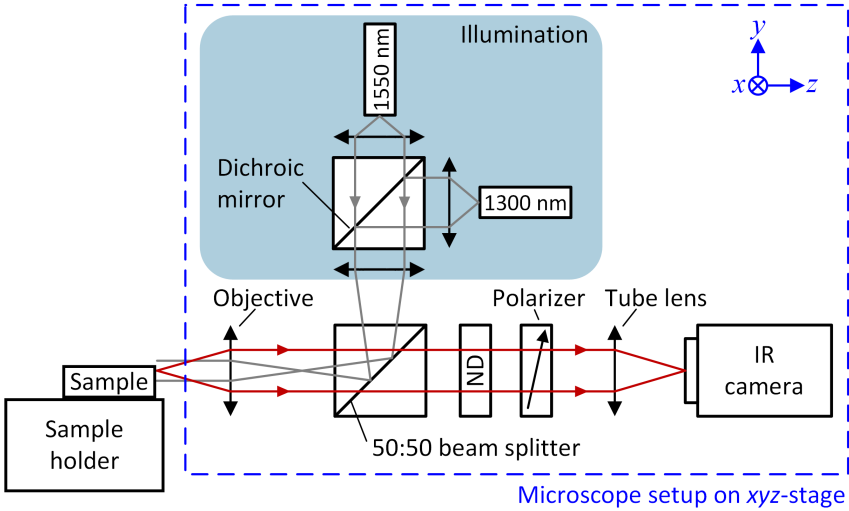
Fig. 2.12: Measurement setup for phase-resolved mode-field characterization. The setup is based on a horizontally mounted infrared (IR) microscope, using a near IR objective and an IR camera. Horizontal mounting facilitates operation of the device under observation. The sample cannot be moved, once contacted. Therefore, the entire microscope setup is mounted on a stage and is moved along the axial z-direction automatically. The collimated beam section between the objective and the tube lens contains a set of exchangeable neutral density (ND) filters as well as a removable and adjustable polarizer. An additional illumination (shaded box, grey ray paths) allows to observe the device facet simultaneously. The illumination uses two separate light sources, centered around the wavelengths of 1300 nm and 1550 nm, respectively. Additional components related to electrical and/or optical sample probing are omitted for brevity.

phase plate increases linearly from 0 to $\nu \times 2\pi$ along the azimuthal direction. Figure 2.13(b) depicts an exemplary structure for $\nu = 2$.

The experimental results are shown in Figs. 2.14 and 2.15, for the π-step in Fig. 2.13(a) and the spiral phase plate in Fig. 2.13(b), respectively. The fibers are back-illuminated with a laser at $\lambda = 1550$ nm, and images are recorded at various focal planes covering an axial distance of 60 μm. The first images at $z = z_0$,
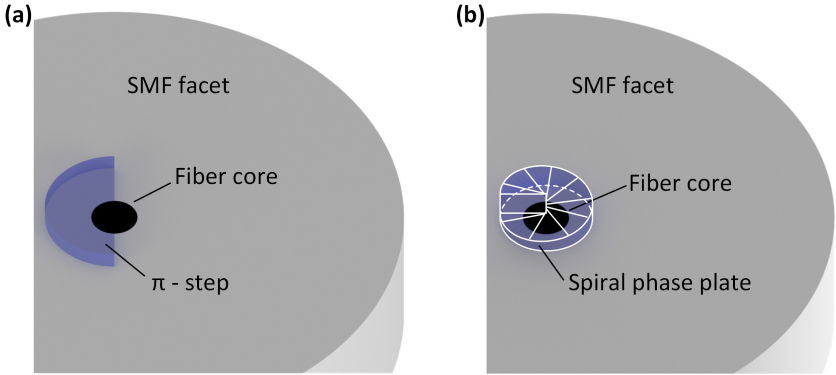
Fig. 2.13: Thin phase-mask structures on single-mode fibers (SMF), designed for light at a wavelength of 1550 nm. **(a)** Step ("π-step") which covers half of the fiber core and which retards the phase by π compared to the uncovered part. **(b)** Spiral phase plate for generation of an orbital angular momentum (OAM) beam of the order $\nu = 2$.

Fig. 2.14(a) and 2.15(a) are taken right after the printed structure[29]. A lateral grid area of 120 µm $\times$ 120 µm is considered for the computation with a resolution of $\lambda/4$. Figures 2.14 and 2.15 show a magnified view of a 50 µm $\times$ 50 µm grid area for better visibility of details.

For the π-step, the retrieved phase distribution $\varphi_{0,\mathrm{ret}}(x, y)$, Fig. 2.14(b), was obtained using a plane-phase-front initial guess, and clearly shows the expected step behavior in the retrieved phase ($\varphi_{0,\mathrm{ret}}(x, y) \approx -0.5\pi$ for the left half, and $\varphi_{0,\mathrm{ret}}(x, y) \approx +0.5\pi$ on the right half of the spot). The measured magnitude $|E_0(x, y)| = \sqrt{I_0(x, y)}$ at the first image plane, Fig. 2.14(a), and the retrieved phase distribution, Fig. 2.14(b), are combined to a complex field. This field is propagated to predict the magnitude at a distance $z = z_0 + 20$ µm, Fig. 2.14(c),

---

[29]   The focal position z_{visual} where the last part of the printed structure appears sharpest can be visually determined with an uncertainty of ± 1 µm based on the experimental setup in Fig. 2.12. The position of the first image is chosen to be $z_0 = z_{\mathrm{visual}} + 2$ µm, to prevent that z_0 accidentally still lies within the structure.

and compared to actual measurement, Fig. 2.14(d). A great similarity is found, proving the consistency of the method[30].
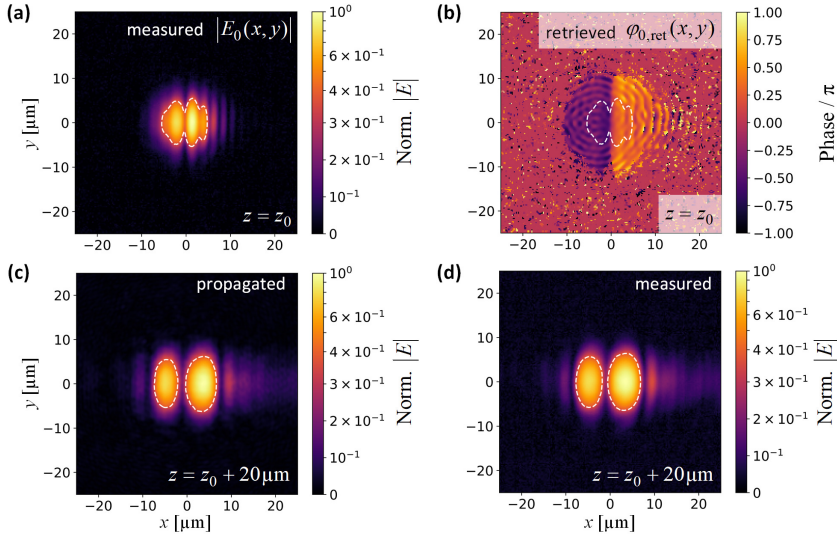
Fig. 2.14: Phase retrieval results for the π-step sample, Fig. 2.13(a), using the algorithm illustrated in Fig. 2.11. The fiber is fed by a laser at $1550\,\mathrm{nm}$ from the remote end, and images are recorded at various focal planes covering an axial distance of $60\,\mu\mathrm{m}$. **(a)** Magnitude $\left|E_0(x,y)\right| = \sqrt{I_0(x,y)}$ derived from the measured intensity distribution $I_0(x,y)$ at the plane $z = z_0$ right after the printed structure. The dashed white line indicates a lateral decay of the field magnitude by $1/\mathrm{e}$, i.e., an intensity decay by $1/\mathrm{e}^2$. **(b)** Retrieved phase distribution $\varphi_{0,\mathrm{ret}}(x,y)$ at the plane $z = z_0$. A plane-phase-front initial guess was used. **(c)** Propagated field at the plane $z = z_0 + 20\,\mu\mathrm{m}$, based on the measured magnitude at $z = z_0$, Subfigure (a), and on the retrieved phase at $z = z_0$, Subfigure (b). **(d)** Magnitude from measured intensity distribution at the plane $z = z_0 + 20\,\mu\mathrm{m}$. We find the expected step in the retrieved phase and a great similarity between measured and propagated intensity distributions at each of the recorded image planes, proving the consistency of the method.

---

30   Corresponding comparison images for the other measured planes are omitted for brevity.

For the spiral phase plate, a plane-phase-front initial guess does not work[31]. Using various ideal OAM phase distributions as initial guesses furthermore leads to different results, depending on the assumed order. However, the divergence of OAM beams depends on the order [94]. The algorithm can therefore test different ideal OAM initial guesses and "pick" the correct one by comparing the residual errors according to Eq. (2.27) after a few pilot iterations. Figure 2.15(b) shows the final retrieved phase distribution based on this premise. As before, this phase distribution is again used to compute a propagated field. The predicted magnitude at the plane $z = z_0 + 20\,\mu\text{m}$, Fig. 2.15(c), is compared to the actual measurement, Fig. 2.15(d), and a great similarity is again found.

Note that various related publications escaped the author's attention in a first literature search. The modified phase retrieval method has hence been developed independently. Individual contributing ideas are however also found in various slightly different combinations and contexts in existing literature. We therefore end this section with a short literature survey. The inclusion of data from multiple planes for phase retrieval has previously been proposed by [95], [96], and [97]. The propagation scheme in this work is identical to the one in [95], while [96] uses a "circular" propagation scheme of the form $z_0 \to z_1 \to \ldots \to z_m \to z_0 \ldots$ (again with replacements of the magnitude at each plane). A direct optimization of the phase distribution using a nonlinear gradient optimization method has been proposed in [97]. The associated gradients are computed efficiently by making use of both forward propagations ($z_0 \to z_1$; $z_0 \to z_2$; ... ; $z_0 \to z_m$) as well as backward propagations ($z_1 \to z_0$; $z_2 \to z_0$; ... ; $z_m \to z_0$). Employing the angular spectrum method according to Eqs. (2.12) and (2.15) for the propagation is proposed in [97, 98] as well. However all preceding publications only show simulations and charaterizations of macroscopic low numerical-aperture[32] beams.

---

[31] This is not surprising considering symmetry arguments. An ideal OAM beam possesses an azimuthally symmetric intensity distribution. The phase distribution however only satisfies an azimuthal consistency condition, but is not symmetric.
[32] Divergence angles of $0.6°$ in [97, 98], as opposed to $5.4°$ from an SMF at a wavlength of 1550 nm
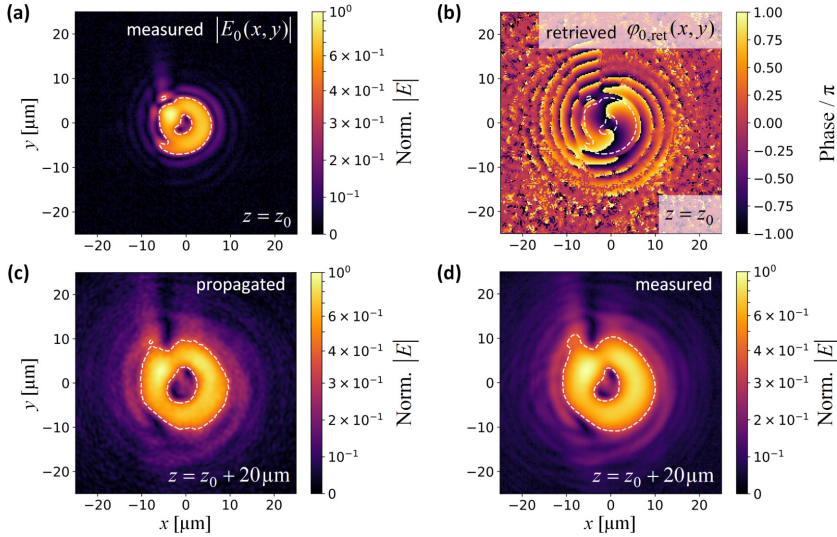
Fig. 2.15: Phase retrieval results for the spiral phase plate sample, Fig. 2.13(b), using the algorithm illustrated in Fig. 2.11. The fiber is fed by a laser at 1550 nm from the remote end, and images are recorded at various focal planes covering an axial distance of 60 µm. **(a)** Magnitude $|E_0(x,y)| = \sqrt{I_0(x,y)}$ derived from the measured intensity distribution $I_0(x,y)$ at the plane $z = z_0$ right after the printed structure. The dashed white line indicates a lateral decay of the field magnitude by $1/e$, i.e., an intensity decay by $1/e^2$. **(b)** Retrieved phase distribution $\varphi_{0,\mathrm{ret}}(x,y)$ at the plane $z = z_0$. For such an orbital angular momentum (OAM) beam, a plane-phase-front initial guess does not work. Instead, the algorithm was provided with a set of ideal OAM phase distributions of various orders as initial guess, and the correct one was "picked", based on comparison of residual errors according to Eq. (2.27) after a few pilot iterations. **(c)** Propagated field at the plane $z = z_0 + 20\,\mu\mathrm{m}$, based on the measured magnitude at $z = z_0$, Subfigure (a), and on the retrieved phase at $z = z_0$, Subfigure (b). **(d)** Magnitude from measured intensity distribution at the plane $z = z_0 + 20\,\mu\mathrm{m}$. We find the expected spiral behavior in the retrieved phase and a great similarity between measured and propagated intensity distributions at each of the recorded image planes, proving the consistency of the method.

2.3.2 Influence of immersion on mode fields and on mode-field measurements

The characterization of small mode fields of integrated devices with mode-field diameters (MFD) well below 3 µm needs to consider the influence of the immersion medium, i.e, the medium into which the optical facet is embedded, as well as

the influence of the microscopy-based observation system used for measuring the mode field, e.g., as illustrated in Fig. 2.12. The following discussion contains a quantitative study.

The first important notion is that the relevant mode field is an aperture field and not a near field, i.e., the MFD relevant for coupling to waveguides and lenses is the one related to propagating waves and does not include any evanescent modes. However, the spatial frequencies associated with propagating waves depend on the refractive index n of the surrounding medium. We therefore carefully distinguish between three different MFD, denoted by the according subscript. The first one, $\mathrm{MFD_{chip}}$, is the mode-field diameter of the on-chip waveguides as, e.g., obtained by Eigenmode simulations. Waveguides with high index contrast allow for small values of $\mathrm{MFD_{chip}}$. An extreme example is given by a silicon photonic (SiP) waveguide with refractive indices of $n_{\mathrm{Si}} \approx 3.48$ and $n_{\mathrm{SiO_2}} \approx 1.44$ in the silicon core and the silicon oxide cladding, respectively. For such waveguide, a typical value for $\mathrm{MFD_{chip}}$ is $\mathrm{MFD_{chip}} \approx 500\,\mathrm{nm}$, measured in the horizontal direction. We further consider a waveguide, ending directly at the chip facet and emitting light directly in free space (refractive index $n_{\mathrm{air}} = 1$). In this case, not all spatial frequencies associated with $\mathrm{MFD_{chip}}$ propagate in air, and the transition from chip to air acts as a spatial-frequency lowpass filter. The mode-field diameter in air, $\mathrm{MFD_{air}}$, therefore becomes larger than the $\mathrm{MFD_{chip}}$. For photonic wire bonds (PWB) and most facet-attached microlenses (FaML) the polymerized photoresist (refractive index $n_{\mathrm{resist}} = 1.53$) is in direct contact with the device facet. Again, not all spatial frequencies associated with $\mathrm{MFD_{chip}}$ propagate in resist, leading to yet another mode-field diameter $\mathrm{MFD_{resist}}$ in resist.

However, because $n_{\mathrm{air}} < n_{\mathrm{resist}}$, the effect is less strong in resist than in air, i.e., $\mathrm{MFD_{air}} > \mathrm{MFD_{resist}} > \mathrm{MFD_{chip}}$ for strongly guiding high-index contrast waveguides. Clearly, $\mathrm{MFD_{resist}}$ is the relevant mode-field diameter for the design of PWB and FaML. However, typical mode-field measurements are conducted in air. Measurement in immersion with the same refractive index as the photoresist material are particularly cumbersome with the current horizontal measurement setup, Fig. 2.12, which facilitates contacting of unpackaged devices.

Using microscopy-based observation systems for mode-field measurements further introduces an additional observation error due to the limited numerical aperture (NA) of the microscope objective. The observed mode-field diameter in air, $\text{MFD}_{\text{obs,air}}$, represents a fourth value which may be even larger, $\text{MFD}_{\text{obs,air}} > \text{MFD}_{\text{air}} > \text{MFD}_{\text{resist}} > \text{MFD}_{\text{chip}}$, due to the low-pass characteristics of the microscope objective. To deduce the relevant mode-field diameter $\text{MFD}_{\text{resist}}$ from the values MFD_{air} in air, and from non-ideal measurements with given objective numerical aperture ($\text{MFD}_{\text{obs,air}}$), the following simple numerical study is conducted, see Fig. 2.16 and 2.17.

The integrated devices of interest either emit or are operated with coherent laser light. Therefore, complex electric fields are considered in the following. Within the simple numerical study, we assume monochromatic light with vacuum wavenumber k_0, principal propagation direction z and a scalar complex amplitude $\underline{E}(x, y)$ of the electric field, which stands for the complex amplitude of the dominant vectorial component. We start with an on-chip field distribution $\underline{E}_{\text{chip}}(x, y)$ right before the facet, as shown exemplarily in Panel (i) of Fig. 2.16 using a round Gaussian mode field with $\text{MFD}_{\text{chip}} = 1.0\,\mu\text{m}$. We assume that this field distribution acts as a source[33] for emission into the half-space following the facet. We then compute the two-dimensional (spatial) Fourier transform

$$\widetilde{\underline{E}}_{\text{chip}}(k_x, k_y) = \mathcal{F}_{xy}\{\underline{E}_{\text{chip}}(x, y)\}, \tag{2.29}$$

visualized in Panel (ii) of Fig. 2.16. The spatial-frequency lowpass filtering when transitioning from the chip into a medium with refractive index n is performed by multiplying with the appropriate amplitude transfer function $\mathcal{H}(k_x, k_y)$. The

---

[33] Note that the effective source field might differ from the eigenmode of the on-chip waveguide due to scattering and backreflection at the waveguide facet. This aspect is subject to ongoing investigation.
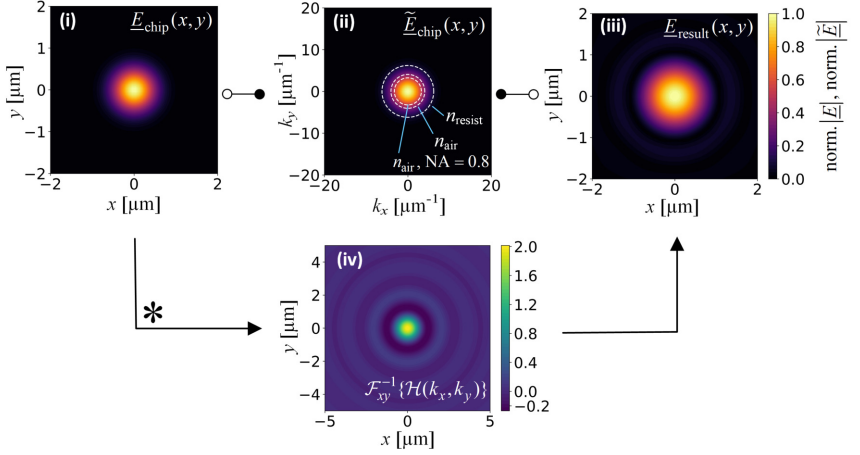
Fig. 2.16: Illustration of the numerical procedure for deducing the relevant mode-field diameter in resist from ideal and non-ideal measurements in air. Simulations are exemplarily shown for a round Gaussian mode field with $\mathrm{MFD_{chip}} = 1.0\,\mu\mathrm{m}$ at a wavelength of $\lambda = 1.55\,\mu\mathrm{m}$. **(i)** Scalar complex amplitude $\underline{E}_{\mathrm{chip}}(x, y)$ of the on-chip electric field right before the facet. **(ii)** A two dimensional (spatial) Fourier transform $\underline{\widetilde{E}}_{\mathrm{chip}}(k_x, k_y) = \mathcal{F}_{xy}\{\underline{E}_{\mathrm{chip}}(x, y)\}$ is computed. Spatial frequency filtering is applied by multiplication of an amplitude transfer function $\mathcal{H}(k_x, k_y)$, Eq. (2.30), which sets the values outside a respective circle to zero. The dashed lines indicate the corresponding circle sizes for the transition from chip to resist (largest circle, $n_{\mathrm{resist}} = 1.53$), for the transition from chip to air (intermediate circle, $n_{\mathrm{air}} = 1$), and for the observation in air with a limited NA (smallest circle, $n_{\mathrm{air}} = 1$, NA $= 0.8$) according to Eq. (2.31) and Eq. (2.33), respectively. **(iii)** Subsequent Fourier back-transform, Eq. (2.32), leads to the resulting complex amplitude $\underline{E}_{\mathrm{result}}(x, y)$, from which the respective mode-field diameter is derived. As an example, the color plot depicts the field distribution for propagating fields in air. **(iv)** Alternative computation route, Eq. (2.34). The complex field $\underline{E}_{\mathrm{chip}}(x, y)$ is convolved ($\ast$) with the (inverse) Fourier transform $\mathcal{F}_{xy}^{-1}\{\mathcal{H}(k_x, k_y)\}$ of the amplitude transfer function, see Eq. (2.35), again exemplarily shown for the case of propagating fields in air.

transfer function is unity within a circle with radius corresponding to the maximum allowed spatial frequency $k_{\mathrm{max}}(n) = nk_0$, and zero outside, i.e.,

$$\mathcal{H}(k_x, k_y) = \mathrm{circ}\left(\frac{\sqrt{k_x^2 + k_y^2}}{k_{\mathrm{max}}(n)}\right) = \begin{cases} 1 & \text{if } \sqrt{k_x^2 + k_y^2} < k_{\mathrm{max}}(n) \\ 0 & \text{else} \end{cases} \qquad (2.30)$$

where

$$k_{\max}(n) = nk_0 \,, \tag{2.31}$$

indicated in Panel (ii) of Fig. 2.16 as largest dashed circle for transition to photoresist ($n_{\mathrm{resist}} = 1.53$) and as intermediate-sized dashed circle for transition to air ($n_{\mathrm{air}} = 1$), both for a wavelength of $\lambda = 1.55\,\mu\mathrm{m}$. Subsequent Fourier back-transform leads to the the resulting complex amplitude $\underline{E}_{\mathrm{result}}(x, y)$,

$$\underline{E}_{\mathrm{result}}(x, y) = \mathcal{F}_{xy}^{-1}\left\{\underline{\widetilde{E}}_{\mathrm{chip}}(k_x, k_y)\mathcal{H}(k_x, k_y)\right\}\,, \tag{2.32}$$

and the resulting mode-field diameter is found from the magnitude (squared) of the resulting complex amplitude. As an example, Panel (iii) of Fig. 2.16 depicts the field distribution comprising only those plane-wave components that can propagate in air. The observation through a microscope objective is additionally affected by the maximum acceptance angle $\theta_{\max}$ of the objective. For simplicity, we assume a rectangular angular transmission curve of the objective, i.e., unity transmission up to a maximum acceptance angle of $\theta_{\max}$ that is measured with respect to the optical axis, and no transmission beyond $\theta_{\max}$. The maximum acceptance angle $\theta_{\max}$ corresponds to a maximum spatial frequency in the transverse direction, $k_{\max} = n_{\mathrm{air}}k_0\sin\theta_{\max}$, that can be captured by the objective. To find the observed mode-field diameter $\mathrm{MFD}_{\mathrm{obs,air}}$, we hence simply replace Eq. (2.31) with

$$k_{\max} = n_{\mathrm{air}}k_0\sin\theta_{\max}\,, \tag{2.33}$$

indicated in Panel (ii) of Fig. 2.16 by the smallest dashed circle, shown for an expemplary value of $n_{\mathrm{air}}\sin\theta_{\max} = \mathrm{NA} = 0.8$. As an alternative computation route, visualized in Panel (iv) of Fig. 2.16, one might also convolve the complex field $\underline{E}_{\mathrm{chip}}(x, y)$ with the (inverse) Fourier transform $\mathcal{F}_{xy}^{-1}\{\mathcal{H}(k_x, k_y)\}$ of the amplitude transfer function,

$$\underline{E}_{\mathrm{result}}(x, y) = \underline{E}_{\mathrm{chip}}(x, y) * \mathcal{F}_{xy}^{-1}\{\mathcal{H}(k_x, k_y)\}\,, \tag{2.34}$$

where

$$\mathcal{F}_{xy}^{-1}\{\mathcal{H}(k_x, k_y)\} = \frac{J_1\left(k_{\max}\sqrt{x^2 + y^2}\right)}{\sqrt{x^2 + y^2}} \, . \tag{2.35}$$

In this relation $J_1(\cdot)$ denotes the first-order Bessel function of the first kind. The depicted function in Panel (iv) of Fig. 2.16 again exemplarily corresponds to the case of propagating fields in air at a wavelength of $\lambda = 1.55\,\mathrm{\mu m}$.

A frequently encountered, but conceptually erroneous and practically unprecise deconvolution procedure for microscopy-based measurement of small mode fields uses a value $\mathrm{MFD}_{\mathrm{PSF}}$ obtained from an approximately Gaussian *intensity* point spread function of the microscope objective, and assumes that

$$\mathrm{MFD}_{\mathrm{obs,air}} = \sqrt{\mathrm{MFD}_{\mathrm{air}}^2 + \mathrm{MFD}_{\mathrm{PSF}}^2} \, , \tag{2.36}$$

based on the notion that the convolution of two (approximatively) Gaussian distributions yield another (approximatively) Gaussian distribution, where the variances of the distributions add up. However, such approach, in particular the direct calculation using the widths of *intensity* distributions, is only valid for *incoherent* image formation and therefore not applicable in this context. Note further, that the function in Eq. (2.35), colloquially referred to as "mexican hat" or "sombrero"-function, cannot be well approximated by a Gaussian distribution. It takes on negative values, which leads to a less pronounced widening of the observed spot upon convolution, in comparison to a convolution with a Gaussian distribution which approximates the center part of the "sombrero". Equation (2.36) therefore overestimates the impact of observation with a finite-aperture objective[34]. However, by erroneously applying Eq. (2.36) and by simultaneously neglecting the influence of the fact that different immersion media are used during measurement

---

[34] To highlight the difference between coherent and incoherent imaging, we specifically consider a round Gaussian spot with $\mathrm{MFD}_{\mathrm{air}} = 2.5\,\mathrm{\mu m}$. At a wavelength of $\lambda = 1.55\,\mathrm{\mu m}$, the corresponding asymptotic divergence angle is approximately $\theta_{\mathrm{div}} \approx 23°$, which fits well into the acceptance angle of an objective with $\mathrm{NA} = 0.8$, $\theta_{\max} \approx 53°$ in air. For coherent imaging, the observed spot size therefore widens hardly, $\mathrm{MFD}_{\mathrm{obs,air}} \approx 2.54\,\mathrm{\mu m}$. However, Eq. (2.36) with a value of $\mathrm{MFD}_{\mathrm{PSF}} \approx 1.6\,\mathrm{\mu m}$ would predict a spot size of $\mathrm{MFD}_{\mathrm{obs,air}} \approx 3\,\mathrm{\mu m}$.

and during operation of the device, one commits a double mistake, where the two mistakes at least partially compensate each other.

To establish a numerical relationship for various mode-field diameter values, see Fig. 2.17, we again assume a round Gaussian on-chip mode field. We sweep the value of $\mathrm{MFD_{chip}}$ and calculate the resulting MFD values according to the procedure described in Fig. 2.16. The results are shown in Fig. 2.17(a). The black curve indicates the values of $\mathrm{MFD_{resist}}$ in resist ($n_{\mathrm{resist}} = 1.53$). The red one shows the values of $\mathrm{MFD_{air}}$ in air. The values $\mathrm{MFD_{obs,air}}$ for an observation in air are depicted for an objective with NA of 0.8 (solid blue line), and for a slightly worse performing objective (NA $= 0.65$, dashed blue line). The direct comparison between $\mathrm{MFD_{resist}}$ and $\mathrm{MFD_{obs,air}}$ is shown in Fig. 2.17(c). Obviously, the MFD in resist and air are equal for large MFD. For very small MFD, the ratio of $\mathrm{MFD_{resist}}/\mathrm{MFD_{air}}$ approaches the refractive index n_{resist}. This can be easily understood by looking at the procedure in Fig. 2.16 for the limit, where the on-chip field distribution approaches a delta distribution $\delta(x, y)$. In this case, the spectrum is uniform over the (x, y)-plane, and the resulting fields correspond to the (inverse) Fourier transform of the respective circular transfer function, Eq. (2.35). With $r = \sqrt{x^2 + y^2}$ we thus find

$$\underline{E}_{\mathrm{result}}(x, y) \propto \frac{J_1(nk_0 r)}{r} = nk_0 \frac{J_1(nk_0 r)}{nk_0 r} \propto \frac{J_1(nk_0 r)}{nk_0 r}, \tag{2.37}$$

where $n = n_{\mathrm{air}} = 1$ in air, respectively $n = n_{\mathrm{resist}}$ in photoresist. The resulting field distribution is hence n_{resist}-times wider in photoresist than in air. However, many chips employ tapered spot-size converters for edge coupling, leading to resulting mode-fields which can neither be considered sufficently large, nor a good approximation of a delta distribution. Therefore, a detailed calculation such as the present one is required. Finally, Fig. 2.17(c) shows the ratio $\mathrm{MFD_{resist}}/\mathrm{MFD_{obs,air}}$ as function of $\mathrm{MFD_{obs,air}}$ observed in air. The solid and the dashed line again show the case for NA $= 0.8$ and NA $= 0.65$, respectively. For any practical observation $\mathrm{MFD_{obs,air}}$ in air, the relevant value for $\mathrm{MFD_{resist}}$ is simply found by dividing by the depicted ratio.

(a)

(b)

(c)
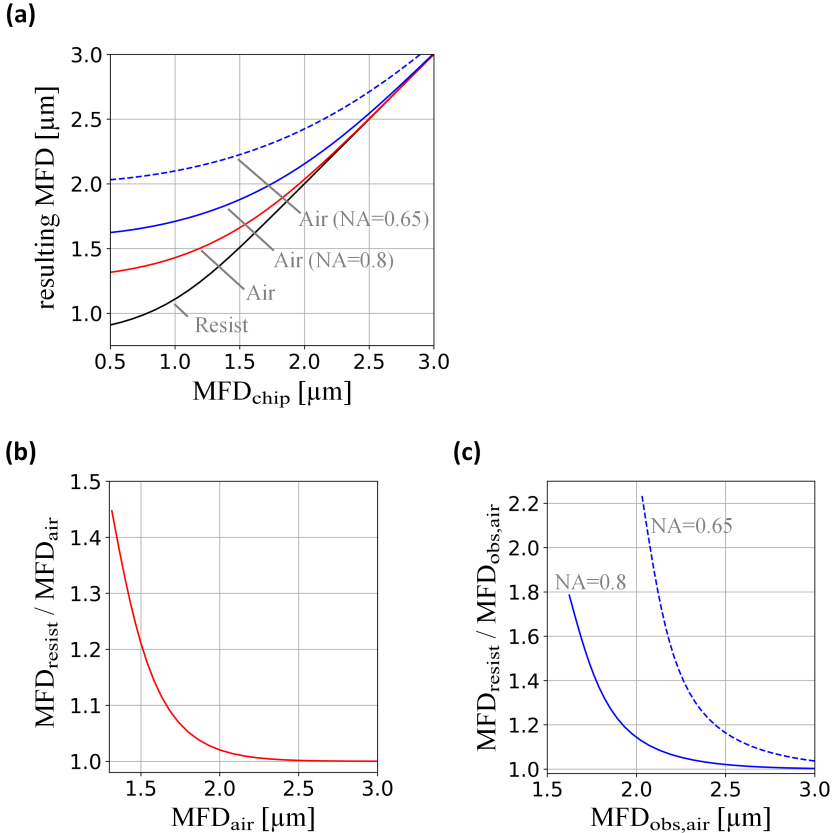
Fig. 2.17: Numerical relationship between the various mode-field diameters $\mathrm{MFD_{chip}}$, $\mathrm{MFD_{resist}}$, and $\mathrm{MFD_{obs,air}}$. **(a)** The on-chip mode-field diameter $\mathrm{MFD_{chip}}$ is swept, and the resulting MFD are calculated according to the procedure described in Fig. 2.16. The black curve indicates the values of $\mathrm{MFD_{resist}}$ in resist ($n_{\mathrm{resist}} = 1.53$). The red one shows the values of $\mathrm{MFD_{air}}$ in air. The values $\mathrm{MFD_{obs,air}}$ for an observation in air are depicted for an objective with NA of 0.8 (solid blue line), and for a slightly worse performing objective (NA $= 0.65$, dashed blue line). **(b)** Ratio $\mathrm{MFD_{resist}}/\mathrm{MFD_{air}}$ as function of $\mathrm{MFD_{air}}$. The MFD in resist and air are equal for large MFD, and the ratio approaches the refractive index n_{resist} for very small MFD. **(c)** Ratio $\mathrm{MFD_{resist}}/\mathrm{MFD_{obs,air}}$ as function of $\mathrm{MFD_{obs,air}}$ observed in air. The solid and the dashed line again show the case for NA $= 0.8$ and NA $= 0.65$, respectively.

Above calculations are based on a series of simplifications. Realistic objectives do not possess a rectangular angular transmission curve and the microscope's amplitude transfer function $\mathcal{H}(k_x, k_y)$ should thus be derived from measurement instead. For observation of laser emission, a coherent image is formed based on the convolution of the amplitude point-spread function with the complex mode field. The correct coherent deconvolution requires knowledge of the phase distribution of the field under observation. However, a phase retrieval algorithm based on observed intensities as described in Section 2.3.1 is inherently inaccurate, if no deconvolution technique is applied beforehand. Phase retrieval and deconvolution must therefore be considered in a joint algorithm and cannot be separated. Typical semiconductor laser emission is furthermore polarized. The polarization dependent shape of the PSF of a high numerical aperture objective [62] thus needs to be considered. Finally, diffraction of linearly polarized light from a tiny circular aperture does not lead to an isotropic radiation when considering the vectorial nature of light [99]. A correct modeling of the last aspect is obviously beyond the capabilities of simple scalar methods.

3 Hybrid external-cavity lasers

This chapter reports on a new class of hybrid external-cavity laser (ECL), that relies on a photonic wire bond (PWB) to connect an InP gain element to an external feedback circuit on a silicon photonic (SiP) chip. It has been published in *Scientific Reports* [J1]. The material from the publication has been adapted to comply with the layout and the structure of this thesis. Associated supplementary information can be found in Supplementary Section A.

Note that Pascal Maier and the author of this dissertation contributed equally to this publication. A large part of the experimental results were obtained during the Master's thesis of Pascal Maier, supervised by the author. The experiments were conceived by Pascal Maier, Matthias Blaicher, Wladislaw Hartmann, Christian Koos and the author. Matthias Blaicher and the author developed the advanced lithography tools required for precise fabrication of the PWB at device facets. Preliminary experiments were conducted by the author. The final ECL module was jointly fabricated by Pascal Maier and the author, supported by discussions with Muhammad Rodlin Billah. The layout of the SiP chip was done by Wladislaw Hartmann. Philipp-Immanuel Dietrich provided the photoresist used in the experiment. The associated device characterization and demonstration experiments were executed and evaluated by Pascal Maier and the author, with the help of Pablo Marin-Palomo for the linewidth measurements and Huanfa Peng for the RIN measurements. The study of nonlinear effects in the external cavity circuit as well as the theoretical analysis of the ECL linewidth were performed by the author. Yiyang Bao helped with the automation of the ECL tuning, and Stefan Singer contributed the reference measurement for nonlinear losses in SiP waveguides. Ute Troppenz and Martin Möhrle contributed the InP-based components. All authors discussed the data. The project was supervised by Wolfgang Freude, Sebastian

Randel, and Christian Koos. The author wrote the manuscript with support by Pascal Maier, Wolfgang Freude and Christian Koos. The manuscript is partially based on the prior conference contribution [C1] to OFC 2020.

[Beginning of paper [J1]. This article is licensed under a Creative Commons Attribution 4.0 International License.]

Hybrid external-cavity lasers (ECL) using photonic wire bonds as coupling elements

Scientific Reports, Volume 11, Article number 16426 (2021)

`https://doi.org/10.1038/s41598-021-95981-w`

Yilin Xu[1,2,†], Pascal Maier[1,2,†], Matthias Blaicher[1,2], Philipp-Immanuel Dietrich[1,2,3], Pablo Marin-Palomo[1], Wladislaw Hartmann[1], Yiyang Bao[1], Huanfa Peng[1], Muhammad Rodlin Billah[1,2,3], Stefan Singer[1], Ute Troppenz[4], Martin Moehrle[4], Sebastian Randel[1], Wolfgang Freude[1] & Christian Koos[1,2,3]

[1]Institute of Photonics and Quantum Electronics (IPQ), Karlsruhe Institute of Technology (KIT), 76131 Karlsruhe, Germany.

[2]Institute of Microstructure Technology (IMT), KIT, 76344 Eggenstein-Leopoldshafen, Germany.

[3]Vanguard Automation GmbH, 76185 Karlsruhe, Germany.

[4]Fraunhofer Institute for Telecommunications, Heinrich Hertz Institute (HHI), 10587 Berlin, Germany

[†]Both authors contributed equally to this work

Combining semiconductor optical amplifiers (SOA) on direct-bandgap III–V substrates with low-loss silicon or silicon-nitride photonic integrated circuits (PIC) has been key to chip-scale external-cavity lasers (ECL) that offer wideband tunability along with small optical linewidths. However, fabrication of such devices still relies on technologically demanding monolithic integration of heterogeneous material systems or requires costly high-precision package-level assembly, often based on active alignment, to achieve low-loss coupling between the SOA and the external feedback circuits. In this paper, we demonstrate a novel class of hybrid ECL that overcome these limitations by exploiting 3D-printed photonic wire bonds as intra-cavity coupling elements. Photonic wire bonds can be written

in-situ in a fully automated process with shapes adapted to the mode-field sizes and the positions of the chips at both ends, thereby providing low-loss coupling even in presence of limited placement accuracy. In a proof-of-concept experiment, we use an InP-based reflective SOA (RSOA) along with a silicon photonic external feedback circuit and demonstrate a single-mode tuning range from 1515 to 1565 nm along with side mode suppression ratios above 40 dB and intrinsic linewidths down to 105 kHz. Our approach combines the scalability advantages of monolithic integration with the performance and flexibility of hybrid multi-chip assemblies and may thus open a path towards integrated ECL on a wide variety of integration platforms.

3.1 Introduction

Tunable semiconductor lasers are key building blocks of integrated optics. Among the various approaches, external-cavity lasers (ECL) are particularly promising, combining direct-bandgap III–V materials that offer broadband optical gain with passive external feedback circuits that may be tuned over a wide wavelength range. The feedback circuits may be realized on advanced photonic integration platforms such as silicon photonics (SiP) [100–107] or silicon nitride [19, 108–110], thereby offering a direct route towards efficient co-integration of the ECL with other highly functional building blocks. Recent demonstrations of integrated ECL rely on two main approaches: heterogeneous integration [101–103, 110, 111], where dies of III–V gain materials are bonded onto passive waveguides for further front-end of line (FEOL) processing on a wafer scale, or hybrid integration, where readily processed III–V semiconductor optical amplifiers (SOA) are attached to passive feedback circuits in a back-end of line (BEOL) assembly process [19, 104–109, 112]. While heterogeneous integration paves a path towards highly scalable production using, e.g., advanced micro-transfer printing processes [111, 113–115], the associated technical complexity is still considerable. In particular, ultra-clean and extremely smooth surfaces are required, along with precise control over materials and environmental conditions [25]. Moreover, heterogeneous

integration makes it difficult to test individual components prior to integration into more complex systems and hence requires tight process control to maintain high yield. Consequently, this approach is mainly suited for high-volume applications that justify the associated technological overhead. In addition, heterogeneously integrated optical gain material may consume considerable space on the SiP chip, and heat sinking is challenging due to the high thermal resistance of the III–V-to-Si bonding layer and the buried oxide [116]. Hybrid integration, in contrast, can overcome these limitations, is non-invasive to the front-end fabrication process flow of the passive external-cavity circuit [117], and can thus be applied to a wide range of integration platforms such as SiP [104–107], silicon nitride [19, 108, 109], or planar lightwave circuits (PLC) [106, 112]. However, the concept crucially relies on high-precision assembly with tolerances in the lower micrometer or even sub-micrometer range, often requiring slow and expensive [118] active alignment techniques to achieve low-loss coupling. Scalability to high production volumes is therefore limited.

In this paper, we demonstrate a new class of hybrid external-cavity lasers (ECL) that do not require any high-precision alignment techniques. Instead, the devices rely on 3D-printed polymer waveguides, so-called photonic wire bonds (PWB) [33, 34, 119], that connect the active III–V gain die to an external feedback circuit on a SiP chip. In this approach, the shape of the PWB can be adapted to the actual positions of the chip facets at both ends, thereby compensating for placement inaccuracies. In a proof-of-concept experiment, we demonstrate a hybrid ECL with a tuning range of more than $50\,\mathrm{nm}$, a side mode suppression ratio (SMSR) above $40\,\mathrm{dB}$, and an intrinsic linewidth of $105\,\mathrm{kHz}$. The process of photonic wire bonding can be efficiently automated and allows to connect photonic dies with vastly different mode-field sizes, thereby making the concept compatible with a wide range of integration platforms. We believe that our approach has the potential to offer a route towards advanced ECL that combine the flexibility of hybrid integration with the scalability of waver-level heterogeneous integration concepts.
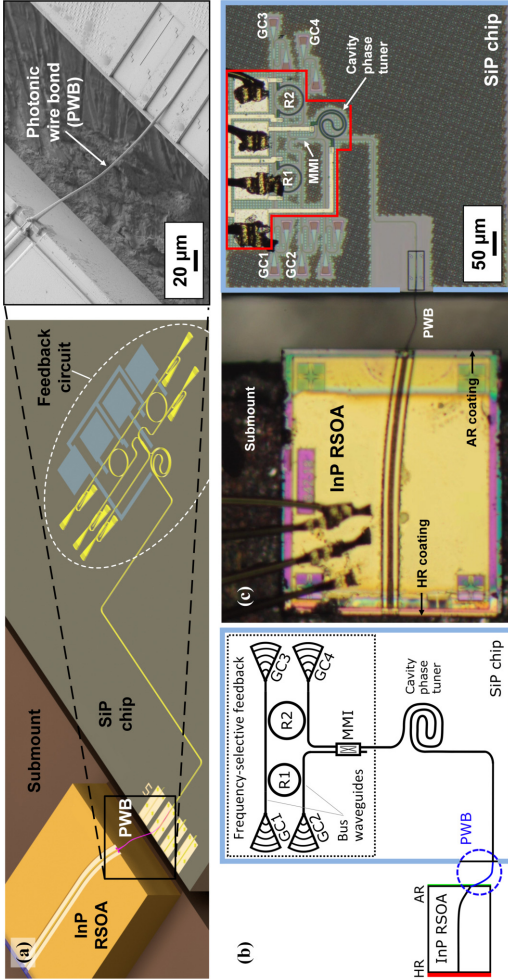
Fig. 3.1: Concept and realization of a hybrid ECL with a photonic wire bond (PWB) as intra-cavity coupling element. **(a)** Concept: The device consists of an InP-based reflective semiconductor optical amplifier (RSOA) that is connected to a thermally tunable feedback circuit on a silicon photonic (SiP) chip. A photonic wire bond (PWB, see Inset) connects the facet of the RSOA to the SiP external-cavity feedback circuit. The assembly is built on a metal submount that simultaneously acts as an efficient heat sink. **(b)** Building blocks of the device realized for our proof-of-concept demonstration. The 600 µm-long RSOA is equipped with a high-reflectivity (HR) coating at the back facet. The front facet is angled (tilt angle 9°) and anti-reflection-(AR)-coated with respect to polymer (refractive index $n = 1.56$). The SiP external-cavity circuit (framed in light blue) comprises a 350 µm-long spiral-shaped phase shifter for adjusting the intra-cavity phase (cavity phase tuner) and a tunable frequency-selective feedback structure. Frequency selectivity is provided by two symmetrically coupled Vernier ring resonators R1 and R2 in add-drop configuration with diameters $D_1 = 62$ µm (R1) and $D_2 = 67$ µm (R2) and with coupling gaps of 180 nm. Note that the cascaded Vernier rings can thus be assumed to be reciprocal, such that the feedback circuit behaves similarly to a Sagnac loop mirror. The lower left-hand input port of the 2×2 MMI can thus in principle be left uncomnected, and the associated grating coupler shown in Subfigure (a) was omitted here for simplicity. **(c)** Microscope image of the assembled device. Left-hand side: InP RSOA; right-hand side: SiP chip (framed light blue). The relevant part of the external-cavity circuit is marked by a red bounding box.

3.2 Results and discussion

3.2.1 Device concept

The concept of a hybrid ECL with a photonic wire bond (PWB) as chip-to-chip coupling element is shown in Fig. 3.1. The device consists of an InP-based reflective semiconductor optical amplifier (RSOA) that is coupled to a thermally tunable feedback circuit on a silicon photonic (SiP) chip, see Fig. 3.1(a). The 3D-printed PWB shown in the Inset of Fig. 3.1(a) allows to connect the edge-emitting RSOA to an adiabatic downtapered strip waveguide [34] on the surface of the SiP chip — without the need for any high-precision assembly techniques. The RSOA can be directly mounted onto a metal heat sink, thereby ensuring efficient cooling of the device. A more detailed description of the assembly built in the course of our experiments is given in Fig. 3.1(b). The RSOA is 600 µm long and has a high-reflectivity (HR) coating at the back facet, while the front facet is angled and coated with an anti-reflection (AR) layer. The external-cavity circuit on the SiP chip consists of a 2.2 mm-long strip waveguide (WG), that includes a 350 µm-long thermally tunable spiral-shaped phase-shifter for adjusting the cavity phase, and of a tunable frequency-selective feedback structure. The feedback structure relies on a Vernier pair of thermally tunable ring resonators R1 and R2 in add-drop configuration, where each ring is coupled to two bus waveguides. A multi-mode interference (MMI) coupler is used to split and combine the signals propagating through the feedback structure. The silicon chip was fabricated in a standard silicon photonics process using 248 nm deep-UV lithography. Figure 3.1(c) shows a top view of the fabricated ECL assembly. Compared to the InP RSOA, the relevant part of the external-cavity circuit, marked by a red bounding box, is rather small.

3.2.2 Component characterization

To fully evaluate our integration concept, all components of the ECL are individually characterized prior to assembly. The ability to start the assembly from

fully characterized knowngood components highlights one of the key advantages of our hybrid approach as compared to heterogeneous integration concepts. The following sections describe the measured performance of the RSOA and of the feedback circuit.

RSOA. The 600 µm long C-band RSOA has a back facet with a HR coating (90% reflectivity with respect to air) and an angled front facet (9°) with AR coating designed for emission into polymer ($n = 1.56$). The typical measured input/output power characteristics and gain spectra for different currents are shown in Fig. 3.2. All power levels refer to the on-chip power. At a bias current of $100\,\mathrm{mA}$, the saturation output power, defined by a gain compression of $3\,\mathrm{dB}$, is $12.5\,\mathrm{dBm}$, Fig. 3.2(a), while the near-maximum small-signal gain at $\lambda = 1550\,\mathrm{nm}$ is $23\,\mathrm{dB}$, Fig. 3.2(b). All measurements were taken using a lensed fiber. Separate reference measurements were performed to correct for the coupling loss of the lensed fiber, see Supplementary Section A.1 for details on the RSOA characterization. Note that the data shown in Fig. 3.2(a,b) was taken from two distinct devices with nominally identical parameters, fabricated on the same wafer.

Feedback circuit. Frequency selective optical feedback is provided by two symmetrically coupled Vernier ring resonators R1 and R2 in add-drop configuration with diameters $62\,\mathrm{\mu m}$ (R1) and $67\,\mathrm{\mu m}$ (R2), see Fig. 3.1(b). For stand-alone ring resonators, asymmetric coupling can be used to achieve critical coupling when sending light through one of the bus waveguides. In contrast to this, our devices rely on symmetrical coupling, because light is sent into the ring simultaneously from the top and bottom waveguide. Both rings have equal waveguide crosssections, therefore identical propagation constants, and slightly different free spectral ranges (FSR). The individual ring resonators are characterized by through-port power-transmission measurements via grating couplers GC 1 and GC 3, see Fig. 3.1(b) and Supplementary Section A.2. The measured data are then fit by a model according to Supplementary Eq. (A.2). At a wavelength of $1550\,\mathrm{nm}$, we extract FSR of $368.2\,\mathrm{GHz}$ and $340.7\,\mathrm{GHz}$ for R1 and R2, respectively, along with approximately equal Q-factors of roughly $28\,000$ for the coupled resonators. The complete set of fitted parameters is given in Supplementary Section A.2.

(a)

(b)
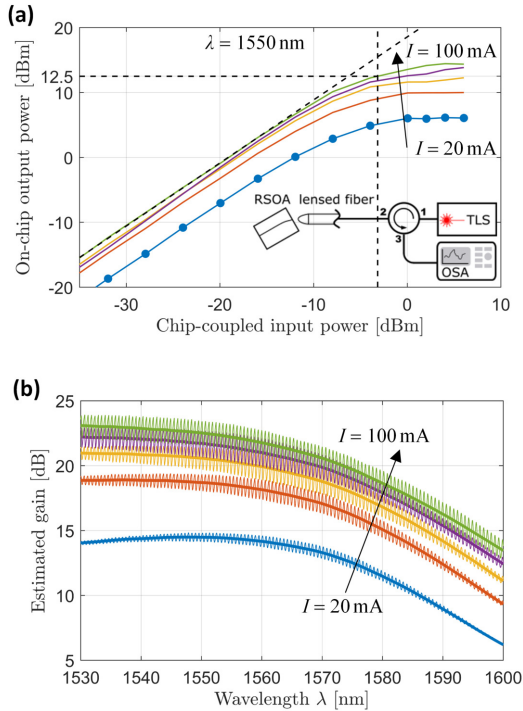
Fig. 3.2: RSOA characterization. **(a)** Typical on-chip output power vs. chip-coupled input power for various injection currents I. In the experiment, the device was tested with 12 discrete input power levels — for the sake of readability, the corresponding measurement points are indicated for the curve $I = 20\,\mathrm{mA}$ only. At a bias current of $100\,\mathrm{mA}$, the saturation output power, defined by a $3\,\mathrm{dB}$ gain compression, amounts to $12.5\,\mathrm{dBm}$. Inset: Simplified sketch of the underlying experimental setup, consisting of a tunable laser source (TLS), an optical circulator, and an optical spectrum analyzer (OSA). Details of the data evaluation can be found in Supplementary Section A.1. **(b)** Typical RSOA gain as a function of wavelength for various injection currents I. The ripples stem from reflections at the facets of the $600\,\mathrm{\mu m}$-long RSOA waveguide and have a periodicity of $73\,\mathrm{GHz}$. Note that the ripple height does not only depend on the gain, but also exhibits a wavelength dependence. We attribute this to the residual reflectivity of the anti-reflection (AR) coating on the front facet of the RSOA, which was designed for coupling to polymer with a refractive index of 1.56 and which leads to stronger residual reflections when operating the device in air as in this experiment. The residual reflectivity of the AR coating reaches a minimum at around $1530\,\mathrm{nm}$, leading to an effective suppression of the ripples at this wavelength, despite the comparatively high gain. Towards bigger wavelengths, the ripples naturally reduce with gain. At a bias current of $100\,\mathrm{mA}$, the near-maximum small-signal gain at $\lambda = 1550\,\mathrm{nm}$ amounts to $23\,\mathrm{dB}$. Note that the measurement data shown in Subfigure (a) and (b) was taken from two distinct devices with nominally identical parameters, fabricated on the same wafer.

The two rings of slightly different FSR form a Vernier pair such that the external-cavity circuit offers significant optical feedback only if two ring resonances coincide sufficiently well. To quantify the frequency-selective feedback, we calculate the drop-port transmission of each individual ring, indicated in blue and orange in Fig. 3.3(a) and in the associated Inset. To this end, we use Eq. (A.5) along with the fit values from the previous through-port measurements for each individual ring. For the plot in Fig. 3.3(a), we assume that the rings are tuned to maximum transmission at the center wavelength of the gain spectrum, $\lambda_c = 1550$ nm, such that the calculated transmission resonances coincide at this wavelength. The overall frequency-selective reflection results from multiplication of the individual drop-port power transmission spectra and is shown in Fig. 3.3(b). The peak height at the common resonance indicates the loss which occurs during propagation through the pair of ring resonators. In our case, we find a value of 1.7 dB.

A key parameter of an ECL is the achievable frequency tuning range Δf_{tun} for emission into a single longitudinal mode. For feedback circuits based on Vernier rings, a large Δf_{tun} can be achieved without the need for exceedingly small ring resonators, which would lead to increased bending loss and smaller Q-factors. Nevertheless, Δf_{tun} is usually limited by the finite Q factor of the rings and the associated non-zero resonance widths, which can lead to significant optical feedback even for an imperfect overlap of two closely spaced resonance peaks. In combination with a spectrally non-uniform and possibly inhomogeneously broadened gain spectrum, this feedback could allow lasing at an unwanted secondary longitudinal mode. We estimate a lower bound Δf_{min} for the achievable tuning range Δf_{tun} by calculating the spectral spacing between the strong main reflection peak and the two most prominent side peaks that are most prone to generate unwanted lasing modes, see Fig. 3.3(b). To this end, we use the so-called tuning enhancement factor T, which quantifies the increased tuning efficiency of the Vernier rings in comparison to a single ring resonator. For the Vernier pair, the difference in FSR is by far smaller than the FSR of each individual ring. Hence, only a small refractive-index tuning is required to line up adjacent peaks.
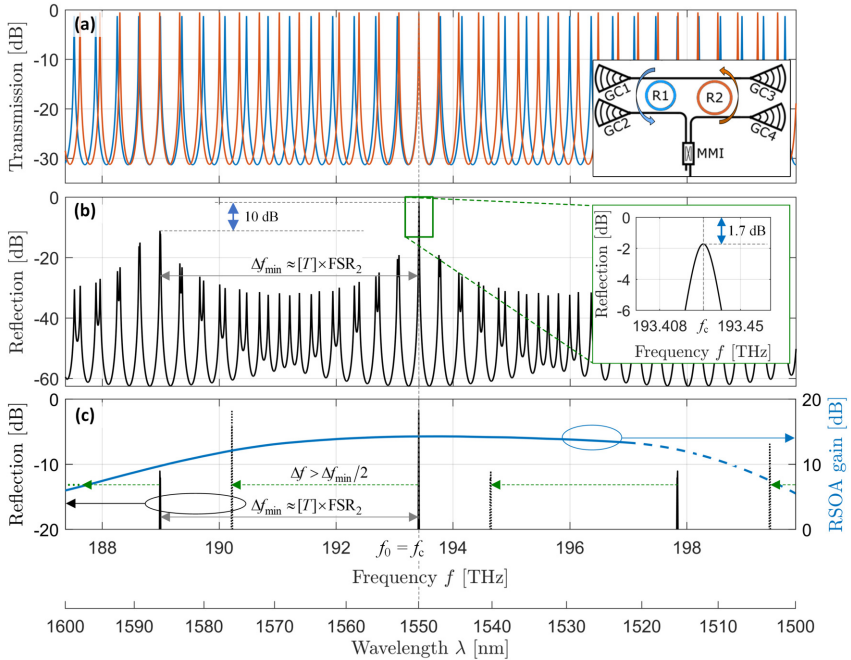
Fig. 3.3: Frequency-dependent reflection characteristics of the external-cavity circuit calculated with the parameters extracted from through-measurement (GC 1 → GC 3), see Supplementary Section A.2. **(a)** Drop-port transmission of the individual rings. **(b)** Overall reflection spectrum of the external-cavity circuit. The main peak height indicates a minimum on-chip reflection loss of 1.7 dB, see Inset. **(c)** Exemplary gain spectrum of the RSOA according to Fig. 3.2(b) for an injection current of $I = 20$ mA (blue line) with schematic resonance peaks (black lines) as in (b). The blue solid line corresponds to measured values of the RSOA gain, whereas the blue dashed line is an estimated extrapolation towards higher frequencies. The solid black lines indicate the strong main reflection peak at the target frequency f_0, which, for the depicted case, corresponds to the center frequency ($f_c = 193.2$ THz; $\lambda_c = 1550$ nm) of the gain spectrum, along with the most prominent side peaks that are most prone to unwanted lasing. The dotted black lines indicate the corresponding peaks after a detuning by $\Delta f > \Delta f_{min}/2$ where $\Delta f_{min} \approx [T] \times \mathrm{FSR}_2$, indicated by green arrows.

Compared to the refractive-index change required to tune a single ring across one FSR, this corresponds to a tuning enhancement factor [120, 121] of

$$T = \frac{\text{FSR}_1}{\Delta\text{FSR}}, \qquad \Delta\text{FSR} = \text{FSR}_1 - \text{FSR}_2 > 0. \tag{3.1}$$

The tuning enhancement factor T is at the same time closely related to the frequency spacing between the main reflection peak and the most prominent side peaks that arise from nearly-overlapping resonances of the individual rings. Assuming that the main peak consists of two perfectly aligned resonances at the target frequency f_0, the next side peaks would appear at $f_0 \pm \Delta f_{\min}$, $\Delta f_{\min} \approx [T] \times \text{FSR}_2 \approx [T-1] \times \text{FSR}_1$, where [.] denotes a rounding operation to the nearest integer, see Fig. 3.3(c) and Supplementary Section A.3 for details. To simplify the estimation of the achievable tuning range, we assume a homogeneous gain spectrum in the following that is broad enough and thereby does not directly limit Δf_{tun}. If the target frequency f_0 is identical or close to the center frequency f_c of the gain spectrum, lasing will occur at f_0 only, because the side peaks experience less gain as well as higher reflection loss, see Fig. 3.3(c). If the target frequency is tuned away from the center of the gain spectrum, lasing may also occur at the side peaks. Assuming that the gain spectrum is approximately symmetric with respect to its center frequency f_c and that the side peaks have the same height as the main peak, a shift by $\pm\Delta f_{\min}/2$ would position two resonance peaks of equal height symmetrically to the center frequency of the gain spectrum and would hence lead to lasing in the first side peak. Under these simplifying assumptions, the minimum tuning range would be slightly less than $\pm\Delta f_{\min}/2$.

In our device, the side peaks of the reflection spectrum at $f_0 \pm \Delta f_{\min}/2$ are about $10\,\text{dB}$ lower than the main peak. In comparison to this, the gain roll-off at $f_c \pm \Delta f_{\min}/2$ is around $3\,\text{dB}$ only. We hence find a bigger tuning range, $\Delta f_{\text{tun}} > \Delta f_{\min}$. This is illustrated in Fig. 3.3(c), where the dotted lines indicate a reflection spectrum which is shifted by $\Delta f > \Delta f_{\min}/2$. We confirm this aspect experimentally: From the passive characterization of our device, we find $T = 13.4$ and $\Delta f_{\min} \approx 4.4\,\text{THz}$, corresponding to $\Delta\lambda_{\min} \approx 35\,\text{nm}$ at a wavelength of $1.55\,\mu\text{m}$, while our experiments exhibit a single longitudinal lasing mode over a

tuning range between 191.7 THz (1565 nm) and 198.0 THz (1515 nm), i.e., over $\Delta f_{\text{tun}} = 6.33$ THz ($\Delta\lambda_{\text{tun}} = 50$ nm), see Section 3.2.4 below.

3.2.3 Module assembly

For assembly, the RSOA is glued to a copper heat sink using thermally conductive silverfilled glue (EPO-TEK H20E). The copper heat sink and the silicon chip are then coarsely aligned to each other and glued to a common metal submount. The submount contains a step that has been designed such that the chip surface on the RSOA side is approximately 60-80 µm above the chip surface on the Si side, which turned out to allow for a convenient 3D routing of the PWB. An SEM picture of the fabricated PWB is shown in Fig. 3.4. The PWB trajectory accounts for the chip positions and the oblique emission from the angled RSOA facet. At the interface to the InP RSOA, the PWB comprises a taper with an initial cross-section of 4 µm × 4 µm, matched to the mode-field diameter on the InP side. This cross section is then linearly tapered to that of the freeform section of the bond (2.4 µm × 2.0 µm). At the SiP chip, a polymer-to-silicon double-taper transition [33, 34] connects the PWB to a standard SiP strip waveguide with 500 nm width and 220 nm height. This double taper contains a down-tapered silicon waveguide with a tip width of 180 nm. An additional attachment structure, depicted in red, is added on the RSOA facet for mechanical stability.

Figure 3.1(c) shows a microscope image of the fully assembled ECL module. Note that the refractive index of the cured resist ($n_{\text{r}} = 1.53$) does not perfectly match the refractive index for which the AR-coating of the RSOA is designed ($n = 1.56$), but the influence is negligible. We estimate a PWB loss of (2.1 ± 0.2) dB from amplified spontaneous emission (ASE) measurements before and after module assembly, see Supplementary Section A.1 for details. The estimated PWB loss is slightly higher than previously published results [33, 34], but is still on par with many results demonstrated with butt coupling and active alignment [106, 107, 122]. We attribute the additional loss mainly to a non-optimum design of the inverse taper on the SiP chip and to the fact that the waveguide was operated in air rather
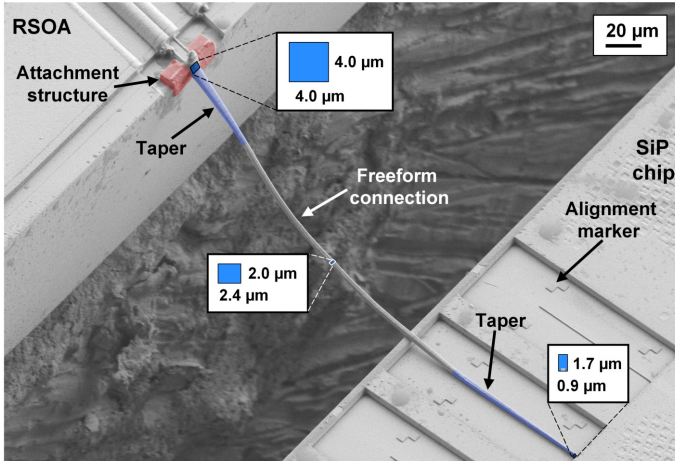
Fig. 3.4: False-colored SEM picture of the fabricated PWB between the InP RSOA and the SiP external feedback circuit. The fabricated cross-section in each part of the PWB is indicated. On the InP side, a taper (blue) is used to transform the mode field on the RSOA facet to that of the freeform PWB connection. At the SiP chip, a polymer-to-silicon double-taper transition [33, 34] is used for efficient connections. The blue rectangles indicate the cross sections at the respective positions along the PWB trajectory. An additional attachment structure (red) is added on the RSOA facet for mechanical stability. Alignment markers on the SiP chip facilitate exact localization of the coupling interface.

than in a low-index cladding, which would render the curved freeform connection single mode and thus decrease the insertion loss. Note also that the design of the taper towards the facet of the InP chip is based on a mode-field measurement of the RSOA, which was performed using an infrared microscope with an air objective. In contrast to this, the device is finally operated with the facet in direct contact to the polymerized resist of the PWB, having a refractive index of $n_r = 1.53$. Since the mode field is of the order of the vacuum wavelength, the emission from the RSOA facet might depend on the refractive index of the adjacent medium, and the microscope images captured in air might lead to an over-estimation of the mode-field diameter that is effective when the facet is in contact with resist. This effect might be taken into account in the next device generation, e.g., by performing the mode-field measurement under immersion. Another source of additional loss is the fact that the relative position of the reference points on the surface of the InP chip and the emission spot at the facet might be subject to

71

tolerances due to finite overlay accuracy of the lithography layers used during chip fabrication. For a batch of RSOA from the same chip, which should all be subject to the same offset, this effect might be measured and taken into account during PWB fabrication.

3.2.4 Functional demonstration and characterization

For demonstrating the functionality of the device, we select the ECL wavelength by tuning the two ring resonators to a common resonance and by optimizing the cavity phase for maximum output power at GC 1, see Fig. 3.1(b). Once the appropriate tuning parameters are found, they can be stored in a look-up table for later use and for rapid tuning, see Supplementary Section A.4. In a first step, we tune the ECL to a wavelength of 1550 nm and measure the P-I-characteristics, Fig. 3.5(a), where I is the pump current and where P refers to the on-chip output power in the bus waveguide between R2 and GC 4, see Fig. 3.1(b). The P-I-curve does not exhibit any kinks that are typical signs of mode hops, even when leaving the cavity phase tuner unchanged while ramping up the current to its final value of 100 mA. Note, however, that such kink-free P-I-curves require proper initial adjustment of the cavity phase tuner. These findings are in line with the existing literature, where some integrated ECL exhibit mode hops when not adjusting the phase [19, 102], while others do not shown any signs of mode hops over a large range of drive currents [102, 104]. We believe that the occurrence of mode hops depends strongly on the specific design of the RSOA, in particular the device length, and on the pump current. Note also that our device is operated only up to a rather modest pump current of 100 mA, limited by imperfect thermal contact of the RSOA and the metal submount. From the measurement in Fig. 3.5(a), we find a threshold pump current of 30 mA and a slope efficiency of 35 mW/A. Note that our current device features four outputs (GC 1-4), Fig. 3.1(b). Using an appropriate design, the emission can be concentrated to a single dominant port, thereby increasing the output power as well as the slope efficiency.
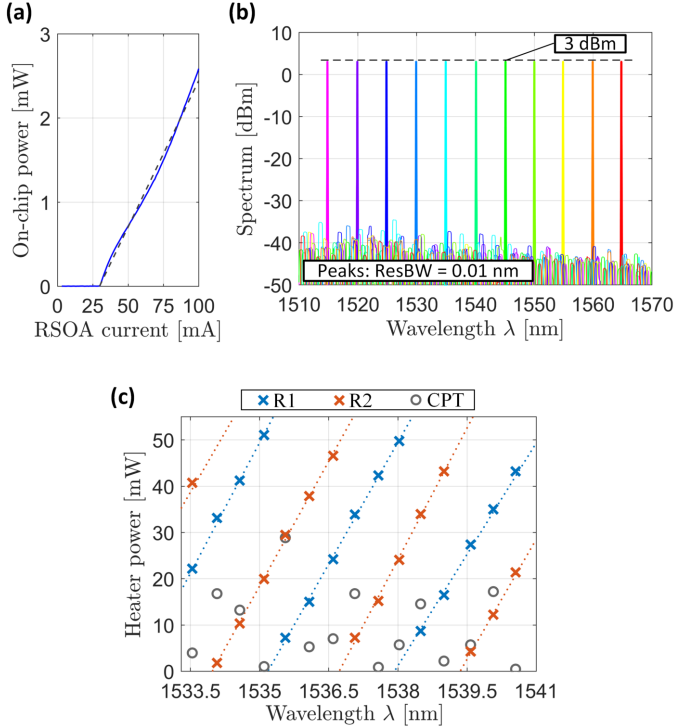
Fig. 3.5: Device characterization results. **(a)** P-I-curve recorded for lasing operation at 1550 nm. A threshold current of 30 mA and slope efficiency of roughly 35 mW/A are found from the measurement. The output power P refers to the on-chip power in the bus waveguide between R2 and GC 4, see Fig. 3.1(b). **(b)** Superimposed lasing spectra recorded in steps of 5 nm within the single-mode tuning range between 1515 and 1565 nm, covering the complete telecommunication C-band. The RSOA bias current was adjusted for each operating point to maintain a constant output power level of 3 dBm. We verify longitudinal single-mode operation by observing the full emission spectrum across the entire RSOA gain bandwidth, finding an SMSR that is consistently better than 40 dB. **(c)** Tuning map of the laser emission, indicating the heater powers of the rings R1 and R2 (blue and red crosses) and of the cavity phase tuner (CPT, grey circles) to reach a certain target wavelength. For better visibility, we only plot a small part of the overall tuning range. The fitted ramps (dotted lines) for the ring heater powers serve as a guide to the eye. The vertical offset of the fitted ramps corresponds to twice the π-power P_π of the respective ring heater, which is independently measured to be $P_{\pi,\mathrm{R1}} = 24.4$ mW for R1 and $P_{\pi,\mathrm{R1}} = 24.1$ mW for R2, see Supplementary Section A.4.

In a second step, we then record lasing spectra within the available tuning range, which covers a bandwidth of $\Delta\lambda_{\text{tun}} = 50\,\text{nm}$ between 1515 and $1565\,\text{nm}$ and thus comprises the complete optical telecommunication C-band, see Fig. 3.5(b) for a superposition of all recorded spectra. For simplicity, we choose wavelength steps of $5\,\text{nm}$, and we verify longitudinal single-mode operation for each wavelength by recording the full spectrum across the RSOA gain bandwidth. From these spectra, we also extract the SMSR, which exceed $40\,\text{dB}$. The RSOA pump current was chosen to be approximately $100\,\text{mA}$ and was then fine-tuned for each operating point to maintain an equal on-chip power level of around $3\,\text{dBm}$ in the waveguide leading to GC 1. Figure 3.5(c) shows a tuning map of the laser emission, indicating the heater powers for the rings R1 and R2 (blue and red crosses) and for the cavity phase tuner (CPT, grey circles) to reach a certain target wavelength. The fitted ramps (dotted lines) for the ring heater powers serve as a guide to the eye. The vertical offset of the fitted ramps corresponds to twice the π-power P_π of the respective ring heater, which is independently measured to be $P_{\pi,\text{R1}} = 24.4\,\text{mW}$ for R1 and $P_{\pi,\text{R1}} = 24.1$ mW for R2, see Supplementary Section A.4. Exploiting the fact that all phase tuners have the same cross section and hence the same tuning efficiency, we estimate a single-pass π-power of approximately $P_{\pi,\text{CPT}} = 24\,\text{mW}$ for the cavity phase tuner. Note that the heater power for the cavity phase tuner (grey circles) in Fig. 3.5(c) does not follow a systematic trend but appears rather random. This is due to the fact that the different emission wavelengths measured for recording the tuning map correspond to different longitudinal modes of the laser cavity. Note also that, for tuning one of the cavity modes to the targeted emission wavelength, it is sufficient to operate the cavity phase tuner in a single-pass phase shift range between 0 and π.

All experiments were performed at room temperature, with the metal submount of the multi-chip assembly placed on a vacuum chuck. Since this vacuum chuck is rather massive, it maintains a constant temperature during operation of the device, even without additional temperature control. Note that photonic wire bonds have been demonstrated to be resilient with respect to temperature changes [33]. Assuming that the temperature-dependence of the RSOA gain and of the operating points of the ring resonators can be accounted for by closed-loop wavelength- and

power-control algorithms in combination with on-chip wavelength monitors [123, 124], we believe that the hybrid ECL may eventually be operated without active temperature control of the package. In our experiments, the thermal coupling between the RSOA and the submount leaves room for further improvement. With proper thermal coupling, the device can be operated with a maximum current of $200\,\mathrm{mA}$ rather than the $100\,\mathrm{mA}$ used in our experiment, which leaves room for further increasing the output power.

We further measure the phase-noise characteristics of the emitted laser line. To this end, we use a setup similar to the one described in [125], which relies on a heterodyne measurement technique [126]. In this approach, the output of the ECL is superimposed with a narrow-linewidth local oscillator (LO) tone in a $90°$ optical hybrid, and the superimposed signals are then detected by a set of balanced photodetectors and digitized with an oscilloscope. The measurements are carried out at a tuned ECL wavelength close to $1550\,\mathrm{nm}$, where the exact operating point has been fine-tuned for minimum linewidth. The result of the FM-noise spectrum calculation [126] is shown as a red trace in Fig. 3.6. The intrinsic (Lorentzian) linewidth is obtained by first fitting a model function of the form $S_\mathrm{F}(f) = S_0 + S_1 f^{-1}$ to the measured FM-noise spectrum. This leads to $S_0 = 3.3 \times 10^4\,\mathrm{Hz}$ and to a Lorentzian linewidth of $\delta f = \pi S_0 \approx 105\,\mathrm{kHz}$, indicated by a dashed blue line in Fig. 3.6. We also measure the phase-noise characteristics of the LO laser (Keysight N7714A) in an independent experiment, where we superimpose the tones of two nominally identical LO lasers and extract the FM noise spectrum of each of them, see black trace in Fig. 3.6. The FM noise level of the LO laser lines is at least an order of magnitude below that of the ECL-LO beat note, thereby confirming that the extracted Lorentzian linewidth of $\delta f = \pi S_0 \approx 105\,\mathrm{kHz}$ can indeed be attributed to the phase noise of the ECL. To benchmark our measurement, we have theoretically estimated the linewidth that could be expected based on the characteristics of the RSOA and the external feedback circuit, see Supplementary Section A.6. The theoretical prediction and the actually measured intrinsic line width are in reasonable agreement.

As another figure of merit, we tried to measure the relative intensity noise (RIN) spectrum of our ECL. The sensitivity of this measurement, however, was limited by
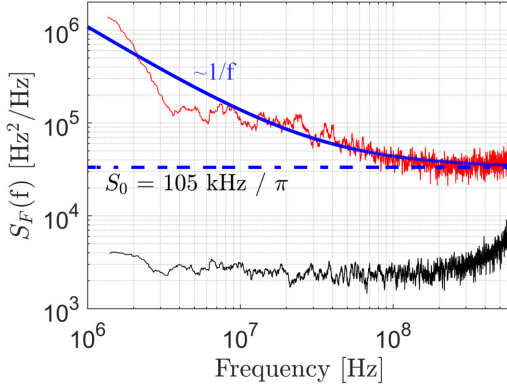
Fig. 3.6: FM-noise spectrum and linewidth measurement. The FM-noise spectrum of the ECL is obtained through heterodyne detection with a narrow-band reference LO laser (Keysight N7714A) and subsequent digital signal processing (red trace). The sampled time-domain waveform comprises 9×10^5 points, recorded at a sampling rate of $256\,\text{GSa/s}$. The spectrum is first smoothed by taking a moving average over 50 neighboring points, and then fitted by a model function of the form $S_F(f) = S_0 + S_1 f^{-1}$ (solid blue line). An instantaneous linewidth of $\delta f = \pi S_0 \approx 105\,\text{kHz}$ is extracted from the spectrally white part of the FM noise spectrum (dashed blue line). In an independent experiment, we also superimpose the tones of two nominally identical LO lasers and extract the FM noise spectrum for each of these lasers (black trace). This measurement confirms that the FM noise level of the LO laser line is at least one order of magnitude below that of the ECL-LO beat note, thereby supporting the assumption that the extracted Lorentzian linewidth of 105 kHz can indeed be attributed to the phase noise of the ECL for the frequency range considered here.

the fact that the fiber-coupled output power of the device is rather low. Specifically, as indicated in Fig. 3.1(a), our chip contains unnecessary 2×2 MMI before the grating coupler outputs, which themselves feature coupling losses of at least 5 dB. In addition, we used a fiber-coupled circulator with an additional loss of 1.5 dB to avoid back-reflection of light from our measurement setup into the laser. These additional losses limit the sensitivity of the RIN measurement to approximately $-140\,\text{dBc/Hz}$, dictated by the noise floor of our electrical spectrum analyzer (Agilent N9030A). In our measured RIN spectrum, we do not find any peaks in the RIN spectrum that exceed this limit and that could be an indication of reflections from within or outside the laser cavity. Our findings are consistent with published results on hybrid ECL [19, 109, 127], in which RIN levels below $-140\,\text{dBc/Hz}$ have been regularly obtained.

Note that the coupling losses between the InP gain chip and the SiP chip [34] as well as the losses in the external-cavity circuit may be further reduced, thereby leaving room for improving the emission power and the linewidth of the ECL. Still, the performance of our current devices is already on par with that of previously demonstrated hybrid ECL that combine standard SiP feedback circuits with InP gain elements through active alignment [104, 106, 107]. Specifically, these devices exhibit linewidths between 37 kHz and 27 MHz along with tuning ranges between 35 and 95 nm and output powers between 0 and 13 dBm. Generally, the performance of ECL can be improved by optimizing the external feedback circuit. When it comes to linewidth, decreasing the propagation losses and thus increasing the cavity Q-factors is key. On the silicon photonic platform, this can be achieved by using, e.g., lowloss rib waveguides, which are obtained by partial etching of rather thick silicon-on-insulator (SOI) device layers and which allow to reduce the propagation losses down to 0.2 dB/cm. Since optical guidance in rib waveguides is weaker than in the strip waveguides used in our device, the rings usually become larger and the FSR reduces accordingly, which may be compensated by a third ring to maintain wide-band tunability [102]. Using low-loss SiP rib waveguides in combination with three-ring external cavity circuits, heterogeneously integrated ECL with linewidth down to 220 Hz have been demonstrated [102], along with tuning ranges of 110 nm. Even smaller linewidths down to 40 Hz can be achieved by using ultra-low-loss silicon nitride (SiN) waveguides for the feedback circuit [109]. Exploiting the flexibility of the photonic wire bonding approach, the distinct strengths of advanced SiP or SiN external-cavity circuits may be readily leveraged without re-design of on-chip coupling interfaces.

When it comes to maximizing the output power, external feedback circuits based on silicon photonic (SiP) waveguides face the problem of nonlinear loss due to two-photon absorption (TPA) and subsequent free-carrier absorption (FCA), which eventually limits the intra-cavity power and thereby the overall output power. In fact, the power levels found in our device are already in a regime where nonlinear losses such as TPA and TPA-induced FCA in the rings play a role, see Supplementary Section A.5 for a more detailed analysis. This problem can be overcome by using SiN-based feedback circuits, which have led to hybrid ECL that exploit

two intra-cavity gain elements to offer record-high output powers [19] of more than 100 mW along with a tuning range of 100 nm and linewidths around 320 Hz. Another approach to achieve high output powers is to boost the laser emission by an external SOA [105]. In this concept, the photonic wire bonding technique may again offer the advantage of efficient heat sinking, which is particularly crucial for high-power booster SOA.

3.3 Summary

We demonstrated a novel approach to hybrid integrated ECL that exploits 3D-printed photonic wire bonds (PWB) to efficiently connect an InP gain chip to a silicon photonic (SiP) external feedback circuit. Our concept avoids high-precision active alignment of the dies with respect to each other and allows to flexibly leverage the distinct strengths of advanced SiP or SiN-based external-cavity circuits. In a proof-of concept, we demonstrated a first-generation hybrid ECL with a tuning range of more than 50 nm, a side mode suppression ratio (SMSR) above 40 dB, and an intrinsic linewidth of 105 kHz. To the best of our knowledge, our work represents the first demonstration of a chip-scale laser that relies on a 3D-printed coupling element within the cavity. The process of photonic wire bonding can be efficiently automated, thereby paving a path towards efficient mass production of ECL.

3.4 Methods

RSOA mode-field size and location. Prior to module assembly, the mode-field size of the RSOA as well as the location of the emission spot with respect to a reference point on the RSOA chip were measured to ensure correct dimensioning and placement of the PWB on the chip facet. To this end, we operate the RSOA at large injection currents and investigate its amplified spontaneous emission (ASE) without external resonator. We then assume that the ASE in the high-current limit

reliably indicates the mode field and the emission spot that the RSOA will exhibit under lasing conditions in the cavity. In our experiments, the intensity distribution of the mode field at the device facet is captured by an infra-red microscope and processed further to extract size and position of the emitted mode field.

Fabrication. Fabrication is done in-situ by a two-photon lithography step in a negative-tone photoresist (Vanguard Automation GmbH). We used a self-built lithography system, equipped with a $63\times$ microscope objective lens (numerical aperture 1.4) and galvanometer mirrors for rapid lateral beam movement. A fs-laser (C-Fiber 780 HP, Menlo) with a pulse length of 58 fs and a repetition rate of 100 MHz serves as lithography light source. Details of the fully automated fabrication are also found in previous publications [33]. The start and the end point and the corresponding local directions of the PWB trajectory are found by scanning and imaging the object with the focused writing beam at low intensity. Upon exposure, the fabricated structure is developed in propylene-glycol-methyl-ether-acetate (PGMEA), flushed with isopropanol, and subsequently blow-dried.

[End of paper [J1]]

4 Optical packaging using 3D-printed facet-attached microlenses

This chapter reports on advances in multi-connection alignment tolerant optical assembly techniques using facet-attached microlenses (FaML).

The approaches and experiments were conceived by Pascal Maier, Mareike Trappen, Pilipp-Immanuel Dietrich, Matthias Blaicher, Christian Koos, and the author. Matthias Blaicher and the author developed the advanced microlens design tools and the lithography tools required for the precise fabrication of microlenses at device facets. The author designed the microlenses. The demonstrators were built by the author with the help of Pascal Maier. Philipp-Immanuel Dietrich developed the photoresist used in the experiments. Achim Weber and Colin Dankwart designed and implemented the assembly machine. Pascal Maier, Mareike Trappen, Torben Kind, and the author developed the assembly processes. The author performed the experimental characterization of the various assemblies with the help of Pascal Maier, and analyzed the measurement data. Rokas Jutas assisted with the process development for lenses at the facets of SiP chips. Padraic Morrissey and Kamil Gradkowski contributed to the LEGO demonstrator. Jens Stephan and Andreas Stephan contributed the InP phododiodes, and Brian Kelly the InP lasers. The layout of the SiP chip was done by Amin Abbasi. All authors discussed the data. The project was supervised by Wolfgang Freude, Peter O'Brien, and Christian Koos. The author wrote the manuscript with support by Wolfgang Freude and Christian Koos.

The chapter is taken from the manuscript [J2], that is to be submitted for publication in a scientific journal. The material from the manuscript has been adapted to comply with the layout and the structure of this thesis. Further supplementary information can be found in Supplementary Section B.

[Beginning of paper [J2]]

3D-printed facet-attached microlenses for advanced photonic system assembly

Yilin Xu[1,2], Pascal Maier[1,2], Mareike Trappen[1,2], Philipp-Immanuel Dietrich[1,2,3], Matthias Blaicher[1,2], Rokas Jutas[1], Achim Weber[3,4], Torben Kind[4], Colin Dankwart[4], Jens Stephan[5], Andreas Steffan[5], Amin Abbasi[6], Padraic Morrissey[7], Kamil Gradkowski[7], Brian Kelly[8], Peter O'Brien[7], Wolfgang Freude[1], and Christian Koos[1,2,4]

[1]Institute of Photonics and Quantum Electronics (IPQ), Karlsruhe Institute of Technology (KIT), Engesserstr. 5, 76131 Karlsruhe, Germany.

[2]Institute of Microstructure Technology (IMT), KIT, Hermann-von-Helmholtz-Platz 1, 76344 Eggenstein-Leopoldshafen, Germany.

[3]Vanguard Automation GmbH, Gablonzerstr. 10, 76185 Karlsruhe, Germany

[4]ficonTEC Service GmbH, Im Finigen 3, 28832 Achim, Germany.

[5]II-VI Inc, Reuchlinstraße 10/11, 10553 Berlin, Germany.

[6]Photonics Research Group, Ghent University – imec, Technologiepark-Zwijnaarde 126, B-9052 Gent, Belgium.

[7]Tyndall National Institute, T12 R5CP Cork, Ireland

[8]Eblana Photonics Ltd., West Pier Business Campus, 3 Old Dunleary Rd, Dún Laoghaire, Dublin, A96 A621, Ireland.

For interconnecting photonic integrated circuits (PIC) inside a package and to the outside world, high-volume and cost-efficient assembly techniques are required.

Frequently, tiny and vastly different optical mode-field diameters are involved, for instance when connecting silicon photonic (SiP) waveguides (WG) to single-mode fibers (SMF). Our solution is to print free-form optical structures like lenses and prisms on chip facets and fiber end-faces using multi-photon lithography. Our lens design matches the mode-field diameters, relaxes lateral alignment tolerances, and therefore allows passive alignment. Coupling losses between SMF and SiP WG or InP lasers range between $1.4\,\mathrm{dB}$ (SiP WG) and $2\,\mathrm{dB}$ (InP laser). Specially designed lenses further help to increase the free-space coupling distance to the millimeter range such that discrete optical components can be inserted. For avoiding linewidth broadening and instabilities of a semiconductor laser, the back-reflection factor can be reduced to $-44\,\mathrm{dB}$ by free-form lenses and prisms which are attached to the laser end-face. Remarkably, printing and packaging can be done in a fully automated process.

4.1   Introduction

Photonic integrated circuits (PIC) are about to disrupt a variety of applications, ranging from high-speed data transmission [128] and ultra-broadband signal processing [129, 130], to distance metrology and light detection and ranging [10, 131, 132] (LiDAR) and further to chemical sensing and medical diagnostics [11, 133–135]. This success largely relies on advanced wafer-level fabrication of miniaturized photonic devices that combine outstanding functionality and robustness with unprecedented performance and scalability. However, while cost-efficient mass production of PIC has become widely available through dedicated foundry services, scalable photonic packaging and system assembly still represents a major challenge and an obstacle towards accelerated commercial uptake. Specifically, package-level optical chip-to-chip and fiber-to-chip connections often rely on

so-called butt coupling, where device facets are brought in close proximity or even in direct physical contact. This approach often requires high-precision active alignment with sub-micrometer accuracy, thereby inherently limiting fabrication throughput. Moreover, matching of the mode fields can represent a challenge, in particular when coupling waveguides with vastly different refractive-index contrasts. This challenge may be overcome by coupling of devices via intermediate discrete optical components such as ball lenses or graded-index (GRIN) structures. While this approach increases the design flexibility and opens a path towards integrating free-space optical elements such as polarization beam splitters or optical isolators into the beam paths, it renders the assembly process even more complex by increasing the number of components that have to be aligned. There is hence a strong need for scalable and flexible packaging concepts that can complement wafer-level mass fabrication of the underlying PIC.

In this paper, we show that 3D-printed facet-attached microlenses (FaML) offer an attractive option for advanced photonic system assembly. FaML can be printed with high precision to the facets of optical components [2] using multi-photon lithography, thereby offering the possibility to shape the emitted beams by freely designed refractive surfaces. Specifically, these beams can be collimated to a comparatively large diameter that is independent of the device-specific mode fields. This relaxes both axial and lateral alignment tolerances to the extent that costly active alignment becomes obsolete and can be replaced by passive [136, 137] alignment based on machine vision and/or simple mechanical stops. In contrast to direct butt coupling, the FaML concept opens the possibility to insert discrete optical elements such as optical isolators into the free-space beam paths between PIC facets. We show the viability and the versatility of the scheme in a series of selected demonstrations of high technical relevance. In a first set of experiments, we couple fiber arrays to arrays of edge-coupled silicon photonic (SiP) chips, reaching insertion losses of $1.4\,\mathrm{dB}$ per interface with a lateral $1\,\mathrm{dB}$ alignment tolerance of $\pm 6\,\mathrm{\mu m}$. To the best of our knowledge, this is the lowest loss demonstrated for an edge-emitting SiP waveguide interface with micron-scale alignment tolerances. We also demonstrate that the outstanding alignment tolerance of our scheme allows for reproducible coupling using a LEGO

brick for detachable mechanical connection. In a second set of experiments, we further demonstrate free-space transmission over distances in the mm-range, using standard machine-vision techniques for alignment. In this experiment, we further insert a discrete optical polarization beam splitter prism into the beam path between a single-mode fiber (SMF) array and array of edge-coupled indium-phosphide (InP) photodetectors. A third set of experiments is dedicated to interfaces between InP lasers and SMF arrays. In this context, we demonstrate coupling with ultra-low back-reflection by connecting planar devices through non-planar beam paths that only comprise tilted optical surfaces. We estimate -44 dB of spurious back reflection, comparable to the performance of advanced lensed fibers with anti-reflection (AR) coating [138]. Based on these exemplary demonstrations of the outstanding versatility of the FaML concept, we believe that the approach opens an attractive path towards advanced photonic system assembly that may overcome most of the current challenges.

4.2 Concept and approach

Our optical packaging concept is illustrated in Fig. 4.1, which shows an exemplary assembly for an optical transmitter consisting of an array of InP lasers with angled facets, an optical isolator block, and an array of modulators on a silicon-photonic (SiP) chip. The output of the SiP chip is connected to a pluggable array of single-mode fibers (SMF), which is positioned by mechanical alignment pins. The insets show magnified views of different FaML, which can be designed to collimate the free-space beams to diameters of up to $60 \, \mu\text{m}$, thereby greatly relaxing translational alignment tolerances. Inset (i) shows the schematic of a FaML assembly printed to the facet of an angled edge-emitting InP laser. The FaML assembly consists of a free-form lens and a prism, which jointly expand, collimate and redirect the beam. The angled plane surfaces and the strongly curved lens surface reduce unwanted back-reflections into the laser cavity. Insets (ii) and (iii) show schematics of free-form FaML, printed to the facet of an edge-coupled SiP chip, and to the facet of a SMF, respectively.
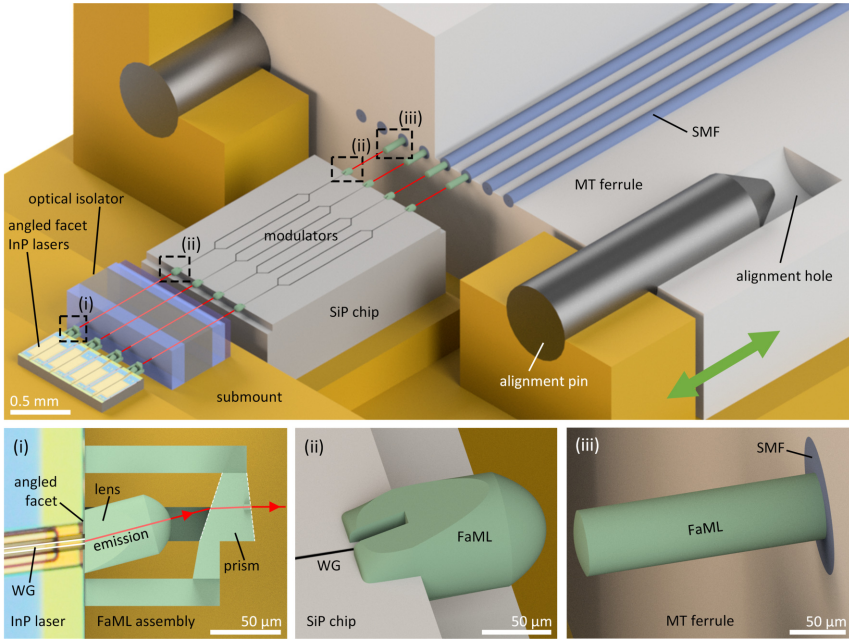
Fig. 4.1: Illustration of an optical assembly based on 3D-printed facet-attached microlenses (FaML). The assembly consists of an array of angled-facet InP lasers, an optical isolator block, and a silicon photonic (SiP) chip with an array of modulators. The output of the SiP chip is connected to an array of single-mode fibers (SMF) in a mechanical transfer (MT) ferrule. The ferrule is part of a pluggable connector (green arrow) and is positioned by mechanical alignment pins. Free-form FaML on each facet, Insets (i), (ii), and (iii), expand and match the mode fields of the different components, and enable low-loss coupling with relaxed alignment tolerances. **Inset (i):** Schematic of a FaML assembly printed to the facet of an angled edge-emitting InP laser. An assembly with a free-form lens and a prism expands, collimates and redirects the beam. The angled plane surfaces and the strongly curved lens keep parasitic back-reflections into the laser cavity minimal. **Insets (ii) and (iii):** Schematic of free-form FaML, printed to the facet of an edge-coupled SiP chip, and to the facet of a SMF, respectively. These FaML can be designed to collimate the free-space beams to diameters of up to 60 µm, thereby greatly relaxing translational alignment tolerances and enabling highly reproducible pluggable connections.

The concept shown in Fig. 4.1 illustrates four key functionalities that are generic for advanced optical assemblies: Redirection of beams emitted by arrays of angled-facet lasers, which is key to efficient coupling to device arrays with standard facet-normal emission, optical coupling over mm-scale distances, which allows for insertion of discrete micro-optical elements such as isolators into the free-space beam paths, low-loss coupling to arrays of edge-emitting SiP chips with relaxed alignment tolerances, as well as assembly by passive positioning and pluggable optical connections, that allow for reproducible low-loss coupling to PIC facets based on mechanical alignment structures. In the following sections, we describe a series of proof-of-concept experiments that demonstrate these generic functionalities using FaML in different settings involving SiP chips, active and passive InP dies, as well as single-mode fiber arrays.

4.3 Facet-attached microlens on an SiP chip

In our first set of experiments we demonstrate low-loss coupling to edge-emitting SiP chips as well as pluggable optical connections based on simple mechanical alignment structures. To this end, we print an array of FaML to the edge of a SiP chip and investigate the coupling efficiency to an array of lensed single-mode fibers (SMF) along with the associated alignment tolerances. We further highlight the benefit of relaxed alignment tolerances by demonstrating pluggable fiber-chip connections based on a pair of off-the-shelf injection-molded LEGO® bricks. For our experiments, we use standard SMF arrays and SiP chips, which contain inverse-tapered edge couplers (EC), arranged in a loopback-configuration with a pitch of $127\,\mu m$, see Fig. 4.2. Details on the SiP chips can be found in the Materials and Methods, Section 4.8. Using multi-photon lithography, we 3D-print FaML directly to the facets of the SiP chip and the fiber array (FA), see Insets (i) and (ii) of Fig. 4.2, targeting an expanded mode field diameter (MFD, defined at $1/e^2$ of the maximum intensity) of $25\,\mu m$. We measure the spots generated by the FaML using an IR microscope, see Supplementary Section B.1 for details. When coupling $1550\,nm$-light to the SMF, the lenses produce round spots with a

consistent MFD of 25 µm at a distance of 150 µm from the lens apex, as expected. For the FaML attached to the SiP chip, the measured spots turn out to be slightly elliptical with a size of 25 µm × 20 µm at a distance of 280 µm away from the lens apex, i.e., the extension in the vertical direction is slightly smaller than designed.

To characterize the performance of the FaML-based coupling interfaces we conduct coupling experiments with the chip fixed in place and the FA mounted on a 6-axis stage, see Fig. 4.2. First, light at a wavelength of 1550 nm is coupled into the fiber of Channel 1, and the output power is recorded at the loopback Channel 8. In this step, we use quasi-TE polarization, having a dominant electric field component parallel to the substrate. We optimize all six degrees of freedom of the stage to achieve maximum received power after the Loopback $(1, 8)$. After that, we keep the position and measure the signals through the other Loopbacks $(2, 7)$, $(3, 4)$ and $(5, 6)$. Assuming that both fiber-chip interfaces in each loopback have the same performance, we estimate the coupling losses per interface, each comprising a pair of FaML and a waveguide-based edge coupler (EC) on the SiP chip. The results for the four loopbacks are very uniform with an average value of 1.44 dB, see Table 4.1, which represents a significant improvement to our previous results [9] of 4 dB. The numbers given are obtained after correction for on-chip losses, see Materials and Methods (Section 4.8). Using 3D-printed microlenses without anti-reflection coating, we cannot avoid Fresnel reflection at the two lens surfaces, which amount to a total of approximately 0.4 dB, estimated for perpendicular incidence and a refractive index of the lens material (VanCoreA, Vanguard Automation GmbH) of $n = 1.53$. The remaining loss of approximately 1.0 dB is attributed to transition losses within the EC and to mode mismatch. We also repeated the same measurement for quasi-TM polarization, having a dominant magnetic field component parallel to the substrate. Note that the Loopbacks $(1, 8)$ and $(2, 7)$ contain two waveguide crossings, indicated by white circles in Fig. 4.2, which were designed only for TE polarization and thus prevent a measurement in TM-polarization. The Loopbacks $(3, 4)$ and $(5, 6)$ have both a loss of 2.2 dB in TM-polarization per fiber-chip interface. This value is slightly larger than for TE-polarization due to polarization-dependent loss (PDL) of the edge-coupler
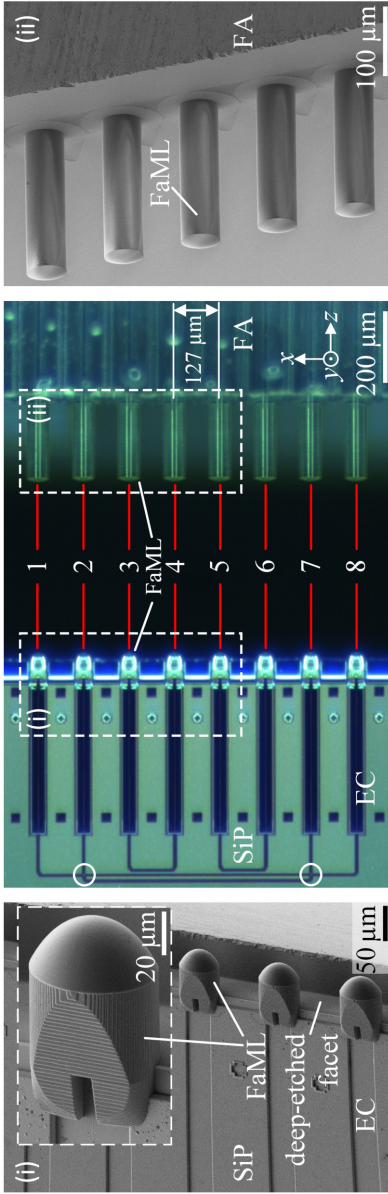
Fig. 4.2: Coupling between a single-mode fiber array (FA) and an array of edge-emitting SiP waveguides using 3D-printed facet-attached microlenses (FaML, centered photograph). The Insets (i) and (ii) to the left and to the right show magnified scanning electron microscope (SEM) images of the FaML on the SiP and FA sides, respectively. The SiP chip contains waveguides with tapered edge couplers (EC), arranged in a loopback-configuration with a pitch of 127 μm. The outer loopbacks contain a pair of waveguide crossings, marked by the white circles. We conduct coupling experiments with the chip fixed in place and the fiber array (FA) mounted on a six-axis stage. First, light at a wavelength of 1550 nm is coupled into the fiber of Channel 1, and the output power is recorded at the loopback Channel 8. For the coupling, all degrees of freedom of the six-axis stage are used to maximize the signal of the Loopback (1, 8). After that, the signals through the other Loopbacks (2, 7), (3, 4) and (5, 6) are simultaneously measured, resulting in an average loss of 1.44 dB per fiber-chip interface for TE-polarized light, see Table 4.1.

89

transition as specified in the Process Design Kit of the associated foundry, see Materials and Methods (Section 4.8).

Besides low coupling losses, the alignment tolerances are of key importance for highly scalable packaging processes. We switch back to quasi-TE polarization and investigate the lateral alignment tolerance by moving the fiber array in the (x, y)-plane perpendicular to the fiber axis, see Fig. 4.2, while recording the output power of Loopback $(1, 8)$. In this experiment, the angular orientation of the fiber is kept as previously optimized. Figure 4.3(a) shows the excess coupling loss per fiber-chip interface as a function of the lateral misalignment. The dashed-dotted red circle with radius of 6 µm indicates the theoretical radial 1 dB coupling tolerance for a Gaussian beam with a mode field diameter of 25 µm, see Supplementary Eq. (B.27), which is in excellent agreement with measured data . Note that the slightly asymmetric spot generated by the FaML on the SiP side results in a hardly noticeable asymmetry of the measured 1 dB contour line.

Table 4.1: Losses for simultaneous coupling of 8 channels from a fiber array to a SiP-chip after active alignment.

TE loopback path	$(1, 8)$	$(2, 7)$	$(3, 4)$	$(5, 6)$	avg.
Loss per fiber-chip interface [dB]	1.46	1.43	1.45	1.40	1.44

For measuring the angular coupling tolerance, Fig. 4.3(b), the fiber array is rotated, followed by a pivot-point correction of rotation-induced translation. We record data points for an in-plane rotation (circles, rotation in the (x, z)-plane of Fig. 4.2) as well as an out-of-plane tilt (squares, rotation in the (y, z)-plane of Fig. 4.2). The solid lines show fits of the angular coupling tolerance based on a Gaussian beam model according to Supplementary Eq. (B.17). In case of the in-plane rotation, the fit corresponds to a beam waist diameter of 25 µm. For the out-of-plane tilt, the fit corresponds to a slightly smaller beam waist diameter of 23 µm, because the spot generated by the lens on the SiP side was indeed slightly smaller in the vertical direction than in the horizontal direction. In summary, we find a radial
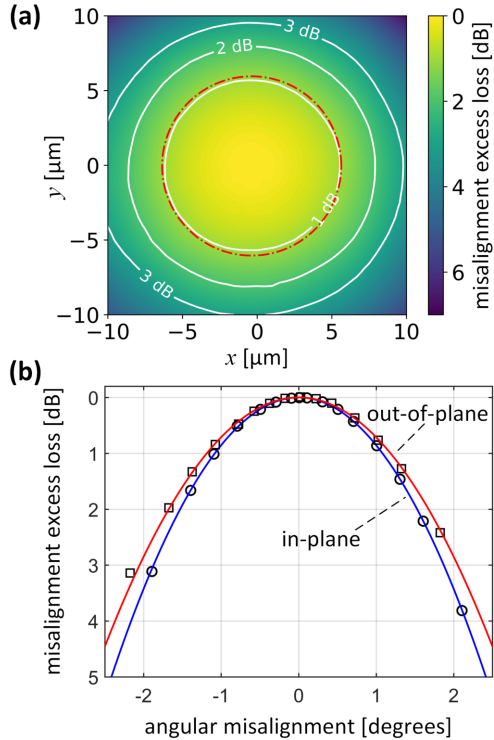
Fig. 4.3: Relative power loss for a lateral and angular misalignment of the SMF-array relative to the SiP chip using 3D-printed microlenses, see Insets (i) and (ii) of Fig. 4.2. The depicted values refer to the loss per FaML pair including one EC, see Fig. 4.2. The optimum position corresponds to a coupling loss of 1.4 dB including one EC, see Table 4.1. **(a)** Radial tolerances in the (x,y)-plane of Fig. 4.2. The radial 1 dB tolerance amounts to 6 µm and corresponds to the predicted contour line for a Gaussian beam with a MFD of 25 µm (red dash-dotted circle), see Supplementary Section B.2.5. **(b)** Angular tolerances measured in-plane (circles, rotation in the (x,z)-plane of Fig. 4.2) and out-of-plane (squares, rotation in (y,z)-plane of Fig. 4.2). The solid lines fit a Gaussian with a beam waist diameter of 25 µm (23 µm) to the in-plane (out-of-plane) data, Supplementary Eq. (B.17).

1 dB alignment tolerance of 6 µm and an angular alignment tolerance of 1.1°. Note that lateral and angular tolerances are subject to a fundamental tradeoff, see Supplementary Fig. B.3.

For coupling of waveguide and fiber arrays, one would expect a slight deviation of the optimum coupling positions for the various channels. To investigate this aspect, we return to the previous optimum fiber array position and orientation for Loopback $(1, 8)$ and move the fiber array laterally while measuring the power transmission through the various loopbacks. In this measurement, we keep the angular alignment of the fiber array fixed. We find that the optimum positions for the various loopbacks deviate by less than 1 µm, mainly in the horizontal x-direction. This confirms the high precision of the fabricated FaML, given the fact that the spacing of the fibers within the array is specified by the manufacturer with an accuracy of ±0.3 µm [J6, 139]. This associated excess loss is, however, negligible for a MFD of 25 µm, for which a lateral misalignment of 1 µm translates into an excess loss of less than 0.05 dB per FaML pair, see Supplementary Section B.2.5.

Finally, we investigate the uniformity of the emission direction of the various FaML. To this end, we individually maximize the transmission of each of the Loopbacks $(2, 7)$, $(3, 4)$, and $(5, 6)$ by optimizing the position and the orientation of the fiber array in all six degrees of freedom. In the respective optimum positions and orientations, we then compare the fiber axis rotation angles $R_{x,y,z}$ to the ones previously found when optimizing the signal to the Loopback $(1, 8)$. We find that the individual optimum angles are highly consistent, making it impossible to measure any deviations within the measurement accuracy of $\pm0.05°$ of our stage. This highly reproducible emission direction of the individual FaML is of utmost importance when aligning waveguide and fiber arrays, in particular when bigger distances in the millimeter-scale need to be bridged to allow for inserting of discrete micro-optical elements, see Fig. 4.1. In this context, automated fabrication of FaML with high alignment precision to on-chip structures is key to achieve the necessary reproducibility, see Materials and Methods (Section 4.8) for details.
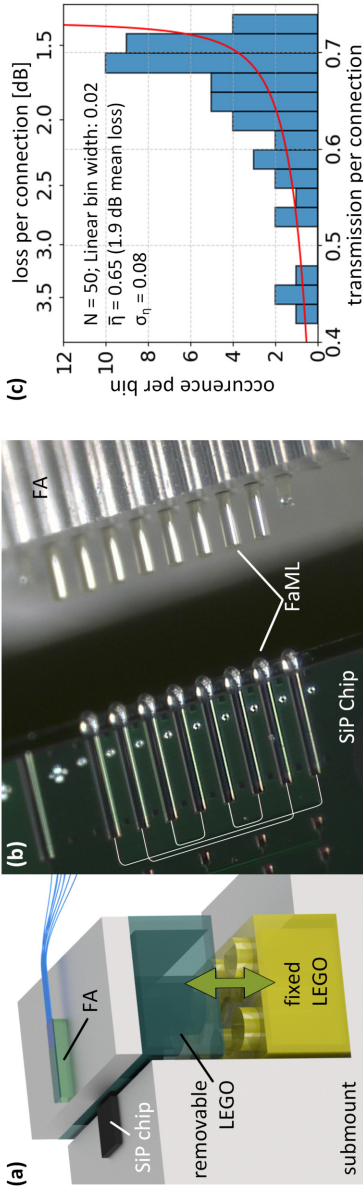
Fig. 4.4: Re-pluggable single-mode fiber-chip connection using FaML and plastic injection molded LEGO bricks. **(a)** Schematic view of the assembly. The LEGO-plug consists of a fixed (yellow) brick and a removable (dark, transparent) brick with an attached plane cover plate (grey). The direction of separation and reconnection is indicated by a green double arrow. The silicon photonic (SiP) chip is glued on the submount first, and the fiber array (FA) is subsequently aligned actively and glued onto the removable part, with the LEGO bricks stuck together. No significant drift is observed while curing the UV-glue. Finally, the insertion loss is measured after breaking and re-establishing the connection, indicated by the green arrow. **(b)** Zoom-in of the FaML-based optical interconnects. **(c)** Histogram of measured power transmission factors per fiber-chip interface, each comprising a FaML pair and a tapered edge coupler (EC), see Fig. 4.2. The connection was re-plugged $N = 50$ times, and the histogram is shown with a linear binning of the power transmission factor η with a bin width of 0.02. The mean transmission per connection amounts to $\overline{\eta} = 0.65$ with a standard deviation of $\sigma_\eta = 0.08$. The interval $\overline{\eta} \pm \sigma_\eta$ corresponds to losses between 1.41 dB and 2.46 dB around a mean loss of 1.9 dB, about 0.5 dB higher than the value found with active alignment, see Table 4.1.

Such tolerances bring the fiber-to-chip connection within the dimensional accuracy range of injection-molded plastics. We demonstrate pluggable connections using LEGO bricks, in analogy to [140], where a similar fiber-to-chip connection has been built for surface coupling using a combination of grating couplers and fused-silica microlenses. Figure 4.4(a) shows a schematic view of our assembly. The LEGO connection consists of a fixed (yellow) brick and a removable (dark transparent) brick with an attached plane aluminum cover plate (grey). The SiP chip is glued on the submount first, and the FA is subsequently aligned actively and glued onto the cover plate on the right-hand side, while the LEGO bricks are stuck together. No significant drift is observed while curing the UV glue, see Materials and Methods (Section 4.8). Finally, the insertion loss is measured after disassembling and re-establishing the LEGO connection for a total of $N = 50$ times. The mean transmission per connection amounts to $\overline{\eta} = 0.65$ with a standard deviation of $\sigma_\eta = 0.08$. The interval $\overline{\eta} \pm \sigma_\eta$ corresponds to losses between $1.41\,\mathrm{dB}$ and $2.46\,\mathrm{dB}$, with a mean loss of $1.9\,\mathrm{dB}$, see Fig. 4.4(b), about $0.5\,\mathrm{dB}$ higher than the value initially found with active alignment, see Table 4.1.

We furthermore measure the spectral bandwidth of our FaML-based fiber-chip interfaces, see Fig. 4.5. The depicted values take into account one FaML pair including one tapered EC, see Fig. 4.2. The waveguide loss as specified by the foundry for wavelength of $1550\,\mathrm{nm}$ was subtracted. We find a noticeable wavelength dependence and clear differences between TE and TM polarization, which we attribute to the transmission characteristics of the EC. We confirm this notion by simulating the wavelength dependence of the FaML, which would lead to variations of the coupling efficiency well below $0.1\,\mathrm{dB}$ within the wavelength range used in our measurements. The $1\,\mathrm{dB}$ bandwidth significantly exceeds the $150\,\mathrm{nm}$ tuning range of our laser sources both for TE and TM polarization. Independently of the polarization, the transmission is virtually flat ($\pm 0.1\,\mathrm{dB}$) within the C-band ($1530\,\mathrm{nm}$ to $1570\,\mathrm{nm}$, blue shaded region).
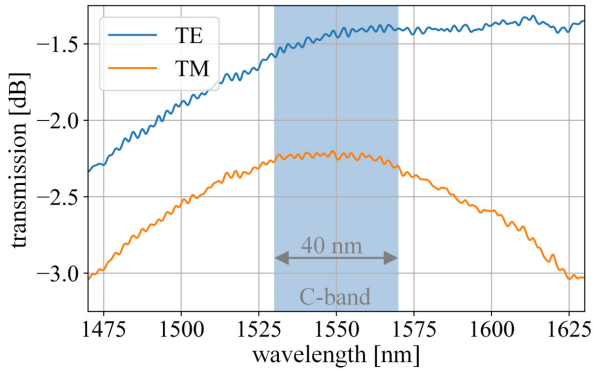
Fig. 4.5: Measured wavelength-dependent transmission per fiber-chip interface, each including a FaML pair and an EC, see Fig. 4.2. We attribute the noticeable wavelength dependence and the differences between TE and TM polarization to the transmission characteristics of the edge coupler (EC). In both cases, the 1 dB bandwidth significantly exceeds the 150 nm tuning range of our laser sources.

4.4 Passive positioning, large-distance optical coupling, and combination with discrete micro-optical elements

In the previous section, the FaML were designed to produce a beam-waist diameter of 25 µm, presenting a good trade-off between translational and rotational alignment tolerances, see Supplementary Section B.2.7 for details. Clearly, the structures can be designed to produce even larger beam diameters, thereby reducing the beam divergence. This allows for bridging of large, e.g., mm-scale distances between the FaML of the associated coupling interface thus allowing to insert discrete micro-optical components such as optical isolators, see Fig. 4.1. At the same time, larger beam diameters further relax the translational alignment tolerances at the expense of their rotational counterparts. In the following, we describe our proof-of-concept demonstrations related to large-distance optical coupling with and without intermediate micro-optical elements.
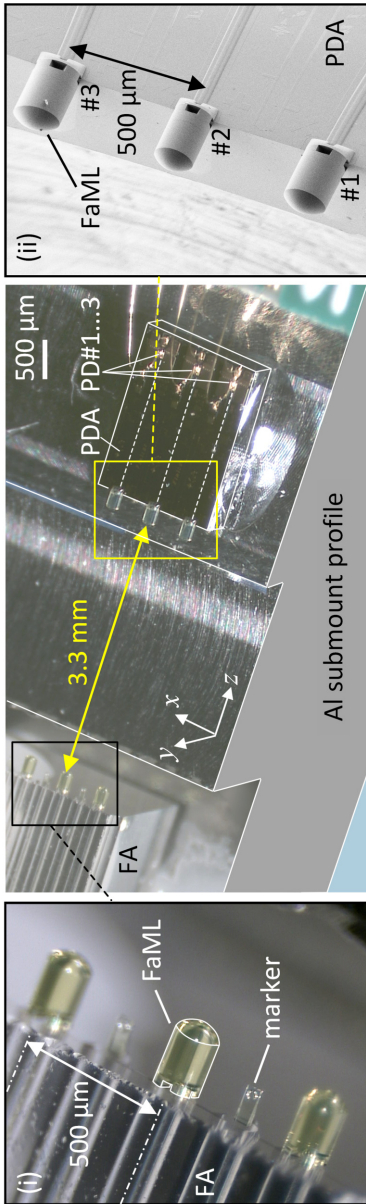
Fig. 4.6: Passively aligned SMF-array-to-chip assembly using FaML. The free-space coupling distance amounts to 3.3 mm and allows for inserting optical components such as beam splitters or optical isolators into the beam path, see, e.g., Fig. 4.1 and Fig. 4.10. Three fibers of the fiber array (FA, Inset (i)) are coupled to three waveguides leading to the photodiodes PD#1, #2, #3 of an edge-coupled InP photodiode array (PDA, Inset (ii)). Fiber cores and on-chip waveguides are illustrated by dashed lines. FaML are printed to the facets of the FA and the PDA chip. In the assembly process, we first glue the lensed PDA chip to an aluminum submount and then align the lensed FA passively with an automated assembly machine (ficonTEC Service GmbH), see Section 4.8 (Materials and Methods) and Supplementary Section B.3 for details. The aligned components are fixed with a UV-curable glue. Printed alignment markers help with the detection of the FA during the assembly process, see Inset (i) and Supplementary Section B.3 for details.

For our experiments, we use standard SMF arrays and edge-coupled InP photodiode arrays (PDA, Finisar / II-VI Inc.). We 3D-print FaML to the fiber array (FA), Fig. 4.6 Inset (i), and to the PDA chip, Fig. 4.6 Inset (ii). With these components, we demonstrate a passive SMF-array-to-chip assembly with a free-space coupling distance as large as $3.3\,\mathrm{mm}$. The lenses on the FA transform the SMF mode field diameters of $10\,\mathrm{\mu m}$ to a free-space Gaussian beam waist diameter of $60\,\mathrm{\mu m}$ at a distance of $1.65\,\mathrm{mm}$ from the FaML apex, i.e., in the center of the free-space beam path. The PDA chip is designed for butt-coupling to SMF, containing an on-chip tapered spot-size converter that is designed for a $10\,\mathrm{\mu m}$-wide field at the chip facet. We print lenses to the chip having the same optical design as printed to the FA to transform an incoming Gaussian beam with a waist diameter of $60\,\mathrm{\mu m}$ to a Gaussian spot with a $10\,\mathrm{\mu m}$ diameter at the PDA chip facet.
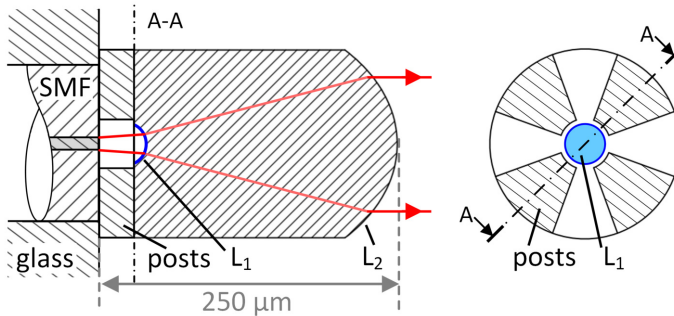
Fig. 4.7: Design drawing of the FaML on the FA side of Fig. 4.6. The FA end-faces are flush with the embedding glass block. The body of the lens sits on four posts with a small air gap between the waveguide end-face and the first refractive surface of the lens. This lens surface is concave (L1, highlighted in blue) and increases the divergence of the beam. The second lens surface (L2) is convex and collimates the beam. Both surfaces form a Galilean telescope which enlarges the SMF mode field diameter (MFD) of $10\,\mathrm{\mu m}$ to a beam waist diameter of $60\,\mathrm{\mu m}$ at the shortest possible axial distance. The choice of the expanded beam diameter considers tolerances of the 3D-printing and of the passive assembly processes. The original PDA chip (see Fig. 4.6) is designed for butt-coupling using SMF with a MFD of $10\,\mathrm{\mu m}$. We therefore use the same optical lens design as for the FA.

The lens design for the FA is shown in Fig. 4.7. The FA end-faces are flush with the embedding glass block. The body of the lens sits on four posts with a small air gap between the waveguide end-face and the first refractive surface of

the lens. This lens surface is concave (L1, highlighted in blue) and increases the divergence of the beam. The second lens surface (L2) is convex and collimates the beam. Both surfaces form a Galilean telescope which enlarges the incoming beam diameter at the shortest possible axial distance. The PDA lens follows the same design as for the FA.

In the assembly process, we first glue the lensed PDA chip to an aluminum sub-mount and then align the lensed FA passively with a custom assembly machine (ficonTEC Service GmbH, see Materials and Methods (Section 4.8), and Supplementary Section B.3 for details). The aligned FA is fixed with glue. The three waveguides leading to the photodiodes PD#1, #2, #3 on the PDA chip are spaced by 500 µm, while the FA has a pitch of 250 µm. We therefore print a lens on every second fiber of the FA only, while the remaining fiber facets are used for printing alignment markers for the passive assembly process, see Inset (i) of Fig. 4.6 and Supplementary Section B.3 for details.

The choice of the expanded beam diameter 60 µm is a compromise and considers the tolerances of the passive assembly process. In particular, the orientation of the chip edges of FA and PDA might be erroneously measured by machine vision and could therefore be misaligned in the assembly process. The resulting beam-pointing error leads to a coupling loss which is the smaller the larger the mode field diameter becomes. However, too large a mode field diameter leads to a low tolerance with respect to an angular misalignment. These considerations are elaborated in Supplementary Section B.2.8. The measured excess loss for a lateral shift of the FA with respect to the optimum position is shown in Fig. 4.8(a). The radial 1 dB tolerance amounts to 14.4 µm and corresponds to the predicted contour line for a Gaussian beam with a MFD of 60 µm (red dash-dotted circle), see Supplementary Section B.2.5. The measured excess loss for an angular in-plane offset in the (x, z)-plane of Fig. 4.6 is given by the black circles in Fig. 4.7(b). The angular 1 dB tolerance amounts to $0.48°$ only and corresponds to the predicted coupling loss for a Gaussian beam with a MFD of 57 µm (blue line), see Supplementary Eq. (B.17).

Fig. 4.8: Relative power loss for a lateral and angular misalignment of the SMF-array relative to the PDA chip in Fig. 4.6. **(a)** Relative loss for a lateral shift of the FA with respect to the optimum position. The radial 1 dB tolerance amounts to $14.4\,\mu\text{m}$ and corresponds to the predicted contour line for a Gaussian beam with a MFD of $60\,\mu\text{m}$ (red dash-dotted circle), see Supplementary Section B.2.5. **(b)** Excess loss for an angular in-plane offset ((x,z)-plane of Fig. 4.6). The angular 1 dB tolerance amounts to $0.48°$ only and corresponds to the predicted coupling loss for a Gaussian beam with a MFD of $57\,\mu\text{m}$ (blue line), see Supplementary Eq. (B.17).

To quantify the absolute coupling losses of the lenses and of the passive assembly, we measure the photocurrents $i = S \times (\eta P)$ at different stages of the assembly process while varying the input power into the associated SMF, see Fig. 4.9 for results obtained from PD#1 in TE polarization. In a first stage, we butt-couple an
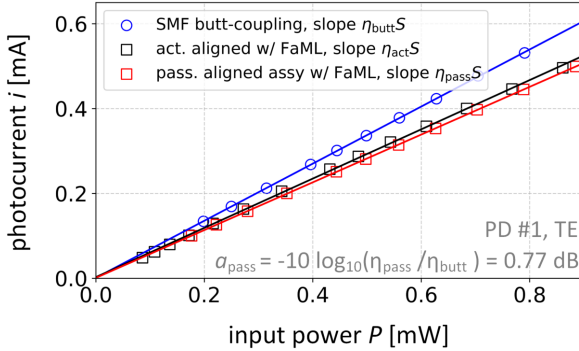
Fig. 4.9: Coupling losses of the lenses and of the passive assembly as shown in Fig. 4.6. We measure the power dependent photocurrent $i = S \times (\eta P)$ of PD#1 in TE polarization in different stages of the assembly experiment: Blue circles refer to a measurement prior to printing the FaML using SMF butt-coupling with coupling efficiency η_{butt}, black open squares give the results for active alignment after printing the FaML (no glue, coupling efficiency η_{act}), and red squares refer to passive alignment using the automated assembly machine (FA fixed with glue, coupling efficiency η_{pass}). The measurements confirm that FaML allow for low-loss coupling via passive alignment without any performance penalty compared to active alignment. The excess alignment loss $\eta_{\text{pass}}/\eta_{\text{butt}}$ corresponds to $a_{\text{pass}} = 0.77\,\text{dB}$.

SMF to the PDA chip facet and measure the photocurrents of PD#1, #2, #3 for two orthogonal polarizations, blue circles. This measurement and the associated coupling efficiency η_{butt} is used as a baseline for the subsequent experiments. We then print the lenses both on the FA and the PDA, adjust the alignment for PD#1, #2, #3 actively, and again record the photocurrents, black squares, leading to the coupling efficiency η_{act}. In the third stage, we use an automated procedure to passively align height, lateral position, and tilt of the FA to the PDA chip, and fix it with glue applied to the edges of the glass block. The measurement results are indicated by red squares in Fig. 4.9, leading to the coupling efficiency η_{pass}. Within the measurement uncertainty of $\pm 3\%$, the coupling efficiencies

η_{act} and η_{pass} do not differ. This is the consequence of the high position and angular orientation accuracy of the passive alignment. Starting from the passive alignment (prior to gluing), an additional lateral active alignment corrected the position by only $2\,\mu\text{m}$. An angular correction was not required within the angular accuracy of $\pm 0.1°$. The optical excess loss for the passive alignment is found by comparing to butt coupling. With the ratio of the respective photocurrents, we find $a_{\text{pass}} = -10 \log_{10}(\eta_{\text{pass}}/\eta_{\text{butt}})$. For better accuracy we fit straight lines to the recorded photocurrents in Fig. 4.9 and extract the respective slopes $\eta \times S$ to estimate a_{pass}. We find $a_{\text{pass}} = 0.77\,\text{dB}$. We also measure all channels for TM polarization, finding very similar behavior as for TE polarization, see Table 2.

Table 4.2: Slopes $\eta S = i/P$ measured from graphs as in Fig. 4.9. Three cases are compared: SMF butt-coupling without FaML ($\eta_{\text{butt}}S$), coupling after printing FaML with active alignment but without glue ($\eta_{\text{act}}S$), and coupling after printing FaML with passive alignment and fixed with glue ($\eta_{\text{pass}}S$). The assembly losses $a_{\text{pass}} = -10 \log_{10}\left((\eta_{\text{pass}}S)/(\eta_{\text{butt}}S)\right)$ are calculated from the ratio of measured slopes of the photocurrent i as a function of optical input power P.

Photodiode number	#1		#2		#3	
and polarization type	TE	TM	TE	TM	TE	TM
SMF butt-coupling: $\eta_{\text{butt}}S$ [A/W]	0.67	0.54	0.68	0.55	0.66	0.55
Active alignment w/ FaML, no glue applied: $\eta_{\text{act}}S$ [A/W]	0.58	0.47	0.58	0.48	0.58	0.47
Passively aligned assembly w/ FaML, fixed with glue: $\eta_{\text{pass}}S$ [A/W]	0.56	0.48	0.59	0.49	0.57	0.45
Assembly loss $a_{\text{pass}}S$ [dB]	**0.77**	**0.59**	**0.61**	**0.50**	**0.67**	**0.86**

Using the same type of lensed FA and lensed PDA chips, we additionally demonstrate that discrete optical components can be inserted into the collimated free-space beam path. In our proof-of-principle assembly, we insert a polarization beam splitter (PBS), see Fig. 4.10. The PBS consists of two right-angle glass prisms, and a dielectric polarization-sensitive reflecting surface S_{pol} in between. The beam paths in Fig. 4.10 and Inset (iii) are shown as dashed lines. The input fields at points A and B are arbitrarily polarized, i.e., the linearly polarized constituents could
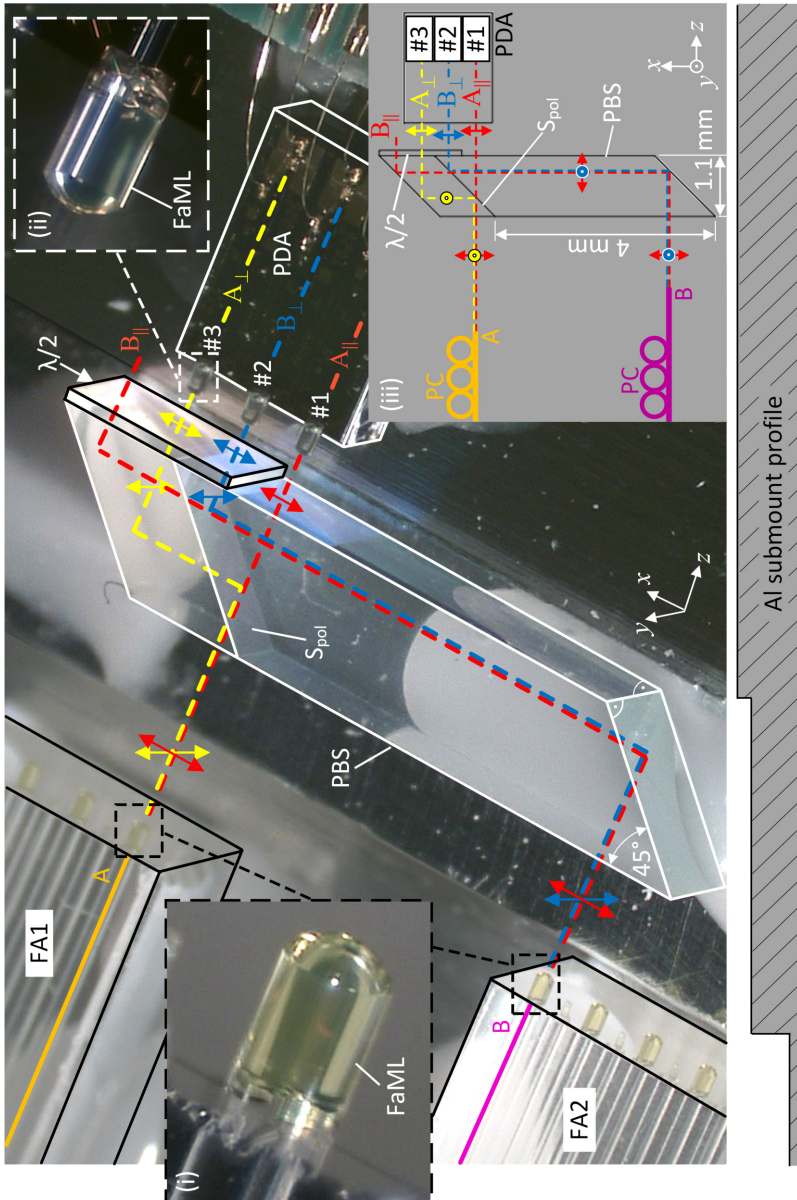
Fig. 4.10: Demonstration of an optical assembly using FaML, see Insets (i) and (ii) for a magnified view, including a discrete polarization beam splitter (PBS) in the collimated free-space beam path between a pair of FA and an optical chip with a PDA. The PBS consists of two right-angle glass prisms with a dielectric polarization-sensitive reflecting surface S_{Pol} in between. The beam paths are shown as colored dashed lines in the figure and in the top view schematic of Inset (iii). The input fields at point A of FA1 and point B of FA2 are arbitrarily polarized, i.e., the linearly polarized constituents could have different amplitudes and phases. For coupling to a polarization-sensitive photonic integrated circuit (PIC), all output beams $A_\perp$, $A_\parallel$, and $B_\perp$ (beam $B_\parallel$ is lost) should be identically polarized. To this end, a half-wave plate ($\lambda/2$) is used to rotate the "vertical" linear polarization (blue, yellow) into the orientation of the "horizontal" linear polarization. Such an assembly could be used as a dual-polarization coherent receiver with the signal supplied by FA1 and the local oscillator by FA2, when replacing the rather simple PDA by a chip carrying a pair of 90° optical hybrids, each followed by a pair of balanced photodiodes. For measuring the coupling loss of each beam path, we subsequently feed the assembly with optical power through the FA1 and FA2 and maximize the photocurrents of PD#1, #2, #3 using fiber-based polarization controllers (PC). The resulting photocurrents are again compared to those obtained by directly feeding horizontally polarized light to the PDA chip via butt-coupled SMF. The losses are calculated according to the procedure described in the context of Table 4.2. We find an excess loss compared to butt coupling of 0.95 dB for path A–PD#1 (red), 1.44 dB for path A–PD#3 (yellow), and 2.18 dB for path B–PD#2 (blue). For the assembly, we first glue the PDA chip to the aluminum submount, followed by passive alignment and gluing of the PBS to the submount. The stepped profile of the aluminum submount is illustrated in the cross-sectional view at the bottom of the figure. In a second step, we align each FA passively with respect to the PDA chip, and for each FA, we again compare our passive alignment to an active alignment. Contrary to the previous demonstration without PBS, see Fig. 4.6, we now find a significant lateral (x-axis) offset between passive and active alignment positioning of the FA. Most prominently, the optimum entry points of paths A–PD#1 and A–PD#3 differ by 9 µm. We attribute these deviations to the manufacturing tolerances of the PBS, which are specified with ±25 µm for all length dimensions and ±0.2° for all cut angles, and which are significantly larger than the 2 µm translational and sub-0.1° rotational deviations that we have estimated for our FaML-assisted assembly process in the context of Fig. 4.6.

103

have different amplitudes and phases. For coupling to a polarization-sensitive PIC, it would be desirable that all output beams $A_\perp$, $A_\parallel$, and $B_\perp$ (beam $B_\parallel$ is lost) are identically polarized. To this end, the PBS is equipped with a half-wave plate ($\lambda/2$) that rotates the "vertical" linear polarizations (blue, yellow) into the orientation of the "horizontal" linear polarization. Such an assembly could be used as a dual-polarization coherent receiver with the signal supplied by FA1 and the local oscillator by FA2, when replacing the rather simple PDA by a chip carrying a pair of $90°$ optical hybrids, each followed by a pair of balanced photodiodes. In our experiments, we use a simple PDA chip to simplify the characterization of the various coupling losses. To this end, we subsequently feed the assembly with optical power through the FA1 and FA2 and maximize the photocurrents of PD#1, #2, #3 using fiber-based polarization controllers (PC). The resulting photocurrents are again compared to those obtained by directly feeding horizontally polarized light to the PDA chip via butt-coupled SMF. The losses are calculated using the procedure described in the context of Table 4.2. We find an excess loss compared to butt coupling of $0.95\,\mathrm{dB}$ for coupling from FA1 to PD#1 (path A–PD#1, red), $1.44\,\mathrm{dB}$ for coupling from FA1 to PD#3 (path A–PD#3, yellow), and $2.18\,\mathrm{dB}$ for coupling from FA2 to PD#2 (path B–PD#2, blue). The free-space beam in the connection B–PD#2 has an optical path length of $8.3\,\mathrm{mm}$, which is $5\,\mathrm{mm}$ longer than the free-space path in connection A–PD#1. However, because we wanted to use one single lens design for all paths, the longer optical path length widens the beam and leads to higher losses. A free-space coupling distance of $3.3\,\mathrm{mm}$ would have been optimum.

For the assembly, we first glue the PDA chip to the aluminum submount, see Fig. 4.10, followed by passive alignment and gluing of the PBS. In a second step, we align FA1 and FA2 passively with respect to the PDA chip and again compare our passive alignment to an active alignment. This time, we find considerable lateral (x-axis) offsets between passive and active alignment of the FA. Most prominently, the optimum positions of FA1 for paths A–PD#1 and A–PD#3 differ by $9\,\mu\mathrm{m}$. For our proof-of-principle demonstration, we therefore manually fix FA1 in the middle between the optimized positions for PD#1 and #3. These deviations between passive and active alignment are in sharp contrast to our results

from the assembly experiments without PBS, see Figs. 4.6 and 4.9. In those experiments, the free-space path length was also 3.3 mm as in the connection A–PD#1, but the optimum position of the FA could directly be found by passive alignment techniques, relying on machine vision only. We hence conclude that the fabrication tolerances of the PBS are the main reason for the alignment errors in the experiments shown in Fig. 4.10. Specifically, the tolerances of the PBS are specified to be $\pm 25\,\mu m$ for all length dimensions and $\pm 0.2°$ for all cut angles, which is significantly worse than the $2\,\mu m$ translational and sub-$0.1°$ rotational deviations that we have estimated for our FaML-assisted assembly process in the context of Fig. 4.6. This demonstrates that the level of precision that can be achieved with FaML-based optical microsystems is on par with or even exceeds the accuracy levels offered by standard discrete micro-optical components.

4.5 Coupling to device arrays with angled facets

Finally, in our third set of experiments, we consider FaML assemblies printed to angled chip facets, see Inset (i) of Fig. 4.1, which are commonly used for semiconductor lasers and amplifiers, where unwanted back-reflections need to be effectively suppressed. In our experiments, we couple an InAlGaAs-based Discrete Mode [141] DFB laser array to a single-mode fiber array (FA) using dedicated FaML both on the active chip and the fiber side. Figure 4.11(a) shows a single connection of the assembly. The FaML are specifically designed to produce a non-planar beam path between the two facets, that contain only tilted or strongly curved optical surfaces S1, S2, S3, and S4, thereby greatly reducing back-reflections into the DFB chip. Note that the non-planar beam path is designed such that the top-view projection of the free-space section between the FaML is perpendicular to the chip and the FA edge, see Fig. 4.11(b). This greatly simplifies alignment of the devices in assembly processes that are based on top-view camera vision in combination with linear translation parallel to the chip edges.
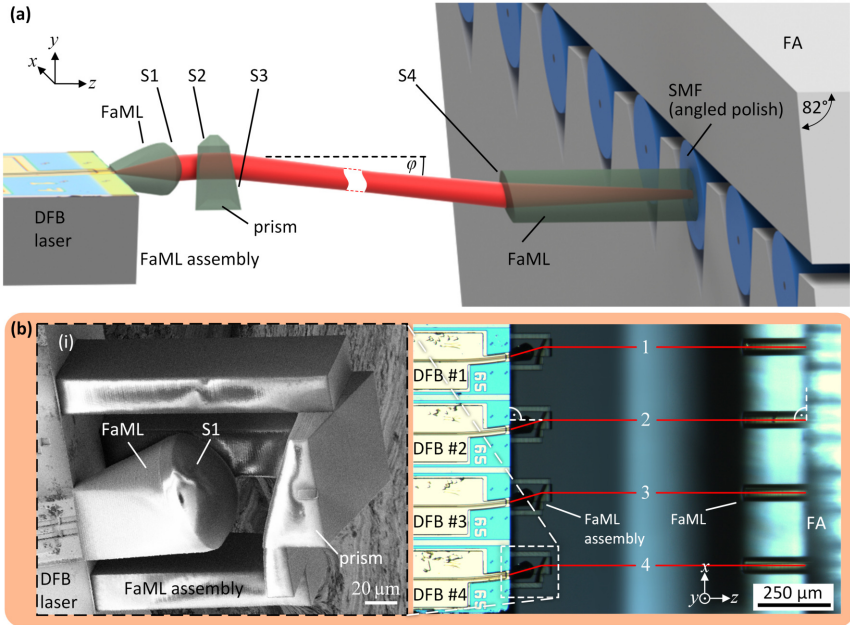
Fig. 4.11: Demonstration of an assembly consisting of an angled DFB laser array coupled a single-mode fiber array (FA) through dedicated FaML both on the laser and the fiber facets. **(a)** Artist's view of a single connection of the assembly. The FaML are designed to produce a non-planar beam path between the two facets that contains only tilted or strongly curved optical surfaces S1, S2, S3, and S4 and thereby reduces unwanted back-reflection into the laser. On the DFB side (left), a combination of a free-form lens and a prism expands, collimates, and redirects the beam. Mechanical support structures are omitted for better visibility. The strongly curved lens surface S1 collimates the beam to a diameter of 25 µm. The beam is then bent to the right with respect to the beam propagation direction by the first prism surface S2. Inside the prism, the light propagates parallel to the surface-normal of the DFB facet (z-axis). The second prism surface S3 then deflects the beam downwards in the (y,z)-plane by $\varphi = 7°$ with respect to the z-axis. The FA features an end-face, which is polished at an angle of $8°$ from the (x,y)-plane, and which is equipped with a corresponding 3D-printed off-axis free-form lens (lens surface S4) that receives the beam. This arrangement shows minimal back-reflections and a coupling loss of about 2 dB, see Table 4.3. **(b)** Top-view image of the assembly. An array of four angled InP lasers is coupled to four fibers of an FA. Inset (i) shows an SEM picture of the FaML assembly on the laser side

The lasers and fibers used in the experiment are spaced at a pitch of $250\,\mu m$. At the DFB side, a combination of a free-form lens and a prism expands, collimates, and redirects the beam. The strongly curved lens surface S1 collimates the beam to a diameter of $25\,\mu m$. The beam is then bent to the right with respect to the beam propagation direction by the first prism surface S2. Inside the prism, the light propagates parallel to the surface-normal of the DFB facet (z-axis). The second prism surface S3 then deflects the beam downwards in the (y, z)-plane by $\varphi = 7°$ with respect to the z-axis, Fig. 4.11(a). The FA features an end-face, which is polished at an angle of $8°$ from the (x, y)-plane, and which is equipped with a corresponding 3D-printed off-axis free-form lens that receives the beam.
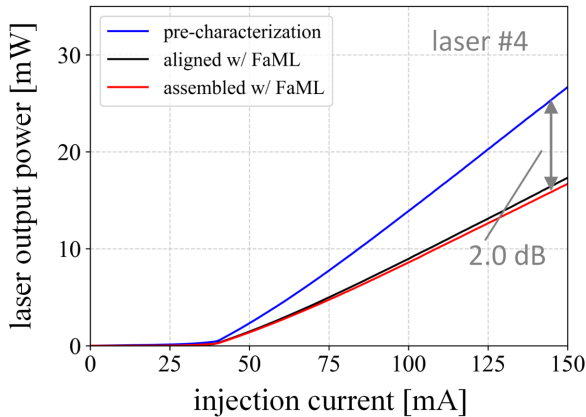
Fig. 4.12: Coupling losses for the laser-to-SMF assembly with angled facets, see Fig. 4.11. We measure the laser output power vs. injection current (P-I-curves) for DFB #4 in different stages of the assembly experiment: The blue trace (pre-charaterization) refers to the bare DFB, measured using an integrating sphere. The black trace (aligned w/ FaML) and the red trace (assembled w/ FaML) give the results for active alignment after printing the FaML and before, respectively after applying the UV glue. The threshold current remains unchanged, and we find an assembly loss of $2.0\,dB$.

For proper evaluation of the coupling efficiency in the assembly process, we first measured the laser output power vs. the injection current (P-I-curve) of each DFB laser prior to printing the FaML, see blue curve Fig. 4.12. We then fabricate the FaML and actively align the FA to the DFB chip. In this step, the DFB chip is

fixed in place, while the FA is positioned such that the light of DFB#1 and #4 is optimally coupled to the respective fiber, see Fig. 4.11(b) for the corresponding numbering. We again measure the P-I-curve of each laser through the fibers, see black trace in Fig. 4.12 for DFB#4. In a next step, we fix the FA with an UV glue, see Materials and Methods (Section 4.8), and measure the P-I-curves again, see red trace in Fig. 4.12 for DFB#4. Comparing the P-I-curves before and after assembly, we find identical threshold currents and no indication of mode-hopping. Table 4.3 indicates the measured coupling losses before and after gluing the FA for all four DFB. Prior to gluing the FA, the coupling losses

Table 4.3: Coupling losses for simultaneous coupling of a bar of 4 angled InP lasers to a fiber array.

laser number	1	2	3	4	avg.
Loss per FaML pair (actively aligned) [dB]	1.9	1.9	2.0	1.9	1.92
Loss per FaML pair (glued assembly) [dB]	**2.3**	**2.5**	**2.3**	**2.0**	**2.28**

are very consistent with an average of $1.92\,\mathrm{dB}$. For DFB#4, this value remains essentially unchanged after gluing the FA, whereas a small deviation is visible for DFB#1 . . . 3. This is attributed to the fact that the glue used for fixing the FA in our experiment was slightly thicker than designed. Specifically, the experiment relied on a milled aluminum sub-mount to account for the different thicknesses of the DFB chip and the FA. This step came out slightly larger than designed, which had to be compensated by an approximately $400\,\mathrm{\mu m}$-thick layer of glue, which is subject to shrinkage during the curing process. More precise fabrication of the sub-mount step-height should alleviate this problem, see description of our first set of experiments in Section 4.3. Still, the average loss per FaML pair amounts to $2.28\,\mathrm{dB}$ only, which is only $0.36\,\mathrm{dB}$ higher than the losses found for optimum alignment, see Table 4.3. We also investigated the relative loss for a lateral and angular misalignment with respect to the optimum position prior to gluing the FA, see Fig. 4.13(a) and (b), respectively. We find a slight deviation from an ideal

rotationally symmetric characteristic, while the tolerances are similar to the ones observed in our first set of experiments in Section 4.3.

(a)

(b)
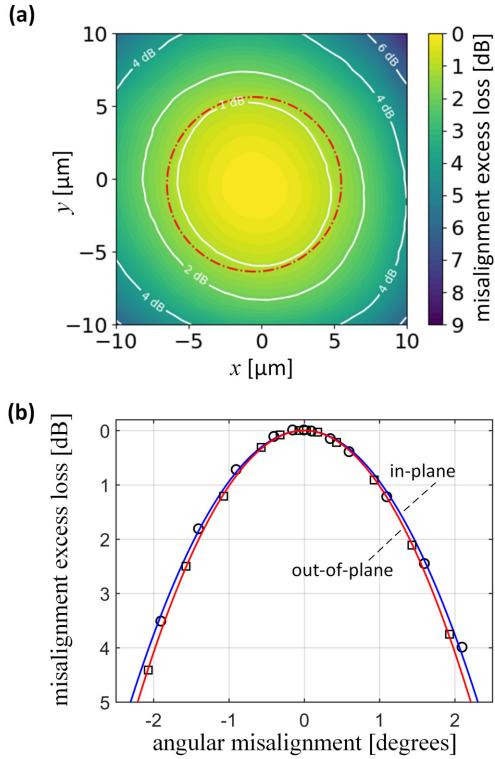
Fig. 4.13: Alignment tolerances for the laser-to-SMF assembly with angled facets, Fig. 4.11. **(a)** Excess loss for lateral misalignment in the (x,y)-plane of Fig. 4.11. The red dash-dotted circle indicates the expected radial 1 dB tolerance for a Gaussian beam with a MFD of 25 µm, see Supplementary Section B.2.5 **(b)** Excess loss for angular misalignment both in the substrate plane (circles, in-plane) and vertically to the substrate plane (squares, out-of-plane). The solid lines indicate Gaussian fits.

We furthermore compare the spectra for one angled laser with and without the coupling arrangement of Fig. 4.11. For the spectra of the bare laser as a function of the operating current, see upper plot in Fig. 4.14, we pick up the light with a
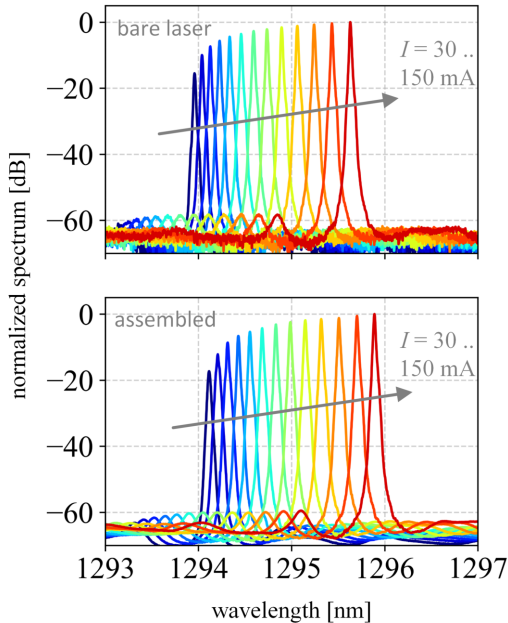
Fig. 4.14: Comparison of current-dependent emission spectra (resolution bandwidth 0.01 nm) of DFB #2 with and without the coupling arrangement shown Fig. 4.11. For the spectra of the bare laser we pick up the light with a fiber placed deliberately at a large distance from the emitting facet (upper plot) for avoiding back-reflections. The corresponding spectra of the packaged device (lower plot) with the coupling arrangement of Fig. 4.11 remain essentially unchanged, besides a small spectral shift because of slight temperature differences. We conclude that back-reflections do not spoil the laser spectrum. In Supplementary Fig. B.8 the influence of back-reflections is discussed in detail.

fiber placed deliberately at large distance for avoiding back-reflections. For the measurement of the packaged laser, lower plot in Fig. 4.14, we use a dual stage fiber optic in-line isolator (approximately 60 dB isolation), since the input to the optical spectrum analyzer (OSA) uses a mating sleeve for an open-ended fiber FC/PC connector without angle-polish. The spectra of the packaged device remain essentially unchanged, besides a small spectral shift, which we attribute to the commonly rather high thermally induced frequency shifts of InP-based DFB lasers (22 GHz / K) in combination with the fact that the temperature of the submount was not stabilized. We hence conclude that the back-reflections of our FaML

assembly do not spoil the laser spectrum, even for highly sensitive DFB devices. In our experiments, we also observed that leaving out the fiber-optic in-line isolator in the connection to the OSA lead to significantly broadened and distorted spectra due to reflections from the open fiber end. We further investigate the influence of back-reflections by conducting a separate experiment, in which we replace the isolator by a variable optical attenuator with angled physical contact (APC) connectors, see Supplementary Figs. B.7 and B.8. From this experiment, we estimate the spurious back-reflections from our FaML to be below $-44\,$dB, see Supplementary Section B.4 for details.

4.6 Discussion

3D-printed facet-attached microlenses open a path towards efficient assembly of advanced photonic systems that may combine chip-based photonic integrated circuits (PIC) and free-space micro-optical elements. The concept thus offers an attractive alternative to currently used approaches for optical chip-chip and fiber-chip connections that mainly rely on grating couplers (GC) or edge couplers (EC). Grating couplers are only available for high index-contrast platforms such as SiP and suffer from strong polarization sensitivity [142] and narrow spectral bandwidth [143]. Moreover, sophisticated designs such as bottom reflectors [144] are required to achieve very low insertion loss, and package geometries with fibers connected to the top of the chip are often unfavorable. Using EC, it is possible to achieve very low insertion loss, large spectral bandwidth, and low sensitivity to polarization [145]. However, EC require very tight alignment tolerances, often on the sub-micrometer level such that active alignment is unavoidable. This leads to slow and costly assembly processes, in particular when simultaneous coupling of multiple channels is required. In addition, proper matching of mode fields may represent a challenge, especially when connecting waveguides with vastly different refractive-index-contrasts. Recently, a highly scalable passive edge-coupling approach was demonstrated, which couples light from a ribbon fiber to a SiP chip using metamaterial suspended membrane tapers [146, 147] and

etched V-grooves on the SiP chip. Insertion losses of $0.9 \ldots 1.5$ dB were measured. However, additional process steps are required for the metamaterial under-etch, which are not generally available. Furthermore, the proposed method requires tapers of around 1 mm and V-grooves around 300 µm length and hence comes with precious space consumption on the PIC. Photonic wirebonding [33, 34] represents an alternative approach that circumvents the need for active alignment. However, the method is only suited for bridging comparatively short distances (typically < 400 µm) between devices and requires good accessibility of the facets upon fixing the chips, thereby restricting the design freedom for the assembly architectures.

Our work demonstrates that FaML can overcome these problems, enabling low-loss edge coupling with relaxed alignment tolerances over mm-scale distances. Specifically, we demonstrate low-loss FaML-based coupling interfaces for edge emitting SiP chips, featuring transverse 1 dB-alignment tolerances of ± 6 µm. The relaxed alignment tolerances open a path towards passive assembly techniques exploiting machine vision and/or simple mechanical stops and even permit re-pluggable fiber-to-chip connectors based on mass-producible injection-molded plastic parts. In comparison to aforementioned metamaterial-based suspended-membrane tapers [146, 147], our method provides similar coupling performance, while being much more flexible. Facet-attached microlenses are compatible with all photonic integration material platforms, and can be applied to vastly different multi-chip and fiber-to-chip assemblies — without any need for technologically demanding under-etching at the chip facet. Our approach further allows to insert discrete micro-optical components into the collimated beams between chip-based photonic integrated circuits, and the design of FaML based micro-optical coupling elements can be easily adapted for angled facets with low-back-reflection. We further believe that our approach is highly scalable from a fabrication point of view. Printing on facets of FA and cleaved bars of InP devices can be efficiently accomplished by working with device stacks that can be processed from the surface-normal direction of the facets. In case of chips with deep-etched optical facets, FaML can be printed on a wafer-level from a direction normal to the wafer surface, see Materials and Methods (Section 4.8). Exploiting fully automated multi-photon

lithography processes might hence open a path towards highly scalable and robust assembly processes of advanced photonic integrated systems.

4.7 Summary

We demonstrate the potential of 3D-printed facet-attached microlenses (FaML) for advanced photonic system assembly. FaML can be printed with high precision to the facets of optical components using multi-photon lithography, thereby offering the possibility to shape the emitted beams by freely designed refractive surfaces. These beams can be collimated to comparatively large diameters that are independent of the device-specific mode fields, thereby relaxing both axial and lateral alignment tolerances. This renders costly active alignment obsolete and opens the possibility to insert discrete optical elements such as optical isolators into the free-space beam paths between PIC facets. We show the viability and the versatility of the concept in a series of selected demonstrations. In a first set of experiments, we couple fiber arrays (FA) to arrays of edge-coupled silicon photonic (SiP) chips, reaching insertion losses of $1.4\,$dB per interface with a lateral $1\,$dB alignment tolerance of $\pm 6\,$µm and an angular alignment $1\,$dB tolerance of $1.1°$. To the best of our knowledge, this is the lowest loss so far demonstrated for an edge-emitting SiP waveguide interface with micron-scale alignment tolerances. We also show that the outstanding alignment tolerance of our scheme allows for reproducible coupling using a simple LEGO brick for detachable mechanical connection. In a second set of experiments, we further demonstrate free-space transmission over distances in the mm-range, using standard machine-vision techniques for alignment. In this experiment, we insert a discrete optical polarization beam splitter prism into the beam path between a single-mode fiber (SMF) array and array of edge-coupled indium-phosphide (InP) photodetectors. A third set of experiments is dedicated to interfaces between angled DFB lasers and SMF arrays. In this context, we demonstrate coupling with ultra-low back-reflection by connecting planar devices through non-planar beam paths that only comprise tilted optical surfaces. We achieve coupling losses of approximately $2\,$dB and estimate

$-44\,\text{dB}$ of spurious back reflection. Based on these exemplary demonstrations of the outstanding versatility of the FaML concept, we believe that the approach opens an attractive path towards advanced photonic system assembly that may overcome most of the current challenges.

4.8 Materials and Methods

Silicon photonic (SiP) chips: The SiP chips used in our experiments were fabricated at IMEC, Belgium (ISIPP50G platform). The test chips contain inverse-tapered edge couplers (EC), which are arranged in a loopback-configuration with a pitch of $127\,\mu\text{m}$, see Fig. 4.2. By observation with an IR microscope objective (Olympus LMPlan IR $100\times/0.80$) with a numerical aperture (NA) of 0.8, the mode-field diameter (MFD) was measured to be $2.5\,\mu\text{m}$ at the chip facet. For calculating coupling losses, we assume a waveguide loss of $0.17\,\text{dB/mm}$ and $0.08\,\text{dB/mm}$ for TE and TM-polarization, respectively. For the Loopbacks $(1, 8)$ and $(2, 7)$, see Fig.4.2, we further account for a loss of $0.3\,\text{dB}$ per waveguide crossing. These numbers are specified by IMEC's Process Design Kit (PDK), along with a polarization dependent loss (PDL) of $0.5\,\text{dB}$ for the EC.

Multi-photon lithography: The 3D-printed microlenses were fabricated from negative-tone photoresist (VanCoreA, Vanguard Automation GmbH, Karlsruhe, Germany; refractive index $n = 1.53$ at $1550\,\text{nm}$) using an in-house-built lithography system with a $63\times/1.4$ objective (Zeiss Plan-Apochromat $63\times/1.4$ Oil DIC M27), galvanometer-actuated mirrors, and a $780\,\text{nm}$ femtosecond laser (Menlo C-Fiber 780 HP, pulse width $58\,\text{fs}$). We use automate procedures techniques for detection of the height and tilt of chips and FA. For the SiP chips, we reach a lateral and vertical alignment precision [33] of the order of $100\,\text{nm}$.

Lenses are printed to the fiber arrays (FA) with the axis of the lithography beam perpendicular to the fiber facets, while the fiber cores are back-illuminated for easier detection. Similarly, the lenses on the InP components are printed with the axis of the lithography laser beam perpendicular to the chips facets, and the

geometry of the ridge waveguide structure is detected for position referencing. In contrast to this. We print the SiP lenses with the axis of the lithography perpendicular to the top surface of the chip. This allows for precise detection of marker structures on the chip surface and opens a path towards wafer-level printing of FaML to deep-etched device facets prior chip separation. When printing to the vertical device facet, the opaque chip edge blocks part of the lithography beam, thus reducing the power in the focus. This is compensated by using a position-depend dose adaptation close to the device facet.

Passive alignment and assembly process: For passive alignment and assembly we use a custom assembly machine (ficonTEC Service GmbH) that relies on industry-standard machine vision techniques, see Supplementary Section B.3 for details. The alignment is based on data from a top-view and a bottom-view camera, as well as on high-precision distance measurements using a sensor that exploits a chromatic confocal measurement principle [148]. To aid the detection of fiber arrays, we use 3D-printed markers, see Inset (i) of Fig. 4.6 and Supplementary Section B.3 for details. Once aligned, the components are fixed in place using UV glue (Optocast 3410 Gen 2, EMI Inc.). The chosen glue contains silica filling material and features low shrinkage to permit gluing gaps of variable widths up to at least 200 µm without notable displacement of the devices during curing.

Microlens simulation: For the numerical optimization of microlens surfaces, we use an in-house simulation software written in Python and running on a graphic processing unit (GPU). The software relies on the scalar wide-angle unidirectional wave-propagation method proposed in [36]. This allows for fast and realistic wave-optical modeling of micro-optical components beyond the thin-element approximation and for wave-optical assessment of alignment tolerances for both the lithography and the assembly process. Various simulated field plots are found in Supplementary Fig. B.9.

[End of paper [J2]]

5 Superconducting nanowire single-photon detector with 3D-printed free-form microlenses

This chapter reports on superconducting nanowire single-photon detectors (SNSPD) which are supplemented by free-form microlenses, resulting in a significant increase of the effective light-receiving area. It has been published in *Optics Express* [J3]. The material from the publication was adapted to comply with the layout and the structure of this thesis. Further supplementary information can be found in Appendix C.

The experiments were conceived by Artem Kuzmin, Konstantin Ilin, Michael Siegel, Christian Koos and the author. The author developed the advanced simulation and lithography tools required for precise fabrication of microlenses to the SNSPD, building upon earlier work by Matthias Blaicher. The author further performed the analytical calculations in conjunction with the optimum lens shape, with advice from Christian Koos. The layout of the SNSPD chip was done by Artem Kuzmin, supported by discussions with the author. Artem Kuzmin fabricated the SNSPD chip, based on processes developed by Konstantin Ilin in earlier work. The microlenses were designed and fabricated by the author. Philipp-Immanuel Dietrich provided the photoresist used in the experiment. The cryogenic photon count rate experiments were performed at the Institute of Micro- and Nanoelectronic Systems (IMS, KIT) by Artem Kuzmin and Emanuel Knehr. Artem Kuzmin analyzed the experimental data. All authors discussed the data. The author wrote the manuscript with support by Artem Kuzmin, Wolfgang Freude and Christian Koos.

[Beginning of paper [J3]. This article is reprinted under the terms of OSA's "Copyright Transfer and Open Access Publishing Agreement".]

Superconducting nanowire single-photon detector with 3D-printed free-form microlenses

Yilin Xu[1,2], Artem Kuzmin[3], Emanuel Knehr[3], Matthias Blaicher[1,2], Konstantin Ilin[3], Philipp-Immanuel Dietrich[1,2,4], Wolfgang Freude[1], Michael Siegel[3], and Christian Koos[1,2,4]

[1]Institute of Photonics and Quantum Electronics (IPQ), Karlsruhe Institute of Technology (KIT), 76131 Karlsruhe, Germany.

[2]Institute of Microstructure Technology (IMT), KIT, 76344 Eggenstein-Leopoldshafen, Germany.

[3]Institute of Micro- and Nanoelectronic Systems (IMS), KIT, 76187 Karlsruhe, Germany.

[4]Vanguard Automation GmbH, 76185 Karlsruhe, Germany.

We present an approach to increase the effective light-receiving area of superconducting nanowire single-photon detectors (SNSPD) by free-form microlenses. These lenses are printed *in situ* on top of the sensitive detector areas using high-resolution multi-photon lithography. We demonstrate a detector based on niobium-nitride (NbN) nanowires with a $4.5\,\mu m \times 4.5\,\mu m$ sensitive area, supplemented with a lens of 60-µm-diameter. For a plane-wave-like free-space illumination at a wavelength of $1550\,nm$, the lensed sensor has a 100-fold increased effective collection area, which leads to a strongly enhanced system detection efficiency without the need for long nanowires. Our approach can be readily applied to a wide range of sensor types. It effectively overcomes the inherent design conflict between high count rate, high timing accuracy, and high fabrication yield on the one hand and high collection efficiency through a large effective detection area on the other hand.

5.1 Introduction

Superconducting nanowire detectors [149] are key to many applications that require single-photon detection in the optical and near-infrared spectral region. Superconducting nanowire single-photon detectors (SNSPD) are fabricated from a thin superconducting film patterned to a stripe (nanowire), which is biased close to the critical current where superconductivity disappears. If any extra energy, e.g., from a photon, is absorbed by the nanowire, a so-called hot spot appears, i.e., a region with suppressed superconductivity. The nanowire then switches to the normal conducting state, and a voltage pulse from this event can be detected in an external circuit [150]. Despite the requirement of cryogenic operating temperatures, SNSPD are attractive due to their ability to cover a broad spectral range from ultra-violet (UV) to mid-infrared with a quantum efficiency of up to 98% [151]. Picosecond timing jitter [152], gigahertz photon count rates (PCR) [153], and sub-$1\,$Hz dark count rates (DCR) are further advantages. Promising results with SNSPD were already obtained in laser ranging (LiDAR) [154, 155], spectroscopy [156–158], quantum key distribution [159, 160], as well as in particle and nuclear physics [161]. Further application fields are deep-space communications [162] and integrated quantum photonics [163].

In most cases, SNSPD consist of meander-like nanowires with typical widths of the order of $100\,$nm that are fabricated on a plane substrate and illuminated from a direction normal to the substrate plane to avoid technically complex and lossy coupling of photons into integrated optical waveguides. This leads to design conflicts regarding the nanowire length: While high PCR, low DCR, and low timing jitter require a short nanowire, the system detection efficiency (SDE) crucially depends on the covered area and thus calls for a long nanowire. In addition, large-area SNSPD with long nanowires are prone to random fabrication defects, thereby reducing the process yield. SNSPD based on niobium nitride (NbN) are widely used due to rather high operating temperatures up to $5\,$K, and have been demonstrated with active areas of, e.g., $26\,\mu\text{m} \times 290\,\mu\text{m} = 7540\,\mu\text{m}^2$ and area fill factors of up to 0.28 [164]. In these devices, however, the PCR is typically limited to less than $10\,$MHz due to the high kinetic inductance of the underlying

20-mm-long nanowire. In addition, the timing accuracy of such devices degrades with increasing detector length due to the so-called geometrical jitter [165], a random delay of an electrical pulse propagating from different absorption sites along the nanowire. On the other hand, maximum PCR of $2\,$GHz have been shown in SNSPD with $500\,\mu$m-long nanowires, but the active area of these devices is usually less than $100\,\mu$m^2 [166], which leads to rather low SDE in typical applications.

In this paper we show that this design conflict can be overcome by exploiting advanced 3D laser lithography for *in situ* fabrication of large-area light-collection lenses on top of compact SNSPD with short nanowires. In our proof-of-concept experiments, we show 3D-printed free-form lenses on top of high-PCR SNSPD made from a 100-nm-wide NbN stripe. The 3D-printed lenses focus the incident light to the associated SNSPD with a lateral precision better than $100\,$nm and offer effective collection areas of more than $2000\,\mu$m^2, while keeping the nanowire length as short as $100\,\mu$m. This leads to short reset times of less than $2\,$ns, thereby enabling peak PCR of hundreds of MHz, which might be further increased to a few GHz. Our approach is general and can be transferred to extended SNSPD arrays that combine high detection efficiency with high peak PCR and high fabrication yield.

5.2 Improving detection efficiency of SNSPD by 3D-printed microlenses

The concept of 3D-printed microlenses on top of an SNSPD is illustrated in Fig. 5.1. Figure 5.1(a) shows a schematic view of a 16-pixel SNSPD array with hexagonal arrangement. The SNSPD array is combined with an associated array of 3D-printed microlenses, each of which collects incoming light from an effective collection area A_C and focuses it to a spot within the active area A_D of the corresponding SNSPD. The inset of Fig. 5.1(a) shows a magnified view of a single SNSPD, which, in our case, has an active detection area of $A_D = 4.5 \times 4.5\,\mu$m^2 into which a circle with radius r_D can be inscribed. Figure. 5.1(b) shows a

schematic cross-section through an individual lens with apex height h_0 having a rotationally symmetric lens surface that is described in cylindrical coordinates by the function $h(r)$. The lens geometry is characterized by a physical aperture with radius r_A, which denotes the distance from the optical axis at which the lens profile is clipped. Note that the radius r_C of the effective collection area $A_C = \pi r_C^2$ may be additionally limited by strong Fresnel reflection at the increasingly steep lens surface in the regions that are further away from the optical axis, i.e., $r_C \leq r_A$. The effective collection area of a certain lens is defined as the area oriented perpendicular to the direction of an incoming plane wave, which would collect the same optical power as the lens itself (see Section C.1.1 for details).

To quantify the performance of our 3D-printed lenses, we first introduce a quantitative description of the system detection efficiency (SDE), which may be improved by the increased collection area A_C of the 3D-printed microlenses. In the following, R_i denotes the rate of photons which are incident on an input aperture of the detection system. This input aperture may be defined by the end-face of an optical fiber or, in case of free-space illumination, by an optical window in the cryostat. The SDE is defined as the ratio of the average photon count rate PCR captured by the SNSPD and the photon rate R_i incident on the input aperture, $\mathrm{SDE} = \mathrm{PCR}/R_i$. We further introduce the rate R_r of photons received by the active detector area A_D and the rate R_a of photons absorbed by the detector. The system detection efficiency can then be represented as a product of the optical coupling efficiency $\mathrm{OCE} = R_r/R_i$, the absorption efficiency $\mathrm{ABS} = R_a/R_r$, and the intrinsic detection efficiency $\mathrm{IDE} = \mathrm{PCR}/R_a$, where IDE represents the fraction of absorbed photons that lead to hot spots and therefore cause observable detector pulses. The system detection efficiency can thus be written as

$$\mathrm{SDE} = \mathrm{OCE} \times \mathrm{ABS} \times \mathrm{IDE}\,, \tag{5.1a}$$

$$\mathrm{SDE} = \frac{\mathrm{PCR}}{R_i}\,, \quad \mathrm{OCE} = \frac{R_r}{R_i}\,, \quad \mathrm{ABS} = \frac{R_a}{R_r}\,, \quad \mathrm{IDE} = \frac{\mathrm{PCR}}{R_a}\,, \tag{5.1b}$$

where all the efficiencies SDE, OCE, ABS, and IDE depend on the photon energy.
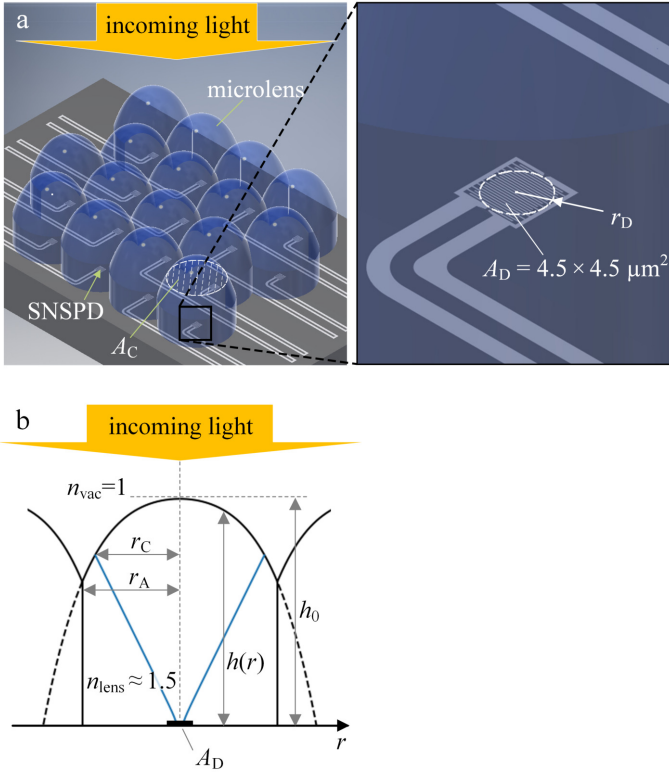
Fig. 5.1: Concept of 3D-printed microlenses on top of SNSPD. **(a)** Schematic of a 16-pixel SNSPD array with a corresponding microlens array in hexagonal arrangement. Each microlens collects incoming light from an effective collection area A_C (hatched area) and focuses it to a spot within the active area A_D of the respective SNSPD, into which a circle with radius r_D can be inscribed. **(b)** Schematic cross-section through an individual lens with apex height h_0. Plane-wave-like light incident along the surface normal of the SNSPD substrate is focused to a spot with a radius smaller than r_D, where r_D describes the radial extension of the SNSPD. The rotationally-symmetric lens surface is described in cylindrical coordinates by the function $h(r)$, where r denotes the radial coordinate. The lens surface is clipped at the radius r_A, thereby defining the lens aperture. The radius r_C of the effective collection area $A_C = \pi r_C^2$ may be additionally limited by strong Fresnel reflection at the increasingly steep lens surface in the regions that are further away from the optical axis, i.e., $r_C \leq r_A$, see Section C.1.1 for a quantitative description.

For a plane-wave-like illumination, the microlenses improve the system detection efficiency SDE foremost by effectively enlarging the detector area from A_D to A_C. Photons are thus extracted from a larger portion of the input aperture, i.e., the optical coupling efficiency OCE is improved. In the following, we compare a single lensed detector (subscript "lens") to an identical reference detector without lens (subscript "ref"). The improvement of the optical coupling efficiency OCE is then described by the effective lens gain $G_\mathrm{D} = \mathrm{OCE}_\mathrm{lens}/\mathrm{OCE}_\mathrm{ref} = A_\mathrm{C}/A_\mathrm{D}$. Assuming further that both detectors have equal absorption and intrinsic detection efficiencies, $\mathrm{ABS}_\mathrm{lens}/\mathrm{ABS}_\mathrm{ref}$ and $\mathrm{IDE}_\mathrm{lens}/\mathrm{IDE}_\mathrm{ref}$, we find according to Eq. (5.1) that G_D also describes the increase of PCR and the improvement in SDE,

$$\frac{\mathrm{SDE}_\mathrm{lens}}{\mathrm{SDE}_\mathrm{ref}} = \frac{\mathrm{PCR}_\mathrm{lens}/R_\mathrm{i}}{\mathrm{PCR}_\mathrm{ref}/R_\mathrm{i}} = \frac{\mathrm{OCE}_\mathrm{lens}}{\mathrm{OCE}_\mathrm{ref}} = G_\mathrm{D}\,, \quad G_\mathrm{D} = \frac{A_\mathrm{C}}{A_\mathrm{D}} = \frac{\pi r_\mathrm{C}^2}{A_\mathrm{D}}\,. \quad (5.2)$$

Note that fabrication defects and thermal fluctuations deteriorate the IDE in SNSPD with long nanowires [167]. Hence, the SDE of a lensed detector with collection area A_C should be higher than the one of a long-nanowire SNSPD that covers the same equivalent area — in addition to the improved timing accuracy and detector speed [166]. Note also that, in practical applications, the propagation direction of the incident light might be misaligned with respect the optical axis of the 3D-printed lens by an angle γ and that the improvement of the OCE by microlenses is subject to a fundamental tradeoff between the collection area A_C and the maximum tolerable angular misalignment γ_max. This aspect is discussed in more detail in the following section.

5.3 Design of 3D-printed microlenses

As a first step of the design procedure, we consider a plane-wave illumination and use a simple ray-optics model to design a lens surface that focusses the incoming light to a single point in the center of the SNSPD. Based on this lens design, we then use a wave-optics model to estimate the achievable spot size on the SNSPD, and we derive analytical expressions to quantify the dependence of the

effective lens gain G_D and the maximum tolerable angular misalignment γ_{max} of the illumination on the lens size. These considerations are followed by more detailed numerical simulations.

## 5.3.1 Analytic considerations

For the ray-optics lens design, we consider incident rays parallel to the optical axis of a rotationally symmetric lens, which is surrounded by vacuum (refractive index $n_{vac} = 1$), Fig. 5.2. We use cylindrical coordinates to describe the lens shape by the dependence of the height $h(r)$ on the radial coordinate r. We consider a ray impinging on the lens surface at an angle α_{vac} with respect to the local lens surface normal, see Fig. 5.2, and we denote the corresponding angle inside the lens with α_{lens}, which is connected to α_{vac} by Snell's law, $n_{lens} \sin \alpha_{lens} = n_{vac} \sin \alpha_{vac}$. We can then express the propagation angle $\theta = \alpha_{vac} - \alpha_{lens}$ of the internal ray with respect to the optical axis,

$$\theta = \alpha_{vac} - \arcsin\left(\frac{n_{vac}}{n_{lens}} \sin \alpha_{vac}\right) < \theta_{max} , \qquad (5.3)$$

where the maximum ray angle θ_{max} inside the bulk of the lens is limited by the refractive index of the lens, since α_{vac} cannot exceed $\pi/2$,

$$\theta_{max} = \frac{\pi}{2} - \arcsin\left(\frac{n_{vac}}{n_{lens}}\right) . \qquad (5.4)$$

Note that the maximum ray angle corresponds to the case of total internal reflection at the lens surface when considering a ray with reversed propagation direction from the inside of the lens to the outside. The optimum lens shape within this approximation of geometric optics is a spheroid, i.e., an ellipsoid that is rotationally symmetric with respect to the optical axis [168, 169]. The two foci S1 and S2 of the spheroid are stacked vertically on the optical axis with the SNSPD placed in the lower one, see Fig. 5.2. The ratio ξ between the major (vertical) half-axis b
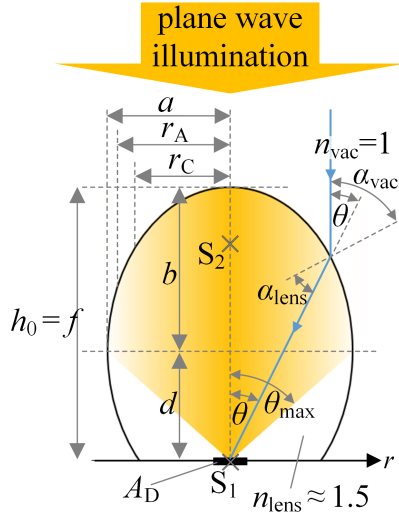
Fig. 5.2: Cross section of the idealized spheroidal lens shape, which can be derived from ray-optical considerations [168, 169]. The two foci S1 and S2 of the spheroid are stacked vertically. The SNSPD with area A_D is located in the lower focus S1, and the ratio $\xi = b/a$ between the half-axes b and a is fixed by the refractive index of the lens material, see Eq. (5.5). The apex height equals the material-sided focal distance f and is given by Eq. (5.8). An exemplary ray (blue) impinges on the lens surface at a radial position r with an angle $\alpha_\mathrm{vac}(r)$ against the local surface normal and is refracted to an angle $\alpha_\mathrm{lens}(r)$ within the lens. The associated angle to the optical axis is denoted as $\theta(r)$. The maximum possible aperture angle θ_max corresponds to the case of total internal reflection at the lens surface when considering a ray with reversed propagation direction from the inside of the lens to the outside, see Eq. (5.3).

and the minor (horizontal) half-axis a of the spheroid is related to the refractive index of the lens [168],

$$\xi = \frac{b}{a} = \frac{n_\mathrm{lens}}{\sqrt{n_\mathrm{lens}^2 - n_\mathrm{vac}^2}}\,. \tag{5.5}$$

The distance d between the center of the spheroid and any of the two foci is also referred to as the linear eccentricity

$$d = eb\,, \tag{5.6}$$

125

which depends on the eccentricity

$$e = \sqrt{1 - \left(a/b\right)^2} = \sqrt{1 - 1/\xi^2}\,. \tag{5.7}$$

The material-sided focal distance f of the spheroid lens equals the apex height h_0, see Fig. 5.2, and scales with the size of the half axes as

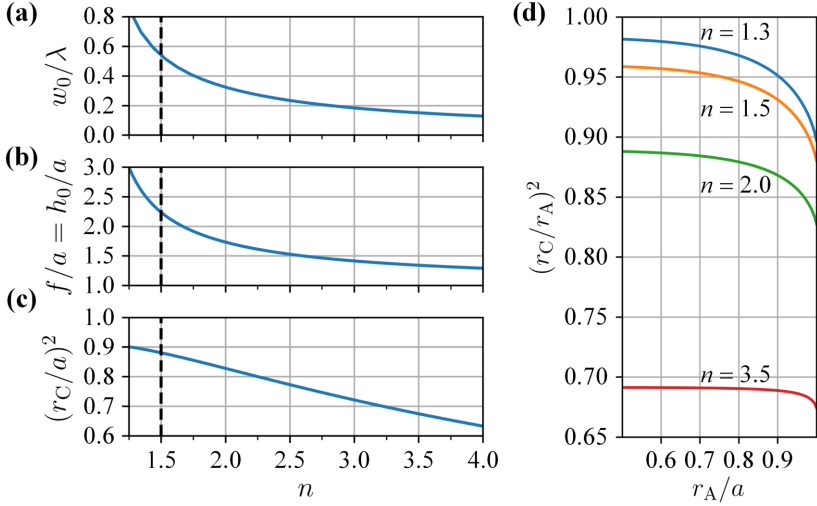$$f = h_0 = b + d = (1 + e) \times b = \xi(1 + e) \times a\,. \tag{5.8}$$

For such an spheroidal lens, we thus find that both the effective collection radius r_C (see Section C.1.1 for details), and the focal distance f are proportional to the horizontal half-axis a. By linear scaling of the lens, an arbitrarily high collection radius r_C and thus an arbitrarily high lens gain G_D can be achieved, see Eq. (5.2), provided that light is incident only along the major axis of the spheroid. In many practical applications, however, propagation direction of the incident light might be misaligned with respect the optical axis of the 3D-printed lens by an angle γ, which translates into a lateral displacement Δr. For small incidence angles γ, we find $\Delta r \approx f\gamma/n_{\text{lens}}$, i.e., the displacement Δr increases in proportion to the focal distance f, which in turn is proportional to the collection radius r_C. The maximum tolerable lateral displacement Δr_{max} is dictated by the finite detector size quantified by r_D and by the focal spot size, e.g., quantified as second-moment-radius $w_0 = 2\sigma$ of a spot with an approximately Gaussian intensity distribution. In summary, we find

$$\gamma_{\text{max}} \approx n_{\text{lens}} \frac{\Delta r_{\text{max}}}{f} \propto \frac{\Delta r_{\text{max}}}{a} \propto \frac{\Delta r_{\text{max}}}{\sqrt{A_C}}\,, \quad \Delta r_{\text{max}} \approx r_D - w_0\,. \tag{5.9}$$

Thus, increasing the effective collection radius r_C by scaling the lens size comes at the price of lowering the maximum tolerable angular misalignment γ_{max}. In practice, lenses should hence be designed as big as the required angular alignment tolerance permits. In cryogenic systems, the achievable angular alignment tolerances might typically range from $0.2°$ to $2°$, depending on the exact optomechanical implementation.

With these considerations, we can now outline a design procedure, which takes all limitations and trade-offs into account, see Fig. 5.3 and Section C.1 for details. For a given refractive index n, we first consider the achievable spot size w_0, see

Fig. 5.3: Design procedure for a lensed SNSPD. Both the effective collection radius r_C (see Section C.1.1 for details), and the focal distance f are proportional to a. The size of the lens should thus be chosen as large as the required angular alignment tolerance permits, see Eq. (5.9). **(a)** Achievable second-moment-radius $w_0 = 2\sigma$ of a spot with an approximately Gaussian intensity distribution vs. refractive index n of the lens material (see Section C.1.2 for details). The vertical dashed line indicates the typical available refractive index of $n_{\text{lens}} \approx 1.5$ for 3D-printed polymer lenses. **(b)** Ratio of focal length f and minor half axis a vs. refractive index n. For highest possible lens gain, Eq. (5.2), the half-axis a should be chosen as large as possible while still respecting the upper limit for the focal distance f, which can be estimated through Eq. (5.9) based on the known spot size w_0, see Subfigure (a), the known detector size r_D, and the desired angular alignment tolerance. **(c)** Ratio of the effective collection area πr_C^2 and the geometrical cross-section πa^2 of the lens vs. refractive index n. The ratio decreases with increasing refractive index due to strong Fresnel reflections at the lens surface. **(d)** Effect of clipping the lenses, e.g., when integrated into a two-dimensional lens pattern. For simplicity, we assume that the pitch of the detectors can essentially be chosen freely and that the lenses are clipped circularly at an aperture radius $r_A < a$. The clipping removes the outer strongly inclined regions of the lens surfaces, which are subject to higher Fresnel reflections, such that strong clipping leads to an increased effective collection efficiency of the overall lens array. We find that the value of $(r_C/r_A)^2$ does not increase significantly with decreasing r_A as soon as $r_A < 0.7 \times a$, i.e., clipping the lens surfaces to even smaller aperture radii does not pay out any more. This estimate helps to determine the number of detectors that are needed to realize a high-fill-factor array.

Fig. 5.3(a), where the vertical dashed line indicates the typical available refractive index of $n_{\text{lens}} \approx 1.5$ [170, 171], which is a typical number for polymer photoresists at wavelengths in the visible and near-infrared spectral range. This spot size is dictated by the maximum ray angle of $\theta_{\text{max}} \approx 48°$ according to Eq. (5.4) and by the fact that the Fresnel reflection at the lens surface increases with increasing distance from the optical axis. Figure 5.3(a) is based on Eq. (C.14) of Section C.1.2, which gives a more detailed description on how the spot size is extracted from the vectorial point-spread function and the associated distribution of the Poynting vector in the focal plane of the lens. Note that the consideration in Fig. 5.3(a) is independent of the absolute size of the lens. In a next step, we choose the minor half-axis a of the lens as large as possible, given the limited angular alignment tolerance. To this end, we consider the ratio of the focal distance f and the minor half-axis a, which is solely dictated by the refractive index n, see Fig. 5.3(b). The upper limit for the focal distance can be estimated through Eq. (5.8) based on the known spot size w_0, see Fig. 5.3(a), the known detector size r_{D}, and the required angular alignment tolerance as dictated by the application of the lens-equipped SNSPD. The lens gain G_{D} is finally quantified by the effective collection radius r_{C}, see Eq. (5.2), which increases in proportion to the minor half axis a of the lens and which, in addition, depends on the Fresnel reflection at the lens surface as dictated by refractive index n_{lens}, see Fig. 5.3(c). Figure 5.3(c) is based on Eqs. (C.1) and (C.2) in Section C.1.1, which account for the position-dependent Fresnel reflection at the lens surface to calculate the effective collection area A_{C} and the associated radius r_{C}.

Finally, we consider the case of an array of lensed detectors. For simplicity, we assume that the pitch of the detectors can essentially be chosen freely, thereby clipping the spheroidal lens surfaces along the perpendicular bisectors of the lines connecting the center points of neighboring detectors. This clipping removes the outer strongly inclined regions of the lens surfaces, which are subject to higher Fresnel reflections, such that strong clipping leads to an increased effective collection efficiency of the overall lens array. For a simplified calculation, we consider the case where the lens is clipped along a circular contour of radius r_{A}, centered about the optical axis, and we calculate the squared ratio of the effective

collection radius r_C and the geometrical contour radius r_A for different refractive indices, see Fig. 5.3(d). For $r_A \to a$, the value of $(r_C/r_A)^2$ corresponds to the one calculated in Fig. 5.3(c), whereas for $r_A \to 0$, it approaches the Fresnel-limited power transmission in the case of normal incidence on a plane surface. We find that the value of $(r_C/r_A)^2$ does not increase significantly with decreasing r_A as soon as $r_A < 0.7 \times a$, i.e., clipping the lens surfaces to even smaller contour radii r_A does not lead to significant additional gain in the collection efficiency of the overall array. This estimate helps to determine the number of detectors and lenses that are needed or realize a high-fill-factor array with power transmission close to the Fresnel-limited value for the case of normal incidence on a plane surface. Note that typical photoresists used for multi-photon polymerization exhibit absorption of the order $1\,\mathrm{dB/cm}$. For typical lens heights h_0 of less than $100\,\mathrm{\mu m}$, this leads to absorption losses of less than 0.2%, which can be neglected for most cases of practical interest. Note also that extended arrays of clipped lenses might also be efficiently produced by high-volume replication techniques such as nano-imprinting or hot embossing.

5.3.2 Numerical simulations

The spheroidal lens shape has been obtained in Section 5.3.1 based on simplified ray-optics considerations. For the clipped lens, however, additional side lobes of the point-spread function might occur, such that a wave-optical optimization could result in a slightly different optimum lens shape. In addition, the case of a slightly tilted illumination can only be analyzed in full using a wave-optical simulation. We therefore complement our design considerations by a numerical simulation of a specific lens design for a lensed SNSPD array. In the following, we consider a vacuum wavelength of $\lambda = 1550\,\mathrm{nm}$, a refractive index of $n_{\mathrm{lens}} = 1.53$ and an SNSPD size of $A_D = 4.5 \times 4.5\,\mathrm{\mu m^2}$, which is consistent with the devices used for the experimental demonstration described in Section 5.4. We choose lenses with an apex height $h_0 = f = 70\,\mathrm{\mu m}$. For a spheroidal lens surface, Fig. 5.2, the minor half axis of the spheroid is $a = 32.0\,\mathrm{\mu m}$, the effective collection radius amounts to $r_C = 30.0\,\mathrm{\mu m}$, and the effective lens gain is $G_D = 140$ for the unclipped lens, see

Eqs. (5.2) and (5.8) and Figs. 5.3(b) and 5.3(c). We further estimate an achievable spot size radius of $w_0 = 0.80\,\mu\mathrm{m}$, see Fig. 5.3(a). This leads to a maximum allowed lateral displacement of $\Delta r_{\mathrm{max}} = 1.45\,\mu\mathrm{m}$ for a detector size of radius $r_{\mathrm{D}} = 2.25\,\mu\mathrm{m}$, corresponding to a maximum illumination tilt of $\gamma_{\mathrm{max}} = 1.8°$, see Eq. (5.9), which can be well achieved in a fixed cryogenic setup without any means for further adjustment during the experiment.

Based on this design, we then investigate the behavior of densely packed lenses as part of an array. Naturally, arranging lenses in a gapless array requires some kind of clipping, depending on the structure of the underlying lattice. For the clipped lens, additional side lobes of the point-spread function might occur, and the spheroidal refracting surface of the lenses might not any more lead to the maximum possible concentration of incident optical power into the active area of a commonly rectangular SNSPD. To investigate this effect, we numerically optimize the refracting surfaces of clipped lenses and compare the resulting shapes and collection efficiencies to the ones of spheroidal surfaces. For the numerical optimization, we use an in-house simulation software written in Python and running on a graphic processing unit (GPU). The software uses the scalar wide-angle unidirectional wave-propagation method for step-index structures proposed in [36]. This allows for fast and realistic wave-optical modeling of micro-optical components beyond the thin-element approximation. For this method, exceptional consistency with rigorous finite-difference time-domain (FDTD) solutions of Maxwell's equations has been shown in terms of focal intensity distributions [36], while the underlying calculations are considerably faster than those associated with various wide-angle beam-propagation-methods. Note that the field computation could be further accelerated by exploiting the rotational symmetry of the problem in case the incident plane wave propagates along the optical axis [172].

For a simple implementation of the design procedure, we assume a rotationally symmetric lens with a fixed apex height of $h_0 = 70\,\mu\mathrm{m}$, see Fig. 5.1(b), and parametrize the height of the refracting surface by a polynomial $h(r) = h_0 + c_2 r^2 + c_4 r^4 + \ldots$ as a function of the lens radius r. In a first step, we further assume clipping along a circular contour $r_{\mathrm{A}} = 22.4\,\mu\mathrm{m}$, corresponding to a clipping ratio of $r_{\mathrm{A}}/a = 70\%$ for the spheroidal lens shape. According to

Table 5.1: Comparison of lenses with various shapes of the refracting surface [a]

Lens shape	Optimized as	Clipping radius $r_A = 22.4$ μm			Hexagonal array	
		c_2 (μm^{-2})	c_4 (μm^{-4})	Max. deviation to spheroid (μm)	w_0 (μm)	G_D
Clipped spheroid	—	(-0.0202)	(-7.36×10^{-6})	—	1.118	76.5
Clipped sphere	Single lens ($r_A = 22.4$ μm)	(-0.0176)	(1.16×10^{-5})	0.45	1.182	72.1
Clipped polynomial	Single lens $r_A = 22.4$ μm	-0.0193	-9.34×10^{-6}	0.12	1.120	76.1
Clipped polynomial	Hexagonal array	-0.0190	-9.10×10^{-6}	0.23	1.143	76.3

[a] All lenses have an apex height of $h_0 = 70$ μm above the substrate. The coefficients c_2 and c_4 in the third and the fourth columns refer to a parametrization of the radius-dependent height above the substrate of the form $h(r) = h_0 + c_2 r^2 + c_4 r^4 + \ldots$ For the spheroidal and the spherical shape, c_2 and c_4 refer to a polynomial surface that leads to the smallest sum of squared deviations from the respective surface within a circular aperture of radius $r_A = 22.4$ μm. The last two columns refer to the spot radius w_0 and the lens gain obtained in a hexagonal array with spacing $2r_A = 2 \times 22.4$ μm, see inset of Fig. 5.4.

Fig. 5.3(d), this choice of the clipping radius should allow for a lens array with an overall collection efficiency that is close to its theoretical optimum dictated by Fresnel losses at normal incidence. For the optimization, we consider a single free-standing lens, which is illuminated by a plane wave incident along the optical axis of the lens, and we optimize the polynomial coefficients c_k for maximum power in the detector area $A_D = 4.5 \times 4.5 \, \mu m^2$. We find that, when using only two free coefficients c_2 and c_4, the numerical optimization of the clipped lens surface leads to a rather marginal improvement of 0.1% with respect to the reference case of a clipped spheroid — the numerical values of the coefficients are specified in the third row of Table 5.1 below (clipped polynomial, optimized as single lens with $r_A = 22.4 \, \mu m$). For 3 free coefficients c_2, c_4, and c_6, this improvement increases to 0.3%. We may hence conclude that lens arrays on top of SNSPD may indeed be designed by merging simple spheroids, without the need for further numerical optimization.

In a second step, we extend the simulation to an entire hexagonal array of lens-equipped SNSPD with spacing $2r_A$, see inset of Fig. 5.4. For this array, we chose again $r_A/a = 70\%$. The white line in Fig. 5.4 indicates the shape of the underlying unclipped spheroid, and the green line refers to the contour of the previously numerically optimized lens surfaces with only two free coefficients c_2 and c_4. The two shapes hardly differ, which is consistent with the fact that they result in essentially the same performance. The colors in Fig. 5.4 refer to the electric-field magnitude which is depicted in the (x, z)-plane. The blue dashed rectangle in the inset refers to the computational area, for which we use periodic boundary conditions to mimic an infinitely extended lens array. From the simulation, we also extract the intensity distribution along the x-axis in the focal plane, both for normal and for slightly angled incidence, see Fig. 5.5(a). The solid black line refers to the simulated intensity profile obtained for the clipped lens array, and the blue line gives the profile obtained for the full unclipped spheroid, both for normal incidence. As expected, the clipping leads to a broadening of the intensity profile — the second-moment-radius of the intensity distribution of the clipped lens amounts to $w_{0,c} = 2\sigma_c = 1.1 \, \mu m$, whereas a second-moment-radius of $w_{0,nc} = 2\sigma_{nc} = 0.7 \, \mu m$ is found for the non-clipped spheroid lens. The

simulated value for the non-clipped lens is in reasonable agreement with the value $w_0 = 0.8\,\mu m$ estimated based on Fig. 5.3(a) and Section C.1.2. We attribute the slight differences mainly to the approximations related to the position-dependent Fresnel losses in both techniques. Note that even for the clipped lens, side lobes of the intensity distribution do not play a significant role. The area shaded in blue in Fig. 5.5(a) indicates the actual width of the SNSPD. We further simulate the intensity distributions for a direction of incidence that deviates from the optical
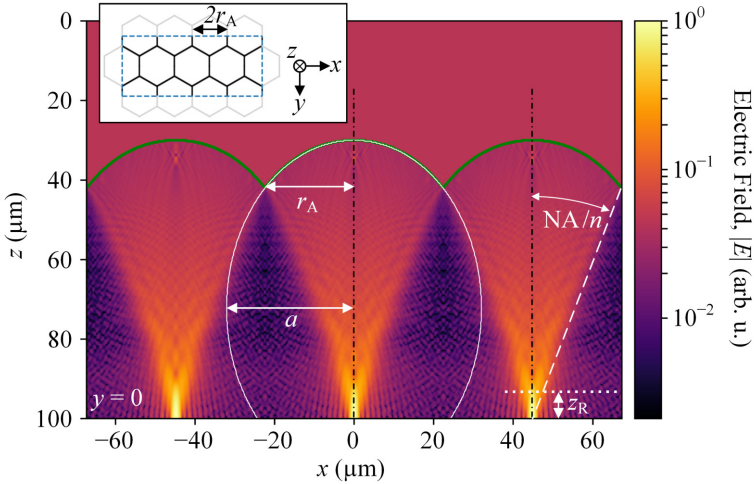
Fig. 5.4: Simulation of an arrangement of densely packed pillar-shaped microlenses with hexagonal cross-section using the wave-propagation-method [36]. Each SNSPD has a detector area of $A_D = 4.5 \times 4.5\,\mu m^2$, and the apex height of the lenses is fixed to $h_0 = 70\,\mu m$. The arrangement is illuminated by a plane wave from the top. For designing the surface shape, we first consider individual free-standing lenses with circular cross-section (clipping radius $r_A = 22.4\,\mu m$), which could be inscribed into the hexagonal pillars, see inset. We numerically optimize the lens shape such that maximum power is collected by the detector. The figure shows a cross section through the hexagonal microlens array with spacing $2r_A$. The green contour lines show an optimized polynomial lens surface with two free coefficients c_2 and c_4. For comparison, the white line shows the spheroidal surface contour with the same height (minor half-axis of ellipsoid a, $r_A/a = 70\%$, Fig. 5.3(d)). The colors refer to the electric-field magnitude. The asymptotic divergence angle $\beta = 0.37$ (corresponding to 21°) inside the lens is given by $n \sin\beta = \text{NA}$, leading to a (one-sided) depth of field of $z_{DOF} = (1.77/2)(\lambda/n)/(\text{NA}/n)^2 = 7\,\mu m$ according to [64, 65]. The blue dashed rectangle in the inset designates the computational region. We use periodic boundary conditions to mimic an infinitely extended lens array.

133
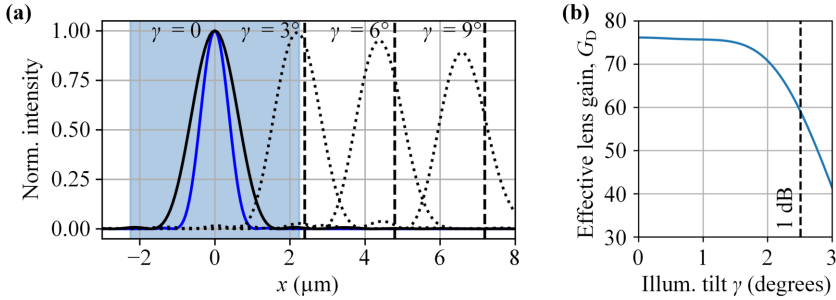
Fig. 5.5: Focal intensity distribution and expected effective lens gain for the simulation in Fig. 5.4. **(a)** Intensity distribution along the x-axis on the chip surface, both for normal (solid lines) and for slightly angled incidence (dotted lines). The solid black line refers to the normalized intensity profile obtained for the hexagonal lens array with optimized polynomial surface, and the solid blue line gives the intensity profile for a free-standing unclipped spheroid, both for normal incidence of a plane wave. The blue shaded area indicates the width of the SNSPD. The dotted curves are the normalized intensity distributions for a plane wave incident with tilt angles γ of 3°, 6°, and 9° measured towards the surface normal of the substrate. The dashed vertical lines correspond to the associated lateral offsets $\Delta r \approx f\gamma/n_{\mathrm{lens}}$ of the focal spot as estimated by geometrical optics using a focal length of $f = h_0 = 70\,\mu\mathrm{m}$. **(b)** Expected effective lens gain G_{D} as a function of the tilt angle. The dashed line indicates the 1 dB decay, which occurs at an illumination tilt angle γ of approximately 2.5°.

axis by tilt angles γ of 3°, 6°, and 9°, see dotted curves in Fig. 5.5(a). The dashed vertical lines correspond to the associated lateral offsets Δr of these intensity distributions, obtained by assuming a focal length of $f = h_0 = 70\,\mu\mathrm{m}$ and a linear relationship $\Delta r \approx f\gamma/n_{\mathrm{lens}}$. Note that this linear relationship is only valid in the limit of small angular deviations $\gamma < 5°$ and that the maximum of the intensity distribution clearly deviates from the respective dashed line for tilt angles γ of 6°, and 9°.

We further numerically calculate the effective gain G_{D} of an individual clipped lens as a function of the tilt angle, see Fig. 5.5(b). To this end, we integrate the intensity in the focal plane of the lens over the active area $A_{\mathrm{D}} = 4.5 \times 4.5\,\mu\mathrm{m}^2$ of the SNSPD, which leads to an almost constant lens gain $G_{\mathrm{D}} \approx 77$ for tilt angles $\gamma \leq 1.5°$ with a 1 dB decay at $\gamma_{\mathrm{1dB}} = 2.5°$. This result is in reasonable agreement with maximum illumination tilt of $\gamma_{\mathrm{max}} = 1.8°$ estimated for the corresponding ideal un-clipped lens. Note that the lateral extension of the dashed intensity

distributions in Fig. 5.5(b) does not change strongly with tilt angle γ. The lens array can hence be deliberately designed for reception of light from directions that slightly deviate from normal incidence by simply introducing a lateral offset between the SNSPD and the optical axis of the corresponding lens. Similarly, a single lens may be combined with multiple SNSPD that are directly adjacent to each other to increase the maximum tolerable angular misalignment or to enable angle-resolved reception of incoming signals. We finally calculate the effective fill factor η of the hexagonally arranged lensed detectors. Each lens covers a hexagonal cross-section area of $A_{\mathrm{L}} = 2\sqrt{3} \times r_{\mathrm{A}}^2$. Thus we find

$$\eta = \frac{A_{\mathrm{C}}}{A_{\mathrm{L}}} = \frac{A_{\mathrm{C}}}{A_{\mathrm{D}}} \frac{A_{\mathrm{D}}}{A_{\mathrm{L}}} = G_{\mathrm{D}} \frac{A_{\mathrm{D}}}{A_{\mathrm{L}}} \approx 77 \times \frac{A_{\mathrm{D}}}{2\sqrt{3} \times r_{\mathrm{A}}^2} \approx 89\% \,. \qquad (5.10)$$

This is more than two times higher than the best effective fill factor of $\eta = 36\%$ that was previously reported for an SNSPD array consisting of 1024 individual detectors that cover an area of $1.6\,\mathrm{mm} \times 1.6\,\mathrm{mm}$ [173]. Note that a single detector of this array has a size of $30\,\mu\mathrm{m} \times 30\,\mu\mathrm{m}$ and a nanowire length larger than $3\,\mathrm{mm}$ — much larger than the $100\,\mu\mathrm{m}$ used for the SNSPD in our experiment.

To provide an overview and a comparison of the different aspherical lens surfaces considered in this section, we summarize them in Table 5.1 together with the respective lens gain G_{D} and spot-size radius w_0, that can be expected from a lens arranged into a hexagonal array with spacing $2r_{\mathrm{A}} = 2 \times 22.4\,\mu\mathrm{m}$, see inset of Fig. 5.4. As a reference, we consider a spheroid surface that is clipped to the hexagonal contour dictated by the array, second row in Table 5.1 ("Clipped spheroid"). As a very simple alternative, we consider a spherical surface that is clipped to the same contour, third row ("Clipped sphere"). The radius of curvature of this surface is chosen to provide maximum lens gain for a clipping along a circular contour with radius $r_{\mathrm{A}} = 22.4\,\mu\mathrm{m}$. These shapes are then benchmarked against a clipped polynomial surface with two free coefficients c_2 and c_4, again optimized for best coupling under circular clipping with radius $r_{\mathrm{A}} = 22.4\,\mu\mathrm{m}$, fourth row. For comparison, we also specify the coefficients c_2 and c_4 of a polynomial surface that leads to the smallest sum of squared deviations from the spheroidal and the spherical surface within a circular aperture of radius

$r_A = 22.4\,\mu m$, indicated in parentheses in the third and the fourth columns of Table 5.1. We further validate the designs by comparison to a clipped polynomial surface, again with two free coefficients c_2 and c_4, which has been optimized for highest lens gain within the entire hexagonal array, fifth row. Interestingly, the resulting lens gain of $G_D = 76.3$ is even slightly worse than the gain $G_D = 76.5$ obtained for the simple spheroidal shape. We attribute this to the limitations of the two-coefficient polynomial in representing the ideal surface, which becomes more apparent for larger apertures. For practically relevant use cases, however, these deviations are insignificant. In the fifth column, we specify the maximum deviation of the respective surface to the ideal spheroid shape, measured parallel to the optical axis. We find that the spherical shape shows the largest deviation to the ideal spheroid shape, which ranges up to $0.45\,\mu m$. For the other considered lens shapes, the deviations are smaller, and the values for the lens gain G_D as well as the achievable spot sizes w_0 differ from the optimum spheroid only insignificantly.

5.4 Experimental demonstration

5.4.1 Device fabrication

To prove the practical viability of our approach, we fabricated a pair of SNSPD from a magnetronsputtered, 5-nm-thick niobium nitride (NbN) film on a sapphire substrate, see [167, 174] for details of the fabrication process. For the experiment, two identical $4.5\,\mu m \times 4.5\,\mu m$ detectors, designed for DC operation, were structured $150\,\mu m$ apart from each other in the center of a $3\,mm \times 3\,mm$ chip, see Fig. 5.6(a). One detector of the pair is used with a 3D-printed microlens ("lensed detector"), while the other is left blank ("reference detector"). The meandered nanowires in both detectors are $110\,nm$ wide, $105\,\mu m$ long, and cover the detector area with a fill factor of about 50%. Insets 1 and 2 of Fig. 5.6(a) show scanning electron microscope (SEM) images of the lens and the meandered SNSPD, respectively. For passivation, the nanowires are covered with a 20-nm-thick aluminum-nitride (AlN) layer to prevent oxidation, see Inset 3 of Fig. 5.6(a).

The critical temperature of the samples is $T_c = 12\,\mathrm{K}$, achieved by tuning the stoichiometry of the NbN film. Together with the patterning technique used [167], this leads to comparatively high values of the so-called switching currents I_{sw}, at which the devices switch from superconducting to normal state. For the two SNSPD used in our experiment, we find a switching current I_{sw} of $51\,\mathrm{\mu A}$ for the lensed device and of $55\,\mathrm{\mu A}$ for the device without lens. The 3D-printed microlenses were fabricated from negative-tone photoresist (VanCoreA, Vanguard Automation GmbH, $n = 1.53$ at $1550\,\mathrm{nm}$) by multi-photon lithography [2, 33, 168] using an in-house-built lithography system with a $63\times/1.4$ objective (Zeiss Plan-Apochromat $63\times/1.4$ Oil DIC M27), galvanometer-actuated mirrors and a $780\,\mathrm{nm}$ femtosecond laser (Menlo C-Fiber 780 HP, pulse width $58\,\mathrm{fs}$). We use a numerically optimized lens design based on a fourth-order polynomial $h(r) = h0 + c_2 r^2 + c_4 r^4$ which very well approximates a theoretically optimum spheroidal shape with a minor half axis of $a = 32.0\,\mathrm{\mu m}$ and a focal length of $f = 70\,\mathrm{\mu m}$ (see Section 5.3.2 for details of the design). Since our experimental validation is limited to a free-standing lens, we chose a slightly larger clipping radius of $r_A = 30\,\mathrm{\mu m}$, for which we expect a lens gain $G_D = 117$ along with a $1\,\mathrm{dB}$ decay at a tilt angle of $\gamma_{1dB} = 2.9°$.

For fully automated 3D lithography, we use markers in the direct vicinity of each detector along with techniques for detection of the chip height and tilt. This leads to a lateral and vertical alignment precision of the order of $100\,\mathrm{nm}$ [33]. Our lithography process produces approximately spheroidal voxels with axes of about $0.5\,\mathrm{\mu m} \times 0.5\,\mathrm{\mu m} \times 1.6\,\mathrm{\mu m}$, where the longest dimension is oriented along the illuminating beam axis of the lithography system. In addition, the photoresist features an isotropic linear shrinkage of less than 1%. These effects are known and can be compensated in the design, leading to an overall precision of the total structure height and consequently of the axial position of the refracting surface significantly better than $1\,\mathrm{\mu m}$. Besides that, the lens surface might be subject to shape deviations that we measure by white-light interferometry. We find that the typical deviation of actually printed surfaces from their respective theoretical shape is below $100\,\mathrm{nm}$ over the entire aperture and that the typical root-mean-square (RMS) surface roughness is of the order of $40\,\mathrm{nm}$ [2]. For
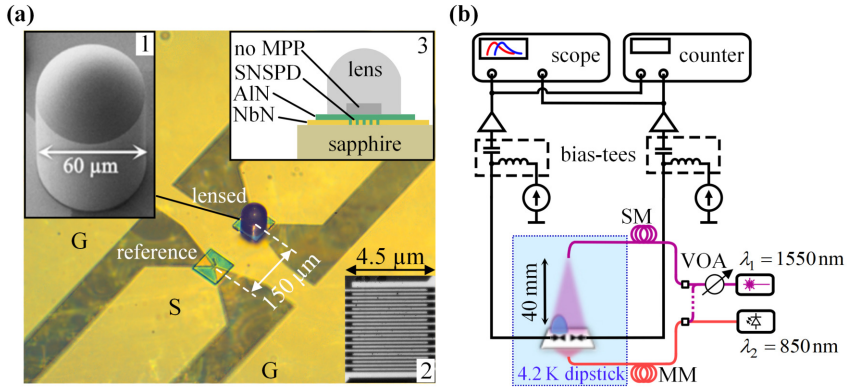
Fig. 5.6: Experimental demonstration using a pair of SNSPD on the same chip. One detector is equipped with a 3D-printed lens ("lensed detector") while the other is left blank ("reference detector"). **(a)** Optical microscope image of the dual-detector SNSPD chip. The nanowires are patterned into a 5-nm-thick NbN layer on a sapphire substrate and passivated with a 20-nm-thick layer of AlN. Detectors are biased and read out using coplanar waveguide transmission line with ground (G) and signal (S) electrodes patterned in the same NbN layer. The scanning electron microscope (SEM) images in Insets 1 and 2 show the lens and the meandered SNSPD (4.5 µm × 4.5 µm), respectively. Inset 3 shows a schematic cross section of a lensed detector. To avoid degradation of the nanowire during lens fabrication by multi-photon polymerization (MPP), a small cylindrical volume ("no MPP", dark grey) is left unexposed during the lithography. The material in this region is then solidified by UV flood exposure after development of the structure. **(b)** Experimental setup for characterizing the dual-detector SNSPD chip. The chip is mounted in a dipstick tube, and both detectors are connected to individual coaxial cables, which are used for biasing through a pair of bias tees and for reading out the electrical pulses from the SNSPD. The pulses are amplified and fed to a counter and a real-time oscilloscope. The optical test signal is derived from a fs-laser with an emission wavelength of 1550 nm, which is coupled to a subsequent variable optical attenuator (VOA). The SNSPD are front-side illuminated by the open end of a single-mode (SM) fiber that is approximately 40 mm away from the chip surface. This leads to an approximately equal plane-wave-like illumination of both devices. The backside can be illuminated via a multimode (MM) fiber with a continuous-wave laser source having a wavelength of 850 nm or with the 1550 nm femtosecond laser, see dotted line. The facet of the MM fiber is fixed 3 mm from the chip's backside. The dipstick is gradually cooled down to 4.2 K in liquid helium.

estimating the impact of these inaccuracies on the lens performance, we first separate the influence of the shape of the refracting surface from the influence of its axial position, directly linked to the lens height. The one-sided depth of field $z_{\mathrm{DOF}} = (1.77/2)(\lambda/n)/(\mathrm{NA}/n)^2$ [64, 65] of the focused beam inside the polymer lens is $z_{\mathrm{DOF}} = 7\,\mu\mathrm{m}$ for $\lambda = 1.55\,\mu\mathrm{m}$, $n = 1.53$, and $\mathrm{NA}/n = 0.37$, see horizontal dotted line in Fig. 5.4. Assuming a maximum height deviation of $1\,\mu\mathrm{m}$, we estimate a deterioration of the coupling efficiency to the SNSPD by approximately 0.2%, which is of no practical relevance. The tolerable shape deviation from the optimum spheroidal lens surface cannot be estimated as easily, because the impact on the coupling efficiency depends on the exact type of the associated aberration. For an order-of-magnitude estimate, we compare the expected shape deviations to those that occur between the ideal spheroidal surface and its spherical approximation as specified in the second and the third row of Table 5.1. For the circular aperture radius of $r_{\mathrm{A}} = 22.4\,\mu\mathrm{m}$ considered in Table 5.1, the maximum deviation between spheroidal surface and its spherical approximation amounts to $450\,\mathrm{nm}$, while the lens gain deteriorates only slightly — from an initial value of $G_{\mathrm{D,spheroid}} = 76.5$ of the ideal spheroid to $G_{\mathrm{D,sphere}} = 72.1$ for the spherical approximation, corresponding to a reduction of approximately 6%. Since the systematic shape deviations due to fabrication tolerances amount to only $100\,\mathrm{nm}$, the impact on the lens gain should be much smaller. Similarly, surface roughness with a root-mean-square deviation of $40\,\mathrm{nm}$ can be expected to have no significant influence on the overall detector performance. The lenses were written with conservative writing parameters, without any special acceleration techniques, leading to rather high printing times of approximately $20\,\mathrm{min}$ per lens. We expect that this time can be greatly reduced by optimized writing techniques. We found the printing processes to be very reliable, once the correct printing parameters have been found. In the course of our experiments, we printed multiple chips with the same set of parameters, comprising more than 30 lenses overall, which were all fully functional.

The microlenses can be operated over a broad wavelength range. For the currently used resist materials, absorption is typically negligible down to wavelengths of approximately $500\,\mathrm{nm}$ [171]. The transparency range can be extended further

down to 300 nm by using suitable photo initiators [175]. The slightly higher refractive index $n_{\text{lens}} = 1.58$ at 300 nm does not have any significant effect on the effective lens gain according to our simulations. Note that the SNSPD might experience significant degradation when directly exposed to the focused laser light of the lithography system. In such cases, we observed that the room-temperature resistance of the device increases by a factor of more than three. At the same time, the critical temperature of the superconducting transition in the nanowire is found to be reduced to $(6\ldots7)$ K, and the critical currents fall below 10 µA. To avoid this degradation we use a technique similar to the one reported in [168], leaving a small cylindrical volume with diameter of 12 µm and height of 3 µm unexposed during lithography, see Inset 1 of Fig. 5.6(a). The fabricated structures are developed in propylene-glycol-methyl-ether-acetate (PGMEA), flushed with isopropanol, and subsequently blow-dried. A post-exposure with UV light (EFOS Novacure N2000, 500 mW/cm² for 40 s) [168] solidifies the liquid resist, which is encapsulated in the vicinity of the meandered nanowire. Note that this UV dose is rather low in comparison to those reported in [171]. This might be attributed to the rather small volumes of the 3D-printed microlenses (maximum apex height of $h_0 < 100$ µm) in comparison to the 2-mm-thick layers investigated in [171] and to the fact that small curing-induced changes of the refractive index as observed in [171] are not crucial for the functionality of our structures.

5.4.2 Experimental setup

The experimental setup for characterizing the fabricated pair of SNSPD is shown in Fig. 5.6(b). The detectors are directly connected to individual 50 Ω coplanar on-chip transmission lines for readout and biasing, see Fig. 5.6(a). For introducing the sample into the cryostat, the chip is attached to a submount comprising an adapter plate for two coaxial cables. The assembly is inserted into a vacuum-tight dipstick tube with helium (He) contact gas at a pressure of 10 mbar at 300 K. The dipstick is gradually immersed in a liquid-⁴He transport dewar and reaches 4.2 K within approximately 30 min. Similar to [168, 176, 177], the printed lenses proved to be stable during repeated cool down/warm-up cycles in a temperature range from

300 K down to 4.2 K — we performed around 10 cycles without observing any lens detachment or peeling-off. For testing, light is supplied to the device by a pair of fibers inside the dipstick tube and emitted towards the front and the back surface of the chip, see Fig. 5.6(b). For front-side illumination, we use a standard single-mode (SM) fiber (Thorlabs SMF-28-J9, Hytrel jacket with 900-µm-diameter), which is fed by a pulsed femtosecond laser emitting at a wavelength of 1550 nm with a repetition rate $f_{\text{rep}} = 100$ MHz and a pulse duration of approximately 150 fs. The fiber ends about 40 mm above the center of the chip, which leads to an approximately equal plane-wave-like illumination of both SNSPD that are spaced by only 150 µm with a lens of 60 µm diameter on top of one of the devices. The backside of the chip can be illuminated via a multimode (MM) fiber using either the 1550 nm femtosecond laser, see dotted purple line in Fig. 5.6(b), or a continuous-wave laser with an emission wavelength of 850 nm, solid red line. The facet of the MM fiber is fixed 3 mm from the chip's backside. A DC bias is applied to the SNSPD through coaxial cables using a pair of bias-tees. Voltage pulses from the detectors are transmitted through the RF branches of the bias-tees, amplified by room-temperature amplifiers (MITEQ AFS4), and finally detected by a real-time oscilloscope (Keysight Infiniium, 33 GHz acquisition bandwidth) and a pulse counter (SRS SR620). Using the real-time oscilloscope, a reset time of both detectors of $t_{\text{res}} \approx 2$ ns is measured from the 90% to 10% fall times. In this measurement, we evaluated 10 000 pulses and averaged the individual fall times. The reset time is smaller than the repetition period of the fs-laser, such that no detrimental impact on the pulse counting rate is to be expected.

5.4.3 Count-rate measurements

We measure the photon count rates PCR_{lens} and PCR_{ref} of the lensed and the reference detector at several average incident optical powers of the femtosecond laser. To extract the lens gain G_{D}, we need to assume equal absorption efficiencies ABS and intrinsic detection efficiencies IDE for both detectors, see prerequisites of Eq. (5.2). Because the detectors are made from the same film, have the same geometry and orientation of the nanowires, and are placed close to each other, it is

safe to assume equal ABS. Regarding intrinsic detection efficiency IDE, we have to account for its dependence $\text{IDE}(\lambda, I_b/I_{sw})$ on both the wavelength λ and the relative bias current I_b/I_{sw} (see Appendix C.2 for an exemplary behavior of similar detectors). To experimentally adjust for similar intrinsic detection efficiencies IDE, we first measure the dependencies of the pulse count rate $\text{CR}(I_b/I_{sw})$ on the relative bias current for both detectors under pulsed back-side illumination with a wavelength of $1550\,\text{nm}$, see Fig. 5.7(a). We find that both devices exhibit nearly the same behavior such that operating them at the same relative bias current I_b/I_{sw} leads to the same IDE. In our measurement, we found similar absolute values of the count rates CR, which means that both devices are subject to the same flux of incoming photons and should hence feature the same rate R_a of absorbed photons. We collectively fit the measured data points of both detectors with a theoretical model function that is adapted from Eqs. (8) and (9) in [178],

$$\text{PCR}(I_b/I_{sw}) = R_a \times \text{IDE}(I_b/I_{sw}) = \frac{R_a}{2}\,\text{erfc}\left[q\left(1 - \frac{I_b/I_{sw}}{I_{0.5}/I_{sw}}\right)\right] . \quad (5.11)$$

In this relation, erfc denotes the complementary error function, and R_a is the rate of absorbed photons. $I_{0.5}$ refers to the so-called inflection current at which the IDE amounts to 50%, and q is a dimensionless parameter. Assuming identical rates R_a of absorbed photons and identical parameters $I_{0.5}$, I_{sw} and q for both devices, the best fit of the measured PCR is obtained for $q = 10.5$, $I_{0.5}/I_{sw} = 1.063$ and $R_a = 2.16 \times 10^5\,\text{s}^{-1}$. From the plot in Fig. 5.7(a), we find that the PCR does not reach a plateau within the range of usable bias currents $I_b < I_{sw}$. This indicates that the device is operated in its non-saturated regime [113] with IDE $\ll 1$, as expected for NbN SNSPD at $4\,\text{K}$ [179]. To further support the notion that identical relative bias currents I_b/I_{sw} lead to similar IDE for both detectors, we illuminate the devices from the backside with alternating wavelengths $\lambda_1 = 850\,\text{nm}$ and $\lambda_2 = 1550\,\text{nm}$ and compare the associated PCR (see Appendix C.2 for details).

For the lens gain measurement with frontside illumination, Fig. 5.7b, we operate the detectors at a fixed relative bias $I_b/I_{sw} \gg 0.95$ and sweep the incident optical power. Sweeping the optical power rather than the bias current allows to isolate
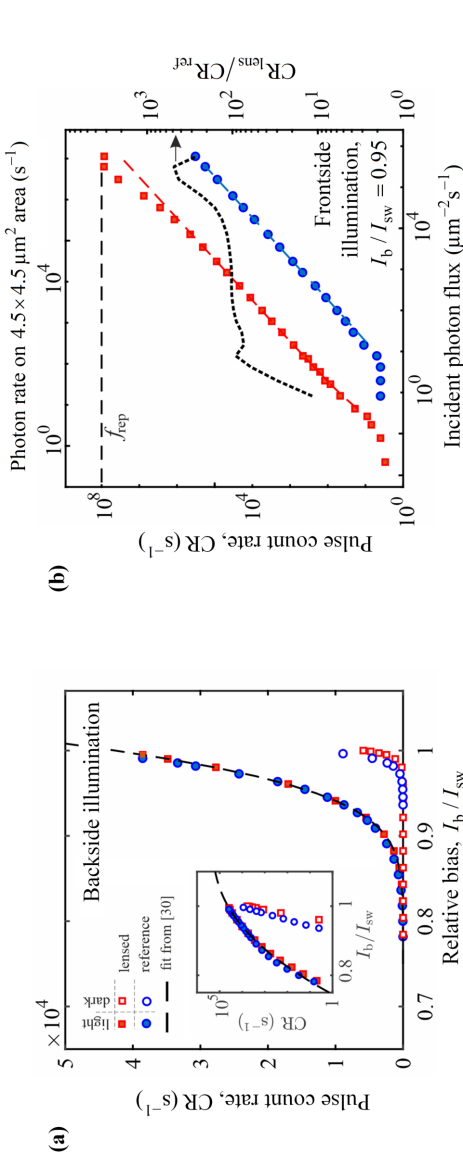
Fig. 5.7: Experimental results for the dual SNSPD chip with lensed detector ($\blacksquare$, $\square$) and with reference detector ($\bullet$, $\circ$), illuminated with light at a wavelength of 1550 nm. **(a)** Dependence of pulse count rates (CR) on the relative bias current I_b/I_{sw}. The closed markers ($\blacksquare$, $\bullet$) show the data together with a fit (– – –) according to Eq. (5.11) [178], when illuminating the detectors from the back side. The measurements are taken at an estimated rate of approximately 4.8×10^5 photons per second that are incident on the $4.5\,\mu\text{m} \times 4.5\,\mu\text{m}$ area covered by the meandered nanowire of the SNSPD. The open markers ($\square$, $\circ$) show the dark count rates (DCR), measured with a metal cap on the FC/APC connector of the vacuum feedthrough to block any stray optical photons. The DCR are negligible for bias currents $I_b < 0.98\,I_{sw}$. The CR are plotted on a logarithmic scale in the inset. **(b)** Double-logarithmic plot of the pulse count rate CR for frontside illumination. The lower horizontal axis indicates the incident photon flux, which may be translated into a rate of photons incident on the reference detector with an active area of $4.5\,\mu\text{m} \times 4.5\,\mu\text{m}$, see upper horizontal axis. For the lensed detector, the rate of captured photons is increased according to the lens gain. The dashed lines are fits of the form $\text{PCR} = c_1 P_{opt}$ with parameter c_1 resulting from a fit to the central portion of the curves. At high photon rates, the CR dependence of the lensed SNSPD is super-linear, which might be attributed to the multi-photon bolometric regime (MBR) [181]. The horizontal dashed line shows the maximum CR dictated by the repetition rate f_{rep} of the femtosecond laser. Right-hand axis: Ratio $\text{CR}_{lens}/\text{CR}_{ref}$ of measured pulse count rate CR. At the plateau in the single-photon regime, we find an effective lens gain $G_D \approx 100$, which is in reasonable agreement with a simulated value of $G_D = 117$.

143

the effect of the lens from potential distortions of the measurement results due to bias-dependent non-uniformities of the detection efficiency along the tightly bent meandered nanowires, which may be subject to current-crowding effects at low bias currents [180]. The relative biases $I_b/I_{sw} \gg 0.95$ were chosen to ensure stable operation without excessive impairments by dark counts.

To determine the incoming photon flux in the frontside illumination experiment, we first measure the optical power in the SMF at the input to the dipstick. Accounting for the optical losses of the subsequent fiber assembly, we can then estimate the optical power radiated towards the detector chip and the optical intensity on the chip surface. To this end, we assume a diverging Gaussian beam having its waist at the output facet of the illuminating SMF, $40\,\text{mm}$ away from the chip surface. This intensity is then translated into the incident photon flux, see horizontal axis at the bottom of Fig. 5.7(b). We also calculate the rate of photons that are incident on the $4.5\,\mu\text{m} \times 4.5\,\mu\text{m}$ area of the reference detector, see upper horizontal axis of Fig. 5.7(b). Note that we did not directly measure the photon flux associated with the backside illumination experiment in Fig. 5.7(a), since the losses of the underlying multi-mode fiber (MMF) assembly were not exactly known. We may, however, estimate the flux associated with Fig. 5.7(a) from the data shown in Fig. 5.7(b). Specifically, we find a measured pulse count rate CR of $1.3 \times 10^4\,\text{s}^{-1}$ at a bias of $I_b = 0.95\,I_{sw}$ in the back-side illumination experiment, Fig. 5.7(a). According to Fig. 5.7(b), this pulse count rate can be associated with a photon rate of 4.8×10^5 photons per second, incident on the $4.5\,\mu\text{m} \times 4.5\,\mu\text{m}$ area of the reference detector.

To evaluate the lens gain, we need to check whether the detectors operate in the single-photon regime. At the input aperture of the detection system, the laser pulses have an average power P_{opt}, corresponding to an average number of $m = P_{opt}/(f_{rep}\hbar\omega)$ photons per impulse, where $\hbar$ is the reduced Planck's constant and ω is the angular frequency of the light. For each laser pulse, the

probability to observe a voltage pulse originating from n absorbed photons can be estimated from Mandel's formula [182] for light with Poisson statistics,

$$p_m(n) = \frac{(\text{SDE} \times m)^n}{n!} e^{-\text{SDE} \times m} . \tag{5.12}$$

The total photon detection probability $p_{m,\text{tot}}$, i.e, the probability to detect at least one photon per impulse, can then be expressed and approximated for the case of very high and very low average photon numbers m,

$$p_{m,\text{tot}} = \sum_{n=1}^{\infty} p_m(n) \approx \begin{cases} \text{SDE} \times m \approx p_m(1) & \text{for SDE} \times m \ll 1 \\ 1 & \text{for SDE} \times m \gg 1 \end{cases} . \tag{5.13}$$

For small average detected photon numbers $\text{SDE} \times m \ll 1$, the detection probability $p_{m,\text{tot}}$ is approximately equal to the probability $p_m(1)$ to detect exactly one photon and approximately equal to the detected average number of photons per impulse. In this case, the photon count rate (PCR) is approximately equal to the observed count rate (CR) of voltage pulses. For large detected average photon numbers, the detection probability approaches unity, and the CR of the voltage pulses approaches the repetition rate f_{rep} of the laser. The measured average count rate of voltage pulses depends on the detection probability $p_{m,\text{tot}}$ and on the repetition frequency of the laser pulses,

$$\text{CR} = p_{m,\text{tot}} f_{\text{rep}} . \tag{5.14}$$

Figure 5.7(b) shows the measured average CR as a function of the incident photon rate for both the lensed (■) and for the reference detector (●). Obviously, the average count rate CR of voltage pulses cannot exceed the laser repetition rate f_{rep}, indicated by a horizontal dashed line. Except for the case of the lensed detector and the highest optical powers, even $\text{CR} \ll f_{\text{rep}}$ holds, and thus the case $\text{SDE} \times m \ll 1$ in Eq. (5.13) applies. In this case, the linear relation between $p_{m,\text{tot}}$ and m from Eq. (5.13) is indeed seen in Fig. 5.7(b) as a linear dependence of CR on the incident photon rate, indicated by a line with unity slope in the

double-logarithmic plot over most of the measurement range. For the chosen relative biases of $I_\mathrm{b}/I_\mathrm{sw} \approx 0.95$ we find a dark count rate for both detectors of $\mathrm{DCR} \approx 5\,\mathrm{s}^{-1}$. This leads to the deviation from the linear dependence at low incident photon rates. For the lensed detector, a super-linear dependence is observed at high incident photon rates, before the pulse count rate (CR) finally approaches the repetition rate f_rep of the laser. We attribute this behavior to the multi-photon bolometric regime (MBR) [181], which is caused by simultaneous absorption of multiple photons within a region comparable to the mean hot-spot size of the nanowire. These multi-photon-generated hot-spots have a much higher probability of switching the SNSPD from the superconducting to the normal state than their single-photon-generated counterparts, thereby leading to a higher intrinsic detection efficiency IDE and thus a higher SDE in Eq. (5.12). As expected, multi-photon bolometric events are more likely to happen for the lensed device because of the increased optical intensity, whereas they are not observed for the reference detector. In addition, we display the ratio $\mathrm{CR}_\mathrm{lens}/\mathrm{CR}_\mathrm{ref}$ in Fig. 5.7(b), see axis on the right-hand side. In the single-photon regime, i.e., for medium optical input powers, where neither the DCR nor the MBR plays a role, this ratio exhibits a plateau, which corresponds to the effective lens gain G_D. The obtained value $G_\mathrm{D} \approx 100$ is in reasonable agreement with the simulated value of $G_\mathrm{D} = 117$.

5.5   Discussion

We have demonstrated that SNSPD with 3D-printed light-collection lenses can overcome the design conflict between large collection area and short nanowire length. This applies not only to illumination through free-space plane waves, but also to coupling of SNSPD to optical fibers. Specifically, 3D-printed lenses allow to reduce the spot size of the focused light to a second-moment spot radius of $w_0 \approx 0.5\lambda$. At a wavelength of $\lambda = 1.55\,\mu\mathrm{m}$, it is hence possible to reduce the detector area to approximately $2\,\mu\mathrm{m} \times 2\,\mu\mathrm{m}$, when disregarding any angular alignment tolerance. This area could be covered with a fill factor of $\mathrm{FF} = 50\%$

by using a nanowire with a typical width of $0.1\,\mu m$ and a length of only $20\,\mu m$. This is much shorter than the nanowire length of $1.7\,mm$ used in a previous demonstration of a fiber-coupled SNSPD [183] in which the detector area was $15\,\mu m \times 15\,\mu m$, slightly bigger than the size of a SMF core with a typical diameter of $10\,\mu m$. Nanowires as short as $20\,\mu m$ allow for even shorter reset times than experimentally demonstrated in this work, enabling maximum photon count rates in the GHz range [153]. Our lens design considerations show that, in case of illumination by free-space plane waves, numerically optimized surfaces do not offer a significant advantage over idealized spheroid surfaces, even for clipped lenses that arrange in densely packed hexagonal arrays. The shape of the refracting surfaces can be simply derived from an analytic representation of a spheroid.

Moreover, when it comes to using SNSPD as part of an optical assembly, 3D-printed lenses can greatly relax the associated alignment accuracy requirements, which is particularly important for cryogenic systems, where mechanical stress during cool-down can lead to significant misalignment. In particular, 3D-printed lenses can help to greatly simplify the coupling of SNSPD to single-mode fibers (SMF), as used in many experiments. To this end, lenses printed both on the SNSPD and on the fiber facets allow to enlarge the diameter of the free-space beam and thus to increase the resilience with respect to translational movements of the components [2, 176, 177]. Lenses printed to the facets of SMF to facilitate coupling have previously been demonstrated in a series of experiments [2, 46, J6, 176, 177, 184, 185]. Regarding multi-channel detectors, 3D-printed lenses further offer the possibility to interface on-chip SNSPD arrays to arrays of optical fibers, which are commercially available with standard pitches of, e.g., $127\,\mu m$ or $250\,\mu m$. This leads to greatly improved detector performance and to simplified assembly processes compared to conventional approaches that rely on mounting of optical fibers by means of dedicated micromachined alignment structures [186, 187]. Note that 3D-printed structures can also be used for efficient coupling of light into on-chip waveguides [2, 33, 34, 79], which can then be equipped with SNSPD [153, 188–190].

5.6 Summary

We have demonstrated a new approach that exploits 3D-printed microlenses to increase the effective collection area of superconducting nanowire single-photon detectors (SNSPD) while keeping the nanowire short, thereby overcoming a fundamental design conflict of such devices. In a proof-of-concept experiment, we show that, for a plane-wave-like illumination at a wavelength of $1550\,\mathrm{nm}$, a lens of $60\,\mathrm{\mu m}$ diameter can provide a 100-fold increase of the effective area of a niobium nitrate (NbN) SNSPD with physical area of $4.5 \times 4.5\,\mathrm{\mu m}^2$. Since the length of the nanowire can remain small, its maximum achievable count rate is high and its geometrical jitter stays low. In addition, under the constraints of realistically achievable film homogeneity and defect density, SNSPD with small active detection areas offer higher fabrication yield. Our approach enables simplified fabrication of extended SNSPD arrays that feature unprecedented effective fill factors while offering high detection efficiency, high photon count rate (PCR), and high fabrication yield.

[End of paper [J3]]

6 Summary and Outlook

Scalable optical packaging and assembly of photonic integrated systems still represents a substantial obstacle to the widspread use of powerful photonic integrated circuits (PIC) in a broad range of applications. Within this thesis, this technology gap is addressed by demonstrating hybrid multi-chip assemblies and fiber-chip connections that exploit 3D-printed coupling structures such as photonic wire bonds (PWB) and facet-attached microlenses (FaML). A detailed summary and outlook is given for each individual topic and application that is addressed within this thesis.

Hybrid external-cavity lasers

A new class of hybrid external-cavity laser (ECL) is demonstrated that relies on a PWB to connect an InP gain element to an external feedback circuit on a silicon photonic (SiP) chip. A proof-of-concept device offers a tuning range of more than $50\,\text{nm}$, a side mode suppression ratio (SMSR) above $40\,\text{dB}$, and an intrinsic linewidth of $105\,\text{kHz}$.

Future devices may utilize external feedback circuits on a silicon nitride platform to obtain even better performance. This particularly simple and powerful laser integration technology may open a series of novel applications that rely on highly frequency-agile chip-scale light sources. At the time of writing, swept-source optical coherence tomography (OCT) using an integrated ECL is being studied as a potential application in preliminary experiments [C2]. Another currently studied potential application uses an ECL as pump source for Kerr frequency combs [C3].

Optical packaging using 3D-printed facet-attached microlenses

Using FaML, an array of eight single-mode fibers (SMF) is connected to a SiP chip with an average loss of 1.44 dB per connection. A 1 dB tolerance of $6\,\mu m$ and $1.1°$ is achieved for radial and angular misalignment, respectively. To the best of our knowledge, this is the lowest loss demonstrated for an edge-emitting SiP waveguide interface with micron-scale alignment tolerances. Based on these lenses, we further demonstrate the first pluggable connection between an SMF and an edge-coupled SiP waveguide, leading to coupling losses of only (1.9 ± 0.5) dB. Machine vision assisted passive alignment requires that FaML-equipped chips emit precisely and consistently into the direction expected from the chip geometry and measurement of the chip orientation within the assembly machine. To this end, the underlying processes for printing of FaML are thoroughly optimized. Automated alignment procedures are developed on an assembly machine similar to ones used by industrial manufacturers. A passively aligned assembly demonstrates that no excess losses occur compared to active alignment, within a measurement uncertainty of $\pm 3\%$. The microlens-based free-space coupling distance is extended into the millimeter range, allowing the insertion of an additional discrete optical component into the path of the collimated free-space beam. An exemplary assembly including a polarization beam splitter prism is presented. Alignment tolerant coupling of arrays of backreflection-sensitive angled-facet semiconductor lasers is demonstrated using a novel FaML arrangement. The concept is demonstrated by a fiber-coupled laser module, within which a bar of angled-facet InP distributed feedback (DFB) lasers is connected to an SMF array. The novel facet-attached 3D-printed coupling element consists of a special combination of microlenses and prisms and offers average coupling losses of 2 dB along with a return loss of 44 dB. The performance is comparable to advanced lensed fibers with anti-reflection (AR) coating, while offering much larger alignment tolerances. The printed structures are found to neither spoil the laser spectrum, nor to modify the threshold current.

Facet-attached microlenses (FaML) have been proven to be very potent for optical packaging. Depending on the package requirements, multiple lens surfaces might be required. However, no compatible anti-reflective (AR) coating technology has

been found. Future research should therefore specifically target this important aspect. One intriguing idea is the possibility of realizing 3D-printed AR-coatings by cascaded printing steps with photoresists of different refractive index. Furthermore, large-scale industrial usage of FaML would ideally require printing times which are orders of magnitudes faster than current processes, while not sacrificing the high level of alignment accuracy and shape fidelity. Despite the evolving printing technologies, this remains a significant challenge. A combination of 3D-printed refractive and diffractive elements in conjunction with novel optimization methods might further reduce the net volume of printed coupling structures.

3D-printed coupling structures for novel quantum applications

The concept of 3D-printed coupling structures has been successfully extended to cryogenic applications. Free-form microlenses are printed on top of the sensitive areas of superconducting nanowire single-photon detectors (SNSPD) to increase the effective light-receiving area. Operation is demonstrated at a temperature of $4\,\mathrm{K}$. Using a detector with $4.5\,\mathrm{\mu m} \times 4.5\,\mathrm{\mu m}$ sensitive area and a lens of $60\,\mathrm{\mu m}$ diameter, a 100-fold increased effective collection area is achieved for a plane-wave-like free-space illumination. This represents the first demonstration of 3D-printed microlenses that supplement SNSPD.

Compact multi-chip modules with low thermal mass are of particular interest for the emerging field of integrated quantum optics, and the viability of PWB under cryogenic conditions is therefore an interesting topic for further studies. A preliminary demonstration of fiber-coupled SNSPD has already been made in the framework of this thesis [191, C4]. However, the assembly uses thick and mechanically stable but strongly multimoded PWB. A suitable cladding technique which enables single-mode operation under cryogenic conditions still needs to be developed.

Mode-field characterization techniques

Finally, another topic for future research is the improvement of microscopy-based mode-field characterization techniques. A fast and reliable process chain is envisioned, where printed microlenses would meet the design goals after the very first design and printing iteration. Within this thesis, the scalar micro-optical design tools based on the wave propagation method has therefore been supplemented with the idea of a phase-resolved mode field measurement technique. The proof-of-principle study, however, only analyzed comparably big mode fields so far, with a size in the order of the mode-field diameter (MFD) of a single-mode fiber. For extending the method to MFD below $3\,\mu m$, various additional aspects need to be considered. At a distance larger than a few wavelengths, the MFD is related to longitudinally propagating waves inside the medium into which the device facet is embedded. The approximative impact of such an effect together with a limited numerical aperture (NA) of the observing microscope objective has been analyzed within this thesis. This analysis can be used for an estimation of relevant MFD from observed values. However, a proper inclusion of the impact of the microscope within the phase-resolved mode field measurement technique requires further studies. For observation of laser emission, a coherent image is formed based on the convolution of the microscope's amplitude point-spread function with the mode field. The correct coherent deconvolution requires knowledge of the phase distribution of the mode field under observation. However, a phase retrieval algorithm based on observed intensities is inherently inaccurate, if no deconvolution technique is applied beforehand. Phase retrieval and deconvolution must therefore be considered in a joint algorithm and cannot be separated. Typical semiconductor laser emission is furthermore polarized. The polarization dependent shape of the PSF of a high numerical aperture objective [62] thus needs to be considered. Finally, diffraction of linearly polarized light from a tiny circular aperture does not lead to an isotropic radiation when considering the vectorial nature of light [99]. A correct modeling of the last aspect is obviously beyond the capabilities of fast scalar methods, but it might be nevertheless possible to find computationally inexpensive corrections for corresponding lens designs.

Appendices

A Hybrid external-cavity lasers

This chapter has been published as Supplementary Information of [J1]. The material from the publication has been adapted to comply with the layout and the structure of this thesis.

[Beginning of Supplementary Information of [J1]]

A.1 Experimental methods for RSOA characterization and bond loss estimation

To measure the small-signal gain and the saturation output power of the RSOA, we launch light to the device and measure the amplified signal using an AR-coated lensed single-mode fiber (SMF), see Inset of Fig. 3.2(a) of the main manuscript. To determine the coupling loss between the on-chip RSOA waveguide and the lensed SMF, we perform a two-step reference measurement: First, we operate the RSOA without the fiber coupled to it and use an integrating sphere (IS) to measure the overall emitted ASE power as a function of injection current, see Fig. A.1(a). Next, the RSOA is coupled to the lensed SMF, and the position of the lensed SMF is left untouched for the remainder of the measurements. The fiber-coupled ASE power is measured with the same integrating sphere, Fig. A.1(b). From this measurement, we extract the current-dependent ratio of the power $P_{\text{ASE,SMF}}$ captured by the lensed SMF and the overall ASE power $P_{\text{ASE,tot}}$ emitted by the RSOA and measured by the integrating sphere, see Fig. A.1(c). At low currents, this ratio is extremely low, since spontaneous emission occurs into many transverse modes, which are all captured by the IS, whereas only the fundamental
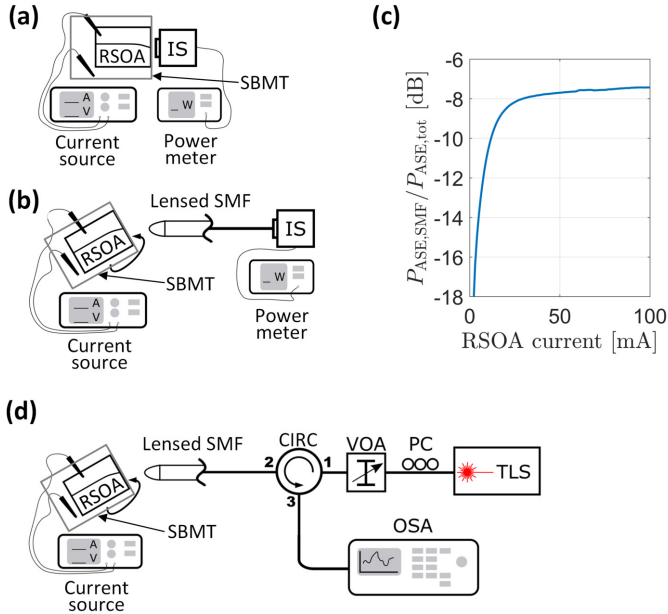
Fig. A.1: Experimental setups for RSOA characterization. Abbreviations: SBMT – Submount; CIRC – Optical circulator; IS – Integrating sphere, SMF – Single-mode fiber, TLS – Tunable laser source (Ando AQ4321D), VOA – Variable optical attenuator, OSA – Optical spectrum analyzer (Ando AQ6317B). **(a)** Reference measurement of the overall ASE power $P_{\mathrm{ASE,tot}}$ as function of the drive current. The ASE is captured by an integrating sphere (IS). **(b)** Measurement of the current-dependent ASE power $P_{\mathrm{ASE,SMF}}$ coupled to a lensed single-mode fiber (SMF). **(c)** Current-dependent ratio $P_{\mathrm{ASE,SMF}}/P_{\mathrm{ASE,tot}}$ of the power captured by the lensed SMF and the overall ASE power emitted by the RSOA. In the high-current limit, this ratio converges to the coupling loss between the fundamental quasi-TE mode of the RSOA waveguide and the horizontally polarized fundamental mode of the lensed SMF. **(d)** Measurement setup for small-signal gain, saturation output power and ASE spectrum. A tunable laser source (TLS) and an optical circulator are used to launch test signals to the RSOA and to extract the amplified output signals.

quasi-TE and quasi-TM mode is captured by the lensed SMF. With increasing current, the fundamental quasi-TE mode of the RSOA waveguide will experience stronger amplification and thus increasingly dominate the overall emitted ASE power. The ratio $P_{\text{ASE,SMF}}/P_{\text{ASE,tot}}$ thus converges asymptotically to the power-transmission factor $\eta_{\text{RSOA,SMF}}$ for coupling of light between the fundamental quasi-TE mode of the RSOA and the horizontally polarized fundamental mode of the lensed SMF. In our experiment, this fiber-chip coupling loss amounts to $-10 \log_{10} \eta_{\text{RSOA,SMF}} = 7.4$ dB. Note that this rather high loss is caused by the fact that we intentionally operated the SMF with a working distance larger than the specified one to reduce unwanted spurious back-reflections into the RSOA. Note also that for drive currents of $I = 5$ mA or higher, most of the ASE emitted by the bare RSOA is horizontally polarized and the measured ASE power can hence be attributed to the TE-polarized waveguide modes, see Fig. A.2(a).

With the coupling loss at hand, we can now determine the RSOA gain. To this end, we launch a test signal through the SMF, extract the output signal via a circulator (CIRC), and estimate the incoming and the outgoing on-chip power in the quasi-TE mode of the RSOA, see Fig. A.1(d) for the corresponding measurement setup. From our measurements, we find a small-signal on-chip gain of 23 dB along with an on-chip saturation output power of 12.5 dBm for a wavelength of $\lambda = 1550$ nm and a drive current of 100 mA, see Fig. 3.2 of the main manuscript.

To estimate the insertion loss of the photonic wire bond, we again use the fiber-coupled ASE power $P_{\text{ASE,SMF}}$ and compare it to the ASE power $P_{\text{ASE,SiP}}$ in the on-chip silicon photonic waveguide that is directly connected to the photonic wire bond. To extract the ASE power $P_{\text{ASE,SiP}}$ in the on-chip waveguide, we operate the assembled module, see Fig.3.1(b) in the main manuscript, with the rings R1 and R2 detuned to one another to avoid feedback into the RSOA. We then measure the ASE spectra through GC 4 and calculate the corresponding power levels $P_{\text{ASE,SiP}}$ in the SiP waveguide directly connected to the PWB by taking into account the wavelength-dependent loss of GC 4 and of the MMI as well as the 0.5 dB of wavelength-independent on-chip propagation loss in the 2.5 mm-long waveguide between the PWB and the MMI. For this analysis, we only consider the ASE power emitted into an approximately 0.8 nm-wide band centered at 1550 nm,
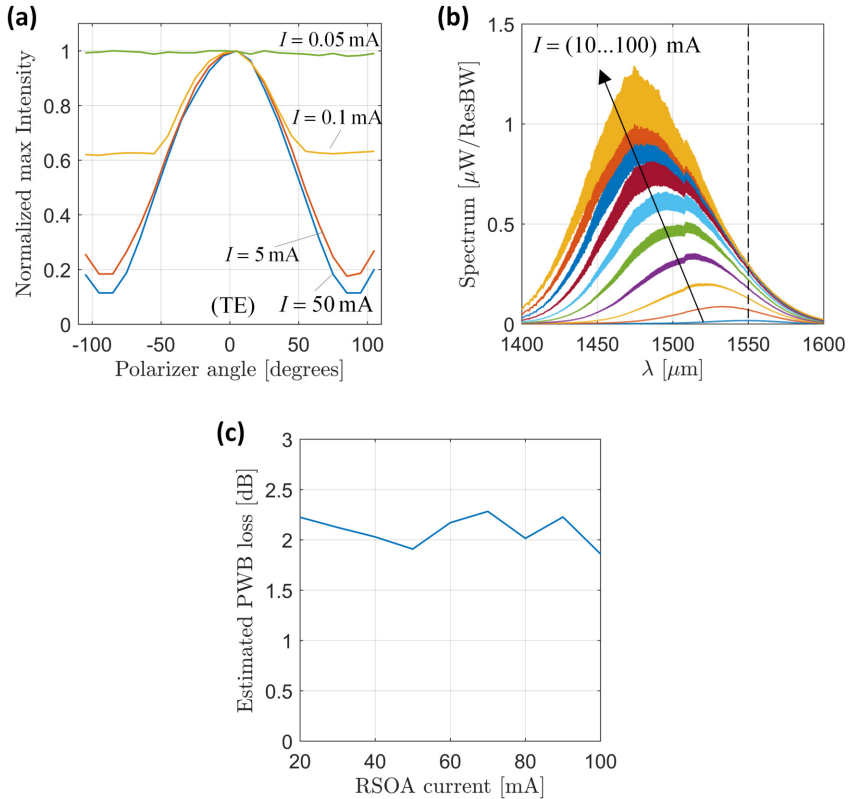
Fig. A.2: Amplified spontaneous emission (ASE) of the RSOA and bond loss estimation. **(a)** Polarization-filtered ASE power emitted by the bare RSOA, measured with an infrared microscope and a linear polarizer in the camera path. The abscissa indicates the orientation of the polarizer, where $0°$ corresponds to maximum transmission for horizontally-polarized light. For drive currents of $I = 5\,\text{mA}$ or higher, most of the emitted ASE is polarized along this direction and may hence be attributed to quasi-TE modes of the on-chip RSOA waveguide. **(b)** ASE power spectra measured through the SMF that is directly coupled to the RSOA, see Fig. A.1(d). The ASE power levels used for estimating the PWB insertion loss are extracted from a $0.8\,\text{nm}$-wide wavelength band centered at $1550\,\text{nm}$ (indicated by a vertical line), i.e., close to the long-wavelength edge of the ASE. In this region, the power spectral density of the ASE saturates for large pump currents, thereby reducing the uncertainty of the measurement technique. **(c)** PWB coupling loss of $-10\log_{10}\eta_{\text{RSOA,SiP}}$ extracted from ASE spectra at different pump currents. From these measurements, we estimate losses of $(2.1 \pm 0.2)\,\text{dB}$.

which does not contain any resonance of R2. The position of the $0.8\,\text{nm}$-wide band is illustrated by a dashed line in Fig. A.2(b). With the power levels $P_{\text{ASE,SiP}}$ and $P_{\text{ASE,SMF}}$ as well as the power transmission $\eta_{\text{RSOA,SMF}}$ between the SMF and the fundamental TE mode of the RSOA at hand, we can then extract the power transmission factor $\eta_{\text{RSOA,SiP}}$ between the fundamental quasi-TE mode of the RSOA and the fundamental quasi-TE mode of the SiP waveguide,

$$\eta_{\text{RSOA,SiP}} = \frac{P_{\text{ASE,SiP}}}{P_{\text{ASE,SMF}}} \eta_{\text{RSOA,SMF}} \,. \tag{A.1}$$

We repeated this procedure for various pump currents, see Fig. A.2(c), finding an insertion loss of the PWB of $-10 \log_{10} \eta_{\text{RSOA,SiP}} \approx (2.1 \pm 0.2)\,\text{dB}$. Note that a small part of the ASE power $P_{\text{ASE,SMF}}$ measured in the fiber should even originate from quasi-TM modes of the RSOA, which cannot be extracted through the highly polarization-sensitive grating coupler (GC 4). To take this effect into account, the measured value of $P_{\text{ASE,SMF}}$ would have to be reduced to only represent the portion coming from quasi-TE modes of the RSOA. This would increase the coupling efficiency according to Eq. (A.1) and hence reduce the coupling loss, such that the number specified above may be considered a conservative estimate of the PWB loss. Note also that the ASE power is extracted around 1550 nm, close to the long-wavelength edge of the ASE spectrum, see Fig. A.2(b). In this region, the power spectral density of the ASE saturates for large pump currents, Fig. A.2(b), thereby reducing the uncertainty of the measurement technique and eliminating the impact of spurious lasing lines that might occur at short wavelengths during measurement of the ASE spectrum through the SiP chip.

A.2 Characterization and modelling of add-drop ring resonators

In Section 3.2.2 ("Component characterization") of the main manuscript, we describe our ring resonators based on a simple model illustrated in Fig. A.3(a) [192, 193]. In this representation, the complex amplitudes of the electric mode fields at

the input, the drop, the through, and the add ports are denoted as $\underline{E}_i$, $\underline{E}_d$, $\underline{E}_t$, and $\underline{E}_a$, respectively. Due to the bidirectional operation of the ring filter, the coupling zones between the bus waveguides and the ring are designed symmetrically. Assuming for simplicity that the coupling zones are lossless, the device can be described by real-valued amplitude transmission and coupling coefficients τ and κ, where $\kappa^2 + \tau^2 = 1$. The round-trip loss of the waveguide is quantified by a real amplitude transmission factor $a = \exp(-\alpha L/2)$, where α denotes the power loss coefficient of the ring waveguide and where L is the circumference of the ring. In our analysis, we use a positive time dependence, i.e., $\exp(j(\omega t - \beta(\omega)z))$ for a wave propagating at angular frequency ω along the positive z-direction with a propagation constant $\beta(\omega)$. We further introduce the round-trip phase $\theta(\omega) = -\beta(\omega)L$. The propagation constant can be approximated by a Taylor series up to the first derivative of β at a center frequency ω_c. We define the effective index $n_{e,SiP} = \beta/k_0$ with the free-space propagation constant $k_0 = \omega/c$, where c denotes the vacuum speed of light. The effective group refractive index is $n_{eg,SiP} = n_{e,SiP} + \omega \, dn_{e,SiP}/d\omega$. The complex through-port amplitude transmission $\underline{E}_t/\underline{E}_i$ is then given by [193]

$$\frac{\underline{E}_t(\omega)}{\underline{E}_i(\omega)} = \frac{\tau - a\tau e^{j\,\theta(\omega)}}{1 - a\tau^2 e^{j\,\theta(\omega)}} \,, \tag{A.2}$$

where

$$\theta(\omega) = -\beta(\omega)L \approx \theta_0 - n_{eg,SiP}(\omega - \omega_c)\frac{L}{c} \,, \tag{A.3}$$

$$\theta_0 = n_{e,SiP}\frac{L}{c} \,. \tag{A.4}$$

Note that by suitable choice of reference planes, we opted for real-valued quantities κ and τ, contrary to [193]. Similarly, by considering outcoupling after half a perimeter, the complex drop port amplitude transmission $\underline{E}_d/\underline{E}_i$ is given by [193]

$$\frac{\underline{E}_d(\omega)}{\underline{E}_i(\omega)} = \frac{-\sqrt{a}\kappa^2 e^{j\,\theta(\omega)/2}}{1 - a\tau^2 e^{j\,\theta(\omega)}} \,. \tag{A.5}$$

From this relation, we can derive the Q-factor of the coupled resonator (loaded Q factor), see Eq. (22) in [194],

$$Q \approx \frac{n_{\text{eg,SiP}}\omega L}{2c}\,\frac{\sqrt{a}\tau}{1-a\tau^2}\,.$$
(A.6)

We determine the parameters a, τ, $n_{\text{eg,SiP}}$, and θ_0 from through-port power transmission measurements via grating couplers GC 1 and GC 3, see Section 3.2.2 ("Component characterization") and Fig. 3.1(b) in the main manuscript. The power transmission measurement is corrected to eliminate the grating-coupler insertion loss, that is independently measured using a dedicated test structure, and Eq. (A.2) is then fitted to the extracted power spectrum $\left|\underline{E}_{\text{t}}/\underline{E}_{\text{i}}\right|^2$. To this end, we directly extract $n_{\text{eg,SiP}}$ from $\text{FSR} = c/(Ln_{\text{eg,SiP}})$ in a first step and use this value to fit Eq. (A.2) to the shape of the individual resonances, assuming a constant $n_{\text{eg,SiP}}$. Since the measured data contains resonances of both rings, we first cut out relevant data segments around each resonance and assign them to the corresponding ring. Measurement data and fit curve are shown for one exemplary resonance dip in Fig. A.3(b). The phase offset θ_0 in Eq. (A.3) can be adjusted by the thermal phase tuners and is responsible for the absolute frequency position of the transmission spectra $\left|\underline{E}_{\text{t}}(\omega)/\underline{E}_{\text{i}}(\omega)\right|^2$ and $\left|\underline{E}_{\text{d}}(\omega)/\underline{E}_{\text{i}}(\omega)\right|^2$ on the frequency axis. For the plot in Fig. 3.3(a) of the main manuscript, θ_0 is adjusted such that the calculated transmission resonances coincide at $\lambda_{\text{c}} = 1550\,\text{nm}$. Around the wavelength of $1550\,\text{nm}$, we measure individual free spectral ranges and find FSR of $368.2\,\text{GHz}$ and $340.7\,\text{GHz}$ for R1 and R2, respectively. This corresponds to $n_{\text{eg,SiP}} \approx 4.18$, in good agreement with platform specifications and with simulations and measurements of waveguides with similar dimensions [195]. We further find $a \approx 0.994$, $\tau \approx 0.973$, $\kappa \approx 0.23$, leading to Q-factors of about $28\,000$ for each of the rings according to Eq. (A.6).
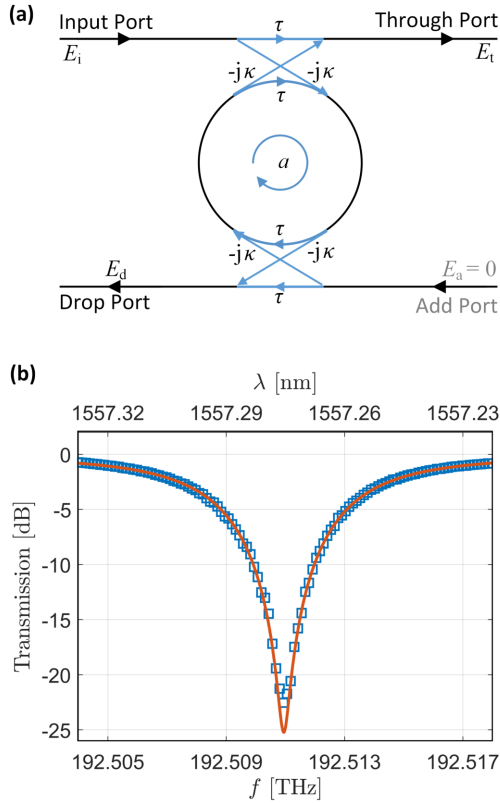
Fig. A.3: Schematic of a symmetrically coupled add-drop ring resonator and measured through-port resonance. **(a)** Complex amplitudes of the electrical mode field at input, drop, through and add port are denoted by $\underline{E}_i$, $\underline{E}_d$, $\underline{E}_t$, and $\underline{E}_a$, respectively. The coupling section is described by the amplitude transmission τ and the coupling coefficient κ, which are both assumed to be real-valued with $\kappa^2 + \tau^2 = 1$ for a lossless coupling zone. The round-trip loss of the waveguide is quantified by a real-valued amplitude transmission factor $a = \exp(-\alpha L/2)$, where α denotes the power loss coefficient of the ring waveguide and where L is the circumference of the ring. **(b)** Measured through-port power transmission $\left|\underline{E}_t/\underline{E}_i\right|^2$ (blue squares) and fit according to Eq. (A.2) (orange line), shown for one exemplary ring resonance of R2.

A.3 Vernier tuning range and tuning enhancement factor

In many cases of practical interest, the tuning range of an ECL with a feedback circuit of two cascaded rings is dictated by the frequency spacing between the main reflection peak and the most prominent side peaks that arise from nearly-overlapping ring resonances. To estimate this frequency spacing, we assume that the two rings R1 and R2 are tuned to a common central resonance frequency f_0 and we express all other resonance frequencies as $f_{\mathrm{R1},m} = f_0 + m \times \mathrm{FSR}_1$ for ring R1 and as $f_{\mathrm{R2},m} = f_0 + m \times \mathrm{FSR}_2$ for ring R2. The difference between the FSR of the two rings is $\Delta\mathrm{FSR} = \mathrm{FSR}_1 - \mathrm{FSR}_2$ with $\mathrm{FSR}_1 > \mathrm{FSR}_2$ without loss of generality, see Eq. (3.1) in the main manuscript. We denote the frequency distance of the R2 resonance number m and the R1 resonance number $(m-1)$ with d_m and find

$$d_m = m \times \mathrm{FSR}_2 - (m-1) \times \mathrm{FSR}_1 = \mathrm{FSR}_1 - m \times \Delta\mathrm{FSR}\,, \qquad \text{(A.7)}$$

$$\Delta\mathrm{FSR} = \mathrm{FSR}_1 - \mathrm{FSR}_2 > 0\,. \qquad \text{(A.8)}$$

If $d_m = 0$ the resonance frequencies would exactly coincide. This is only possible if $m = \mathrm{FSR}_1/\Delta\mathrm{FSR}$ is an integer, i.e., if $T = \mathrm{FSR}_1/\Delta\mathrm{FSR}$ in Eq. (3.1) of the main manuscript happens to be an integer. Otherwise, the modulus $|d_m|$ of the line spacing takes the smallest possible value $\min|d_m| < \Delta\mathrm{FSR}/2$ when m takes the value of the nearest integer to T, $m = [T]$. This can be mathematically proven by using the inequality $T - \frac{1}{2} < m < T + \frac{1}{2}$ in combination with Eq. (A.7), which leads to

$$\min|d_m| = \left|\mathrm{FSR}_1 - [T] \times \Delta\mathrm{FSR}\right| < \Delta\mathrm{FSR}/2\,. \qquad \text{(A.9)}$$

For a finite resonance linewidth δf, an *imperfect* overlap of two lines as in Eq. (A.9) is therefore possible if $\Delta\mathrm{FSR}/2 < \delta f$. In this case, we can calculate the index m of the resonance of R2, that overlaps with the nearest resonance of index $(m-1)$ of R1 and thus leads to the first pair of side peaks,

$$m = [T]\,. \qquad \text{(A.10)}$$

The precise frequency of the side mode, that can occur due to the partially overlapping resonances of R1 and R2, depends on the resonance line shapes of the individual rings and lies in the interval limited by $f_0 + m \times \mathrm{FSR}_2$ and $f_0 + (m-1) \times \mathrm{FSR}_1$. The error when approximating the side mode frequency with either interval limit is smaller than $\Delta\mathrm{FSR}/2$.

A.4   Tuning map

The ECL emission wavelength is selected by aligning the two ring resonators for a common resonance and by optimizing the cavity phase for maximum output power. Once the appropriate tuning parameters are found, they can be stored in a look-up table for later use and for rapid tuning. A simple example of such a tuning map is shown in Fig. A.4. When heating only one ring, the corresponding resonance is detuned in proportion to the heating power, while the resonance of the other ring stays nearly constant, indicating very low thermal crosstalk. The vertical offset of the traces obtained from neighboring resonances corresponds to twice the π-power P_π of the respective ring heater, which amounts to $P_{\pi,\mathrm{R1}} = 24.4\,\mathrm{mW}$ for R1 and $P_{\pi,\mathrm{R2}} = 24.1\,\mathrm{mW}$ for R2. To operate the laser at, e.g., $1549\,\mathrm{nm}$, one can choose the heating powers $P_{\mathrm{R1}} \approx 34.8\,\mathrm{mW}$ and $P_{\mathrm{R1}} \approx 25.0\,\mathrm{mW}$ based on the tuning map, see dashed lines in Fig. A.4. Due to residual thermal crosstalk, the final operation point needs to be fine-tuned in an iterative approach.
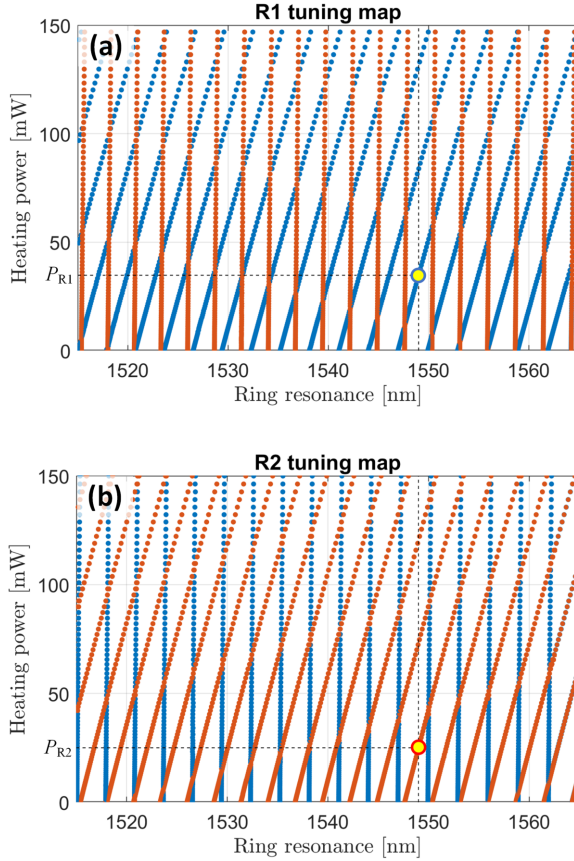
Fig. A.4: Tuning map for the ring resonators. The graphs show the wavelengths of the various ring resonances (horizontal axes) for different heating powers (vertical axes) applied to R1 (blue) or R2 (red). The vertical offset of the traces obtained from neighboring resonances corresponds to twice the π-power of the respective ring heater, which is found to be $P_{\pi,\text{R1}} = 24.4\,\text{mW}$ for R1 and $P_{\pi,\text{R2}} = 24.1\,\text{mW}$ for R2. To operate the laser at, e.g., $\lambda_0 = 1549\,\text{nm}$ (vertical dashed black lines), one can choose the heating powers $P_{\text{R1}} \approx 34.8\,\text{mW}$ and $P_{\text{R1}} \approx 25.0\,\text{mW}$ (horizontal dashed black lines). Note that the tuning range of each ring exceeds the corresponding FSR such that each emission wavelength can be reached by different sets of tuning powers. **(a)** Resonance detuning when heating only R1. The resonance of R1 (blue) is detuned in proportion to the heating power, while the resonance of R2 (red) stays nearly constant, indicating low levels of thermal crosstalk. **(b)** Resonance detuning when heating only R2. The resonance of R2 (red) is detuned in proportion to the heating power, while the resonance of R1 (blue) stays almost constant.

165

## A.5 Two-photon absorption (TPA) and TPA-induced free carrier absorption in the external cavity circuit

The high optical power in the ring-resonator waveguides of the silicon photonic (SiP) external-cavity circuit might lead to detrimental nonlinear effects. To quantify these effects at least approximately, we have performed further estimations and measurements. The power enhancement in a ring resonator as compared to the power in the corresponding bus waveguide can be described by the buildup factor B, see Eq. (2.34) in [193],

$$B = \frac{\kappa^2}{(1 - a\tau^2)^2} \, . \tag{A.11}$$

For our ring resonators, we estimate a round-trip transmission factor of $a = 0.994$ along with transmission and coupling factors $\tau = 0.973$ and $\kappa = 0.23$ for the two coupling zones, see Section A.2, which leads to a build-up factor of $B = 15.2$, corresponding to $11.8\,\mathrm{dB}$. We further consider the maximum emission power of approximately $15\,\mathrm{dBm}$ that the RSOA reaches in the limit of high input powers - slightly more than the saturation output power of $12.5\,\mathrm{dBm}$, that was defined by the $3\,\mathrm{dB}$ gain compression point, see Fig. 3.2(a) in the main manuscript. Taking into account the insertion loss of approximately $2.1\,\mathrm{dB}$ of the PWB, see Section A.1, the on-chip insertion loss of approximately $3\,\mathrm{dB}$ of the $2{\times}2$ MMI, and a single-pass loss of approximately $0.4\,\mathrm{dB}$ of the $2.2\,\mathrm{mm}$ long on-chip strip waveguide. We hence estimate an on-chip power of approximately $9\,\mathrm{dBm}$ that is fed to each of the rings through the bus waveguide connected to the MMI. Assuming an unperturbed resonator in perfect resonance, the power propagating into a single direction within the rings would then amount to more than $19.5\,\mathrm{dBm}$. The overall intra-cavity power is even higher, since the rings are fed from both sides. To estimate the impact of nonlinear losses, we have measured the power-dependent transmission characteristics of a $2.25\,\mathrm{mm}$-long straight silicon photonic waveguide with a cross section of $500\,\mathrm{nm} \times 220\,\mathrm{nm}$ that is identical to that of our ring resonator. The

results are shown in Fig. A.5, exhibiting signs of nonlinear losses such as TPA and TPA-induced FCA for on-chip powers of approximately $19\,\mathrm{dBm}$ ($80\,\mathrm{mW}$). We should hence expect that the rings of our silicon photonic feedback circuit are affected by such effects as well.
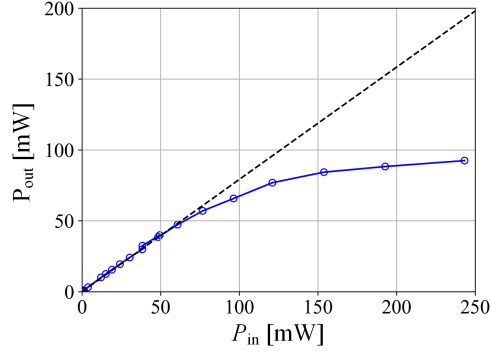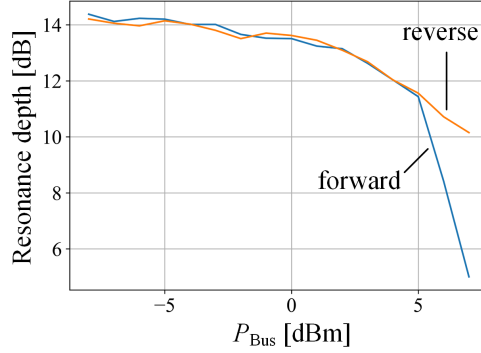

Fig. A.5: Reference transmission measurement of a 2.25-mm-long straight silicon photonic waveguide with the same ($500\,\mathrm{nm} \times 220\,\mathrm{nm}$) cross-section as used in the ECL external cavity circuit. P_{in} refers to the on-chip power level right after the input grating coupler, P_{out} to the on-chip power before the output grating coupler. The measured trace (blue) starts to deviate from the linear fit at low power levels (black dashed line) at input powers around $80\,\mathrm{mW}$ ($19\,\mathrm{dBm}$).

We experimentally confirm this notion by conducting transmission measurements between grating couplers GC 1 and GC 3 of our ECL chip at different optical power levels. To avoid destroying the ECL during the experiment, we used a SiP chip that is nominally identical to the one contained in the ECL and that was fed by a test laser and an EDFA. We tune the laser to an emission wavelength slightly below a resonance of ring R1 and then ramp the heater current of ring R1 up and down to scan the resonance across the fixed laser wavelength while measuring the output power. Figure A.6 shows the on-chip transmission through the bus waveguide of the ring resonator, measured as a function of heater power for different optical input power levels P_{Bus}. For increasing laser power, we make three observations similar to Fig. 20 of [194]: Starting from a power level P_{Bus} of $4\,\mathrm{dBm}$, we first find that the resonance peaks become increasingly skewed, see Fig. A.6(c). At around
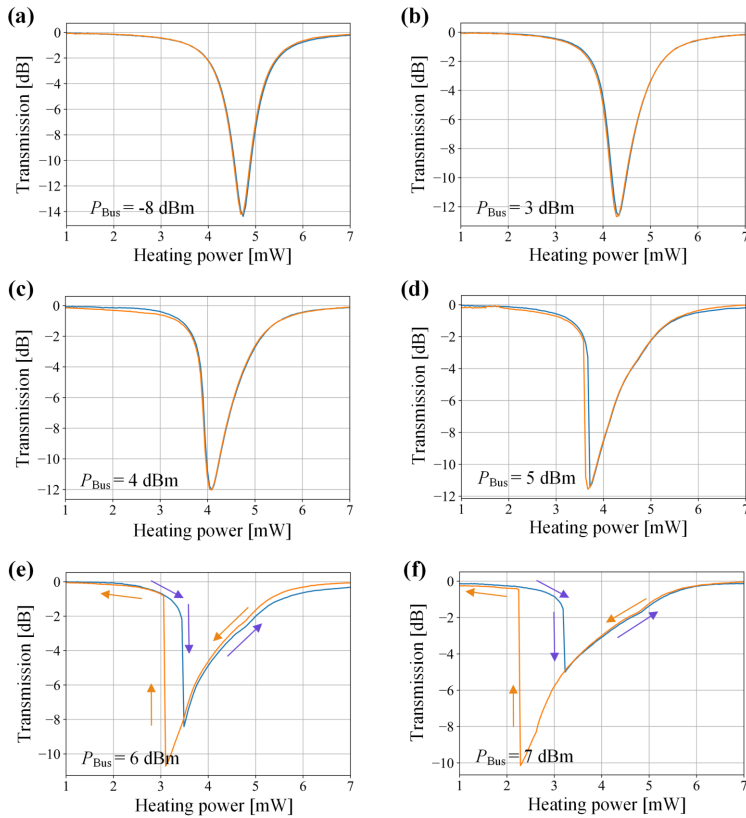
Fig. A.6: Transmission measurements through ring R1 between grating couplers GC 1 and GC 3 at different optical input power levels P_{Bus} in the bus waveguide. To avoid destroying the ECL during the experiment, we used a SiP chip that is nominally identical to the one contained in the ECL and that was fed by a test laser and an EDFA. We tune the laser to an emission wavelength slightly below a resonance of ring R1 and then ramp the heater current of ring R1 up and down to scan the resonance across the fixed laser wavelength while measuring the output power. This experiment is repeated at different levels of the on-chip input power P_{Bus}. Starting from a power level P_{Bus} of 4 dBm, we first find that the resonance peaks become increasingly skewed, see Subfigure (c). At around 5 dBm, we further observe the onset of hysteresis and bi-stable behavior, which becomes more pronounced with increasing power, Subfigures (d),(e),(f). At the same time, we find that the depth of the transmission dip decreases, see Fig. A.7 for details. Heating of the ring due to linear absorption may explain skewing and bi-stability [196], but the reduction of the depth of the resonance dips is a clear indication for nonlinear losses such as TPA and TPA-induced FCA in the rings [197].

5 dBm, we further observe the onset of hysteresis and bi-stable behavior, which becomes more pronounced with increasing power, Fig. A.6(d,e,f). At the same time we find that the depth of the transmission dip decreases, Fig. A.7 – an effect that sets on already at power levels around 0 dBm in the bus waveguide. Heating

Fig. A.7: Resonance depths for different optical power levels P_{Bus} in the bus waveguide, extracted from transmission measurements between grating couplers GC 1 and GC 3, see Fig. A.6. The resonance depths start to decrease already at power levels around 0 dBm in the bus waveguide. At around 5 dBm, we observe the onset of hysteresis and bi-stable behavior, which becomes more pronounced with increasing power. The blue trace shows the resonance depths recorded when ramping the heating power up ("forward") and the orange trace shows the ones when ramping the heating power down ("reverse").

of the ring due to linear absorption may explain skewing and bi-stability [196], but the reduction of the depth of the resonance dips is a clear indication of nonlinear losses such as TPA and TPA-induced FCA in the rings [197]. These experimental findings are in reasonable agreement with the estimated build-up factor B of 11.8 dB and the fact that nonlinear losses in silicon nanowire waveguides start to become relevant at power levels around 19 dBm, see Fig. A.5. Based on these estimations, we should expect that operation of our device is not only subject to heating of the rings due to linear optical intra-cavity losses, but also to TPA and TPA-induced FCA in the ring — at least to some degree. In our experiments, we did not encounter any detrimental effects such as hysteretic wavelength-tuning behavior or unwanted pulsation of the laser emission. Still, implementing ECL

with higher emission power might either require large-area SiP waveguides [102], active removal of free carriers by reverse-biased p-i-n junctions integrated into the ring waveguide [198, 199], or feedback circuits based on waveguides made from large-bandgap silicon dioxide [112] or silicon nitride [19, 109].

A.6 Theoretical discussion of the ECL linewidth

As a reference for the experimentally measured phase-noise properties of our ECL, we theoretically estimate the linewidth that could be expected based on the characteristics of the RSOA and the external feedback circuit. To this end, we follow the formalism described in [19, 102, 200], which is based on [201]. In this model, the laser is simplified to an active section in between two reflecting facets. The back facet has a frequency-independent amplitude reflection coefficient coefficient r_b, while the front facet is represented by a frequency-dependent complex amplitude reflection coefficient $\underline{r}_{eff}(\omega) = |\underline{r}_{eff}(\omega)| e^{j\,\varphi(\omega)}$. The entire external feedback circuit is hence lumped into this frequency-dependent complex reflection factor. The magnitude $|\underline{r}_{eff}(\omega)|$ of the amplitude reflection coefficient accounts for the round-trip losses caused by the PWB and the SiP access waveguides, as well as for the amplitude reflection $|\underline{r}_{mirror}(\omega)|$ of the on-chip Sagnac loop mirror, containing the Vernier ring pair. Neglecting any imbalance of the associated 2×2 MMI, the magnitude reff $|\underline{r}_{eff}(\omega)|$ of the amplitude reflection coefficient can be written as

$$|\underline{r}_{eff}(\omega)| = \sqrt{\eta_{PWB}^2}\sqrt{\eta_{SiP}^2}|\underline{r}_{mirror}(\omega)| = \eta_{PWB}\eta_{SiP}|\underline{r}_{mirror}(\omega)|\,, \quad (A.12)$$

$$|\underline{r}_{mirror}(\omega)| = \left|\frac{\underline{E}_{d,R1}(\omega)}{\underline{E}_{i,R1}(\omega)}\right|\left|\frac{\underline{E}_{d,R2}(\omega)}{\underline{E}_{i,R2}(\omega)}\right|\,. \quad (A.13)$$

The quantities $\underline{E}_{d,R1}$, $\underline{E}_{i,R1}$, $\underline{E}_{d,R2}$, $\underline{E}_{i,R2}$ refer to the complex amplitudes of the electric fields at the input and the drop ports of the two rings, see Section A.2 for details. For the PWB, we find $\eta_{PWB} = 61.6\%$ (2.1 dB loss), see Section A.1. The power transmission $\eta_{SiP} = 88.7\%$ through the passive SiP waveguides is

calculated from a waveguide length of $L_{\mathrm{SiP}} = 2.6\,\mathrm{mm}$ and a waveguide loss parameter of $\alpha_{\mathrm{SiP}} = 2\,\mathrm{dB/cm}$. The drop-port transmissions $\underline{E}_{\mathrm{d,R1}}(\omega)/\underline{E}_{\mathrm{i,R1}}(\omega)$ and $\underline{E}_{\mathrm{d,R2}}(\omega)/\underline{E}_{\mathrm{i,R2}}(\omega)$ are calculated for the individual rings according to Eq. (A.5). The phase $\varphi(\omega)$ of the reflection coefficient accounts for the propagation through the on-chip Si transport waveguides, as well as for the frequency-dependent phase shift associated with the transmission through each of the rings,

$$
\begin{aligned}
\varphi(\omega) = \varphi_0 &- n_{\mathrm{eg,SiP}}(\omega - \omega_{\mathrm{c}})\frac{2L_{\mathrm{SiP}}}{c} \\
&+ \arg\left\{\frac{\underline{E}_{\mathrm{d,R1}}(\omega)}{\underline{E}_{\mathrm{i,R1}}(\omega)}\right\} + \arg\left\{\frac{\underline{E}_{\mathrm{d,R2}}(\omega)}{\underline{E}_{\mathrm{i,R2}}(\omega)}\right\}.
\end{aligned}
\tag{A.14}
$$

For simplicity, we have neglected the phase shift within the photonic wire bond, which is only $200\,\mathrm{\mu m}$ long, and within the 2×2 MMI.

The frequency-dependent phase of the reflection factor reff $\underline{r}_{\mathrm{eff}}(\omega)$ of the external feedback circuit reduces the linewidth δf compared to the linewidth δf_0 of a Fabry-Pérot diode laser with mirror amplitude reflection factors of r_{b} and $|\underline{r}_{\mathrm{eff}}(\omega)|$. This reduction can be quantified [201] by a factor $F^2 = \delta f/\delta f_0$, which accounts for the local frequency dependence of the amplitude and the phase of $\underline{r}_{\mathrm{eff}}(\omega)$ as well as for the Henry factor α_{H} and the photon round-trip time $\tau_{\mathrm{0,RSOA}} = 2n_{\mathrm{eg,RSOA}}L_{\mathrm{RSOA}}/c$ in the RSOA with the effective group refractive index $n_{\mathrm{eg,RSOA}}$,

$$
F = 1 + A + B,
\tag{A.15}
$$

where

$$
A = -\frac{1}{\tau_{\mathrm{0,RSOA}}}\frac{\mathrm{d}\varphi(\omega)}{\mathrm{d}\omega},
\tag{A.16}
$$

$$
B = -\frac{\alpha_{\mathrm{H}}}{\tau_{\mathrm{0,RSOA}}}\frac{\mathrm{d}\ln|\underline{r}_{\mathrm{eff}}(\omega)|}{\mathrm{d}\omega}.
\tag{A.17}
$$

For simplicity, we assume that the resonance frequencies of both rings are tuned to perfectly coincide at or near the lasing frequency, leading to a reflection spectrum as shown in Fig. 3.3(b) of the main manuscript. Tuning of the intra-cavity phase shifts the frequency of the lasing resonator mode with respect to the peak of

Table A.1: Summary of parameters and values used for the theoretical calculation of the ECL linewidth.

Symbol	Description	Value / extracted from
hf	Photon energy	0.80 eV at a center frequency of $f = 193.41$ THz
η_{PWB}	Power transmission of the PWB	$58.9\ldots64.6\%$ (2.1 dB $\pm$ 0.2 dB), see Section A.1
L_{SiP}	Length of passive waveguides on the SiP chip	2.6 mm (2.2 mm transport WG between the PWB and the MMI, see Section 3.2.1; and 0.4 mm of bus WG within the Sagnac loop)
η_{SiP}	Power transmission of the SiP WG	88.7% (2.6 mm-long SiP WG with propagation loss of 2 dB/cm, according to foundry specifications)
a	Round-trip amplitude transmission factor of ring R1 and R2	0.994, see Section A.2
τ	Amplitude transmission coefficient of the coupling zones of ring R1 and R2	0.973, see Section A.2
κ	Ampltiude coupling coefficient of the coupling zones of ring R1 and R2	0.23, see Section A.2
$\eta_{\mathrm{eg,SiP}}$	Effective (modal) group refractive index of the on-chip SiP waveguides	4.18, see Section A.2
$\eta_{\mathrm{eg,RSOA}}$	Effective (modal) group refractive index of the active RSOA section	3.422, from gain ripple frequency spacing, see Fig. 3.2
$L_{\mathrm{eg,RSOA}}$	Length of the RSOA	600 µm, see Section 3.2.1
α_{H}	Henry factor of the RSOA	$2\ldots7$, typical range [202]
P_{o}	Total output power	10 dBm, assuming equal amount of power from GC1-4
n_{sp}	Population inversion factor	$1.25\ldots1.75$, typical range [203]
α_{i}	Internal loss of the RSOA	$14\ldots20\ \mathrm{cm}^{-1}$, estimated range
r_{b}	RSOA back facet amplitude reflection factor	$\sqrt{90\%}$, see Section 3.2.2

the reflection spectrum of the external feedback circuit, and the exact linewidth depends on the detuning between the laser emission frequency and the peak of the reflection spectrum.

The Fabry-Pérot linewidth δf_0 depends on the total output power P_o, the population inversion factor n_{sp}, the internal loss α_i of the RSOA (in units of cm^{-1}), which accounts for excess losses of the active waveguide without the contribution from band-to-band transitions, and the distributed loss α_R, that represents the partially reflective mirrors,

$$\alpha_R(\omega) = -\frac{1}{2L_{RSOA}} \ln\left(r_b^2 |\underline{r}_{eff}(\omega)|^2\right) = -\frac{1}{L_{RSOA}} \ln\left(r_b |\underline{r}_{eff}(\omega)|\right) . \quad (A.18)$$

With these numbers at hand, we can use the estimation of Henry [204] for the Fabry-Pérot linewidth,

$$\delta f_0 = \frac{1}{8\pi} \frac{\left(cn_{eg,RSOA}\right)^2 hfn_{sp}(\alpha_i + \alpha_R)\alpha_R}{P_o} \times (1 + \alpha_H)^2 , \quad (A.19)$$

which then leads to the estimated ECL linewidth

$$\delta f = \frac{\delta f_0}{F^2} . \quad (A.20)$$

Equations (A.12)...(A.20) allow to estimate the linewidth of our ECL, using numerical values for the various parameters as specified in Table A.1.

For the Henry factor, we consider a typical value range of $\alpha_H = 2\ldots7$ for InP/InGaAsP lasers at a wavelength of 1.5 µm, see [202]. For the population inversion factor, we consider a typical range of $n_{sp} = 1.25\ldots1.75$, see p. 198 of [203]. The internal loss of the RSOA is estimated to be in the range of $\alpha_i = (14\ldots20)$ cm^{-1}. Figure A.8 shows the calculated parameters A, B, and F according to Eqs. (A.15) – (A.17) and the corresponding linewidth according to Eqs. (A.19) and (A.20), all as a function of the detuning of the laser emission from the resonance frequency of the two rings. To account for the uncertainties of the various input parameters, we plot two traces for each B, F, and δf, indicating the corresponding lower (subscript "lo") and the upper (subscript "up")
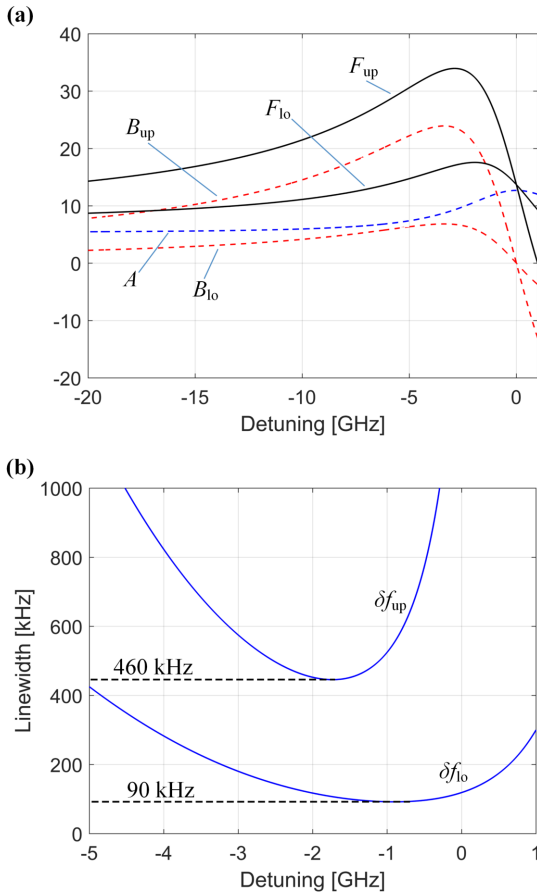
Fig. A.8: Theoretically estimated linewidths of the ECL emission. **(a)** Calculated parameters A, B, and F according to Eqs. (A.15) – (A.17). To account for the uncertainties of the various input parameters listed in Table A.1, we plot two traces for B, F, and δf, indicating the corresponding lower (subscript "lo") and the upper (subscript "up") boundary. **(b)** Corresponding linewidth according to Eqs. (A.19) and (A.20). Assuming optimum detuning, we expect linewidths between 90 kHz and 460 kHz. This is in reasonable agreement with the experimentally measured linewidth of approximately 105 kHz.

boundary. Assuming optimum detuning, we expect linewidths between $90\,\mathrm{kHz}$ and $460\,\mathrm{kHz}$. This is in reasonable agreement with the experimentally measured linewidth of approximately $105\,\mathrm{kHz}$. Note, however, that the calculation model does not account for any potential impact of nonlinear losses such as two-photon absorption (TPA) and TPA-induced free-carrier absorption within the rings that were found to potentially play a role in our devices, see Section A.5.

*[End of Supplementary Information of [J1]]*

B Optical packaging using 3D-printed facet-attached microlenses

This chapter is taken from the Supplementary Information of the manuscript [J2], that has been submitted for publication in a scientific journal. The material from the manuscript has been adapted to comply with the layout and the structure of this thesis.

[Beginning of Supplementary Information of paper [J2]]

B.1 Spot size measurement

To validate the design of the facet-attached microlenses (FaML), we first measure the associate spot sizes using an infrared microscope. Figure B.1 shows the results for FaML on a fiber array (FA) and on a silicon photonic (SiP) chip as used in our first set of experiments, see Section 4.3 of the main manuscript. In this case, the measurements were taken using a $100 \times / 0.8$ objective. The focal position was determined by monitoring the brightness histogram of the image pixels at different axial positions and by identifying the position which produces maximum peak brightness. For the FaML on FA, we find a circular spot with a mode-field diameter (MFD) of $25\,\mu m$, in excellent agreement with the design. For the SiP chips, we fabricate an additional FaML on a separate channel (not shown in Fig. 4.2 of the main manuscript), for which the on-chip edge coupler (EC) is directly connected to a grating coupler (GC) to facilitate in-coupling of light. We
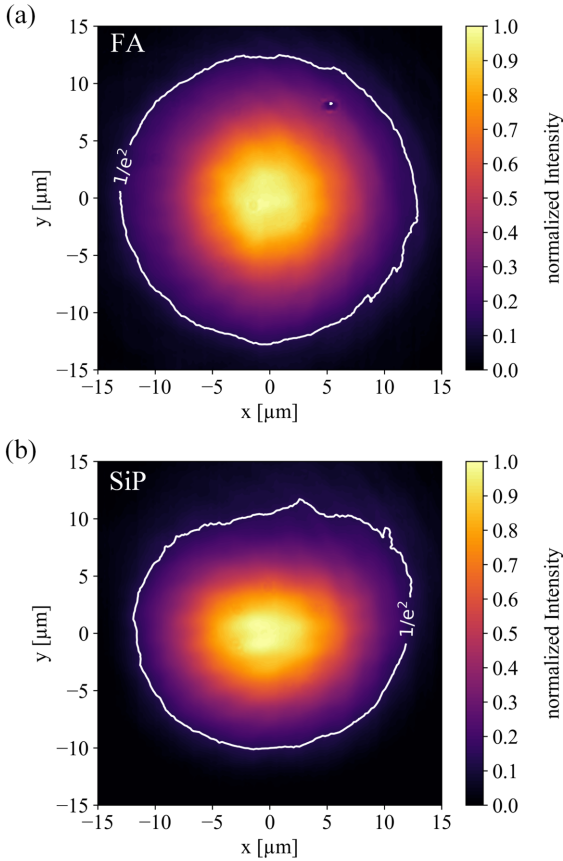
Fig. B.1: Measurement of the focal spots produced by FaML. The images were taken using an infrared microscope equipped with a $100\times / 0.8$ objective. The white lines show the contour for an $1/e^2$ intensity decay with respect to the maximum. **(a)** Focal spot generated by FaML on a fiber array (FA). The circular spot has a mode-field diameter (MFD) of 25 µm, in excellent agreement with the design. **(b)** Focal spot generated by a FaML on a silicon photonic (SiP) chip. The slightly elliptical spot is a bit smaller than designed in the vertical direction with transvers dimensions of 25 µm × 20 µm.

find a slightly elliptical spot, which is a bit smaller than designed in the vertical direction, with transverse dimensions of $25\,\mu\text{m} \times 20\,\mu\text{m}$. Note that this slight mode-field mismatch has only minor impact on the coupling efficiency and the alignment tolerances, see Section 4.3 in the main manuscript.

B.2   Alignment of Gaussian beams

Usually, the facets of micro-optic components have small light-emitting or accepting areas and correspondingly big beam divergence angles. This allows a large angular misalignment, but a low lateral offset only. Our experiments demonstrate that assembly processes can benefit from reducing the divergence and simultaneously expanding the transverse mode-field dimensions by means of facet-attached microlenses (FaML). Our results shown in the main manuscript rely on suitable FaML designs which consider practical limitations such as tolerances of the fabrication and the assembly processes. These designs are based on quantitative models [205] for the lateral and angular alignment tolerances of Gaussian beams, which we explain in the following. These models are also essential for benchmarking our experimental results.

As a model configuration, we consider a free-space connection from a single-mode source to a single-mode sink. We assume Gaussian beams which implies the limitations of paraxial approximation. According to the practical situation, we assume rotationally symmetric beams. Note, however, that the derivations can be extended to elliptic stigmatic beams [205]. The principal beam-propagation direction is z with $z = 0$ in the beam waist, and we use a positive time dependence, i.e., $\exp(\text{j}(\omega t - kz))$ for a wave propagating at angular frequency ω in positive z-direction with a propagation constant k. The only remaining beam parameter is the waist radius w_0. In addition, the beam is characterized by the Rayleigh distance z_{R}, the z-dependent spot radius $w(z)$, the asymptotic divergence angle θ_{div}, the z-dependent phase-front curvature $\kappa(z)$, and the Gouy phase $\zeta(z)$,

$$z_{\text{R}} = \frac{kw_0^2}{2}\,,\tag{B.1}$$

$$w(z) = w_0 \sqrt{1 + \left(\frac{z}{z_{\mathrm{R}}}\right)^2}\,, \tag{B.2}$$

$$\theta_{\mathrm{div}} \approx \tan\theta_{\mathrm{div}} = \frac{2}{k w_0} \tag{B.3}$$

$$\kappa(z) = \frac{z}{z^2 + z_{\mathrm{R}}^2}\,, \tag{B.4}$$

$$\zeta(z) = \arctan\left(\frac{z}{z_{\mathrm{R}}}\right). \tag{B.5}$$

With these parameters, the complex amplitude $\Psi(r, z)$ of the scalar field can be written in cylindrical coordinates (r, z),

$$\Psi(r, z) = \sqrt{\frac{2}{\pi}} \frac{1}{w(z)}\, \mathrm{e}^{-r^2/w^2(z)}\, \mathrm{e}^{-\mathrm{j}\, kr^2 \kappa(z)/2}\, \mathrm{e}^{-\mathrm{j}\left(kz - \zeta(z)\right)}. \tag{B.6}$$

The normalization is chosen such that

$$2\pi \int_0^\infty \left|\Psi(r, z)\right|^2 r\, \mathrm{d}r = 1\,. \tag{B.7}$$

Our model configuration consists of two Gaussian beams, see Fig. B.2. The beam $\Psi(r, z)$ emitted from the source is described by Eq. (B.6) and Eq. (B.7), having its waist located at the origin of the coordinate system, black contours in Fig. B.2(a). It is coupled to a second Gaussian beam $\overline{\Psi}(\overline{r}, \overline{z})$ accepted by the sink, indicated by blue contours in Fig. B.2(a). This beam is described with respect to a second coordinate system $(\overline{r}, \overline{z})$ that may be rotated with respect to the coordinate system (r, z) of the first beam by an angle θ, see Fig. B.2(c). The second beam is also described by Eq. (B.6) and Eq. (B.7), where all quantities but ω, k carry an overbar. We choose an arbitrary reference plane S_{ref} in free space, where the overlap integral is calculated. In addition to a mode-field radius mismatch we specifically consider three types of misalignment, Fig. B.2: Axial offset by a distance s, Fig. B.2(a), axial offset s in combination with radial offset d, Fig. B.2(b), and axial offset s in combination with axial tilt θ, Fig. B.2(c). In
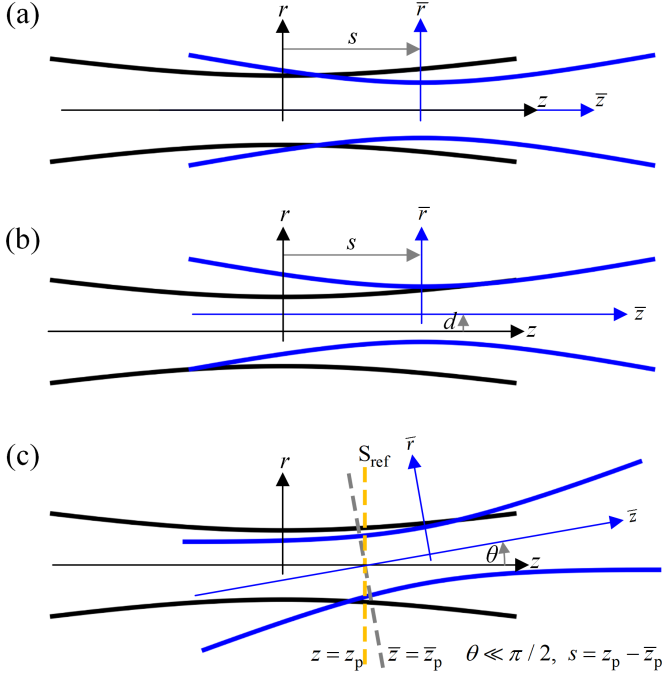
Fig. B.2: Schematic of a Gaussian beam emitted from the source (black contour) and a Gaussian beam accepted by the sink (blue contour). Both beams are described in their respective coordinate systems centered at their respective beam waists. All quantities relating to the sink beam are denoted with an overbar, while all quantities relating to the source beam are denoted without overbar. The two beams may have a mode-field diameter mismatch and an alignment error with respect to each other, leading to a misalignment excess loss. We specifically consider the following misalignment cases: **(a)** Axial offset s only. **(b)** Axial offset s in combination with radial offset d. **(c)** Axial offset s in combination with axial tilt θ. For simplicity, we assume that both beam axes are aligned within a common plane, i.e., we disregard the case of skewed rays. The pivot point is found at the intersection of the two beam axes, at the coordinate $z = z_{\mathrm{p}}$ and $\bar{z} = \bar{z}_{\mathrm{p}}$, respectively. To quantify excess loss due to misalignment, an overlap integral is calculated on the reference plane S_{ref} (dashed orange line, $z = z_{\mathrm{p}}$).

the following, we discuss the different cases and quantify the dependence of the coupling loss on the respective parameters s, d, and θ. For simplicity, we first analyze the case of combined axial offset and axial tilt, Fig. B.2(c), and use the result to derive the relations of the other cases.

B.2.1 Axial offset and axial tilt

The combined axial and angular misalignment of the sink beam (blue) with respect to the source beam (black), Fig. B.2(c), can be constructed in three steps: Starting from a perfect alignment where the coordinate systems of both beams coincide, the sink beam is first shifted by a distance z_p along the still collinear beam axes. The sink beam is then rotated by a small angle θ about its beam waist, followed by another translation $-\overline{z}_\mathrm{p}$ in the rotated coordinate system. The pivot point of combined translation and rotation mapping is finally found at the intersection of the two beam axes, i.e., at a coordinate $z = z_\mathrm{p}$ in the coordinate system of the source beam, and at a coordinate $\overline{z} = \overline{z}_\mathrm{p}$ in the coordinate system of the sink beam. We further introduce the signed axial offset $s = z_\mathrm{p} - \overline{z}_\mathrm{p}$ between the beam waists. Note that both beam axes aligned along the z- and $\overline{z}$-direction still lie within a common plane, i.e., we disregard the case of skewed rays. Within this plane of the rotation, we hence formulate the transformation between the coordinate systems of both beams and the associated approximations for small angles θ as

$$\begin{aligned}
\overline{z} &= (z - z_\mathrm{p})\cos\theta + r\sin\theta + \overline{z}_\mathrm{p} \approx z - s + r\theta\,,\\
\overline{r} &= -(z - z_\mathrm{p})\sin\theta + r\cos\theta \approx -(z - z_\mathrm{p})\theta + r\,.
\end{aligned} \tag{B.8}$$

As reference plane S_ref for performing the overlap integral, we choose the plane $z = z_\mathrm{p}$ parallel to the (x, y)-plane, orange dashed line in Fig. B.2(c), which contains the pivot point of the rotation. For small angles θ, this plane can be described in the coordinate system of the sink beam by using Eq. (B.8),

$$\overline{z} \approx z_\mathrm{p} - s + r\theta\,, \qquad \overline{r} \approx r\,, \tag{B.9}$$

where $s = z_\mathrm{p} - \overline{z}_\mathrm{p}$. We further assume a small divergence angle θ of the sink beam such that the sink beam radius $\overline{w}(\overline{z}_\mathrm{p})$ in plane $\overline{z} = \overline{z}_\mathrm{p}$ corresponds approximately to the radius $\overline{w}(\overline{z}_\mathrm{p}) \cos\theta \approx \overline{w}(\overline{z}_\mathrm{p})$ in plane $z = \overline{z}_\mathrm{p}$. The same argument holds true for the $\overline{z}$-dependent Gouy phase, which is approximated by $\overline{\zeta}(\overline{z}_\mathrm{p})$ in the relevant part of the reference plane $z = \overline{z}_\mathrm{p}$, independent of r. The complex field of the sink beam in the reference plane can hence be approximated by

$$\overline{\Psi}(\overline{r} \approx r, \overline{z} \approx \overline{z}_\mathrm{p} + r\theta) \approx \overline{\Psi}(r, \overline{z}_\mathrm{p})\mathrm{e}^{-\mathrm{j}\,kr\theta}. \tag{B.10}$$

Under these assumptions, the overlap integral for the power transmission T_R in the reference plane S_ref can be written as

$$T_\mathrm{R} = \left| 2\pi \int_0^\infty \Psi^*(r, z_\mathrm{p})\overline{\Psi}(r, \overline{z}_\mathrm{p})\mathrm{e}^{-\mathrm{j}\,kr\theta} \right|^2. \tag{B.11}$$

Using Eqs. (B.1), (B.2), (B.4), and (B.6) leads, after some modifications [205], to a simplified expression for the power transmission,

$$T_\mathrm{R} = \tau_a^2(s)\mathrm{e}^{-(\theta/\theta_\mathrm{e})^2}, \qquad s = z_\mathrm{p} - \overline{z}_\mathrm{p}, \tag{B.12}$$

where $\tau_a(s)$ describes the dependence of the excess loss on a pure axial offset s,

$$\tau_a(s) = \frac{2}{\sqrt{\left(\frac{w_0}{\overline{w}_0} + \frac{\overline{w}_0}{w_0}\right)^2 + \left(\frac{2}{kw_0\overline{w}_0}\right)^2 s^2}}, \tag{B.13}$$

and where θ_e quantifies the $1/\mathrm{e}^2$ angular alignment tolerance for a given axial offset s and positions z_p and $\overline{z}_\mathrm{p}$,

$$\theta_\mathrm{e} = \frac{2\sqrt{2}}{k\tau_a(s)\sqrt{\overline{w}^2(\overline{z}_\mathrm{p}) + w^2(z_\mathrm{p})}}. \tag{B.14}$$

The local spot-size radii $w(z_\mathrm{p})$ and $\overline{w}(\overline{z}_\mathrm{p})$ in Eq. (B.14) are given according to Eq. (B.2). The $1/\mathrm{e}^2$ angular alignment tolerance θ_e assumes its maximum [205] value θ_e if the relation

$$\frac{z_\mathrm{p}}{w^2(z_\mathrm{p})} + \frac{\overline{z}_\mathrm{p}}{\overline{w}^2(\overline{z}_\mathrm{p})} = 0 \,, \tag{B.15}$$

is fulfilled, where

$$\theta_\mathrm{e,max} = \frac{\sqrt{2}\sqrt{1/w_0^2 + 1/\overline{w}_0^2}}{k} \,. \tag{B.16}$$

Note that $\theta_\mathrm{e,max}$ does not depend on the waist separation s, but the transmission $T_\mathrm{R} \leq 1$ according to Eq. (B.12) does and is maximum for $s = 0$, i.e., if the positions $z = 0$ and $\overline{z} = 0$ coincide. In the following, we specialize the relations Eq. (B.12) – (B.14) to axial tilt only ($s = 0$), and to axial offset only ($\theta = 0$).

B.2.2 Axial tilt only

A simplified expression for T_R results when considering the case without any mode-field mismatch ($w_0 = \overline{w}_0$) and without axial offset ($s = 0$). In this case, the $1/\mathrm{e}^2$ angular alignment tolerance $\theta_\mathrm{e} = 2/(kw_0)$ corresponds to the (common) divergence angle of both beams, and the power transmission T_R simplifies to

$$T_\mathrm{R} = \mathrm{e}^{-(\theta/\theta_\mathrm{div})^2} \,, \qquad \theta_\mathrm{div} = \frac{2}{kw_0} \,. \tag{B.17}$$

B.2.3 Axial offset only

The special case of an axial offset only, Fig. B.2(a), is described by setting $\theta = 0$ in Eq. (B.12). The power transmission T_a for an axial offset s is thus

$$T_\mathrm{a} = \tau_\mathrm{a}^2(s) \,, \tag{B.18}$$

with $\tau_a(s)$ from Eq. (B.13). For perfect axial alignment ($s = 0$) and a mode-field-diameter mismatch only, we find

$$\tau_a(0) = \frac{2}{\overline{w}_0/w_0 + w_0/\overline{w}_0} \,. \tag{B.19}$$

If the mode-fields are matched, $w_0 = \overline{w}_0$, an axial misalignment $s \neq 0$ leads to

$$\tau_a(s)\big|_{w_0=\overline{w}_0} = \frac{1}{\sqrt{1 + s^2/(k^2 w_0^4)}} = \frac{2}{\sqrt{4 + (s/z_R)^2}} \,. \tag{B.20}$$

An axial shift of approximately one Rayleigh distance $s = z_R$ hence results in a misalignment loss of approximately $1\,\mathrm{dB}$.

B.2.4 Combination of axial offset and lateral offset

Finally, we discuss the combination of an axial offset s and a lateral offset d, Fig. (B.2)(b). The expression for the associated power transmission T_L is derived from the previously discussed case of a combined axial offset and axial tilt, Eqs. (B.12)...(B.14). To this end and for the depicted case in Fig. B.2(c), we consider the limit [205]

$$z_p \to -\infty \qquad \overline{z}_p = z_p - s \to -\infty \,. \tag{B.21}$$

along with an infinitesimal rotation

$$\theta = \frac{d}{|z_p|} \,. \tag{B.22}$$

According to Eq. (B.1) and (B.2) we then find

$$w(z_p) \to w_0 \frac{|z_p|}{z_R} = \frac{2|z_p|}{k w_0} \,, \qquad \overline{w}(\overline{z}_p) \to \frac{2|z_p - s|}{k \overline{w}_0} \to \frac{2|z_p|}{k \overline{w}_0} \,. \tag{B.23}$$

Inserting Eq. (B.22) and (B.23) into Eq. (B.12) and (B.14) leads to the expression for the power transmission T_L,

$$T_L = \tau_a^2(s)e^{-(d/d_e)^2} \, ,$$

(B.24)

with

$$d_e = \frac{1}{\tau_a(s)} \sqrt{\frac{2}{1/w_0^2 + 1/\overline{w}_0^2}} \, .$$

(B.25)

B.2.5 Lateral offset only

We further give the expression for the simplified case of a lateral offset only ($s = 0$), without any mode-field mismatch ($w_0 = \overline{w}_0$). The power transmission T_L is then found using Eqs. (B.24) and (B.25),

$$T_L = e^{-(d/d_e)^2} \, .$$

(B.26)

From Eq. (B.26), we find that a lateral shift of

$$d_{1dB} = \sqrt{\frac{1}{10 \log_{10} e}} \approx 0.48 \times w_0$$

(B.27)

leads to a misalignment excess loss of $1\,\mathrm{dB}$. This lateral shift is depicted by red dashed circles in Figs. 4.3(a), 4.8(a) and 4.13(a) of the main manuscript, in excellent agreement with experimentally measured data for Figs. 4.3(a) and 4.8(a), and in reasonable agreement with experimentally measured data for the much more complex FaML assembly in Fig. 4.13(a). The smallest MFD used in our experiments amounts to $25\,\mathrm{\mu m}$ ($w_0 = 12.5\,\mathrm{\mu m}$). In this case, a lateral shift of $d = 1\,\mathrm{\mu m}$, e.g. due to irregularities in the spacing of the fibers within the fiber array (FA), only leads to an excess loss of $0.03\,\mathrm{dB}$ according to Eq. (B.26), which is fully negligible.

B.2.6 Measurement of angular tolerances

When experimentally measuring the angular alignment tolerance, the pivot point of the rotation is usually not precisely known. Instead, any rotation of the positioning stage has to be followed by a set of translations that compensate for the unwanted movement of the point $z = z_{\mathrm{p}}$ or $\overline{z} = \overline{z}_{\mathrm{p}}$ that is assumed to be the center of the rotation considered in Sections B.2.1 and B.2.2. These translations are performed as to maximize the coupling between the two beams without changing their angular orientation, thus leading to a configuration in which the center points of the two beam waists, marked by the points $z = 0$ and $\overline{z} = 0$ on the two beam axes, coincide, see discussion after Eq. (B.16) above. The measurement procedure therefore effectively corresponds to a rotation around the pivot point for $s = 0$. In this case, $z_{\mathrm{p}} = \overline{z}_{\mathrm{p}} = 0$, such that Eq. (B.15) is fulfilled. The extracted angular alignment tolerance hence corresponds to the maximum achievable value $\theta_{\mathrm{e,max}}$ according to Eq. (B.16). This measurement procedure is used to obtain the experimental data of angular alignment tolerances in Figs. 4.3(b), 4.8(b) and 4.13(b) of the main manuscript, and the results are then fit by Eq. (B.17) with the common beam-waist radius as a free parameter, from which the angular alignment tolerance $\theta_{\mathrm{e,max}} = \theta_{\mathrm{div}}$ or the corresponding $1\,\mathrm{dB}$ tolerances are extracted.

B.2.7 Tradeoff of lateral and angular tolerances

For visualizing the aforementioned fundamental tradeoff between lateral and angular tolerances, Fig. B.3, we consider the simplified case of a circularly symmetric beam without mode-field mismatch and without axial misalignment. The misalignment-dependent power transmission is thus calculated according to Eq. (B.26) and Eq. (B.27) for a lateral and an angular misalignment, respectively. A small beam waist parameter w_0 results in a small tolerable lateral shift d, Fig. B.3(a), but allows a large angular misalignment θ, Fig. B.3(b). Expanding the mode field increases the lateral tolerance, but decreases the angular one.

(a)

(b)
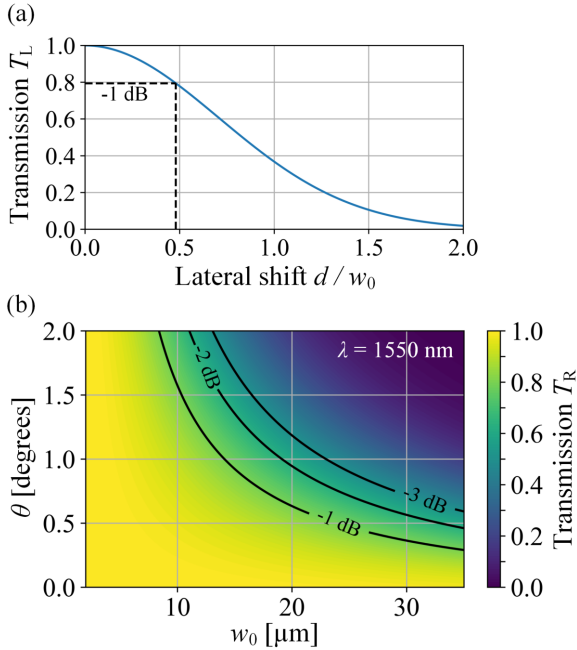
Fig. B.3: Tradeoff of lateral and angular tolerances. A small beam waist parameter w_0 results in a small lateral tolerance and a large angular tolerance. Expanding the mode field hence allows to trade some of the angular tolerance for additional lateral tolerance. **(a)** Alignment tolerances for lateral translation d according to Eq. (B.26). The dashed lines indicate a 1 dB misalignment excess loss at a lateral shift of $d \approx 0.48 \times w_0$, see Eq. (B.27). **(b)** Angular alignment tolerances according to Eq. (B.17), for a wavelength of $\lambda = 1550\,\mathrm{nm}$ in vacuum. The contour lines correspond to a misalignment excess losses of 1 dB, 2 dB and 3 dB, respectively.

B.2.8 Tolerance analysis for passive alignment

To arrive at easy-to-handle design guidelines for passively assembled FaML-based optical systems, we estimate the impact of positioning uncertainties on the excess coupling loss. The underlying passive assembly processes rely on aligning two components to each other by first fixing one component in place and by aligning the second one based on measurement of positions and orientations. For the expanded beam, we may safely assume that slight axial misalignments do not play a significant role such that we only need to consider angular measurement error θ and an independent measurement error d of the lateral position, both of which result in a corresponding combined angular and lateral misalignment. We could represent this combined misalignment as a single axial tilt with a certain pivot point and calculate the net effect according to Eqs. (B.12)...(B.14). This is however complicated, and we instead use an approximation, where we consider the combined misalignment as the result of a rotation of one beam by an angle θ about a common beam waist, followed by a lateral shift by a distance d. We further assume that the losses of these two operations can be independently calculated according to Eq. (B.17) and Eq. (B.26), respectively, and that the corresponding power transmission factors can be simply multiplied to obtain the final power transmission factor of the overall configuration. We further consider a free-space coupling distance D and we assume a symmetric configuration, where the beam waists lie in the middle of the free-space distance. An angular misalignment θ of the second component would then lead to an additional induced lateral shift (pointing error) of the corresponding beam by $(D/2)\tan\theta$ in the plane of the common beam waists, where we evaluate the overlap integral. The worst-case lateral shift $d_{\max}$ to account for with Eq. (B.26) is hence

$$d_{\max} = \left| \frac{D}{2}\tan\theta \right| + |d| \, , \tag{B.28}$$

where we have assumed that the induced lateral shift and the independent measurement error of the lateral position lead to a misalignment in the same direction. In the following, we consider a given free-space distance D and given precisions

189

θ_{ax} and d_{ax} per rotational axis and per translational axis of the alignment machine, respectively. The rotation-independent lateral shift d within Eq. (B.28) is hence $d = \sqrt{2}d_{\text{ax}}$ in the worst case, where we again assume that slight axial misalignments do not play a significant role such that only the misalignment along the two transverse directions contributes to the excess loss. Likewise, for small angles, we consider $\theta = \sqrt{2}\theta_{\text{ax}}$ in Eqs. (B.28) and (B.17), since a rotation about approximately collinear beam axes does not matter for a single free-space connection and rotationally symmetric beams. Note, however, that rotations about approximately collinear beam axes do play a role in case of assembly of device arrays with multiple free-space connections. In this case, the associated loss can be easily estimated based on Eq. (B.26) and is usually not a limiting factor for chip-scale waveguide separations and typical FaML-generated free-space beam diameters of, e.g., 25 µm or larger. Under these premises there exists an optimum beam-waist radius w_0, which yields the lowest reliably achievable loss, see Fig. B.4(a): For a very small waist radius w_0, the expected total loss will be dominated by the worst-case lateral shift, Eqs. (B.28) and (B.26), while for a very large waist parameter, the expected total loss will be dominated by the rotation around the common beam waist and the corresponding inclination of the associated phase fronts, Eq. (B.17). Alternatively, one can use Eq. (B.28) in combination with Eqs. (B.17) and (B.26) to estimate the worst-case coupling loss for given rotational and translational tolerances of the machine-vision-based alignment system, see Fig. B.4(b).

In our passive assembly experiment over a large distance of 3.3 mm, see Section 4.4 of the main manuscript, we used lenses which produce a beam diameter of $2w_0 = 60$ µm (beam radius $w_0 = 30$ µm). Note that, for an initial conservative estimate of $\theta_{\text{ax}} = 0.2°$ for each rotation axis and $d_{\text{ax}} = 3$ µm for each translation axis, a beam diameter of $2w_0 \approx 70$ µm would have been ideal, see Fig. B.4(a). However, we found this beam diameter difficult to reach with only two refractive surfaces under the limitations of the lithography system regarding the maximum structure size. We thus performed our experiments with a slightly smaller beam diameter of 60 µm, which does not severely limit our performance, see Fig. B.4(b). Given the fact that our passive alignment prior to gluing leads to an angular position that is practically identical to the actively optimized position within the
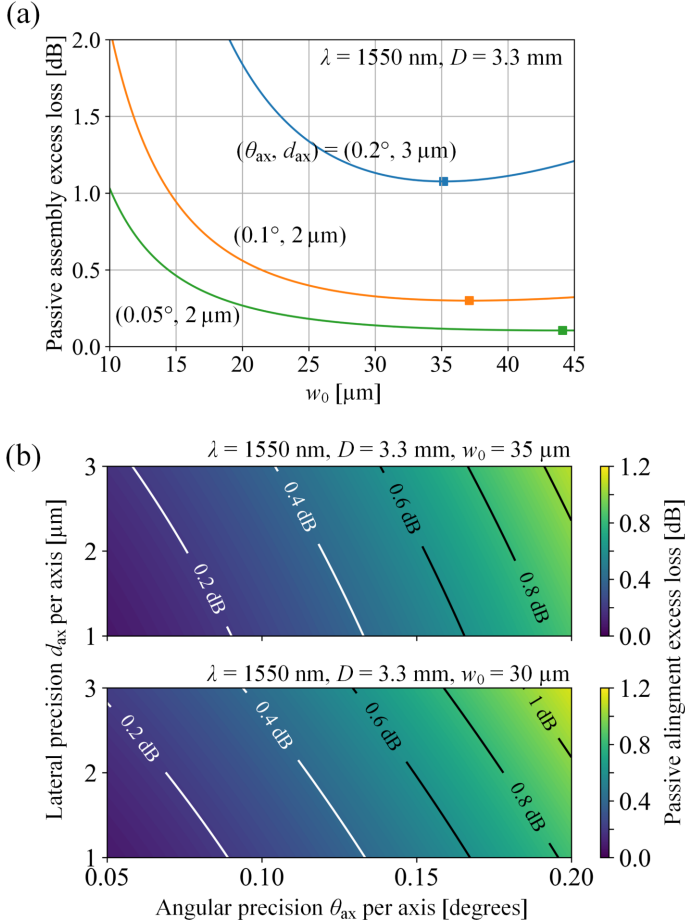
Fig. B.4: Worst-case excess loss for passive alignment, assuming light at a wavelength of $\lambda = 1550$ nm and a free-space coupling distance of $D = 3.3$ mm as used in our experiment in Section 4.4 of the main manuscript. The worst-case loss depends on the beam waist parameter w_0 and on the achievable lateral and angular alignment precision. **(a)** Worst-case excess loss as a function of the beam waist parameter w_0. The curves for three exemplarily chosen combinations of alignment tolerances are shown. The labels refer to the rotational and translational alignment tolerances (θ_{ax}, d_{ax}) per axis. The markers indicate the optimum choice of w_0. **(b)** Excess loss shown as a function of the lateral and angular alignment tolerances (θ_{ax}, d_{ax}) of the alignment machine. The two panels refer to a choice of $w_0 = 35$ µm, which corresponds to the optimum for $\theta_{ax} = 0.2°$ and $d_{ax} = 3$ µm according to Subfigure (a), and of $w_0 = 30$ µm, as used in our Experiments in Section 4.4 of the main manuscript.

measurement accuracy, see Section 4.4 of the main manuscript, we believe that even larger beam diameters could have been used. This would also have decreased the variations of the coupling losses obtained for different path lengths in our experiment including the polarization beam splitter, see Eq. (B.20) and Section 4.4 of the main manuscript.

B.3   Assembly machine and passive alignment process

All assemblies have been built using a semi-automated assembly machine (ficonTEC Service GmbH) that relies on industry-standard machine vision techniques, see Fig. B.5. The submount of the assembly is hold in place at the assembly zone using a vacuum chuck. Components such as optical chips or fiber arrays are mounted using a six-axis positioner (right side) that is equipped with either a gripper or vacuum pick-up-tool (PUT). The positions and orientations of components after pick-up or and/or mounting are measured using a top view (TV) camera and a chromatic confocal distance sensor [148], both mounted on a three-axis positioner (left side), as well as another fixed bottom-view (BV) camera. In a typical assembly workflow, parts are first picked up from the tray, inspected over the BV camera if necessary, and moved over to the assembly zone for final alignment and fixing. In our experiments, we demonstrate a passively aligned assembly with a large coupling distance, see Section 4.4 of the main manuscript, where we couple a fiber array (FA) to a photo diode array (PDA). As a reference, the result of this passive alignment is then compared to an active alignment obtained my maximizing the output current of the photodiodes, which are contacted through an additional pair of DC-probes (not shown).

In our experiments, we first glue the chips to the submount and then align the FA with respect to the chips, where the fibers are typically oriented along the y-direction, see Fig. B.5, for optimum strain relief. The position in the (x, y)-plane and the in-plane-rotation R_z of the mounted chips are measured using the TV camera, while the exact chip height z and the chip tilt angles R_x and R_y are
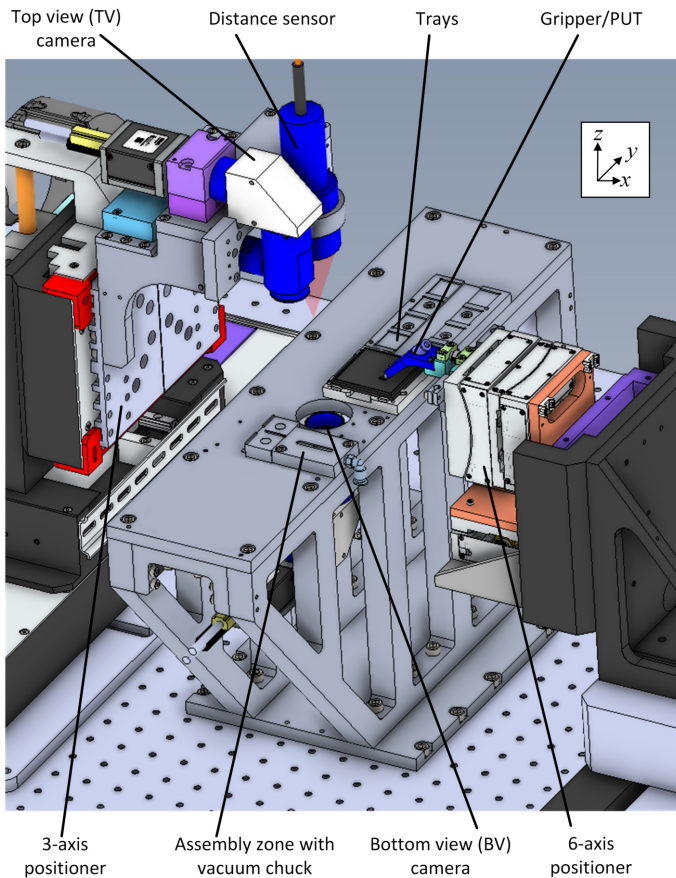
Fig. B.5: Schematic of the assembly machine. The submount of the assembly is fixed at the assembly zone using a vacuum chuck. Components such as optical chips or fiber arrays are mounted using a six-axis positioner (right side) that is equipped with either a gripper or vacuum pick-up-tool (PUT). The positions and orientations of components after pick-up and/or mounting are measured using a top view (TV) camera and a chromatic confocal distance sensor [148], both mounted on a three-axis positioner (left side), as well as another fixed bottom-view (BV) camera. In a typical assembly workflow, parts are first picked up from the tray, inspected over the BV camera if necessary, and moved over to the assembly zone for final alignment and fixing. The results of passive alignment processes can be benchmarked by using active alignment techniques, which can also be executed on the assembly machine.

(a)

Tilted surface

(b) Position for height measurement

125 µm
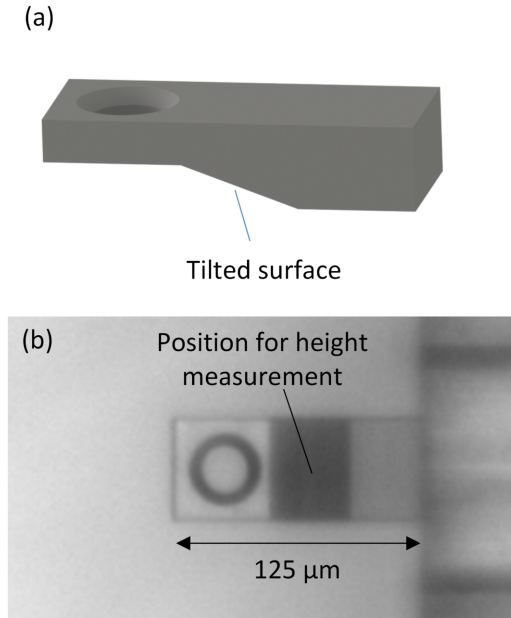
Fig. B.6: 3D-printed alignment markers used for alignment of the fiber arrays (FA), see Inset (i) of Fig. 4.6 of the main manuscript. Detection of a pair of markers allows to find the position of the FA in the (x, y)-plane, the exact height z, the in-plane rotation R_z, as well as the tilt angle R_y. To this end, we first detect the circular feature within the marker using the TV camera in combination with appropriate image recognition and then measure the height on top of the marker using the chromatic confocal distance sensor. **(a)** CAD model of the marker. To get an accurate measurement signal originating from the reflection at the top surface of the marker only, we use structures with an angled bottom surface, such that the unwanted reflection lies outside of the acceptance cone of the chromatic confocal distance sensor. **(b)** Image of the 3D-printed alignment markers, taken from the TV camera of the assembly system. The area suitable for height measurements is clearly seen as a dark rectangle.

measured using line scans with the chromatic confocal distance sensor. For the FA, we first measure the position and orientation after pick-up and then calculate the motion of the six-axis positioner that is required to move the FA to its target position. To this end, we first find the rotation angle R_x from a BV autofocus measurement at the front and back of the FA. All other degrees of freedom of the FA within the gripper are then measured with the help of 3D-printed markers, see Fig. B.6, which are precisely aligned to unused channels of the FA during

lithography. Specifically, we find the position in the (x, y)-plane and the in-plane-rotation R_z by detecting the circular shapes within the markers using the TV camera in combination with appropriate image recognition techniques. The tilt angle R_y as well as the exact height z of the FA are found by height measurements on top of the 3D-printed markers using the chromatic confocal distance sensor. To get an accurate measurement signal originating from the reflection at the top surface of the marker only, we use structures with an angled bottom surface, such that the unwanted reflection lies outside of the acceptance cone of the chromatic confocal distance sensor.

B.4 Estimation of return loss induced by FaML assemblies for angled facets

In our third set of experiments, see Section 4.5 of the main manuscript, we demonstrate the viability of a special FaML configuration with low back-reflection. Such configurations allow, e.g., for coupling of arrays of reflection-sensitive angled-facet lasers to fiber arrays or to other PIC. In our experiments, we find no signs of detrimental effects due to our packaging concept. The exact back-reflection factor induced by the FaML is hard to quantify by a direct measurement. We therefore perform an estimate of the expected levels of back-reflection. To this end, we measure the current-dependent emission spectra of the laser packaged according to Fig. 4.11 of the main manuscript while varying the level of optical back-reflection. This back-reflection originates from an open fiber FC-PC connector without angle-polish at the input of our optical spectrum analyzer, see Fig. B.7, and the back-reflected power is adjusted via a fiber-based variable optic attenuator (VOA), which is inserted between the laser and the OSA. The open fiber end leads to a reflection of 3.25% ($n = 1.44$ to air), corresponding to a Fresnel reflection return loss of $a_{\text{Fresnel}} \approx 15\,\text{dB}$. We record spectra for various levels of single-pass attenuation a_{VOA} of the VOA, Fig. B.8. All spectra are recorded from DFB #2 of our assembly, with a single-pass coupling loss $a_{\text{FaML}} = 2.5\,\text{dB}$ of the FaML-pair, see Table 4.3 of the main manuscript. An unsuppressed OSA
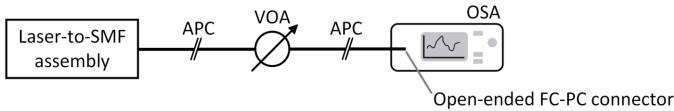
Fig. B.7: Measurement setup for experimental estimation of the levels of back-reflection generated by the FaML configuration shown in Fig. 4.11 of the main manuscript. We measure the current-dependent emission spectra of the laser packaged according to Fig. 4.11 of the main manuscript while introducing different levels of optical back-reflection. The back-reflection originates from an open fiber FC-PC connector without angle-polish at the input of our optical spectrum analyzer, and the back-reflected power is adjusted via a fiber-based variable optic attenuator (VOA), which is inserted between the laser and the OSA using a pair of angled physical contact (APC) connectors. The open fiber end leads to a reflection of 3.25% at the interface of the fused-silica core ($n = 1.44$) to air, corresponding to a Fresnel reflection return loss of 15 dB.

backreflection ($a_{VOA} = 0\,$dB) leads to significant broadened emission peaks ("coherence collapse" [206, 207]). For a single-pass attenuation of $a_{VOA} = (4\ldots10)\,$dB, we observe "satellite modes" [208] with a separation corresponding to the relaxation oscillation frequency. A single-pass attenuation $a_{VOA} \geq 12\,$dB is required to produce spectra without visible distortions, indistinguishable from the reference spectra of the bare laser in Fig. 4.14 of the main manuscript. As described in the main manuscript, these reference spectra were recorded from a bare laser using a fiber that is deliberately placed at a large distance from the facet, thereby avoiding any direct back-reflections from the fiber facet while strongly attenuating any back-reflection from within the fiber-optic setup. Our observations match the typical behavior for feedback effects in DFB lasers according to Tkach and Chraplyvy [35] very well. There, the transition from satellite modes to a single narrow line ("Regime IV" to "Regime III" in [35]) is found at an approximate threshold backreflection factor of $a = -40\,$dB, independent on the distance of the reflection, as long as the distance remains within the coherence length of the laser. We find this transition at $a_{VOA} = 10\,$dB, and hence the very same threshold backreflection factor, $a = -(2a_{FaML} + 2a_{VOA} + a_{Fresnel}) = -40\,$dB. Two more transitions are usually found at even weaker backreflections. In particular, a further transition ("Regime III" to "Regime II" in [35]) is usually approximately found at an distance-independent backreflection factor of $a = -45\,$dB, where the laser would start to show an "apparent splitting" of the emission line, arising from rapid mode
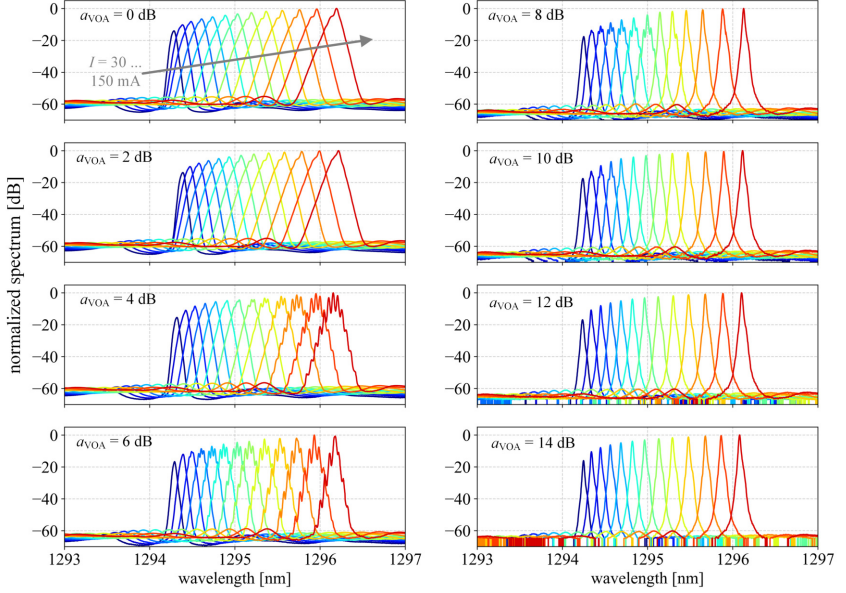
Fig. B.8: Measured spectra (resolution bandwidth 0.01 nm) for different single-pass attenuation levels a_{VOA}, using the measurement setup of Fig. B.7. The unsuppressed OSA backreflection ($a_{\mathrm{VOA}} = 0$ dB) leads to significantly broadened emission peaks ("coherence collapse" [206, 207]). For a single-pass attenuation of $a_{\mathrm{VOA}} = (4 \ldots 10)$ dB, we observe "satellite modes" [208]. A single-pass attenuation $a_{\mathrm{VOA}} \geq 12$ dB is required to produce spectra without visible distortions, indistinguishable from the reference spectra of the bare laser in Fig. 4.14 of the main manuscript. As described in the main manuscript, these reference spectra were recorded from a bare laser using a fiber that is deliberately placed at a large distance from the facet, thereby avoiding any direct back-reflections from the fiber facet while strongly attenuating any back-reflection from within the fiber-optic setup. Our observations match the typical behavior of feedback effects in DFB lasers [35] very well. An estimate of the FaML backreflection factor a based on the absence of "apparent mode splitting", i.e., a rapid mode-hopping inside the observation time [35] for attenuations $a_{\mathrm{VOA}} \geq 12$ dB, leads to a value of $a \leq -44$ dB.

197

hopping [35]. In our experiments, we do not observe this effect when increasing the attenuations to $a_{\mathrm{VOA}} > 12\,\mathrm{dB}$. We attribute this observation to that fact that the FaML introduces a slight amount of backreflection as well, which can lead to an operation regime in which the laser emits a single narrow line while being only sensitive to other reflections of comparable or greater magnitude ("Regime III", between $-40\,\mathrm{dB}$ and $-45\,\mathrm{dB}$ in [35]). Since $a_{\mathrm{VOA}} \geq 12\,\mathrm{dB}$ is required to produce unperturbed spectra, we may further assume that the strength of the backreflection from the FaML is approximately comparable to or smaller than the strength of the external backreflection from the open fiber end for $a_{\mathrm{VOA}} = 12\,\mathrm{dB}$, which amounts to $-(2a_{\mathrm{FaML}} + 2a_{\mathrm{VOA}} + a_{\mathrm{Fresnel}}) = -44\,\mathrm{dB}$.

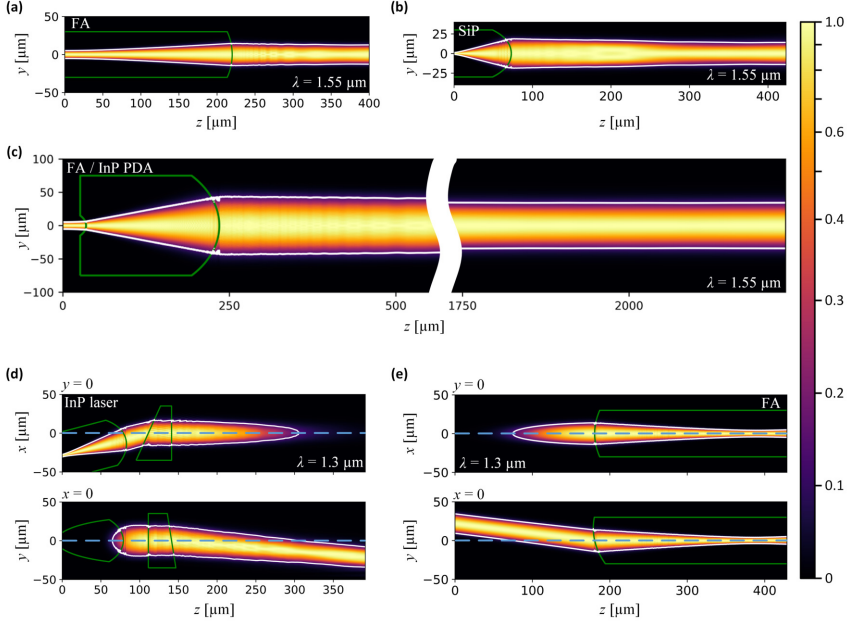## B.5   Microlens simulations

For simulation of the microlenses, we use an in-house developed simulation software based on the scalar wide-angle unidirectional wave-propagation method for step-index structures proposed in [36], see Materials and Methods section of the main manuscript. Instead of simulating the entire propagation through FaML pairs, we split the simulation into two parts, each containing one FaML. The shape of each of the two FaML is then numerically optimized for optimum coupling to a Gaussian mode field in free-space with desired mode-field diameter. Figure B.9 shows the simulated intensity distributions of all printed lens designs, in the order of their mention in the main manuscript. For the sake of better visibility, we normalize the intensity in each z-normal cross section to its respective maximum. The radial $1/\mathrm{e}^2$ intensity drop is marked by white contour lines.

For the lenses in our first and second set of experiments, Fig. B.9(a)-(c), we use a rotational symmetric even-order polynomial representation of the lens surface height,

$$h(r) = c_0 + c_2 r^2 + c_4 r^4 + \dots , \qquad (B.29)$$

where $r = \sqrt{x^2 + y^2}$. The two-surface FaML beam expander, see Fig. B.9(c), produces an expanded MFD of $60\,\mu\mathrm{m}$ and has a correspondingly large second

Fig. B.9: Microlens simulations using in-house-developed simulation software based on a scalar wide-angle unidirectional wave-propagation method [36] for step-index structures. Instead of simulating the entire propagation through FaML pairs, we split the simulation into two parts. The lens shapes of each part are numerically optimized for optimum coupling to a free-space Gaussian with the desired waist diameter at the interface between the two parts. The Subfigures correspond to the various printed designs in the order of their mention in the main manuscript. For the sake of better visibility, we normalize the intensity in each z-normal cross section to its respective maximum. The radial $1/\mathrm{e}^2$ intensity drop is marked by white contour lines. **(a, b)** FaML designs printed on fiber arrays (FA) and on silicon photonic (SiP) chips, respectively, with an expanded beam-waist diameter of $25\,\mu\mathrm{m}$ as used in our first set of experiments, see Section 4.3 of the main manuscript. **(c)** FaML design printed on both FA and InP photo diode arrays (PDA), with an expanded beam-waist diameter of $60\,\mu\mathrm{m}$ as used in our second set of experiments, see Section 4.4 of the main manuscript. **(d, e)** FaML designs printed on arrays of angled facet InP lasers and on FA, respectively, with an expanded beam-waist diameter of $25\,\mu\mathrm{m}$ as used in our third set of experiments, see Section 4.5 of the main manuscript. The simulations are depicted as (x, z)-cut ($y = 0$), and as (y, z)-cut ($x = 0$). For each Subfigure, the dashed lines in the (x, z) and (y, z) cuts indicate the position of the respective other cut.

lens surface. Due to the scaling laws of aberrations [209, 210] we therefore used a maximum of five free parameters c_0, c_2, c_4, c_6 and c_8 for this second surface, whereas all other surfaces required a lesser number of parameters.

For our third set of experiments, we use a more sophisticated parametrization of the lens surfaces. For the FaML on angled facet InP lasers, Fig. B.9(d), we assume a slightly elliptical spot of $3.2\,\mu\text{m} \times 2.2\,\mu\text{m}$ out of the laser, as measured using an infrared microscope equipped with a $100\times / 0.8$ objective in air. To transform the elliptic beam into a beam with a circular cross section, we use a non-rotational symmetric parametrization based on conic sections [211],

$$h(x,y) = h_0 + \frac{x^2 \rho_x + y^2 \rho_y}{1 + \sqrt{1 - (1 + K_x)(x\rho_x)^2 - (1 + K_y)(y\rho_y)^2}} \,, \qquad \text{(B.30)}$$

where ρ_x and ρ_y are the curvatures, i.e., the reciprocal values of the curvature radii, in the respective directions, and where K_x and K_y denote the conic constants in the respective directions. A value of $K > 0$ corresponds to an oblate elliptical cross-section. $K = 0$ corresponds to a spherical cross-section. A value of $0 > K > -1$ corresponds to a prolate elliptical cross-section, $K = -1$ to a parabolic one, and $K < -1$ to a hyperbolic one. For optimization of the lens surface, we vary the parameters ρ_x, ρ_y, K_x, and K_y for best coupling efficiency to a Gaussian beam with the targeted mode-field diameter. Note that a single lens surface is generally insufficient to transform a diverging beam with an elliptic cross section into a collimated beam with a circular cross section and a pre-defined beam diameter. The beam profile generated by the optimized lens surface according to Eq. (B.30) is hence subject to a slight residual ellipticity and astigmatism. The simulated impact on the coupling efficiency, however, is rather small ($< 0.2\,\text{dB}$) and can hence be tolerated.

[End of Supplementary Information of paper [J2]]

C Superconducting nanowire single-photon detector with 3D-printed free-form microlenses

This chapter has been published as Appendix of [J3]. The material from the publication has been adapted to comply with the layout and the structure of this thesis.

[Beginning of Appendix of [J3]]

C.1 Mathematical models and methods for analysis of spheroidal lenses

The ideal lens shapes considered in Section 5.3.1 are obtained by revolving a Cartesian oval curve about its axis of symmetry. This Cartesian oval curve comprises all points having the same linear combination of distances d_1 and $n_{\text{lens}} \times d_2$ from two fixed points F_1 and F_2, respectively, where n_{lens} denotes the refractive index of the lens and where F_2 lies within the lens. The points F_1 and F_2 are referred to as the foci of the lens, where any ray passing through F_1 will be refracted to pass through F_2 as well. In the special case considered in Section 5.3.1, where light is incident as a plane wave, the focus F_1 moves to infinity, and the Cartesian oval turns into an ellipse, which, by revolution about the optical axis, defines the associated spheroidal lens. The geometrical focus S_1 of this spheroid, see Fig. 5.2, then coincides with the internal focus F_2. Starting

from this lens shape, we calculate the effective collection area and the minimum achievable spot size.

C.1.1 Effective collection radius

In the following, we assume a plane-wave-like illumination with approximately constant intensity over the cross section of the lens. To calculate the effective collection area A_C and the associated effective collection radius r_C of such a spheroid, we consider rays that hit the lens surface at a normalized radial position $\rho = r/a$ under an incidence angle $\alpha_\mathrm{vac}(\rho)$ with respect to the local surface normal, see Fig. 5.2. We denote the Fresnel power transmission at this radial position with $\overline{T}(\alpha_\mathrm{vac}(\rho))$, where the overbar denotes the average of the power transmission for p- and s-polarized light. The effective collection area A_C of the lens is defined as the cross-sectional area perpendicular to the optical axis, which would collect the same optical power as the lens itself, and can be calculated by integrating the position-dependent power transmission over the transverse cross section of the spheroidal lens with minor half-axis a,

$$
A_\mathrm{C} = \pi r_\mathrm{C}^2 = \int_0^{2\pi} \int_0^a \overline{T}\left(\alpha_\mathrm{vac}\left(\frac{r}{a}\right)\right) r \, \mathrm{d}r \, \mathrm{d}\varphi
$$
$$
= 2\pi a^2 \int_0^1 \overline{T}\left(\alpha_\mathrm{vac}(\rho)\right) \rho \, \mathrm{d}\rho,
$$
(C.1)

$$
r_\mathrm{C} = a\sqrt{2} \sqrt{\int_0^1 \overline{T}\left(\alpha_\mathrm{vac}(\rho)\right) \rho \, \mathrm{d}\rho}.
$$
(C.2)

The incident angle $\alpha_{\text{vac}}(\rho)$ is found from considering the surface-normal direction of the spheroid and can be calculated from the equation of an ellipse to be

$$\alpha_{\text{vac}}(\rho) = \arctan\left(\xi \frac{1}{\sqrt{(1/\rho)^2 - 1}}\right). \tag{C.3}$$

For the plot in Fig. 5.3(c), we numerically evaluate the integral in Eq. (C.2). For a refractive index $n_{\text{lens}} = 1.5$, we find $r_C \approx 0.94 \times a$.

C.1.2 Estimation of minimum spot size

For estimating the minimum achievable spot size, we calculate the vectorial point spread function according to Richards and Wolf [61, 62]. We chose this approach since the maximum involved ray angle θ_{max} clearly exceeds the validity range of paraxial approximation, see Eq. (5.4) in the main text. We first consider a uniform x-polarized plane-wave illumination at angular frequency ω propagating along the z-direction and use a positive time dependence, i.e., $\exp(\text{j}(\omega t - k_0 z))$, where $k_0 = \omega/c$ is the vacuum wave number and where c denotes the vacuum speed of light. The complex electrical field vector $\underline{\mathbf{E}}(r, \varphi, z)$ is calculated in a cylindrical coordinate system having its origin at the focus S_1 within the lens, see Fig. 5.2. The different components of the vectorial point spread function can be expressed by three integrals I_0, I_1, and I_2 over the ray angle θ, which contain the so-called real-valued pupil apodization function $P(\theta)$, describing the mapping of the incident field amplitudes from a planar to a spherically converging phase front. Denoting the n-th-order Bessel function of the first kind as $J_n(\cdot)$, the E-field can be written as ([61], Eq. (6.5.9) in [62])

$$\underline{\mathbf{E}}(r, \varphi, z) = \text{j}\,A\left\{\left[I_0 + \cos(2\varphi)I_2\right]\hat{\mathbf{e}}_x + \sin(2\varphi)I_2\hat{\mathbf{e}}_y \right.$$
$$\left. + 2\,\text{j}\cos(\phi)I_1\hat{\mathbf{e}}_z\right\}, \tag{C.4}$$

where A is a real-valued amplitude and where the integrals $I_0(r, z)$, $I_1(r, z)$, and $I_2(r, z)$ are calculated as

$$
I_0(r, z) = \int_0^{\theta_{\max}} P(\theta) \sin \theta (1 + \cos \theta) J_0(n_{\text{lens}} k_0 r \sin \theta) \\
\times e^{-j n_{\text{lens}} k_0 z \cos \theta} \, d\theta ,
$$
(C.5)

$$
I_1(r, z) = \int_0^{\theta_{\max}} P(\theta) \sin^2 \theta J_1(n_{\text{lens}} k_0 r \sin \theta) \\
\times e^{-j n_{\text{lens}} k_0 z \cos \theta} \, d\theta ,
$$
(C.6)

$$
I_2(r, z) = \int_0^{\theta_{\max}} P(\theta) \sin \theta (1 - \cos \theta) J_2(n_{\text{lens}} k_0 r \sin \theta) \\
\times e^{-j n_{\text{lens}} k_0 z \cos \theta} \, d\theta .
$$
(C.7)

In these relations, the upper integration limit $\theta_{\max}$ corresponds to the maximum ray angle inside the lens and is given by Eq. (5.4) in the main text. For simplicity, we assume that the SNSPD can be modeled as perfect power detector lying in a z-normal plane that is only sensitive to the flux of incoming photons, irrespective of polarization. We express the flux of photons incident onto the SNSPD by the z-component of the real part of the complex Poynting vector, which turns out to be independent of the azimuthal coordinate φ (Eq. (3.22) in [61]),

$$
S_z(r, z) = \frac{1}{2} \Re\{\underline{\mathbf{E}} \times \underline{\mathbf{H}}^*\} \cdot \hat{\mathbf{e}}_z \propto |I_0|^2 - |I_2|^2 .
$$
(C.8)

To obtain an expression for the pupil apodization function $P(\theta)$, we first consider the so-called ray projection function $g(\theta)$, which can be expressed by the dependence of the radial position $r(\theta)$ of an incident ray on the ray angle within the lens (see Eq. (6.3.1) in [62]),

$$
g(\theta) = r(\theta)/f .
$$
(C.9)

In this relation, f corresponds to the material-sided focal length of the spheroidal lens, see Fig. 5.2 for an illustration of the various quantities. The apodization function can then be derived from energy conservation considerations (see Eq. (6.3.6) in [62]),

$$P(\theta) = \left| \frac{g(\theta)g'(\theta)}{\sin \theta} \right| , \qquad (C.10)$$

where $g'(\theta)$ is the derivative of $g(\theta)$ with respect to θ. We compute the underlying relation between r and θ from the equation of the spheroidal lens surface and geometrical considerations, see Fig. 5.2, and find

$$r(\theta) = \left(\frac{e + \sqrt{1 + \tan^2 \theta}}{1 + \xi^2 \tan^2 \theta} \right) b \tan \theta , \qquad (C.11)$$

where b and e denote the major half axis and the eccentricity of the spheroid, respectively. Using $f = b \times (e + 1)$, see Eq. (5.8), leads to

$$g(\theta) = \left(\frac{e + \sqrt{1 + \tan^2 \theta}}{1 + \xi^2 \tan^2 \theta} \right) \frac{\tan \theta}{e + 1} . \qquad (C.12)$$

For each local incidence angle α_{vac} with respect to the surface normal of the lens, we additionally consider the Fresnel power transmission $\overline{T}(\alpha_{\mathrm{vac}}(r(\theta)/a))$. Note that this represents a simplifying approximation since $\overline{T}(\alpha_{\mathrm{vac}}(r(\theta)/a))$ refers to the average of the power transmission for p- and s-polarized light, whereas our derivation here was based on an incoming x-polarized plane-wave. With this simplification, the modified apodization function can be written as

$$P(\theta) = \left| \frac{g(\theta)g'(\theta)}{\sin \theta} \right| \sqrt{\overline{T} \left(\alpha_{\mathrm{vac}} \left(r(\theta)/a \right) \right)} . \qquad (C.13)$$

The direct relationship between the local incidence angle α_{vac} and the ray angle θ is found by geometrical considerations and Snell's law, see Fig. 5.2, resulting in an implicit equation, see Eq.(5.3) in the main text, which we solve numerically. With this, we can finally evaluate the integrals $I_0(r, z)$, $I_1(r, z)$, and $I_2(r, z)$ in Eqs. (C.5)–(C.7) and calculate the resulting intensity distribution $S(r, z = 0)$

according to Eq. (C.8). The resulting second-moment-radius $w_0 = 2\sigma$ plotted in Fig. 5.3(a) in the main text is obtained from the variance σ^2 of the intensity distribution along the transverse direction,

$$
\begin{aligned}
\sigma^2 &= \frac{\int_0^{2\pi} \int_0^\infty r^2 \cos^2(\varphi) S(r, z=0)\, r\, \mathrm{d}r\, \mathrm{d}\varphi}{\int_0^{2\pi} \int_0^\infty S(r, z=0)\, r\, \mathrm{d}r\, \mathrm{d}\varphi} \\
&= \frac{1}{2} \frac{\int_0^\infty r^2 S(r, z=0) r\, \mathrm{d}r}{\int_0^\infty S(r, z=0) r\, \mathrm{d}r}.
\end{aligned}
\tag{C.14}
$$

C.2 Intrinsic dectection efficiency (IDE) of SNSPD

To draw quantitative conclusions from experimental data, where only the system detection efficiency SDE is accessible, we have to account for the parametric dependency of the intrinsic detection efficiency IDE on the wavelength λ and the bias current I_b. Due to geometrical inhomogeneity, granularity of the nanowire material, and thermally activated fluctuations of its superconducting state, the nanowire randomly switches to the normal conducting state — even in absence of photons — if the bias is close to a so-called switching current I_{sw}, which is usually noticeably lower than the critical current, $I_{\mathrm{sw}}/I_c < 0.7$. The bias-current dependency of the intrinsic detection efficiency $\mathrm{IDE}(\lambda, I_b/I_{\mathrm{sw}})$ is hence typically described using the relative bias I_b/I_{sw}. Regarding the wavelength-dependence for a given bias current, the intrinsic detection efficiency $\mathrm{IDE}(\lambda, I_b/I_{\mathrm{sw}})$ is usually equal to unity up to a bias-dependent cut-off wavelength $\lambda_c(I_b)$. For wavelengths larger than λ_c, $\mathrm{IDE}(\lambda, I_b/I_{\mathrm{sw}})$ decays, where the exact slope of the decay again depends on I_b. At operating temperatures above $4\,\mathrm{K}$, it is not always possible to achieve a cut-off wavelength λ_c larger than the wavelength λ of the test signal by solely increasing the bias current, and the intrinsic detection efficiency remains usually smaller than optimum, $\mathrm{IDE}(\lambda) < 1 \quad \forall \quad I_b < I_{\mathrm{sw}}$. The function $\mathrm{IDE}(\lambda, I_b/I_{\mathrm{sw}})$ can be experimentally inferred from measured photon count rates PCR at different wavelengths λ and bias currents I_b, if the device is operated

under a constant photon flux and if the optical coupling efficiency OCE and the absorption efficiency ABS can be assumed to be wavelength-independent, see Eq.(5.1),

$$
\begin{aligned}
\mathrm{PCR}(\lambda, I_{\mathrm{b}}/I_{\mathrm{sw}}) &\propto \mathrm{SDE}(\lambda, I_{\mathrm{b}}/I_{\mathrm{sw}}) \\
&= \mathrm{OCE} \times \mathrm{ABS} \times \mathrm{IDE}(\lambda, I_{\mathrm{b}}/I_{\mathrm{sw}}) \,.
\end{aligned}
\tag{C.15}
$$

Figure C.1 depicts such a measurement of the photon count rate for an NbN detector that is similar to the devices used in our experiment. The photon count rates are normalized to the maximum values found in the low-wavelength limit, corresponding to an intrinsic detection efficiency $\mathrm{IDE}(\lambda) \approx 1$ below the respective cut-off wavelength $\lambda_{\mathrm{c}}(I_{\mathrm{b}})$. At a temperature of $4.2\,\mathrm{K}$ and a relative bias current $I_{\mathrm{b}}/I_{\mathrm{sw}} = 0.95$, the cut-off wavelength amounts to $\lambda_{\mathrm{c}} \approx 700\,\mathrm{nm}$ [174], indicated by a dashed vertical line in Fig. C.1. Beyond the cutoff wavelength λ_{c}, the IDE roughly follows a straight line in the semi-logarithmic plot, with the magnitude of the slope monotonically decreasing with increasing relative bias $I_{\mathrm{b}}/I_{\mathrm{sw}}$. To adjust bias currents for equal IDE for lensed and reference detector, $\mathrm{IDE}_{\mathrm{lens}} = \mathrm{IDE}_{\mathrm{ref}}$, we use equal relative bias currents $I_{\mathrm{b}}/I_{\mathrm{sw}}$, see Section 5.4.2. To further support the notion that this indeed leads to equal IDE, we perform separate reference measurements using backside illumination of the lensed (lens) detector and the reference (ref) detector at two alternating wavelengths $\lambda_1 = 850\,\mathrm{nm}$ and $\lambda_2 = 1550\,\mathrm{nm}$, and experimentally confirm that the ratios of photon count rates at the two wavelengths are identical,

$$
\frac{\mathrm{PCR}_{\mathrm{lens}}(\lambda_1)}{\mathrm{PCR}_{\mathrm{ref}}(\lambda_1)} = \frac{\mathrm{PCR}_{\mathrm{lens}}(\lambda_2)}{\mathrm{PCR}_{\mathrm{ref}}(\lambda_2)} \,.
\tag{C.16}
$$

If those two ratios are identical, we can infer equal intrinsic detection efficiency even if the backside illumination through the multimode fiber might not be sufficiently homogeneous such that the rate of received photons $R_{r,\mathrm{lens}}$ at the backside of the lensed and $R_{r,\mathrm{ref}}$ at the backside of the reference detector differ. This can be shown by assuming equal and wavelength-independent absorption efficiency ABS, and by substituting $\mathrm{PCR}_{\mathrm{lens}}(\lambda_m) = R_{r,\mathrm{lens}}(\lambda_m) \times \mathrm{ABS} \times$
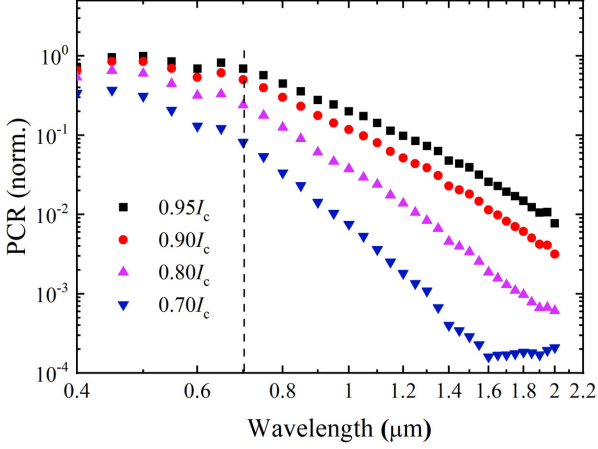
Fig. C.1: Wavelength- and bias-dependent photon count rates of a NbN detector similar to the ones used in our experiment. The device is operated under constant photon flux, and the count rates are normalized to the respective maximum in the limit of low wavelengths. Assuming constant optical coupling efficiency OCE and constant absorption efficiency ABS, these curves represent the dependence of the intrinsic detection efficiency (IDE) on wavelength and bias current. Beyond the bias-current-dependent cutoff wavelength λ_c the curves decay and roughly follow straight lines in the semi-logarithmic plot, with characteristic slopes that monotonically decrease in magnitude with increasing relative bias I_b/I_{sw}. At a temperature of $4.2\,\mathrm{K}$ and bias current $I_b = 0.95 I_{sw}$, the cut-off wavelength amounts to $\lambda_c \approx 700\,\mathrm{nm}$ [174], indicated by a dashed vertical line.

$\mathrm{IDE}_{\mathrm{lens}}(\lambda_m)$, see Eq. (5.1), and analogously $\mathrm{PCR}_{\mathrm{ref}}(\lambda_m) = R_{r,\mathrm{ref}}(\lambda_m) \times \mathrm{ABS} \times \mathrm{IDE}_{\mathrm{ref}}(\lambda_m)$. Equation (C.16) can then be written as

$$\frac{R_{r,\mathrm{lens}}(\lambda_1)}{R_{r,\mathrm{ref}}(\lambda_1)} \frac{\mathrm{IDE}_{\mathrm{lens}}(\lambda_1)}{\mathrm{IDE}_{\mathrm{ref}}(\lambda_1)} = \frac{R_{r,\mathrm{lens}}(\lambda_2)}{R_{r,\mathrm{ref}}(\lambda_2)} \frac{\mathrm{IDE}_{\mathrm{lens}}(\lambda_2)}{\mathrm{IDE}_{\mathrm{ref}}(\lambda_2)} . \tag{C.17}$$

Assuming at least a wavelength-independent ratio of received photons, $R_{r,\mathrm{lens}}(\lambda_1)/R_{r,\mathrm{ref}}(\lambda_1) = R_{r,\mathrm{lens}}(\lambda_2)/R_{r,\mathrm{ref}}(\lambda_2)$, we can further simplify and rearrange Eq. (C.17) to find

$$\frac{\mathrm{IDE}_{\mathrm{lens}}(\lambda_1)}{\mathrm{IDE}_{\mathrm{lens}}(\lambda_2)} = \frac{\mathrm{IDE}_{\mathrm{ref}}(\lambda_1)}{\mathrm{IDE}_{\mathrm{ref}}(\lambda_2)} . \tag{C.18}$$

Equal ratios in Eq. (C.16) thus imply equal decay slopes in the semi-logarithmic plot of Fig. C.1. We can hence conclude that the lensed and reference detector are operated on the same characteristic curve and thus have the same intrinsic detection efficiency IDE if Eq. (C.16) is fulfilled, i.e., if the ratios of photon count rates at the two wavelengths are identical.

[End of Appendix of [J3]]

Bibliography

[1] M. Blaicher, "Photonic packaging enabled by three-dimensional micro-printing", Ph.D. Dissertation, Karlsruher Institut für Technologie (KIT), 2021.

[2] P.-I. Dietrich, M. Blaicher, I. Reuter, M. Billah, T. Hoose, A. Hofmann, C. Caer, R. Dangel, B. Offrein, U. Troppenz, M. Moehrle, W. Freude, and C. Koos, "In situ 3D nanoprinting of free-form coupling elements for hybrid photonic integration", *Nature Photonics* **12**, pp. 241–247 (2018). DOI: `10.1038/s41566-018-0133-4`.

[3] J. Orton, *Semiconductors and the information revolution, Magic crystals that made IT happen.* Elsevier, 2009, ISBN: 978-0-444-53240-4. DOI: `10.1016/b978-0-444-53240-4.x0001-3`.

[4] M. M. Waldrop, "The chips are down for Moore's law", *Nature* **530**, pp. 144–147 (2016). DOI: `10.1038/530144a`.

[5] "Cisco predicts more IP traffic in the next five years than in the history of the internet", The Newsroom — Cisco's Technology News Site. (Nov. 2018), [Online]. Available: `https://newsroom.cisco.com/press-release-content?articleId=1955935` (visited on 12/21/2021).

[6] E. Agrell, M. Karlsson, A. R. Chraplyvy, D. J. Richardson, P. M. Krummrich, P. Winzer, K. Roberts, J. K. Fischer, S. J. Savory, B. J. Eggleton, M. Secondini, F. R. Kschischang, A. Lord, J. Prat, I. Tomkos, J. E. Bowers, S. Srinivasan, M. Brandt-Pearce, and N. Gisin, "Roadmap of optical communications", *Journal of Optics* **18**(6), 063002 (2016). DOI: `10.1088/2040-8978/18/6/063002`.

[7]   C. Doerr, "Silicon photonic integration in telecommunications", *Frontiers in Physics* **3**, 37 (2015). DOI: `10.3389/fphy.2015.00037`.

[8]   E. A. Rank, S. Nevlacsil, P. Muellner, R. Hainberger, M. Salas, S. Gloor, M. Duelk, M. Sagmeister, J. Kraft, R. A. Leitgeb, and W. Drexler, "In vivo human retinal swept source optical coherence tomography and angiography at 830 nm with a CMOS compatible photonic integrated circuit", *Scientific Reports* **11**, 21052 (2021). DOI: `10.1038/s41598-021-00637-4`.

[9]   S. Schneider, M. Lauermann, P.-I. Dietrich, C. Weimann, W. Freude, and C. Koos, "Optical coherence tomography system mass-producible on a silicon photonic chip", *Optics Express* **24**(2), pp. 1573–1586 (2016). DOI: `10.1364/OE.24.001573`.

[10] C. Rogers, A. Y. Piggott, D. J. Thomson, R. F. Wiser, I. E. Opris, S. A. Fortune, A. J. Compston, A. Gondarenko, F. Meng, X. Chen, G. T. Reed, and R. Nicolaescu, "A universal 3D imaging sensor on a silicon photonics platform", *Nature* **590**, pp. 256–261 (2021). DOI: `10.1038/s41586-021-03259-y`.

[11] J. Milvich, D. Kohler, W. Freude, and C. Koos, "Integrated phase-sensitive photonic sensors: A system design tutorial", *Advances in Optics and Photonics* **13**(3), pp. 584–642 (2021). DOI: `10.1364/AOP.413399`.

[12] H. Chen, M. Galili, P. Verheyen, P. De Heyn, G. Lepage, J. De Coster, S. Balakrishnan, P. Absil, L. Oxenlowe, J. Van Campenhout, and G. Roelkens, "100-Gbps RZ data reception in 67-GHz Si-contacted germanium waveguide p-i-n photodetectors", *Journal of Lightwave Technology* **35**(4), pp. 722–726 (2017). DOI: `10.1109/JLT.2016.2593942`.

[13] G. T. Reed, G. Mashanovich, F. Y. Gardes, and D. J. Thomson, "Silicon optical modulators", *Nature Photonics* **4**, pp. 518–526 (2010). DOI: `10.1038/nphoton.2010.179`.

[14] V. Lal, P. Studenkov, T. Frost, H. Tsai, B. Behnia, J. Osenbach, S. Wolf, R. Going, S. Porto, R. Maher, H. Hodaei, J. Zhang, C. Di Giovanni, K. Hoshino, T. Vallaitis, B. Ellis, J. Yan, K. Fong, E. Sooudi, M. Kuntz, S. Buggaveeti, D. Pavinski, S. Sanders, Z. Wang, G. Hoefler, P. Evans,

S. Corzine, T. Butrie, M. Ziari, F. Kish, and D. Welch, "1.6Tbps coherent 2-channel transceiver using a monolithic Tx/Rx InP PIC and single SiGe ASIC", in *Optical Fiber Communication Conference* (OFC 2020), paper M3A.2. DOI: `10.1364/OFC.2020.M3A.2`.

[15] A. Z. Subramanian, P. Neutens, A. Dhakal, R. Jansen, T. Claes, X. Rottenberg, F. Peyskens, S. Selvaraja, P. Helin, B. Du Bois, K. Leyssens, S. Severi, P. Deshpande, R. Baets, and P. Van Dorpe, "Low-loss singlemode PECVD silicon nitride photonic wire waveguides for 532–900 nm wavelength window fabricated within a CMOS pilot line", *IEEE Photonics Journal* **5**(6), 2202809 (2013). DOI: `10.1109/JPHOT.2013.2292698`.

[16] C. G. H. Roeloffzen, M. Hoekman, E. J. Klein, L. S. Wevers, R. B. Timens, D. Marchenko, D. Geskus, R. Dekker, A. Alippi, R. Grootjans, A. van Rees, R. M. Oldenbeuving, J. P. Epping, R. G. Heideman, K. Wörhoff, A. Leinse, D. Geuzebroek, E. Schreuder, P. W. L. van Dijk, I. Visscher, C. Taddei, Y. Fan, C. Taballione, Y. Liu, D. Marpaung, L. Zhuang, M. Benelajla, and K.-J. Boller, "Low-loss Si_3N_4 TriPleX optical waveguides: Technology and applications overview", *IEEE Journal of Selected Topics in Quantum Electronics* **24**(4), pp. 1–21 (2018). DOI: `10.1109/JSTQE.2018.2793945`.

[17] M. H. P. Pfeiffer, A. Kordts, V. Brasch, M. Zervas, M. Geiselmann, J. D. Jost, and T. J. Kippenberg, "Photonic damascene process for integrated high-Q microresonator based nonlinear photonics", *Optica* **3**(1), pp. 20–25 (2016). DOI: `10.1364/OPTICA.3.000020`.

[18] P. Muñoz, G. Micó, L. A. Bru, D. Pastor, D. Pérez, J. D. Doménech, J. Fernández, R. Baños, B. Gargallo, R. Alemany, A. M. Sánchez, J. M. Cirera, R. Mas, and C. Domínguez, "Silicon nitride photonic integration platforms for visible, near-infrared and mid-infrared applications", *Sensors* **17**(9), 2088 (2017). DOI: `10.3390/s17092088`.

[19] K.-J. Boller, A. van Rees, Y. Fan, J. Mak, R. E. M. Lammerink, C. A. A. Franken, P. J. M. van der Slot, D. A. I. Marpaung, C. Fallnich, J. P. Epping, R. M. Oldenbeuving, D. Geskus, R. Dekker, I. Visscher, R. Grootjans, C. G. H. Roeloffzen, M. Hoekman, E. J. Klein, A. Leinse, and

R. G. Heideman, "Hybrid integrated semiconductor lasers with silicon nitride feedback circuits", *Photonics* **7**(1), 4 (2020). DOI: `10.3390/photonics7010004`.

[20] A. R. Cowan, G. W. Rieger, and J. F. Young, "Nonlinear transmission of 1.5 µm pulses through single-mode silicon-on-insulator waveguide structures", *Optics Express* **12**(8), pp. 1611–1621 (2004). DOI: `10.1364/OPEX.12.001611`.

[21] B. Shen, L. Chang, J. Liu, H. Wang, Q.-F. Yang, C. Xiang, R. N. Wang, J. He, T. Liu, W. Xie, J. Guo, D. Kinghorn, L. Wu, Q.-X. Ji, T. J. Kippenberg, K. Vahala, and J. E. Bowers, "Integrated turnkey soliton microcombs", *Nature* **582**, pp. 365–369 (2020). DOI: `10.1038/s41586-020-2358-x`.

[22] A. S. Voloshin, N. M. Kondratiev, G. V. Lihachev, J. Liu, V. E. Lobanov, N. Y. Dmitriev, W. Weng, T. J. Kippenberg, and I. A. Bilenko, "Dynamics of soliton self-injection locking in optical microresonators", *Nature Communications* **12**, 2021 (2021). DOI: `10.1038/s41467-020-20196-y`.

[23] T. Komljenovic, D. Huang, P. Pintus, M. A. Tran, M. L. Davenport, and J. E. Bowers, "Photonic integrated circuits using heterogeneous integration on silicon", *Proceedings of the IEEE* **106**(12), pp. 2246–2257 (2018). DOI: `10.1109/JPROC.2018.2864668`.

[24] P. O'Brien, L. Carrol, C. Eason, and J. S. Lee, "Packaging of silicon photonic devices", in *Silicon Photonics III*, L. Pavesi and D. J. Lockwood, Eds. Springer, 2016, pp. 226–228, ISBN: 978-3-642-10502-9. DOI: `https://doi.org/10.1007/978-3-642-10503-6_7`.

[25] D. Liang, A. W. Fang, H. Park, T. E. Reynolds, K. Warner, D. C. Oakley, and J. E. Bowers, "Low-temperature, strong SiO_2-SiO_2 covalent wafer bonding for III–V compound semiconductors-to-silicon photonic integrated circuits", *Journal of Electronic Materials* **37**(10), pp. 1552–1559 (2008). DOI: `10.1007/s11664-008-0489-1`.

[26] J. S. Lee, L. Carroll, C. Scarcella, N. Pavarelli, S. Menezo, S. Bernabé, E. Temporiti, and P. O'Brien, "Meeting the electrical, optical, and thermal design challenges of photonic-packaging", *IEEE Journal of Selected*

Topics in Quantum Electronics **22**(6), pp. 409–417 (2016). DOI: `10. 1109/JSTQE.2016.2543150`.

[27] R. Marchetti, C. Lacava, L. Carroll, K. Gradkowski, and P. Minzioni, "Coupling strategies for silicon photonics integrated chips", *Photonics Research* **7**(2), pp. 201–239 (2019). DOI: `10.1364/PRJ.7.000201`.

[28] E. R. H. Fuchs, E. J. Bruce, R. J. Ram, and R. E. Kirchain, "Process-based cost modeling of photonics manufacture: The cost competitiveness of monolithic integration of a 1550-nm DFB laser and an electroabsorptive modulator on an inp platform", *Journal of Lightwave Technology* **24**(8), pp. 3175–3186 (2006). DOI: `10.1109/JLT.2006.875961`.

[29] S. Wills. "Photonic pilot lines expand in europe", Optics & Photonics News. (Dec. 2018), [Online]. Available: `https://www.optica-opn. org/home/industry/2018/december/photonic_pilot_lines_ expand_in_europe/` (visited on 12/03/2021).

[30] T. Baldacchini, Ed., *Three-dimensional microfabrication using two-photon polymerization*, 2nd ed. Elsevier, 2020, ISBN: 978-0-12-817827-0. DOI: `10.1016/c2018-0-00278-9`.

[31] I. Sakellari, E. Kabouraki, D. Gray, V. Purlys, C. Fotakis, A. Pikulin, N. Bityurin, M. Vamvakaki, and M. Farsari, "Diffusion-assisted high-resolution direct remtosecond laser writing", *ACS Nano* **6**(3), pp. 2302–2311 (2012). DOI: `10.1021/nn204454c`.

[32] R. Wollhofen, J. Katzmann, C. Hrelescu, J. Jacak, and T. A. Klar, "120 nm resolution and 55 nm structure size in STED-lithography", *Optics Express* **21**(9), pp. 10 831–10 840 (2013). DOI: `10.1364/OE.21.010831`.

[33] M. Blaicher, M. R. Billah, J. Kemal, T. Hoose, P. Marin-Palomo, A. Hofmann, Y. Kutuvantavida, C. Kieninger, P.-I. Dietrich, M. Lauermann, S. Wolf, U. Troppenz, M. Moehrle, F. Merget, S. Skacel, J. Witzens, S. Randel, W. Freude, and C. Koos, "Hybrid multi-chip assembly of optical communication engines by in situ 3D nano-lithography", *Light: Science & Applications* **9**, 71 (2020). DOI: `10.1038/s41377-020-0272-5`.

[34] M. R. Billah, M. Blaicher, T. Hoose, P.-I. Dietrich, P. Marin-Palomo, N. Lindenmann, A. Nesic, A. Hofmann, U. Troppenz, M. Moehrle, S. Randel, W. Freude, and C. Koos, "Hybrid integration of silicon photonics circuits and InP lasers by photonic wire bonding", *Optica* **5**(7), pp. 876–883 (2018). DOI: `10.1364/OPTICA.5.000876`.

[35] R. Tkach and A. Chraplyvy, "Regimes of feedback effects in 1.5-µm distributed feedback lasers", *Journal of Lightwave Technology* **4**(11), pp. 1655–1661 (1986). DOI: `10.1109/JLT.1986.1074666`.

[36] S. Schmidt, T. Tiess, S. Schröter, R. Hambach, M. Jäger, H. Bartelt, A. Tünnermann, and H. Gross, "Wave-optical modeling beyond the thin-element-approximation", *Optics Express* **24**(26), pp. 30 188–30 200 (2016). DOI: `10.1364/OE.24.030188`.

[37] D. Wu, S.-Z. Wu, J. Xu, L.-G. Niu, K. Midorikawa, and K. Sugioka, "Hybrid femtosecond laser microfabrication to achieve true 3D glass/polymer composite biochips with multiscale features and high performance: The concept of ship-in-a-bottle biochip", *Laser & Photonics Reviews* **8**(3), pp. 458–467 (2014). DOI: `https://doi.org/10.1002/lpor.201400005`.

[38] M. Hippler, E. D. Lemma, S. Bertels, E. Blasco, C. Barner-Kowollik, M. Wegener, and M. Bastmeyer, "3D scaffolds to study basic cell biology", *Advanced Materials* **31**, 1808110 (2019). DOI: `https://doi.org/10.1002/adma.201808110`.

[39] J. R. Thompson, K. S. Worthington, B. J. Green, N. K. Mullin, C. Jiao, E. E. Kaalberg, L. A. Wiley, I. C. Han, S. R. Russell, E. H. Sohn, C. A. Guymon, R. F. Mullins, E. M. Stone, and B. A. Tucker, "Two-photon polymerized poly(caprolactone) retinal cell delivery scaffolds and their systemic and retinal biocompatibility", *Acta Biomaterialia* **94**, pp. 204–218 (2019). DOI: `https://doi.org/10.1016/j.actbio.2019.04.057`.

[40] D. Li, C. Liu, Y. Yang, L. Wang, and Y. Shen, "Micro-rocket robot with all-optic actuating and tracking in blood", *Light: Science & Applications* **9**, 84 (2020). DOI: `10.1038/s41377-020-0323-y`.

[41]   C. A. Koepele, M. Guix, C. Bi, G. Adam, and D. J. Cappelleri, "3D-printed microrobots with integrated structural color for identification and tracking", *Advanced Intelligent Systems* **2**, 1900147 (2020). DOI: `https://doi.org/10.1002/aisy.201900147`.

[42]   T. Ergin, N. Stenger, P. Brenner, J. B. Pendry, and M. Wegener, "Three-dimensional invisibility cloak at optical wavelengths", *Science* **328**(5976), pp. 337–339 (2010). DOI: `10.1126/science.1186351`.

[43]   T. Frenzel, M. Kadic, and M. Wegener, "Three-dimensional mechanical metamaterials with a twist", *Science* **358**(6366), pp. 1072–1074 (2017). DOI: `10.1126/science.aao4640`.

[44]   C. He, T. Sun, J. Guo, M. Cao, J. Xia, J. Hu, Y. Yan, and C. Wang, "Chiral metalens of vircular polarization dichroism with helical surface arrays in mid-infrared region", *Advanced Optical Materials* **7**, 1901129 (2019). DOI: `https://doi.org/10.1002/adom.201901129`.

[45]   S. Thiele, K. Arzenbacher, T. Gissibl, H. Giessen, and A. M. Herkommer, "3D-printed eagle eye: Compound microlens system for foveated imaging", *Science Advances* **3**(2), e1602655 (2017). DOI: `10.1126/sciadv.1602655`.

[46]   T. Gissibl, S. Thiele, A. Herkommer, and H. Giessen, "Sub-micrometre accurate free-form optics by three-dimensional printing on single-mode fibres", *Nature Communications* **7**, 11763 (2016). DOI: `10.1038/ncomms11763`.

[47]   H. Wang, Y. Liu, Q. Ruan, H. Liu, R. J. H. Ng, Y. S. Tan, H. Wang, Y. Li, C.-W. Qiu, and J. K. W. Yang, "Off-axis holography with uniform illumination via 3D printed diffractive optical elements", *Advanced Optical Materials* **7**, 1900068 (2019). DOI: `https://doi.org/10.1002/adom.201900068`.

[48]   S. Schmidt, S. Thiele, A. Toulouse, C. Bösel, T. Tiess, A. Herkommer, H. Gross, and H. Giessen, "Tailored micro-optical freeform holograms for integrated complex beam shaping", *Optica* **7**(10), pp. 1279–1286 (2020). DOI: `10.1364/OPTICA.395177`.

[49] M. Göppert-Mayer, "Über Elementarakte mit zwei Quantensprüngen", *Annalen der Physik* **9**, pp. 273–294 (1931).

[50] S. Maruo, O. Nakamura, and S. Kawata, "Three-dimensional microfabrication with two-photon-absorbed photopolymerization", *Optics Letters* **22**(2), pp. 132–134 (1997). DOI: `10.1364/OL.22.000132`.

[51] S. Juodkazis, V. Mizeikis, K. K. Seet, M. Miwa, and H. Misawa, "Two-photon lithography of nanorods in SU-8 photoresist", *Nanotechnology* **16**(6), pp. 846–849 (2005). DOI: `10.1088/0957-4484/16/6/039`.

[52] J. B. Mueller, J. Fischer, F. Mayer, M. Kadic, and M. Wegener, "Polymerization kinetics in three-dimensional direct laser writing", *Advanced Materials* **26**(38), pp. 6566–6571 (2014). DOI: `https://doi.org/10.1002/adma.201402366`.

[53] H.-B. Sun, K. Takada, M.-S. Kim, K.-S. Lee, and S. Kawata, "Scaling laws of voxels in two-photon photopolymerization nanofabrication", *Applied Physics Letters* **83**(6), pp. 1104–1106 (2003). DOI: `10.1063/1.1599968`.

[54] J. Fischer, J. B. Mueller, J. Kaschke, T. J. A. Wolf, A.-N. Unterreiner, and M. Wegener, "Three-dimensional multi-photon direct laser writing with variable repetition rate", *Optics Express* **21**(22), pp. 26 244–26 260 (2013). DOI: `10.1364/OE.21.026244`.

[55] Z. Tomova, N. Liaros, S. A. Gutierrez Razo, S. M. Wolf, and J. T. Fourkas, "In situ measurement of the effective nonlinear absorption order in multiphoton photoresists", *Laser & Photonics Reviews* **10**(5), pp. 849–854 (2016). DOI: `https://doi.org/10.1002/lpor.201600079`.

[56] J. Fischer and M. Wegener, "Three-dimensional optical laser lithography beyond the diffraction limit", *Laser & Photonics Reviews* **7**(1), pp. 22–44 (2013). DOI: `https://doi.org/10.1002/lpor.201100046`.

[57] P. Kiefer, V. Hahn, M. Nardi, L. Yang, E. Blasco, C. Barner-Kowollik, and M. Wegener, "Sensitive photoresists for rapid multiphoton 3D laser micro- and nanoprinting", *Advanced Optical Materials* **8**, 2000895 (2020). DOI: `https://doi.org/10.1002/adom.202000895`.

[58]   L. Yang, A. Münchinger, M. Kadic, V. Hahn, F. Mayer, E. Blasco, C. Barner-Kowollik, and M. Wegener, "On the Schwarzschild effect in 3D two-photon laser lithography", *Advanced Optical Materials* **7**, 1901040 (2019). DOI: `https://doi.org/10.1002/adom.201901040`.

[59]   T. Bückmann, N. Stenger, M. Kadic, J. Kaschke, A. Frölich, T. Kennerknecht, C. Eberl, M. Thiel, and M. Wegener, "Tailored 3D mechanical metamaterials made by dip-in direct-laser-writing optical lithography", *Advanced Materials* **24**(20), pp. 2710–2714 (2012). DOI: `https://doi.org/10.1002/adma.201200584`.

[60]   A. S. van de Nes, L. Billy, S. F. Pereira, and J. J. M. Braat, "Calculation of the vectorial field distribution in a stratified focal region of a high numerical aperture imaging system", *Optics Express* **12**(7), pp. 1281–1293 (2004). DOI: `10.1364/OPEX.12.001281`.

[61]   B. Richards, E. Wolf, and D. Gabor, "Electromagnetic diffraction in optical systems, II. structure of the image field in an aplanatic system", *Proceedings of the Royal Society of London. Series A. Mathematical and Physical Sciences* **253**(1274), pp. 358–379 (1959). DOI: `10.1098/rspa.1959.0200`.

[62]   M. Gu, "Imaging with a high numerical-aperture objective", in *Advanced Optical Imaging Theory*. Springer, 2000, pp. 143–176. DOI: `10.1007/978-3-540-48471-4`.

[63]   E. Abbe, "Beiträge zur Theorie des Mikroskops und der mikroskopischen Wahrnehmung", *Archiv für Mikroskopische Anatomie* **9**, pp. 413–468 (1873). DOI: `10.1007/bf02956173`.

[64]   J. Mertz, *Introduction to Optical Microscopy*, 2nd ed. Cambridge University Press, 2019, p. 77. DOI: `10.1017/9781108552660`.

[65]   M. Pluta, *Advanced Light Microscopy*, *Principles and Basic Properties*, 1st ed. Elsevier, 1988, vol. 1.

[66]   B. Zhang, J. Zerubia, and J.-C. Olivo-Marin, "Gaussian approximations of fluorescence microscope point-spread function models", *Applied Optics* **46**(10), pp. 1819–1829 (2007). DOI: `10.1364/AO.46.001819`.

[67] W. R. Zipfel, R. M. Williams, and W. W. Webb, "Nonlinear magic: Multiphoton microscopy in the biosciences", *Nature Biotechnology* **21**, pp. 1369–1377 (2003). DOI: `10.1038/nbt899`.

[68] C. Ibáñez-López, G. Saavedra, G. Boyer, and M. Martínez-Corral, "Quasi-isotropic 3-D resolution in two-photon scanning microscopy", *Optics Express* **13**(16), pp. 6168–6174 (2005). DOI: `10.1364/OPEX.13.006168`.

[69] J. Fischer, J. B. Mueller, A. S. Quick, J. Kaschke, C. Barner-Kowollik, and M. Wegener, "Exploring the mechanisms in STED-enhanced direct laser writing", *Advanced Optical Materials* **3**(2), pp. 221–232 (2015). DOI: `https://doi.org/10.1002/adom.201400413`.

[70] M. L. Gödecke, "Coupling of photonic wire bonds to vertical device facets", Master's thesis, Karlsruher Institut für Technologie (KIT), 2015.

[71] P. S. Salter and M. J. Booth, "Focussing over the edge: Adaptive subsurface laser fabrication up to the sample face", *Optics Express* **20**(18), pp. 19 978–19 989 (2012). DOI: `10.1364/OE.20.019978`.

[72] M. Blaicher, P.-I. Dietrich, and C. Koos, "Localization of optical coupling points", pat. WO2021175967A1, 2021.

[73] J. W. Goodman, *Introduction to Fourier optics*, 4th ed. Macmillan Learning, 2017, ISBN: 978-1-319-11916-4.

[74] K.-H. Brenner and W. Singer, "Light propagation through microlenses: A new simulation method", *Applied Optics* **32**(26), pp. 4984–4988 (1993). DOI: `10.1364/AO.32.004984`.

[75] M. Fertig and K.-H. Brenner, "Vector wave propagation method", *Journal of the Optical Society of America A* **27**(4), pp. 709–717 (2010). DOI: `10.1364/JOSAA.27.000709`.

[76] M. Fertig, "Vector wave propagation method, Ein Beitrag zum elektromagnetischen Optikrechnen", Ph.D. Dissertation, Universiät Mannheim, 2011.

[77] A. Zangwill, *Modern Electrodynamics*. Cambridge University Press, 2012, p. 690, ISBN: 978-0-521-89697-9. DOI: `10.1017/CBO9781139034777`.

[78] P. Yalamanchili, U. Arshad, Z. Mohammed, P. Garigipati, P. Entschev, B. Kloppenborg, J. Malcolm, and J. Melonakos, *ArrayFire - A high performance software library for parallel computing with an easy-to-use API*, 2015. [Online]. Available: `https://github.com/arrayfire/arrayfire`.

[79] M. Blaicher, M. R. Billah, T. Hoose, P.-I. Dietrich, A. Hofmann, S. Randel, W. Freude, and C. Koos, "3D-printed ultra-broadband highly efficient out-of-plane coupler for photonic integrated circuits", in *Conference on Lasers and Electro-Optics* (CLEO 2018), paper STh1A.1. DOI: `10.1364/CLEO_SI.2018.STh1A.1`.

[80] A. Toulouse, J. Drozella, S. Thiele, H. Giessen, and A. Herkommer, "3D-printed miniature spectrometer for the visible range with a $100 \times 100\ \mu m^2$ footprint", *Light: Advanced Manufacturing* **2**, 2 (2021). DOI: `10.37188/lam.2021.002`.

[81] S. Schmidt, T. Tiess, S. Schröter, A. Schwuchow, M. Jäger, H. Bartelt, A. Tünnermann, and H. Gross, "Noninvasive characterization of optical fibers", *Optics Letters* **42**(23), pp. 4946–4949 (2017). DOI: `10.1364/OL.42.004946`.

[82] K. Weber, F. Hütt, S. Thiele, T. Gissibl, A. Herkommer, and H. Giessen, "Single mode fiber based delivery of OAM light by 3D direct laser writing", *Optics Express* **25**(17), pp. 19 672–19 679 (2017). DOI: `10.1364/OE.25.019672`.

[83] A. Taflove and S. C. Hagness, *Computational electrodynamics: the finite-difference time-domain method*, 3rd ed. Artech House, 2005, p. 9, ISBN: 978-1-58053-832-9.

[84] T. Hoose, M. Blaicher, J. N. Kemal, H. Zwickel, M. R. Billah, P.-I. Dietrich, A. Hofmann, W. Freude, S. Randel, and C. Koos, *Hardwire-configurable photonic integrated circuits enabled by 3D nano-printing*, 2019. arXiv: `1912.09942 [physics.app-ph]`.

[85] M. Mansuripur and E. Wright, "The optics of semiconductor diode lasers", *Optics and Photonics News* **13**(7), pp. 57–61 (2002). [Online]. Available: `https://www.optica-opn.org/home/articles/volume_13/issue_7/departments/none/the_optics_of_semiconductor_diode_lasers/`.

[86] R. W. Gerchberg and W. O. Saxton, "A practical algorithm for the determination of phase from image and diffraction plane pictures", *Optik* **35**, pp. 237–246 (1972).

[87] J. R. Fienup, "Phase retrieval algorithms: A comparison", *Applied Optics*. **21**(15), pp. 2758–2769 (1982). DOI: `10.1364/AO.21.002758`.

[88] G.-Z. Yang, B.-Z. Dong, B.-Y. Gu, J.-Y. Zhuang, and O. K. Ersoy, "Gerchberg–Saxton and Yang–Gu algorithms for phase retrieval in a nonunitary transform system: A comparison", *Applied Optics* **33**(2), pp. 209–218 (1994). DOI: `10.1364/AO.33.000209`.

[89] M. Hayes, "The reconstruction of a multidimensional sequence from the phase or magnitude of its Fourier transform", *IEEE Transactions on Acoustics, Speech, and Signal Processing* **30**(2), pp. 140–154 (1982). DOI: `10.1109/TASSP.1982.1163863`.

[90] M. Pasienski and B. DeMarco, "A high-accuracy algorithm for designing arbitrary holographic atom traps", *Optics Express* **16**(3), pp. 2176–2190 (2008). DOI: `10.1364/OE.16.002176`.

[91] A. Levi and H. Stark, "Image restoration by the method of generalized projections with application to restoration from magnitude", *Journal of the Optical Society of America A* **1**(9), pp. 932–943 (1984). DOI: `10.1364/JOSAA.1.000932`.

[92] V. Soifer, V. Kotlyar, and L. Doskolovich, *Iterative methods for diffractive optical elements computation*. Taylor & Francis, 1997. DOI: `10.1201/9781482272918`.

[93] M. W. Beijersbergen, R. P. C. Coerwinkel, M. Kristensen, and J. P. Woerdman, "Helical-wavefront laser beams produced with a spiral phase-plate", *Optics Communications* **112**(5), pp. 321–327 (1994). DOI: `https://doi.org/10.1016/0030-4018(94)90638-6`.

[94] M. J. Padgett, F. M. Miatto, M. P. J. Lavery, A. Zeilinger, and R. W. Boyd, "Divergence of an orbital-angular-momentum-carrying beam upon propagation", *New Journal of Physics* **17**(2), 023011 (2015). DOI: `10.1088/1367-2630/17/2/023011`.

[95] V. Y. Ivanov, V. P. Sivokon, and M. A. Vorontsov, "Phase retrieval from a set of intensity measurements: Theory and experiment", *Journal of the Optical Society of America A* **9**(9), pp. 1515–1524 (1992). DOI: `10.1364/JOSAA.9.001515`.

[96] L. Bruel, "Numerical phase retrieval from beam intensity measurements in three planes", in *Proc. SPIE* 4932, *Laser-Induced Damage in Optical Materials: 2002 and 7th International Workshop on Laser Beam and Optics Characterization* (2003), pp. 590–598. DOI: `10.1117/12.472377`.

[97] G. R. Brady and J. R. Fienup, "Nonlinear optimization algorithm for retrieving the full complex pupil function", *Optics Express* **14**(2), pp. 474–486 (2006). DOI: `10.1364/OPEX.14.000474`.

[98] F. Zeng, Q. Tan, Y. Yan, and G. Jin, "Hybrid iterative phase retrieval algorithm based on fusion of intensity information in three defocused planes", *Applied Optics* **46**(28), pp. 6872–6878 (2007). DOI: `10.1364/AO.46.006872`.

[99] W. Freude and G. Grau, "Rayleigh-Sommerfeld and Helmholtz-Kirchhoff integrals: Application to the scalar and vectorial theory of wave propagation and diffraction", *Journal of Lightwave Technology* **13**(1), pp. 24–32 (1995). DOI: `10.1109/50.350651`.

[100] L. Chrostowski and M. Hochberg, *Silicon Photonics Design*. Cambridge University Press, 2015. DOI: `10.1017/cbo9781316084168`.

[101]   T. Komljenovic, D. Huang, P. Pintus, M. A. Tran, M. L. Davenport, and J. E. Bowers, "Photonic integrated circuits using heterogeneous integration on silicon", *Proceedings of the IEEE* **106**(12), pp. 2246–2257 (2018). DOI: `10.1109/JPROC.2018.2864668`.

[102]   M. A. Tran, D. Huang, J. Guo, T. Komljenovic, P. A. Morton, and J. E. Bowers, "Ring-resonator based widely-tunable narrow-linewidth Si/InP integrated lasers", *IEEE Journal of Selected Topics in Quantum Electronics* **26**(2), pp. 1–14 (2020). DOI: `10.1109/JSTQE.2019.2935274`.

[103]   T. Komljenovic, L. Liang, R.-L. Chao, J. Hulme, S. Srinivasan, M. Davenport, and J. E. Bowers, "Widely-tunable ring-resonator semiconductor lasers", *Applied Sciences* **7**(7), 732 (2017). DOI: `10.3390/app7070732`.

[104]   H. Guan, A. Novack, T. Galfsky, Y. Ma, S. Fathololoumi, A. Horth, T. N. Huynh, J. Roman, R. Shi, M. Caverley, Y. Liu, T. Baehr-Jones, K. Bergman, and M. Hochberg, "Widely-tunable, narrow-linewidth III-V/silicon hybrid external-cavity laser for coherent communication", *Optics Express* **26**(7), pp. 7920–7933 (2018). DOI: `10.1364/OE.26.007920`.

[105]   N. Kobayashi, K. Sato, M. Namiwaka, K. Yamamoto, S. Watanabe, T. Kita, H. Yamada, and H. Yamazaki, "Silicon photonic hybrid ring-filter external cavity wavelength tunable lasers", *Journal of Lightwave Technology* **33**(6), pp. 1241–1246 (2015). DOI: `10.1109/JLT.2014.2385106`.

[106]   A. Verdier, G. de Valicourt, R. Brenot, H. Debregeas, P. Dong, M. Earnshaw, H. Carrère, and Y.-K. Chen, "Ultrawideband wavelength-tunable hybrid external-cavity lasers", *Journal of Lightwave Technology* **36**(1), pp. 37–43 (2018). DOI: `10.1109/JLT.2017.2757603`.

[107]   J. H. Lee, I. Shubin, J. Yao, J. Bickford, Y. Luo, S. Lin, S. S. Djordjevic, H. D. Thacker, J. E. Cunningham, K. Raj, X. Zheng, and A. V. Krishnamoorthy, "High power and widely tunable Si hybrid external-cavity laser for power efficient Si photonics WDM links", *Optics Express* **22**(7), pp. 7678–7685 (2014). DOI: `10.1364/OE.22.007678`.

[108] B. Stern, X. Ji, A. Dutt, and M. Lipson, "Compact narrow-linewidth integrated laser based on a low-loss silicon nitride ring resonator", *Optics Letters* **42**(21), pp. 4541–4544 (2017). DOI: `10.1364/OL.42.004541`.

[109] Y. Fan, A. van Rees, P. J. M. van der Slot, J. Mak, R. M. Oldenbeuving, M. Hoekman, D. Geskus, C. G. H. Roeloffzen, and K.-J. Boller, "Hybrid integrated InP-Si$_3$N$_4$ diode laser with a 40-Hz intrinsic linewidth", *Optics Express* **28**(15), pp. 21 713–21 728 (2020). DOI: `10.1364/OE.398906`.

[110] C. Xiang, W. Jin, J. Guo, J. D. Peters, M. J. Kennedy, J. Selvidge, P. A. Morton, and J. E. Bowers, "Narrow-linewidth III-V/Si/Si$_3$N$_4$ laser using multilayer heterogeneous integration", *Optica* **7**(1), pp. 20–21 (2020). DOI: `10.1364/OPTICA.384026`.

[111] J. Zhang, Y. Li, S. Dhoore, G. Morthier, and G. Roelkens, "Unidirectional, widely-tunable and narrow-linewidth heterogeneously integrated III-V-on-silicon laser", *Optics Express* **25**(6), pp. 7092–7100 (2017). DOI: `10.1364/OE.25.007092`.

[112] T. Takeuchi, M. Takahashi, K. Suzuki, S. Watanabe, and H. Yamazaki, "Wavelength tunable laser with silica-waveguide ring resonators", *IEICE Transactions on Electronics* **E92.C**(2), pp. 198–204 (2009). DOI: `10.1587/transele.E92.C.198`.

[113] J. Zhang, G. Muliuk, J. Juvert, S. Kumari, J. Goyvaerts, B. Haq, C. Op de Beeck, B. Kuyken, G. Morthier, D. Van Thourhout, R. Baets, G. Lepage, P. Verheyen, J. Van Campenhout, A. Gocalinska, J. O'Callaghan, E. Pelucchi, K. Thomas, B. Corbett, A. J. Trindade, and G. Roelkens, "III-V-on-Si photonic integrated circuits realized using micro-transfer-printing", *APL Photonics* **4**(11), 110803 (2019). DOI: `10.1063/1.5120004`.

[114] B. Haq, S. Kumari, K. Van Gasse, J. Zhang, A. Gocalinska, E. Pelucchi, B. Corbett, and G. Roelkens, "Micro-transfer-printed III-V-on-silicon C-band semiconductor optical amplifiers", *Laser & Photonics Reviews* **14**(7), 1900364 (2020). DOI: `10.1002/lpor.201900364`.

[115] C. O. de Beeck, B. Haq, L. Elsinger, A. Gocalinska, E. Pelucchi, B. Corbett, G. Roelkens, and B. Kuyken, "Heterogeneous III-V on silicon nitride amplifiers and lasers via microtransfer printing", *Optica* **7**(5), pp. 386–393 (2020). DOI: `10.1364/OPTICA.382989`.

[116] I. Lucci, C. Cornet, M. Bahri, and Y. Léger, "Thermal management of monolithic versus heterogeneous lasers integrated on silicon", *IEEE Journal of Selected Topics in Quantum Electronics* **22**(6), pp. 35–42 (2016). DOI: `10.1109/JSTQE.2016.2621558`.

[117] X. Zheng, I. Shubin, J.-H. Lee, S. Lin, Y. Luo, J. Yao, S. S. Djordjevic, J. Bovington, D. Y. Lee, H. D. Thacker, C. Zhang, K. Raj, J. E. Cunningham, and A. V. Krishnamoorthy, "III-V/Si hybrid laser arrays using Back End of the Line (BEOL) integration", *IEEE Journal of Selected Topics in Quantum Electronics* **22**(6), pp. 204–217 (2016). DOI: `10.1109/JSTQE.2016.2593100`.

[118] J. S. Lee, L. Carroll, C. Scarcella, N. Pavarelli, S. Menezo, S. Bernabé, E. Temporiti, and P. O'Brien, "Meeting the electrical, optical, and thermal design challenges of photonic-packaging", *IEEE Journal of Selected Topics in Quantum Electronics* **22**(6), pp. 409–417 (2016). DOI: `10.1109/JSTQE.2016.2543150`.

[119] N. Lindenmann, S. Dottermusch, M. L. Goedecke, T. Hoose, M. R. Billah, T. P. Onanuga, A. Hofmann, W. Freude, and C. Koos, "Connecting silicon photonic circuits to multicore fibers by photonic wire bonding", *Journal of Lightwave Technology* **33**(4), pp. 755–760 (2015). DOI: `10.1109/JLT.2014.2373051`.

[120] L. Coldren, "Monolithic tunable diode lasers", *IEEE Journal of Selected Topics in Quantum Electronics* **6**(6), pp. 988–999 (2000). DOI: `10.1109/2944.902147`.

[121] B. Liu, A. Shakouri, and J. Bowers, "Wide tunable double ring resonator coupled lasers", *IEEE Photonics Technology Letters* **14**(5), pp. 600–602 (2002). DOI: `10.1109/68.998697`.

[122] C. Xiang, P. A. Morton, and J. E. Bowers, "Ultra-narrow linewidth laser based on a semiconductor gain chip and extended Si_3N_4 bragg grating", *Optics Letters* **44**(15), pp. 3825–3828 (2019). DOI: `10.1364/OL.44.003825`.

[123] A. Ruocco and W. Bogaerts, "Fully integrated SOI wavelength meter based on phase shift technique", in *IEEE 12th International Conference on Group IV Photonics* (GFP 2015), pp. 131–132. DOI: `10.1109/Group4.2015.7305985`.

[124] C. Xiang, M. A. Tran, T. Komljenovic, J. Hulme, M. Davenport, D. Baney, B. Szafraniec, and J. E. Bowers, "Integrated chip-scale Si_3N_4 wavemeter with narrow free spectral range and high stability", *Optics Letters* **41**(14), pp. 3309–3312 (2016). DOI: `10.1364/OL.41.003309`.

[125] J. N. Kemal, P. Marin-Palomo, V. Panapakkam, P. Trocha, S. Wolf, K. Merghem, F. Lelarge, A. Ramdane, S. Randel, W. Freude, and C. Koos, "Coherent WDM transmission using quantum-dash mode-locked laser diodes as multi-wavelength source and local oscillator", *Optics Express* **27**(22), pp. 31 164–31 175 (2019). DOI: `10.1364/oe.27.031164`.

[126] K. Kikuchi, "Characterization of semiconductor-laser phase noise and estimation of bit-error rate performance with low-speed offline digital coherent receivers", *Optics Express* **20**(5), pp. 5291–5302 (2012). DOI: `10.1364/oe.20.005291`.

[127] T. Komljenovic, S. Srinivasan, E. Norberg, M. Davenport, G. Fish, and J. E. Bowers, "Widely tunable narrow-linewidth monolithically integrated external-cavity semiconductor lasers", *IEEE Journal of Selected Topics in Quantum Electronics* **21**(6), pp. 214–222 (2015). DOI: `10.1109/JSTQE.2015.2422752`.

[128] P. Dong, Y.-K. Chen, G.-H. Duan, and D. T. Neilson, "Silicon photonic devices and integrated circuits", *Nanophotonics* **3**(4-5), pp. 215–228 (2014). DOI: `doi:10.1515/nanoph-2013-0023`.

[129] T. Harter, S. Muehlbrandt, S. Ummethala, A. Schmid, S. Nellen, L. Hahn, W. Freude, and C. Koos, "Silicon-plasmonic integrated circuits for terahertz signal generation and coherent detection", *Nature Photonics* **12**, pp. 625–633 (2018). DOI: `10.1038/s41566-018-0237-x`.

[130] S. Ummethala, T. Harter, K. Koehnle, Z. Li, S. Muehlbrandt, Y. Kutuvantavida, J. Kemal, P. Marin-Palomo, J. Schaefer, A. Tessmann, S. K. Garlapati, A. Bacher, L. Hahn, M. Walther, T. Zwick, S. Randel, W. Freude, and C. Koos, "THz-to-optical conversion in wireless communications using an ultra-broadband plasmonic modulator", *Nature Photonics* **13**, pp. 519–524 (2019). DOI: `10.1038/s41566-019-0475-6`.

[131] J. Sun, E. Timurdogan, A. Yaacobi, E. S. Hosseini, and M. R. Watts, "Large-scale nanophotonic phased array", *Nature* **493**, pp. 195–199 (2013). DOI: `10.1038/nature11727`.

[132] P. Trocha, M. Karpov, D. Ganin, M. H. P. Pfeiffer, A. Kordts, S. Wolf, J. Krockenberger, P. Marin-Palomo, C. Weimann, S. Randel, W. Freude, T. J. Kippenberg, and C. Koos, "Ultrafast optical ranging using microresonator soliton frequency combs", *Science* **359**(6378), pp. 887–891 (2018). DOI: `10.1126/science.aao3924`.

[133] C. Ranacher, C. Consani, A. Tortschanoff, R. Jannesari, M. Bergmeister, T. Grille, and B. Jakoby, "Mid-infrared absorption gas sensing using a silicon strip waveguide", *Sensors and Actuators A: Physical* **277**, pp. 117–123 (2018). DOI: `https://doi.org/10.1016/j.sna.2018.05.013`.

[134] A. Fernández Gavela, D. Grajales García, J. C. Ramirez, and L. M. Lechuga, "Last advances in silicon-based optical biosensors", *Sensors* **16**(3), 285 (2016). DOI: `10.3390/s16030285`.

[135] P. Steglich, M. Hülsemann, B. Dietzel, and A. Mai, "Optical biosensors based on silicon-on-insulator ring resonators: A review", *Molecules* **24**(3), 519 (2019). DOI: `10.3390/molecules24030519`.

[136] B. Snyder, B. Corbett, and P. O'Brien, "Hybrid integration of the wavelength-tunable laser with a silicon photonic integrated circuit",

Journal of Lightwave Technology **31**(24), pp. 3934–3942 (2013). DOI: `10.1109/JLT.2013.2276740`.

[137] T. Lamprecht, F. Horst, R. Dangel, R. Beyeler, N. Meier, L. Dellmann, M. Gmur, C. Berger, and B. Offrein, "Passive alignment of optical elements in a printed circuit board", in *56th Electronic Components and Technology Conference* (2006), pp. 761–767. DOI: `10.1109/ECTC.2006.1645743`.

[138] M. H. Hu, M. H. Rasmussen, C. Caneau, H. Leblanc, S. Coleman, X. Liu, H. Nguyen, N. Visovsky, and C. Zah, "Measurement of very low residual reflections in lensed-fiber pigtailed semiconductor optical amplifier", in *Optical Amplifiers and Their Applications* (2005), paper WA4. DOI: `10.1364/OAA.2005.WA4`.

[139] "V-grooves and fiber arrays", SQS-Fiberoptics, [Online]. Available: `https://www.sqs-fiberoptics.com/images/pdf-soubory/v-grooves-fiber-optic-arrays.pdf` (visited on 02/23/2022).

[140] C. Scarcella, K. Gradkowski, L. Carroll, J.-S. Lee, M. Duperron, D. Fowler, and P. O'Brien, "Pluggable single-mode fiber-array-to-PIC coupling using micro-lenses", *IEEE Photonics Technology Letters* **29**(22), pp. 1943–1946 (2017). DOI: `10.1109/LPT.2017.2757082`.

[141] R. Phelan, B. Kelly, J. O'Carroll, C. Herbert, A. Duke, and J. O'Gorman, "$-40°C < T < 95°C$ Mode-hop-free operation of uncooled AlGaInAs-MQW discrete-mode laser diode with emission at $\lambda = 1.3\,\mu m$", *Electronics Letters* **45**(1), p. 43 (2009). DOI: `10.1049/el:20092208`.

[142] D. Taillaert, H. Chong, P. Borel, L. Frandsen, R. De La Rue, and R. Baets, "A compact two-dimensional grating coupler used as a polarization splitter", *IEEE Photonics Technology Letters* **15**(9), pp. 1249–1251 (2003). DOI: `10.1109/LPT.2003.816671`.

[143] Z. Xiao, T.-Y. Liow, J. Zhang, P. Shum, and F. Luan, "Bandwidth analysis of waveguide grating coupler", *Optics Express* **21**(5), pp. 5688–5700 (2013). DOI: `10.1364/OE.21.005688`.

[144]   J. Hong, A. M. Spring, F. Qiu, and S. Yokoyama, "A high efficiency silicon nitride waveguide grating coupler with a multilayer bottom reflector", *Scientific Reports* **9**, 12988 (2019). DOI: `10.1038/s41598-019-49324-5`.

[145]   A. He, X. Guo, K. Wang, Y. Zhang, and Y. Su, "Low loss, large bandwidth fiber-chip edge couplers based on silicon-on-insulator platform", *Journal of Lightwave Technology* **38**(17), pp. 4780–4786 (2020). DOI: `DOI: 10.1109/JLT.2020.2995544`.

[146]   B. Peng, T. Barwicz, A. Sahin, T. Houghton, B. Hedrick, Y. Bian, M. Rakowski, S. Hu, J. Ayala, C. Meagher, Z. Sowinski, K. Nummy, A. Stricker, J. Lubguban, H. Chen, B. Fasano, I. Melville, Z.-J. Wu, J. K. Cho, A. Jacob, D. Riggs, D. Berger, T. Letavic, A. Yu, J. Pellerin, and K. Giewont, "A CMOS compatible monolithic fiber attach solution with reliable performance and self-alignment", in *Optical Fiber Communication Conference* (OFC 2020), paper Th3I.4. DOI: `10.1364/OFC.2020.Th3I.4`.

[147]   T. Barwicz, B. Peng, R. Leidy, A. Janta-Polczynski, T. Houghton, M. Khater, S. Kamlapurkar, S. Engelmann, P. Fortier, N. Boyer, and W. M. J. Green, "Integrated metamaterial interfaces for self-aligned fiber-to-chip coupling in volume manufacturing", *IEEE Journal of Selected Topics in Quantum Electronics* **25**(3), pp. 1–13 (2019). DOI: `10.1109/JSTQE.2018.2879018`.

[148]   "Chromatic confocal technology", Precitec GmbH & Co. KG, [Online]. Available: `https://www.precitec.com/optical-3dmetrology/technology/chromatic-confocal-sensors/` (visited on 02/23/2022).

[149]   H. Zhang, L. Xiao, B. Luo, J. Guo, L. Zhang, and J. Xie, "The potential and challenges of time-resolved single-photon detection based on current-carrying superconducting nanowires", *Journal of Physics D: Applied Physics* **53**, 013001 (2019). DOI: `10.1088/1361-6463/ab4146`.

[150]   G. N. Gol'tsman, O. Okunev, G. Chulkova, A. Lipatov, A. Semenov, K. Smirnov, B. Voronov, A. Dzardanov, C. Williams, and R. Sobolewski,

"Picosecond superconducting single-photon optical detector", *Applied Physics Letters* **79**(6), pp. 705–707 (2001). DOI: `10.1063/1.1388868`.

[151] D. V. Reddy, R. R. Nerem, S. W. Nam, R. P. Mirin, and V. B. Verma, "Superconducting nanowire single-photon detectors with 98% system detection efficiency at 1550 nm", *Optica* **7**(12), pp. 1649–1653 (2020). DOI: `10.1364/OPTICA.400751`.

[152] B. Korzh, Q.-Y. Zhao, S. Frasca, D. Zhu, E. Ramirez, E. Bersin, M. Colangelo, A. E. Dane, A. D. Beyer, J. Allmaras, E. E. Wollman, K. K. Berggren, and M. D. Shaw, "WSi superconducting nanowire single photon detector with a temporal resolution below 5 ps", in *Conference on Lasers and Electro-Optics* (CLEO 2018), paper FW3F.3. DOI: `10.1364/CLEO_QELS.2018.FW3F.3`.

[153] W. Pernice, C. Schuck, O. Minaeva, M. Li, G. Goltsman, A. Sergienko, and H. Tang, "High-speed and high-efficiency travelling wave single-photon detectors embedded in nanophotonic circuits", *Nature Communications* **3**, 1325 (2012). DOI: `10.1038/ncomms2307`.

[154] L. Xue, Z. Li, L. Zhang, D. Zhai, Y. Li, S. Zhang, M. Li, L. Kang, J. Chen, P. Wu, and Y. Xiong, "Satellite laser ranging using superconducting nanowire single-photon detectors at 1064 nm wavelength", *Optics Letters* **41**(16), pp. 3848–3851 (2016). DOI: `10.1364/OL.41.003848`.

[155] H. Li, S. Chen, L. You, W. Meng, Z. Wu, Z. Zhang, K. Tang, L. Zhang, W. Zhang, X. Yang, X. Liu, Z. Wang, and X. Xie, "Superconducting nanowire single photon detector at 532 nm and demonstration in satellite laser ranging", *Optics Express* **24**(4), pp. 3535–3542 (2016). DOI: `10.1364/OE.24.003535`.

[156] L. Chen, D. Schwarzer, J. A. Lau, V. B. Verma, M. J. Stevens, F. Marsili, R. P. Mirin, S. W. Nam, and A. M. Wodtke, "Ultra-sensitive mid-infrared emission spectrometer with sub-ns temporal resolution", *Optics Express* **26**(12), pp. 14 859–14 868 (2018). DOI: `10.1364/OE.26.014859`.

[157] R. Cheng, C.-L. Zou, X. Guo, S. Wang, X. Han, and H. X. Tang, "Broadband on-chip single-photon spectrometer", *Nature Communications* **10**, 4104 (2019). DOI: `10.1038/s41467-019-12149-x`.

[158] J. Toussaint, S. Dochow, I. Latka, A. Lukic, T. May, H.-G. Meyer, K. Il'in, M. Siegel, and J. Popp, "Proof of concept of fiber dispersed Raman spectroscopy using superconducting nanowire single-photon detectors", *Optics Express* **23**(4), pp. 5078–5090 (2015). DOI: `10.1364/OE.23.005078`.

[159] R. H. Hadfield, "Single-photon detectors for optical quantum information applications", *Nature Photonics* **3**, pp. 696–705 (2009). DOI: `10.1038/nphoton.2009.230`.

[160] D. Stucki, N. Walenta, F. Vannel, R. T. Thew, N. Gisin, H. Zbinden, S. Gray, C. R. Towery, and S. Ten, "High rate, long-distance quantum key distribution over 250 km of ultra low loss fibres", *New Journal of Physics* **11**, 075003 (2009). DOI: `10.1088/1367-2630/11/7/075003`.

[161] Y. Hochberg, I. Charaev, S.-W. Nam, V. Verma, M. Colangelo, and K. K. Berggren, "Detecting sub-GeV dark matter with superconducting nanowires", *Physical Review Letters* **123**, 151802 15 (2019). DOI: `10.1103/PhysRevLett.123.151802`.

[162] M. D. Shaw, F. Marsili, A. D. Beyer, J. A. Stern, G. V. Resta, P. Ravindran, S. Chang, J. Bardin, D. S. Russell, J. W. Gin, F. D. Patawaran, V. B. Verma, R. P. Mirin, S. W. Nam, and W. H. Farr, "Arrays of WSi superconducting nanowire single photon detectors for deep-space optical communications", in *Conference on Lasers and Electro-Optics* (CLEO 2015), paper JTh2A.68. DOI: `10.1364/CLEO_AT.2015.JTh2A.68`.

[163] M. Schwartz, E. Schmidt, U. Rengstl, F. Hornung, S. Hepp, S. L. Portalupi, K. Ilin, M. Jetter, M. Siegel, and P. Michler, "Fully on-chip single-photon Hanbury-Brown and Twiss experiment on a monolithic semiconductor–superconductor platform", *Nano Letters* **18**(11), pp. 6892–6897 (2018). DOI: `10.1021/acs.nanolett.8b02794`.

[164] C. Zhang, W. Zhang, J. Huang, L. You, H. Li, C. lv, T. Sugihara, M. Watanabe, H. Zhou, Z. Wang, and X. Xie, "NbN superconducting nanowire single-photon detector with an active area of 300 µm-in-diameter", *AIP Advances* **9**, 075214 (2019). DOI: `10.1063/1.5095842`.

[165] N. Calandri, Q.-Y. Zhao, D. Zhu, A. Dane, and K. K. Berggren, "Superconducting nanowire detector jitter limited by detector geometry", *Applied Physics Letters* **109**, 152601 (2016). DOI: `10.1063/1.4963158`.

[166] A. Korneev, P. Kouminov, V. Matvienko, G. Chulkova, K. Smirnov, B. Voronov, G. N. Gol'tsman, M. Currie, W. Lo, K. Wilsher, J. Zhang, W. Słysz, A. Pearlman, A. Verevkin, and R. Sobolewski, "Sensitivity and gigahertz counting performance of NbN superconducting single-photon detectors", *Applied Physics Letters* **84**, 5338 (2004). DOI: `10.1063/1.1764600`.

[167] I. Charaev, T. Silbernagel, B. Bachowsky, A. Kuzmin, S. Doerner, K. Ilin, A. Semenov, D. Roditchev, D. Y. Vodolazov, and M. Siegel, "Enhancement of superconductivity in NbN nanowires by negative electron-beam lithography with positive resist", *Journal of Applied Physics* **122**, 083901 (2017). DOI: `10.1063/1.4986416`.

[168] A. Bogucki, Ł. Zinkiewicz, M. Grzeszczyk, W. Pacuski, K. Nogajewski, T. Kazimierczuk, A. Rodek, J. Suffczyński, K. Watanabe, T. Taniguchi, P. Wasylczyk, M. Potemski, and P. Kossacki, "Ultra-long-working-distance spectroscopy of single nanostructures with aspherical solid immersion microlenses", *Light: Science & Applications* **9**, 48 (2020). DOI: `10.1038/s41377-020-0284-1`.

[169] R. Descartes, "Des figures qui doivent avoir les corps transparents pour detourner les rayons en toutes les facons qui servent a la vue", in *Discours de La Methode Pour Bien Conduire Sa Raison et Chercher La Vérité Dans Les Sciences, plus La Dioptrique, Les Météores et La Géométrie Qui Sont Des Essais de Cette Méthode*. De l'Imprimerie de Ian Maire, 1637, *La dioptrique*, pp. 89–121.

[170]   S. Dottermusch, D. Busko, M. Langenhorst, U. W. Paetzold, and B. S. Richards, "Exposure-dependent refractive index of Nanoscribe IP-Dip photoresist layers", *Optics Letters* **44**(1), pp. 29–32 (2019). DOI: `10.1364/OL.44.000029`.

[171]   M. Schmid, D. Ludescher, and H. Giessen, "Optical properties of photoresists for femtosecond 3D printing: Refractive index, extinction, luminescence-dose dependence, aging, heat treatment and comparison between 1-photon and 2-photon exposure", *Optical Materials Express* **9**(12), pp. 4564–4577 (2019). DOI: `10.1364/OME.9.004564`.

[172]   S. Schmidt, S. Thiele, A. Herkommer, A. Tünnermann, and H. Gross, "Rotationally symmetric formulation of the wave propagation method — application to the straylight analysis of diffractive lenses", *Optics Letters* **42**(8), pp. 1612–1615 (2017). DOI: `10.1364/OL.42.001612`.

[173]   E. E. Wollman, V. B. Verma, A. E. Lita, W. H. Farr, M. D. Shaw, R. P. Mirin, and S. W. Nam, "Kilopixel array of superconducting nanowire single-photon detectors", *Optics Express* **27**(24), pp. 35 279–35 289 (2019). DOI: `10.1364/OE.27.035279`.

[174]   I. Charaev, "Improving the spectral bandwidth of superconducting nanowire single-photon detectors (SNSPDs)", Ph.D. Dissertation, Karlsruher Institut für Technologie (KIT), 2018.

[175]   K. J. Schafer, J. M. Hales, M. Balu, K. D. Belfield, E. W. Van Stryland, and D. J. Hagan, "Two-photon absorption cross-sections of common photoinitiators", *Journal of Photochemistry and Photobiology A: Chemistry* **162**(2-3), pp. 497–502 (2004). DOI: `10.1016/S1010-6030(03)00394-0`.

[176]   M. Sartison, K. Weber, S. Thiele, L. Bremer, S. Fischbach, T. Herzog, S. Kolatschek, M. Jetter, S. Reitzenstein, A. Herkommer, P. Michler, S. L. Portalupi, and H. Giessen, "3D printed micro-optics for quantum technology: Optimised coupling of single quantum dot emission into a single-mode fibre", *Light: Advanced Manufacturing* **2**, 6 (2021). DOI: `10.37188/lam.2021.006`.

[177] L. Bremer, K. Weber, S. Fischbach, S. Thiele, M. Schmidt, A. Kagan-skiy, S. Rodt, A. Herkommer, M. Sartison, S. L. Portalupi, P. Michler, H. Giessen, and S. Reitzenstein, "Quantum dot single-photon emission coupled into single-mode fibers with 3D printed micro-objectives", *APL Photonics* **5**, 106101 (2020). DOI: `10.1063/5.0014921`.

[178] A. G. Kozorezov, C. Lambert, F. Marsili, M. J. Stevens, V. B. Verma, J. P. Allmaras, M. D. Shaw, R. P. Mirin, and S. W. Nam, "Fano fluctuations in superconducting-nanowire single-photon detectors", *Physical Review B* **96**, 054507 (2017). DOI: `10.1103/PhysRevB.96.054507`.

[179] M. Hofherr, D. Rall, K. Ilin, M. Siegel, A. Semenov, H.-W. Hübers, and N. A. Gippius, "Intrinsic detection efficiency of superconducting nanowire single-photon detectors with different thicknesses", *Journal of Applied Physics* **108**, 014507 (2010). DOI: `10.1063/1.3437043`.

[180] J. R. Clem and K. K. Berggren, "Geometry-dependent critical currents in superconducting nanocircuits", *Physical Review B* **84**, 174510 (2011). DOI: `10.1103/PhysRevB.84.174510`.

[181] M. Sidorova, A. Semenov, H.-W. Hübers, A. Kuzmin, S. Doerner, K. Ilin, M. Siegel, I. Charaev, and D. Vodolazov, "Timing jitter in photon detection by straight superconducting nanowires: Effect of magnetic field and photon flux", *Physical Review B* **98**, 134504 (2018). DOI: `10.1103/PhysRevB.98.134504`.

[182] L. Mandel, "Fluctuations of photon beams and their correlations", *Proceedings of the Physical Society* **72**(6), pp. 1037–1048 (1958). DOI: `10.1088/0370-1328/72/6/312`.

[183] S. Miki, T. Yamashita, M. Fujiwara, M. Sasaki, and Z. Wang, "Multi-channel SNSPD system with high detection efficiency at telecommunication wavelength", *Optics Letters* **35**(13), pp. 2133–2135 (2010). DOI: `10.1364/OL.35.002133`.

[184] G. Cojoc, C. Liberale, P. Candeloro, F. Gentile, G. Das, F. De Angelis, and E. Di Fabrizio, "Optical micro-structures fabricated on top of optical fibers by means of two-photon photopolymerization", *Microelectronic*

Engineering **87**(5-8), pp. 876–879 (2010). DOI: `10.1016/j.mee.2009.12.046`.

[185] H. E. Williams, D. J. Freppon, S. M. Kuebler, R. C. Rumpf, and M. A. Melino, "Fabrication of three-dimensional micro-photonic structures on the tip of optical fibers using SU-8", *Optics Express* **19**(23), pp. 22 910– 22 922 (2011). DOI: `10.1364/OE.19.022910`.

[186] A. J. Miller, A. E. Lita, B. Calkins, I. Vayshenker, S. M. Gruber, and S. W. Nam, "Compact cryogenic self-aligning fiber-to-detector coupling with losses below one percent", *Optics Express* **19**(10), pp. 9102–9110 (2011). DOI: `10.1364/OE.19.009102`.

[187] R. Cheng, X. Guo, X. Ma, L. Fan, K. Y. Fong, M. Poot, and H. X. Tang, "Self-aligned multi-channel superconducting nanowire single-photon detectors", *Optics Express* **24**(24), pp. 27 070–27 076 (2016). DOI: `10.1364/OE.24.027070`.

[188] M. A. Wolff, F. Beutel, M. Häußler, H. Gehring, R. Stegmüller, N. Walter, W. Hartmann, M. Tillmann, M. Wahl, T. Röhlicke, A. Bülter, D. Wernicke, N. Perlot, J. Rödiger, W. H. P. Pernice, and C. Schuck, "Waveguide-integrated superconducting nanowire singlephoton detector array for ultra-fast quantum key distribution", in *Conference on Lasers and Electro-Optics* (CLEO 2020), paper SM4O.5. DOI: `10.1364/CLEO_SI.2020.SM4O.5`.

[189] C. Schuck, W. H. P. Pernice, and H. X. Tang, "NbTiN superconducting nanowire detectors for visible and telecom wavelengths single photon counting on Si_3N_4 photonic circuits", *Applied Physics Letters* **102**, 051101 (2013). DOI: `10.1063/1.4788931`.

[190] P. Rath, O. Kahl, S. Ferrari, F. Sproll, G. Lewes-Malandrakis, D. Brink, K. Ilin, M. Siegel, C. Nebel, and W. Pernice, "Superconducting single-photon detectors integrated with diamond nanophotonic circuits", *Light: Science & Applications* **4**, e338–e338 (2015). DOI: `10.1038/lsa.2015.111`.

[191] E. Knehr, "Technology and readout for scaling up superconducting nanowire single-photon detectors", in preparation, Ph.D. Dissertation, Karlsruher Institut für Technologie (KIT), 2022, *in preparation*.

[192] A. Yariv, "Universal relations for coupling of optical power between microresonators and dielectric waveguides", *Electronics Letters* **36**(4), pp. 321–322 (2000). DOI: `10.1049/el:20000340`.

[193] D. G. Rabus, "Ring resonators: Theory and modeling", in *Integrated Ring Resonators*. Springer, 2017, pp. 3–40. DOI: `10.1007/978-3-540-68788-7_2`.

[194] W. Bogaerts, P. De Heyn, T. Van Vaerenbergh, K. De Vos, S. Kumar Selvaraja, T. Claes, P. Dumon, P. Bienstman, D. Van Thourhout, and R. Baets, "Silicon microring resonators", *Laser & Photonics Reviews* **6**(1), pp. 47–73 (2012). DOI: `https://doi.org/10.1002/lpor.201100017`.

[195] E. Dulkeith, F. Xia, L. Schares, W. M. J. Green, and Y. A. Vlasov, "Group index and group velocity dispersion in silicon-on-insulator photonic wires", *Optics Express* **14**(9), pp. 3853–3863 (2006). DOI: `10.1364/OE.14.003853`.

[196] T. Carmon, L. Yang, and K. J. Vahala, "Dynamical thermal behavior and thermal self-stability of microcavities", *Optics Express* **12**(20), pp. 4742–4750 (2004). DOI: `10.1364/OPEX.12.004742`.

[197] C. Xiang, W. Jin, J. Guo, C. Williams, A. M. Netherton, L. Chang, P. A. Morton, and J. E. Bowers, "Effects of nonlinear loss in high-Q Si ring resonators for narrow-linewidth III-V/Si heterogeneously integrated tunable lasers", *Optics Express* **28**(14), pp. 19 926–19 936 (2020). DOI: `10.1364/OE.394491`.

[198] A. C. Turner-Foster, M. A. Foster, J. S. Levy, C. B. Poitras, R. Salem, A. L. Gaeta, and M. Lipson, "Ultrashort free-carrier lifetime in low-loss silicon nanowaveguides", *Optics Express* **18**(4), pp. 3582–3591 (2010). DOI: `10.1364/OE.18.003582`.

[199]   P. Trocha, J. Gärtner, P. Marin-Palomo, W. Freude, W. Reichel, and C. Koos, "Analysis of Kerr comb generation in silicon microresonators under the influence of two-photon absorption and fast free-carrier dynamics", *Phys. Rev. A* **103**, 063515 6 (2021). DOI: `10.1103/PhysRevA.103.063515`.

[200]   T. Kita, R. Tang, and H. Yamada, "Narrow spectral linewidth silicon photonic wavelength tunable laser diode for digital coherent communication system", *IEEE Journal of Selected Topics in Quantum Electronics* **22**(6), pp. 23–34 (2016). DOI: `10.1109/JSTQE.2016.2559418`.

[201]   R. Kazarinov and C. Henry, "The relation of line narrowing and chirp reduction resulting from the coupling of a semiconductor laser to passive resonator", *IEEE Journal of Quantum Electronics* **23**(9), pp. 1401–1409 (1987). DOI: `10.1109/JQE.1987.1073531`.

[202]   M. Osinski and J. Buus, "Linewidth broadening factor in semiconductor lasers — an overview", *IEEE Journal of Quantum Electronics* **23**(1), pp. 9–29 (1987). DOI: `10.1109/JQE.1987.1073204`.

[203]   L. A. Coldren, S. W. Corzine, and M. L. Mashanovitch, *Diode Lasers and Photonic Integrated Circuits*. Wiley, 2012, ISBN: 9781118148181.

[204]   C. Henry, "Theory of the linewidth of semiconductor lasers", *IEEE Journal of Quantum Electronics* **18**(2), pp. 259–264 (1982). DOI: `10.1109/JQE.1982.1071522`.

[205]   W. B. Joyce and B. C. DeLoach, "Alignment of Gaussian beams", *Applied Optics* **23**(23), pp. 4187–4196 (1984). DOI: `10.1364/AO.23.004187`.

[206]   D. Lenstra, B. Verbeek, and A. Den Boef, "Coherence collapse in single-mode semiconductor lasers due to optical feedback", *IEEE Journal of Quantum Electronics* **21**(6), pp. 674–679 (1985). DOI: `10.1109/JQE.1985.1072725`.

[207]   C. Henry and R. Kazarinov, "Instability of semiconductor lasers due to optical feedback from distant reflectors", *IEEE Journal of Quantum Electronics* **22**(2), pp. 294–301 (1986). DOI: `10.1109/JQE.1986.1072959`.

[208]   R. O. Miles, A. Dandridge, A. B. Tveten, H. F. Taylor, and T. G. Giallorenzi, "Feedback-induced line broadening in cw channel-substrate planar laser diodes", *Applied Physics Letters* **37**(11), pp. 990–992 (1980). DOI: `10.1063/1.91744`.

[209]   A. W. Lohmann, "Scaling laws for lens systems", *Applied Optics* **28**(23), pp. 4996–4998 (1989). DOI: `10.1364/AO.28.004996`.

[210]   D. J. Brady and N. Hagen, "Multiscale lens design", *Optics Express* **17**(13), pp. 10 659–10 674 (2009). DOI: `10.1364/OE.17.010659`.

[211]   R. Schuhmann, "Description of aspheric surfaces", *Advanced Optical Technologies* **8**(3-4), pp. 267–278 (2019). DOI: `doi:10.1515/aot-2019-0011`.

Glossary

List of abbreviations

3D	Three-dimensional
ABS	Absorption efficiency
Al	Aluminum
AlN	Aluminum nitride
AOM	Accousto-optic modulator
AR	Anti-reflection
ASE	Amplified spontaneous emission
BEOL	Back-end of line
BPM	Beam-propagation method
CIRC	(Fiber optic) circulator
CPT	Cavity phase tuner
CR	(Pulse) count rate
DC	Direct current
DCR	Dark count rate
DFB	Distributed feedback
EC	Edge coupler
ECL	External-cavity laser
EDFA	Erbium-doped fiber amplifier
FA	Fiber array
FaML	Facet-attached microlens
FCA	Free carrier absorption
FC/PC	Fiber-optic connector ("ferrule connector") with "physical contact" polish

FC/APC	Fiber-optic connector ("ferrule connector") with "angled physical contact" polish
FDTD	Finite-difference time-domain
FEOL	Front-end of line
FF	Fill factor
FFT	Fast-Fourier transform
FM	Frequency modulation
FSR	Free spectral range
GS	Gerchberg-Saxton (phase retrieval algorithm)
GC	Grating coupler
GDD	Group delay dispersion
GPU	Graphic processing unit
GRIN	Graded-index
He	Helium
HR	High-reflectivity
IDE	Intrinsic detection efficiency
IFTA	Iterative Fourier transform algorithm
IMT	Institute of Microstructure Technology
InP	Indium phosphide
InAlGaAs	Indium aluminum gallium arsenide
InGaAsP	Indium gallium arsenide phosphide
IPQ	Institute of Photonics and Quantum Electronics
IS	Integrating sphere
KIT	Karlsruhe Institute of Technology
LiDAR	"Light detection and ranging" or "Laser imaging, detection, and ranging"
LO	Local oscillator
MBR	Multi-photon bolometric regime
MFD	Mode-field diameter
MM	Multimode
MMF	Multimode fiber
MMI	Multimode interference coupler
MPL	Multi-photon lithography

MPP	Multi-photon polymerization
NbN	Niobium nitride
NA	Numerical aperture
OAM	Orbital angular momentum
OCE	Optical coupling efficiency
OSA	Optical spectrum analizer
PBS	Polarization beam splitter
PC	(Fiber optic) polarization controller
PCR	Photon count rate
PD	Photo diode
PDA	Photo diode array
PDK	Process design kit
PDL	Polarization dependent loss
PIC	Photonic integrated circuit
p-i-n	p-doped-intrinsic-n-doped
PGMEA	Poly glycol methyl ether acetate
PLC	Planar lightwave circuit
PWB	Photonic wire bond
RIN	Relative intensity noise
RSOA	Reflective semiconductor optical amplifier
RF	Radio frequency
SBMT	Submount
SDE	System detection efficiency
SEM	Scanning electron microscopy
SI	International System of Units (*"Système international d'unités"*)
SiN	Silicon nitride (integrated optical platform)
SiP	Silicon photonics
SM	Single-mode
SMF	Single-mode fiber
SMSR	Side mode suppresion ratio
SNSPD	Superconducting nanowire single-photon detector
SOA	Semiconductor optical amplifier
SOI	Silicon-on-insulator

SSE	Sum squared error
TE	(Quasi) transverse-electric polarization
TM	(Quasi) transverse-magnetic polarization
TLS	Tunable laser source
TPA	Two-photon absorption
UV	Ultraviolet
VOA	Variable optical attenuator
WG	Waveguide
WPM	Wave-propagation method

List of mathematical symbols

Uppercase Latin symbols

A_C	Effective collection area
A_D	Detector active area
B	Buildup factor (power enhancement factor) of ring resonators
D	Lithographic dose, with polymerization threshold value D_th
D_1, D_2	Diameters of the ring resonators R1, R2
$\underline{E}_\mathrm{i,d,t,a}$	Complex amplitudes of the electric mode fields at input, drop, through, and add port of ring resonators
$\underline{E}(x, y, z)$	Complex electric field in scalar approximation
$\underline{\mathbf{E}}(r, \varphi, z)$	Complex electric field vector in cylindrical coordinate system
F^2	Linewidth reduction factor of ECL, $F^2 = \delta f_0 / \delta f$
$\mathcal{F}_{xy}$	Two-dimensional spatial Fourier transform
G_D	Lens gain
$\mathcal{H}(k_x, k_y)$	Amplitude transfer function
I	Chapter 2: Intensity | Chapters 3 and 4: Pump current
I_b	Bias current of SNSPD
I_sw	Switching current of SNSPD
$J_1(\cdot)$	First-order Bessel function of the first kind
K_x, K_y	Conic constants (lens parametrization based on conic sections)

L	Circumference of ring resonator
N	Order of nonlinearity
$\mathcal{O}()$	Bachmann-Landau notation ("big O notation")
P	(Optical) power
P_{o}	(Total) output power
P_{opt}	Average optical power
P_{π}	π-power for thermal tuning of the ring resonators
$P(\theta)$	Pupil apodization function
Q	Quality factor
$R_{\mathrm{i,r,a}}$	Rate of incident, received, and absorbed photons
S	Responsivity of the photodiode
$S_{\mathrm{F}}(f)$	FM-noise spectrum
S_z	z-component of the real part of the complex Poynting vector
T	Tuning enhancement factor
$T_{\mathrm{a}}, T_{\mathrm{L}}, T_{\mathrm{R}}$	Power transmission factor for an axial, lateral, and angular misalignment, respectively
T_{c}	Critical temperature of SNSPD
T_p, T_s	Fresnel power transmission factors for p and s-polarization, with average $\overline{T}$

Lowercase Latin symbols

a	Unless specified differently: Loss in dB | Chapter 3: Real-valued amplitude round-trip transmission factor for ring resonators | Chapter 5: Minor half-axis of the spheroid
b	Major half-axis of the spheroid
c	Vacuum speed of light, $299\,792\,458$ m/s
$c_0, c_2, \ldots$	Parameters for a rotational symmetric even-order polynomial representation of lens surfaces
d	Chapter 2: (Horizontal) distance to chip facet | Chapter 5: Linear eccentricity of the spheroid | Appendix B: Lateral misalignment
e	Eccentricity of the spheroid
$\hat{\mathbf{e}}_x, \hat{\mathbf{e}}_y, \hat{\mathbf{e}}_z$	Unit vectors in the x, y, z direction

245

e	Euler's number, $2.71828\ldots$
f	Unless specified differently: Frequency | Chapter 5: Focal length
δf	Intrinsic (Lorentzian) linewidth of the ECL
δf_0	Intrinsic (Lorentzian) linewidth of a Fabry-Pérot laser with mirror amplitude reflection factors r_{b} and $|\underline{r}_{\mathrm{eff}}|$
Δf	Frequency detuning
$\Delta f_{\min}$	Lower bound estimate for Δf_{tun}
Δf_{tun}	Achievable frequency detuning for emission into a single longitudinal mode
$g(\theta)$	Ray projection function
h	Chapter 2: (Vertical) distance below chip surface | Appendix A: Planck constant, $6.62607015 \times 10^{-34}$ Js
$\hbar$	Reduced Planck constant, $\hbar = h/(2\pi)$
$h(x,y)$	Lens surface height profile
h_0	Lens apex height
i	photocurrent
$\mathrm{j} = \sqrt{-1}$	Imaginary unit
k_0	Free-space propagation constant, $k_0 = \omega/c$
n	Refractive index
n_{e}	Effective (modal) refractive index
n_{eg}	Effective (modal) group refractive index, $n_{\mathrm{eg}} = n_{\mathrm{e}} + \omega\, \mathrm{d}n/\, \mathrm{d}\omega$
n_{sp}	Population inversion factor
$p_m(n)$	Probability to observe a voltage pulse originating from n aborbed photons for impulses with an average of m photons
$p_{m,\mathrm{tot}}$	Total photon detection probability for impulses with an average of m photons
r	Radius
r_{A}	Aperture radius
r_{C}	Effective collection radius
Δr	Lateral displacement
r_{b}	Frequency-independent amplitude reflection coefficent of back facet
$\underline{r}_{\mathrm{eff}}$	Frequency-dependent complex amplitude reflection coefficent
s	Axial misalignment

t	Time
w_0	Gaussian waist radius, resp. second-moment-radius $w_0 = 2\sigma$ of a spot with approximately Gaussian intensity distribution
$w(z)$	z-dependent spot radius of a Gaussian beam
x, y, z	Cartesian coordinate axes
z_{DOF}	(One-sided) depth of field
z_{R}	Rayleigh distance of a Gaussian beam

Greek symbols

α	Power loss coefficient (unit cm^{-1})
α_{i}	Power loss coefficient for the internal loss of the RSOA, accounting for excess losses of the active waveguide without the contribution from band-to-band transitions
α_{R}	Distributed mirror power loss coefficient
α_{vac}	Angle of impinging ray w.r.t. local lens surface normal
α_{lens}	Ray angle w.r.t. local lens surface normal within the lens
α_{H}	Henry factor (Linewidth enhancement factor)
$\beta(\omega)$	Frequency-dependent propagation constant
γ	Misalignment angle of illumination w.r.t. surface normal
γ_{max}	Maximum tolerable angular misalignment
$\delta(x, y)$	Two-dimensional delta distribution
$\zeta(z)$	z-dependent Gouy-phase of a Gaussian beam
η	Power transmission factor
ϑ	Incidence angle w.r.t. the surface normal of a plane-parallel slab
θ	Unless specified differently: Ray angle w.r.t. optical axis | Appendix B: Angular misalignment
$\theta(\omega)$	Frequency-dependent round-trip phase for ring resonators
θ_{div}	Asymptotic divergence angle of a Gaussian beam
$\Theta_{z,m}(x, y)$	Stencil function
κ	Real-valued amplitude transmission coefficient between ring resonator and bus waveguide
$\kappa(z)$	z-dependent phase-front curvature of a Gaussian beam

λ	Wavelength
ν	Orbital angular momentum (OAM) order
ξ	Ratio between the major half-axis b and the minor half-axis a of the spheroid
π	Archimedes' constant, $3.14159\ldots$
ρ	Normalized radial position, $\rho = r/a$
ρ_x, ρ_y	Curvatures along the x and y direction (lens parametrization based on conic sections)
σ	Standard deviation
τ	Chapter 2: Exposure time | Chapter 3: Real-valued amplitude coupling coefficent between ring resonator and bus waveguide
τ_0	Photon round-trip time
$\tau_{m \to m'}$	Perpendicular amplitude Fresnel transmission coefficient from material m to material m'
ϕ	Photon flux
φ	Chapter 4: Out-of-plane tilt angle | Appendix C: Azimuth angle
$\varphi(\omega)$	Frequency-dependent phase
φ_0	Phase offset
$\varphi(x,y)$	Phase distribution on a transverse plane
$\Psi(x,y,z)$	Optical field in scalar approximation
ω	Angular frequency

Danksagung

Macht's gut und danke für den Fisch (So long, and thanks for all the fish)[1]!

Eine Vielzahl an Personen hat mich in der Entstehung der vorliegenden Arbeit unterstützt und diese ermöglicht. Ihnen allen gilt mein herzlicher Dank. Einigen möchte ich an dieser Stelle meinen ganz besonderen Dank entgegenbringen.

Meinem Doktorvater Professor Christian Koos möchte ich besonders für das mir entgegengebrachte Vertrauen und das hohe Interesse an meiner Arbeit danken. Die wissenschaftliche Freiheit, die er mir gab, und seine ambitionierten Ideen haben wesentlich zur Entstehung und zum Erfolg dieser Arbeit beigetragen.

Herrn Professor Wolfgang Freude gilt mein herzlichster Dank für die geduldige Durchsicht meiner Arbeiten, für die offenen und konstruktiven Diskussionen, und für die wertvolle Kritik. Seine konsequente Arbeitsweise hat mich zutiefst inspiriert. Weiterhin möchte ich mich bei ihm für ein ermutigendes Gespräch in

---

[1] Douglas Adams, "Per Anhalter durch die Galaxis", 4. Band, 1985 ("The Hitchhiker's Guide to the Galaxy", 4th vol., 1984)

meinem ersten Promotionsjahr bedanken, ohne welches die vorliegende Arbeit nie zustandegekommen wäre.

Ein ganz besonderer Dank gilt meinen aktuellen und ehemaligen Bürokollegen. Allen voran bedanke ich mich bei Pascal Maier für die enge Zusammenarbeit und die engagierte Hilfe im Forschungsprojekt PRIMA. Zusammen haben wir wohl die ein oder andere Unmöglichkeit möglich gemacht. Meinem Vorgänger Matthias Blaicher danke ich für das reichhaltige technologische Erbe, auf dem die vorliegende Arbeit aufbauen konnte. Von Tobias Hoose und Muhammad Rodlin ("Oding") Billah durfte ich das nötige handwerkliche Geschick zum Aufbau von Multi-Chip-Modulen erlernen, was mich wohl von einem Grobmotoriker zu einem feinmechanisch geschickten Menschen gemacht hat. Mit Mareike Trappen durfte ich wochenlang das Leid von Schulungen und Prozessvorentwicklung an einer industriellen Assembliermaschine teilen. Philipp-Immanuel Dietrich danke ich für die Bereitstellung diverser Photoresists, sowie für die Beschaffung zahlreicher Testchips. Zu guter Letzt danke ich unserer jüngsten Bürokollegin Yiyang Bao für die künftige Pflege der Quellcode-Repositorien, sowie für kritische Fragen und Anmerkungen, welche zur allgemeinen Verständlichkeit der vorliegenden Arbeit beigetragen haben. An dieser Stelle erlaube ich mir die Anmerkung, dass unser Maskottchen, das Kamel, nur einen Höcker hat, und infolgedessen präziser als Dromedar (lat. *Camelus dromedarius*) zu bezeichnen ist.

Allen anderen aktuellen und ehemaligen wissenschaftlichen Wegbegleitern am IPQ möchte ich ebenfalls herzlich für die schöne Zeit danken. Aus diversen Diskussionen und der Zusammenarbeit im Labor habe ich viel von euch gelernt. Ganz besonderer Dank gebührt in diesem Zusammenhang dem Betreuer meiner Masterarbeit, Clemens Kieninger. Bei Huanfa Peng und Artem Kuzmin bedanke ich mich insbesondere für den Aufwand im Rahmen der Review-Prozesse meiner Publikationen. Pablo Marin-Palomo und Christoph Füllner möchte ich für die Unterstützung bei diversen Linienbreitenmessungen danken. Stefan Singer, Christian Bremauer und Yung Chen danke ich für die anwendungsbezogene Zusammenarbeit. Einige Projekte mögen in Vergessenheit geraten sein, und einige Messungen haben es nie in eine Publikation geschafft. Dennoch sollte der Aufwand dahinter gewürdigt werden. Daher gilt mein besonderer Dank an dieser Stelle Juned Nassir

List of publications

Journal publications

[J1] **Y. Xu**[†], P. Maier[†], M. Blaicher, P.-I. Dietrich, P. Marin-Palomo, W. Hartmann, Y. Bao, H. Peng, M. R. Billah, S. Singer, U. Troppenz, M. Moehrle, S. Randel, W. Freude, and C. Koos, "Hybrid external-cavity lasers (ECL) using photonic wire bonds as coupling elements", *Scientific Reports* **11**, 16426 (2021). DOI: `10.1038/s41598-021-95981-w`.
[†] **authors contributed equally to the work**.

[J2] **Y. Xu**, P. Maier, M. Trappen, P.-I. Dietrich, M. Blaicher, R. Jutas, A. Weber, T. Kind, C. Dankwart, J. Stephan, A. Steffan, A. Abbasi, P. Morrissey, K. Gradkowski, B. Kelly, P. O'Brien, W. Freude, and C. Koos, "3D-printed facet-attached microlenses for advanced photonic system assembly" (2022), *to be submitted*.

[J3] **Y. Xu**, A. Kuzmin, E. Knehr, M. Blaicher, K. Ilin, P.-I. Dietrich, W. Freude, M. Siegel, and C. Koos, "Superconducting nanowire single-photon detector with 3D-printed free-form microlenses", *Optics Express* **29**(17), pp. 27 708–27 731 (2021). DOI: `10.1364/OE.427639`.

[J4] S. Singer, **Y. Xu**, S. T. Skacel, H. Zwickel, P. Maier, L. Freter, P.-I. Dietrich, M. Kaschel, C. Menzel, S. Randel, W. Freude, and C. Koos, "3D-printed facet-attached optical elements for beam shaping in optical phased arrays" (2022), *submitted*. [Online]. Available: `https://arxiv.org/abs/2203.12989`.

[J5] P. Maier[†], **Y. Xu**[†], M. Trappen, M. Lauermann, A. Henninger-Ludwig, H. Kapim, T. Kind, A. Weber, M. Blaicher, P.-I. Dietrich, C. Wurster, S. Randel, W. Freude, and C. Koos, "3D-printed facet-attached optical elements for connecting VCSEL and photodiodes to fiber arrays and multi-core fibers" (2022), *in preparation*.
[†] **authors contributed equally to the work**.

[J6] M. Trappen, M. Blaicher, P.-I. Dietrich, C. Dankwart, **Y. Xu**, T. Hoose, M. R. Billah, A. Abbasi, R. Baets, U. Troppenz, M. Theurer, K. Wörhoff, M. Seyfried, W. Freude, and C. Koos, "3D-printed optical probes for wafer-level testing of photonic integrated circuits", *Optics Express* **28**(25), pp. 37 996–38 007 (2020). DOI: `10.1364/OE.405139`.

[J7] I.-L. Bundalo, A. Annoni, R. Baets, F. Blache, L. Carrol, S. Collins, P.-I. Dietrich, L. Halmo, F. Jorge, M. Karppinen, M. Kaunisto, B. Kelly, C. Koos, M. Lahti, T. Marcello, J. Lee, J. Missinne, P. E. Morrissey, P. Ossieur, R. Pessina, T. Sterken, G. V. Steenberge, A. Vannucci, A. Vannucchi, R. Verplancke, P. Wuytens, **Y. Xu**, M. Zoldak, and P. O'Brien, "PIXAPP Photonics Packaging Pilot Line — development of a silicon photonic optical transceiver with pluggable fiber connectivity", *Journal of Selected Topics in Quantum Electronics* **28**(3), 8300311 (2022). DOI: `10.1109/JSTQE.2022.3158891`.

[J8] T. Anagnos, M. Trappen, B. C. K. Tiong, T. Feger, S. Yerolatsitis, R. J. Harris, J. Lozi, N. Jovanovic, T. A. Birks, S. Vievard, O. Guyon, I. Gris-Sánchez, S. G. Leon-Saval, B. Norris, S. Y. Haffert, P. Hottinger, M. Blaicher, **Y. Xu**, C. H. Betters, C. Koos, D. W. Coutts, C. Schwab, and A. Quirrenbach, "3D-M3: High-spatial-resolution spectroscopy with extreme AO and 3D-printed micro-lenslets", *Applied Optics* **60**(19), pp. D108–D121 (2021). DOI: `10.1364/AO.420855`.

[J9] S. Y. Haffert, R. J. Harris, A. Zanutta, F. A. Pike, A. Bianco, E. M. A. Redaelli, A. Benoît, D. G. MacLachlan, C. A. Ross, I. Gris-Sánchez, M. D. Trappen, **Y. Xu**, M. Blaicher, P. Maier, G. Riva, B. Sinquin, C. Kulcsár, N. A. Bharmal, É. Gendron, L. Staykov, T. J. Morris, S. Barboza, N. Münch, L. F. Bardou, L. Prengère, H.-F. G. Raynaud, P.

Hottinger, T. Anagnos, J. Osborn, C. Koos, R. R. Thomson, T. A. Birks, I. A. G. Snellen, and C. U. Keller, "Diffraction-limited integral-field spectroscopy for extreme adaptive optics systems with the multicore fiber-fed integral-field unit", *Journal of Astronomical Telescopes, Instruments, and Systems* **6**(4), 045007 (2020). DOI: `10.1117/1.JATIS.6.4.045007`.

Conference publications

[C1] **Y. Xu**[†], P. Maier[†], M. Blaicher, P.-I. Dietrich, P. Marin-Palomo, W. Hartmann, M. R. Billah, U. Troppenz, M. Möhrle, S. Randel, W. Freude, and C. Koos, "InP/Silicon hybrid external-cavity lasers (ECL) using photonic wirebonds as coupling elements", in *Optical Fiber Communication Conference* (OFC 2020), paper M4H.6. DOI: `10.1364/OFC.2020.M4H.6`.
[†] **authors contributed equally to the work**.

[C2] P. Maier, C. Bremauer, Y. Bao, **Y. Xu**, W. Freude, and C. Koos, "Swept-source optical coherence tomography (OCT) using a hybrid silicon photonic external-cavity laser (ECL)", in *Conference on Lasers and Electro-Optics* (CLEO 2022), paper AM5I.4.

[C3] P. Maier, Y. Chen, **Y. Xu**, M. Blaicher, D. Geskus, R. Dekker, J. Liu, P.-I. Dietrich, H. Peng, S. Randel, W. Freude, T. J. Kippenberg, and C. Koos, "InP/Si_3N_4 hybrid external-cavity laser with sub-kHz linewidth acting as a pump source for Kerr frequency combs", in *European Conference on Optical Communication* (ECOC 2022), *accepted*.

[C4] E. Knehr, **Y. Xu**, Y. Bao, P. Maier, C. Jimenez, K. Ilin, M. Ziegler, H. Schmidt, S. Kempf, A. Kuzmin, C. Koos, and M. Siegel, "Optical packaging of SNSPDs with photonic wire bonds", in *European Conference on Applied Superconductivity* (EUCAS 2021), *invited*.

[C5]   S. Singer, **Y. Xu**, S. T. Skacel, H. Zwickel, P. Maier, P.-I. Dietrich, M. Kaschel, C. Menzel, W. Freude, and C. Koos, "3D-printed facet-attached optical elements for beam shaping in solid-state phased arrays", in *Conference on Lasers and Electro-Optics* (CLEO 2022), paper SM4P.5.

[C6]   P. Maier[†], **Y. Xu**[†], M. Lauermann, A. Henninger-Ludwig, H. Kapim, M. Trappen, T. Kind, A. Weber, M. Blaicher, P.-I. Dietrich, C. Wurster, S. Randel, W. Freude, and C. Koos, "3D-printed optical elements for coupling of VCSEL and photodiode arrays to multi-core fibers in an SFP transceiver assembly", in *Optical Fiber Communication Conference* (OFC 2022), paper W2A.1. DOI: `10.1364/OFC.2022.W2A.1`.

[†] **authors contributed equally to the work**.

[C7]   T. Anagnos, P. Maier, P. Hottinger, C. H. Betters, T. Feger, S. G. Leon-Saval, I. Gris-Sánchez, S. Yerolatsitis, J. Lozi, T. A. Birks, S. Vievard, N. Jovanovic, A. D. Rains, M. J. Ireland, R. J. Harris, B. C. K. Tiong, O. Guyon, B. Norris, S. Y. Haffert, M. Blaicher, **Y. Xu**, M. Straub, J.-U. Pott, O. Sawodny, P. L. Neureuther, D. W. Coutts, C. Schwab, C. Koos, and A. Quirrenbach, "An innovative integral field unit upgrade with 3D-printed micro-lenses for the RHEA at Subaru", in *Proc. SPIE* 11451, *Advances in Optical and Mechanical Technologies for Telescopes and Instrumentation IV* (2020), paper 114516Y. DOI: `10.1117/12.2560626`.

[C8]   S. Y. Haffert, R. J. Harris, A. Zanutta, F. A. Pike, A. Bianco, E. Redaelli, A. Benoît, D. G. MacLachlan, C. A. Ross, I. Gris-Sánchez, M. D. Trappen, **Y. Xu**, M. Blaicher, P. Maier, G. Riva, B. Sinquin, C. Kulcsár, N. A. Bharmal, E. Gendron, L. Staykov, T. J. Morris, S. Barboza, N. Muench, L. Bardour, L. Prengère, H.-F. Raynaud, P. Hottinger, T. Anagnos, J. Osborn, C. Koos, R. R. Thompson, T. A. Birks, I. A. G. Snellen, C. U. Keller, L. Close, and J. R. Males, "Multi-core fibre-fed integral-field unit (MCIFU): overview and first-light", in *Proc. SPIE* 11448, *Adaptive Optics Systems VII* (2020). DOI: `10.1117/12.2562719`.

[C9]   M. Trappen, M. Blaicher, P.-I. Dietrich, T. Hoose, **Y. Xu**, M. R. Billah, W. Freude, and C. Koos, "3D-printed optics for wafer-scale probing", in *European Conference on Optical Communication* (ECOC 2018), paper Tu4C.2. DOI: `10.1109/ECOC.2018.8535123`.

[C10]   C. Koos, W. Freude, S. Randel, M. R. Billah, M. Blaicher, P.-I. Dietrich, T. Hoose, **Y. Xu**, J. N. Kemal, A. Nesic, and A. Hofmann, "Photonic wire bonding and 3D nanoprinting in photonic integration – from lab demonstrations to production", in *European Conference on Optical Communication* (ECOC 2018), *invited*. DOI: `10.1109/ECOC.2018.8535426`.

[C11]   C. Koos, W. Freude, S. Randel, P.-I. Dietrich, M. Blaicher, **Y. Xu**, M. R. Billah, T. Hoose, M. Trappen, and A. Hofmann, "Efficient coupling interfaces in photonic systems enabled by printed freeform micro-optics", in *International Conference on Transparent Optical Networks* (ICTON 2018), paper Mo.D5.5 (*invited*). DOI: `10.1109/ICTON.2018.8473851`.

[C12]   M. R. Billah, J. N. Kemal, P. Marin-Palomo, M. Blaicher, Y. Kutuvantavida, C. Kieninger, H. Zwickel, P.-I. Dietrich, S. Wolf, T. Hoose, **Y. Xu**, U. Troppenz, M. Moehrle, S. Randel, W. Freude, and C. Koos, "Four-channel 784 Gbit/s transmitter module enabled by photonic wire bonding and silicon-organic hybrid modulators", in *European Conference on Optical Communication* (ECOC 2017), paper Th.PDP.C.1 (*postdeadline*). DOI: `10.1109/ECOC.2017.8346094`.